Deformation and fracture of PMMA with application to nanofoaming and adhesive joints

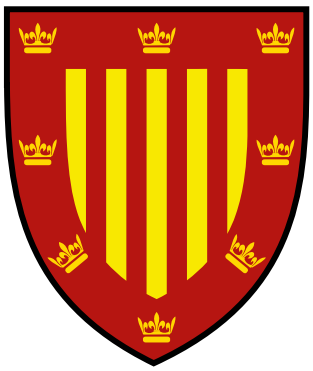

Frederik Van Loock

Peterhouse
University of Cambridge

This dissertation is submitted for the degree of
Doctor of Philosophy

April 2019

Preface

The thesis is submitted for the degree of Doctor of Philosophy at the University of Cambridge. The work presented in this thesis was carried out during the period from October 2015 to March 2019 at the Cambridge University Engineering Department, under the supervision of Professor Norman A. Fleck. The research is funded by the Engineering and Physical Sciences Research Council (EPSRC) and SABIC.

This dissertation is the result of my own work and includes nothing which is the outcome of work done in collaboration except as declared in the preface and specified in the text. It is not substantially the same as any that I have submitted, or, is being concurrently submitted for a degree or diploma or other qualification at the University of Cambridge or any other university or similar institution except as declared in the preface and specified in the text. I further state that no substantial part of my dissertation has already been submitted, or, is being concurrently submitted for any such degree, diploma or other qualification at the University of Cambridge or any other university or similar institution except as declared in the preface and specified in the text. The work in Chapter 4 was done in collaboration with Victoria Bernardo (University of Valladolid) who aided with the set-up and analysis of the foaming tests. The finite element calculations detailed in Appendix A were conducted in collaboration with Ivan Cuesta (University of Burgos).

This thesis contains approximately 53 000 words, 65 figures, and 11 tables, in accordance with the requirements of the Degree Committee.

Frederik Van Loock

Cambridge (UK)

April 2019

"*If a man will begin with certainties, he shall end in doubts;*
but if he will be content to begin with doubts he shall end in certainties."

- Sir Francis Bacon
in 'The Advancement of Learning' (1605)

Acknowledgements

The work in this thesis is the apotheosis of more than three years of research, during which I have been encouraged by many people.

I had the immense privilege to be supervised by Prof. Norman Fleck. His genius, rigour, and passion for science has been, and will be, a continuous source of inspiration. Thank you, Prof. Fleck, for shaping me into a better researcher. I would like to thank my thesis advisor, Prof. Vikram Deshpande, for his brilliant advice and kind encouragement. My thanks also go to the industrial and academic collaborators I had the opportunity to work with. I am indebted to Dr. Martin van Es (SABIC) for his technical advice and support, to Prof. Michael Thouless (University of Michigan) for his guidance and for sharing many insightful suggestions for the adhesive layer study, and to Victoria Bernardo, Judith Martín-de León, and Prof. Miguel Angel Rodríguez Pérez for the many thought-provoking discussions on nanofoams and for the productive (but also very pleasant) research stay at the University of Valladolid.

Many of the experimental results in this thesis would simply not have been achieved without the technical support of Simon Marshall, Alan Heaver, and Graham Smith from the Division C mechanics lab. I would also like to express my gratitude to Hilde Hambro-Fernandez for her support, and to my colleagues at the Cambridge Centre for Micromechanics for the many stimulating discussions and their friendship.

My thanks go to the staff of Peterhouse for providing a warm and vibrant home in Cambridge. Cambridge truly is an inspirational place to conduct research, but it is the people I met in and around Peterhouse who have made this journey so special. I am extremely grateful for the many memorable moments with my ‘new’ friends from Cambridge and with my ‘old’ friends from

Belgium, who frequently visited from across the Channel (and who kept me on my toes during my time here).

This thesis would not have happened without the continued encouragement of a few people who are very dear to me. Thank you, mum and dad, for being my greatest source of inspiration, for always being there for me, and for supporting me in all my pursuits. Thank you, Eveline, for believing in me. Thank you, Camille, for your love, patience, and understanding during the last three years.

Table of contents

List of figures

List of tables

Chapter 1

Introduction

Since their invention and commercialisation at the start of the 20th century, synthetic polymers have become ubiquitous. Synthetic or artificial polymers are typically produced via a polymerisation process during which monomers are covalently bonded to each other to create macromolecular chains. Different skeletal chain structures exist: the chains in the polymer may be represented with two ends (linear polymers), they may have additional side chain branches (branched polymers), or they may be shaped into three-dimensional networks (cross-linked polymers) (Young and Lovell, 2011). For example, the structural formula of a linear polymethyl methacrylate (PMMA) chain, comprising n repeat units based on the methyl methacrylate (MMA) monomer, is shown in Fig. 1.1.

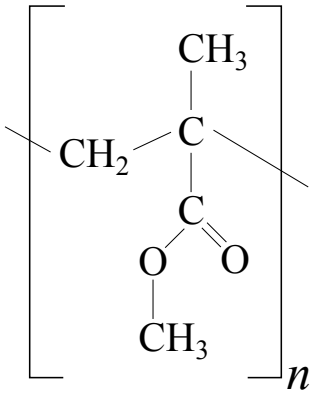

Figure 1.1 The structural formula of linear, amorphous PMMA.

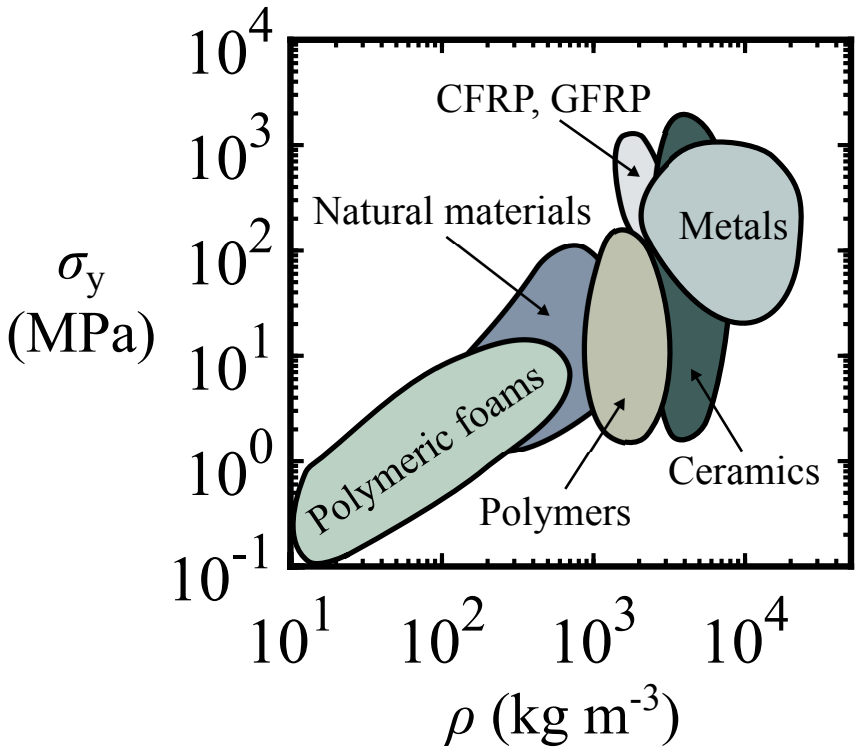

Figure 1.2 Material property chart of strength σ_y versus density ρ showing clusters of common man-made and natural materials. Adapted from Ashby (2010).

The macroscopic properties of a polymer are governed by many structural aspects, including but not limited to, the skeletal structure, the nature of the constituent monomer(s), and the molecular weight distribution (in the case of linear or branched polymers). Polymers encompass a unique area in material property space due to this structural versatility. Most polymers can be formed into complex shapes at low cost, are corrosion resistance, have a low coefficient of friction, and, in some instances, are transparent (Ashby, 2010). In addition, they typically exhibit a strength to weight ratio close to that of metals and ceramics, as shown in the strength σ_y versus density ρ material property chart in Fig. 1.2. Many contemporary technical and non-technical products comprise one or more polymeric components. These components come in various shapes and sizes: polymeric materials can be found in mass-produced electronic products such as smart-phones comprising polycarbonate (PC) shells (see Fig. 1.3a), in biomedical equipment such as transparent intraocular lenses made of polymethyl methacrylate (PMMA) (see Fig. 1.3b), and in load-bearing adhesively-bonded structural components of an aircraft (see Figs. 1.3c and 1.3d).

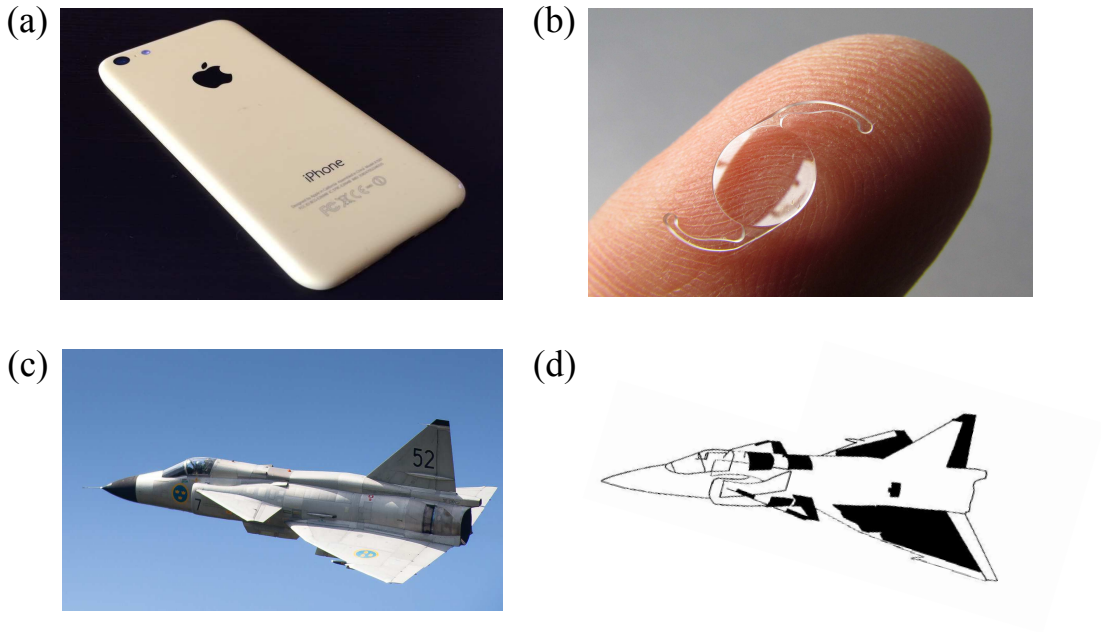

Figure 1.3 Examples of the many applications of synthetic polymeric materials: (a) a polycarbonate shell of a smartphone, (b) a polymethyl methacrylate intraocular lens used for cataract surgery, and (c) the Saab 37 combat aircraft of which the adhesively bonded metal-to-metal regions are shown in (d) (Hart-Smith and Strindberg, 1997).

A polymer may be combined with one or more different organic or inorganic material(s) to produce a hybrid material, such as a carbon fibre- or a glass fibre-reinforced polymer (known as CFRP and GFRP, respectively). Hybrid material concepts may exhibit outstanding combinations of properties compared to those of their individual constituent materials. Composites such as CFRP and GFRP have, for example, a high stiffness to weight and a high strength to weight ratio, see Fig. 1.2. They are therefore attractive material candidates for load-bearing structures in aerospace applications.

A polymeric foam is another example of such a hybrid material. It comprises of gas-filled voids embedded in a polymer matrix. As shown in Fig. 1.2, polymeric foams typically exhibit low strength, but have a relatively high strength to weight ratio. Polymeric foams excel, however, in niche applications where, for example, low density materials with a high impact resistance or with a low thermal conductivity are required (Gibson and Ashby, 2014). Most polymer foaming processes rely on a blowing agent to nucleate and grow voids in a polymer matrix, while it is in a molten state. However, during a solid-state foaming process, the temperature of the polymer matrix remains close to the effective glass transition temperature. Microcellular and nanocellular

polymeric foams, which comprise of voids that have dimensions orders of magnitude smaller than those of conventional macrocellular polymer foams, can be made via the solid-state foaming route, see Figs. 1.4a and 1.4b (Martini, 1981; Youn and Suh, 1985; Costeux, 2014). It is theorised, though only confirmed to a limited extent, in the literature that nanocellular polymeric foams (or polymeric nanofoams) may exhibit enhanced (mass-rationalised) mechanical (Miller and Kumar, 2011; Costeux, 2014), thermal (Notario et al., 2014; Wang et al., 2017), acoustic (Notario et al., 2016a), dielectric (Notario et al., 2016b), and optical (Martín-de León et al., 2017) properties compared to macrocellular and microcellular foams. These enhanced properties are thought to be caused by the nano-scale confinement of the gas phase and the polymer phase in the nanofoam (Costeux, 2014; Pinto et al., 2017). Polymeric nanofoams made of nano-sized voids (< 200 nm) and of a relatively high porosity[1] f (> 0.85) are required to fully exploit these confining effects (Wang et al., 2017). The production of polymeric nanofoams with such a morphology seems to be beyond the limit of the current state-of-the-art solid-state nanofoaming process (Costeux, 2014; Okolieocha et al., 2015; Wang et al., 2017). This limit may be overcome by an improved understanding of the complex interplay between the properties of the polymer matrix and the processing conditions during solid-state nanofoaming.

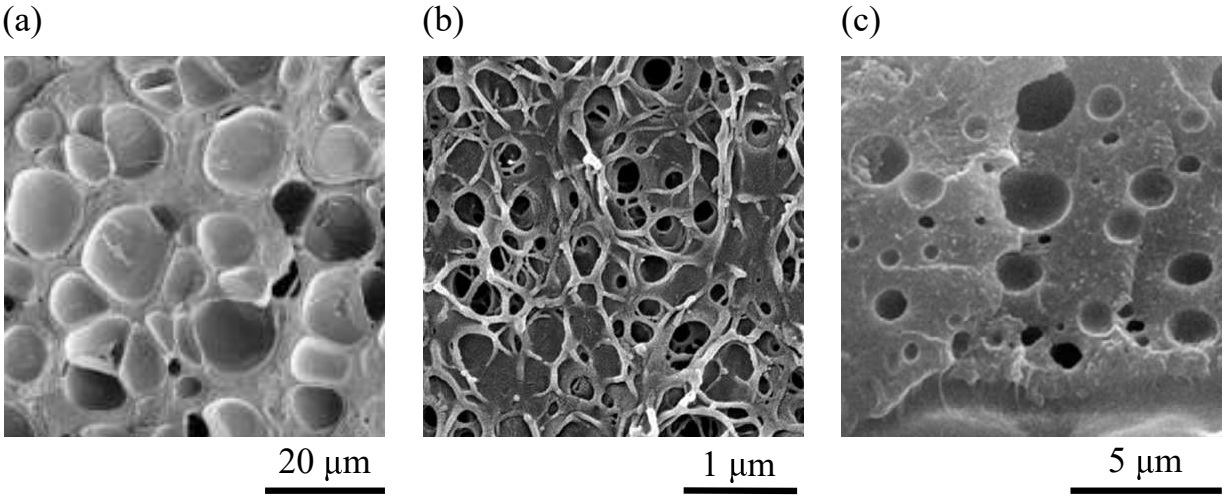

Figure 1.4 Scanning electron microscopy images of (a) a microcellular PMMA foam (Notario et al., 2016a), (b) a nanocellular PMMA foam (Guo et al., 2015b), and (c) a (methaxcryloyloxyethyl trimellitate adhesive layer containing (undesirable) microvoids (Santini and Miletic, 2008).

[1] The porosity of a foam is defined as the ratio of the volume of the voids to the total volume of the foam.

The nucleation and expansion of voids in a polymer may in some situations also lead to undesirable degradation of the polymer's macroscopic properties. An example of this phenomenon is the fracture of polymeric adhesives from pre-existing flaws such as voids or cracks in bonded joints. These flaws may originate from entrapped moisture in the surface layer of the adherends or in the uncured adhesive components. They may also be caused by entrapped air during the application of the adhesive, see Fig 1.4c (Bascom and Cottington, 1972; Pearce et al., 1998; Katnam et al., 2011). The presence of voids or other defects in the adhesive layer may significantly deteriorate the reliability of the joint (da Silva et al., 2018). The ability to accurately predict the magnitude of the knock-down effects on the strength of the joint caused by voids and cracks is of utmost importance for the design of safe and reliable load-bearing structures comprising adhesive joints.

Scope of the thesis

The central theme of this thesis is the deformation and fracture of MMA-based polymers in the context of void growth. Two applications are considered. The first part of the thesis aims to develop an improved understanding of cavity expansion during solid-state nanofoaming of PMMA. The focus of the second part of the thesis is to predict the dependence of the strength of a polymer-based (e.g. MMA) structural adhesive joint upon the size of a pre-existing crack or void in the adhesive layer. The thesis is structured as follows.

A literature review is presented in **Chapter 2** and consists of two parts. The relevant literature on polymeric nanofoams and the solid-state nanofoaming process is discussed in the first part of the review. Emphasis is placed on solid-state foaming of PMMA using CO_2 as the physical blowing or foaming agent. The review also includes an overview of the constitutive laws for PMMA in uniaxial tension close to the glass transition temperature. The second part of the literature review focuses on adhesive joints. Design aspects for adhesive joints are explored and the causes of defects in adhesive layers are briefly outlined. In addition, the role of constraint on the strength and toughness of a confined adhesive layer containing pre-existing voids or cracks is discussed.

The first part of the thesis focuses on cavity growth during solid-state foaming of PMMA by CO_2. A series of uniaxial tensile tests on an PMMA grade of high molecular weight near the glass transition temperature and over two decades of strain rate are conducted in **Chapter 3**. Constitutive equations are calibrated to construct deformation mechanism and failure maps. In addition, uniaxial tensile tests are performed on an PMMA grade of a markedly lower molecular weight. The regimes of deformation and failure of the low molecular weight PMMA are compared with those of the high molecular weight PMMA. Solid-state nanofoaming experiments on the low and high molecular weight PMMA grades tested in Chapter 3 are reported in **Chapter 4**. The dependence of foaming temperature, foaming time, and molecular weight upon the final morphology of the PMMA nanofoams is reported. A one dimensional numerical void growth model is developed in **Chapter 5** to predict cavity expansion during the solid-state foaming process. The foaming model makes use of constitutive laws calibrated to the measured stress-strain response of the two PMMA grades in uniaxial tension. The final porosity of the PMMA nanofoams is predicted as a function of foaming time and foaming temperature, and these predictions are compared with the measured values of porosity reported in Chapter 4. In addition, cell wall failure criteria are explored to explain the observed limit in achievable porosity.

The second part of the thesis focuses on the fracture of adhesively-bonded joints from pre-existing flaws in the adhesive layer. The results of an introductory experimental case study are presented in **Chapter 6**; an MMA adhesive butt joint is tested in tension. Additional uniaxial tensile tests and single edge notch bending tests are conducted to characterise the bulk properties of the MMA adhesive. The tensile strength of a joint comprising a linear, elastic substrate and a linear, elastic adhesive layer is predicted in **Chapter 7**. An analytical framework is developed to explore the roles of crack length, adhesive layer height, joint width, and material mismatch on the strength of the joint. The presence of a process zone at the crack tip is accounted for by making use of a strip yield model. Finite element calculations are conducted to verify the analytical theory, and failure maps are constructed. The analytical model presented in Chapter 7 is validated by an experimental case study in **Chapter 8** with a sandwich layer comprising a centre-cracked cellulose acetate strip and two aluminium alloy substrates. Uniaxial tensile tests and fracture toughness tests on the cellulose acetate are conducted. The tensile strength of the sandwich layer is measured as a function of crack length and adhesive layer height, and

compared with the predicted curves obtained via the analytical theory.

Concluding remarks and suggestions for future work are presented in **Chapter 9**.

Published works

Two papers have been published in an international scientific journal, the references are given below:

Based on Chapter 3:
Van Loock, F. and Fleck, N.A. (2018). Deformation and failure maps for PMMA in uniaxial tension. *Polymer*, 148:259-268.

Based on Chapters 7 and 8:
Van Loock, F., Thouless, M.D., and Fleck, N.A. Tensile fracture of an adhesive joint: the role of crack length and of material mismatch. (2019). *Journal of the Mechanics and Physics of Solids*. 130:330-348.

A publication based on Chapters 4 and 5 is currently under review:

Van Loock, F., Bernardo, V., Rodríguez Pérez, M.A., and Fleck, N.A. The mechanics of solid-state nanofoaming. Under review.

References for other publications of the author on PMMA nanofoams are given below. Although the content of these collaborative publications is not included in this thesis, they contributed significantly to the author's understanding of the solid-state foaming process and the dependence of the properties of PMMA nanofoams upon their morphology.

Bernardo, V., **Van Loock**, F., Martín-de León, J., Fleck, N.A., and Rodríguez Pérez, M.A. (2019). Mechanical properties of PMMA-sepiolite nanocellular materials with a bimodal cellular structure. *Macromolecular Materials and Engineering*. 1900041

Martín-de León, J., **Van Loock**, F., Bernardo, V., Fleck, N.A., and Rodríguez Pérez, M.A. The influence of cell size on the mechanical properties of PMMA nanofoams. Under review.

Chapter 2

Literature review

An overview of the relevant literature on the two research objectives introduced in Chapter 1 is presented. The first part focuses on the topic of polymeric (PMMA) nanofoams. The following research questions are addressed:

- What are polymeric nanofoams and why have they attracted substantial research interest during the last decade?
- How does the solid-state nanofoaming process work?
- Which polymers are attractive candidates to produce high porosity nanofoams via the solid-state foaming route?
- How can one predict void growth during foaming of polymers?
- How can one describe the constitutive behaviour of PMMA in uniaxial tension close to the glass transition temperature in order to predict void growth during solid-state foaming of PMMA?

The second part of the literature review addresses the topic of adhesive joints, and the prediction of the strength of constrained adhesive layers containing voids and cracks. The following research questions are considered:

- What are adhesive joints, and which polymeric-based adhesives and adhesive joint designs are commonly used?

- Which defects may be present in an adhesive layer and how do they occur?
- How can one predict the strength of adhesive joints containing these defects?
- What is the role of constraint on the fracture behaviour of a compliant adhesive layer when clamped between stiffer substrates?

2.1 Polymeric nanofoams

2.1.1 Introduction to polymeric nanofoams

The first synthetic polymeric foams were introduced in the 1930s, shortly after the commercialisation of the first synthetic polymers (Lee and Ramesh, 2004). An increase in industrial demand led to continued development of polymer foaming technologies. One of these developments was the invention of the solid-state foaming process by Suh and co-workers in the 1980s. Microcellular foams with cell sizes in the order of 1 µm to 100 µm can be produced by the solid-state foaming process during which a physical blowing agent (e.g. CO_2) is used to nucleate and grow cells in a polymer matrix (e.g. PMMA). A microcellular foam may offer a 10% to 30% reduction in mass compared to a conventional macrocellular foam of identical tensile strength and impact resistance (Youn and Suh, 1985; Colton and Suh, 1987; Kumar et al., 1994). Microcellular foams are now used in applications such as the soles of running shoes and automobile interior parts.

Further improvement of the solid-state foaming process during the last two decades allowed researchers to produce nanocellular foams or nanofoams with cell sizes in the order of 10 to 100 nm (Krause et al., 2001). As mentioned in Chapter 1, polymeric nanofoams have attracted a lot of attention during the last decade as this relatively new class of porous polymers may exhibit enhanced (mass-rationalised) properties with respect to macro- or microcellular foams (Schmidt et al., 2007; Costeux, 2014; Wang et al., 2017; Martín-de León et al., 2017).

One of these highly cited properties is their thermal conductivity λ, which may be lower than that of air (λ_{air} = 0.025 W $m^{-1}K^{-1}$ at standard temperature and pressure) due to the Knudsen

effect[1]. That is, when the average cell size l of the nanofoam is in the order of the mean free path ξ of the gas molecules in the cells (close to 70 nm for air at standard temperature and standard pressure), the thermal conductivity of the gas phase in the nanofoam is significantly reduced (Schmidt et al., 2007; Wang et al., 2017). The dependence of the thermal conductivity of a gas λ_{gas} in a porous solid upon the average void size may be predicted by the Knudsen equation (Lu et al., 1992):

$$\lambda_{\text{gas}} = \lambda_{\text{gas}}^{0}\left(1+2\beta\frac{l}{\xi}\right)^{-1} \tag{2.1}$$

where λ_{gas}^{0} is the thermal conductivity of the unconfined gas at standard conditions and β a constant close to 2 for air. Equation 2.1 is plotted in Fig. 2.1 for air (ξ = 70 nm at standard temperature and pressure, β = 2). The experimental observation of the ratio $\lambda_{\text{gas}}/\lambda_{\text{gas}}^{0}$ being lower than unity, for l/ξ lower than or close to unity as predicted by Eq. 2.1, is well-documented for (in)organic aerogels and porous ceramics in the literature: see, for instance the work of Lu et al. (1995) and Nait-Ali et al. (2006). The first experimental validation of the Knudsen effect in polymeric nanofoams was reported by Rodriguez-Perez and co-workers (Notario et al., 2014). The reported thermal conductivity of the air phase in nano- and microcellular PMMA foams and in macrocellular polyethylene foams by Notario et al. (2014) is plotted as a function of normalised cell size l/ξ in Fig. 2.1.

Wang et al. (2017) developed a model to predict the thermal conductivity of a polymeric nanofoam by taking into account the Knudsen effect as well as phonon-scattering and thin-film interference phenomena. According to the predictions of Wang et al. (2017), the thermal conductivity of a polymeric nanofoam may be close to or below 0.025 W $m^{-1}K^{-1}$ when the average void size l is below 200 nm and the porosity f of the foam is above 0.85, which requires a cell

[1] The Knudsen effect describes the reduced thermal conductivity of the gas phase in a porous solid when the cell size is close to the mean free path of the gas molecules filling the pores. At this critical cell size, the probability of a gas molecule in a void colliding with the solid phase confining the void significantly increases, while the probability of collision with another gas molecule reduces. This effectively reduces the thermal conduction of the gas phase. A polymeric foam with nano-sized cells may therefore have a thermal conductivity lower than the thermal conductivity of the unconfined gas phase at standard conditions, given the foam is of high porosity to reduce the contribution of the thermal conductivity of the solid phase to the overall thermal conductivity of the foam (Schmidt et al., 2007; Notario et al., 2014).

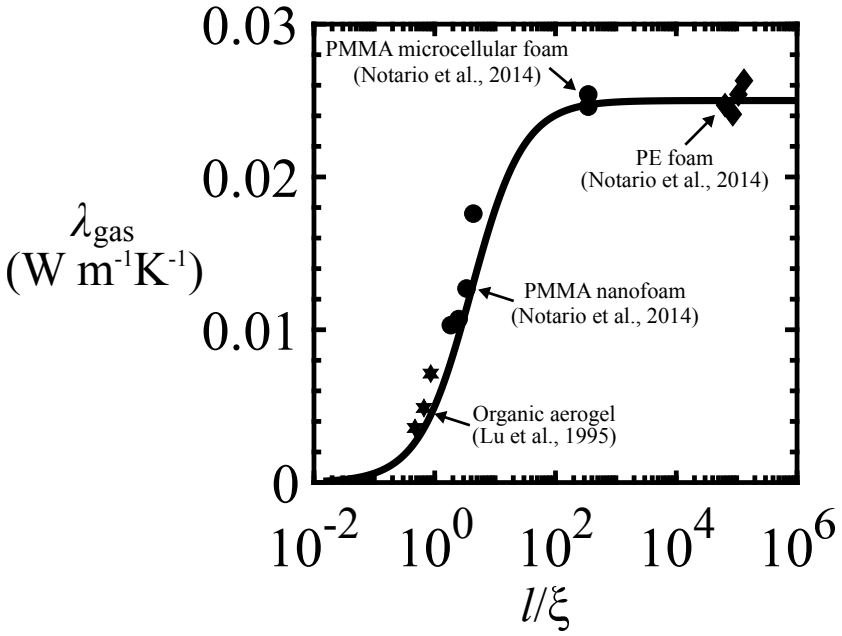

Figure 2.1 The reported thermal conductivity λ_{gas} of the gas phase in nano- and microcellular PMMA foams and in macrocellular polyethylene foams by Notario et al. (2014) as a function of normalised void size l/ξ. The λ_{gas} versus l/ξ curve predicted by Eq. 2.1 for $\xi = 70$ nm and $\beta = 2$ is included. Adapted from the work of Notario et al. (2014).

nucleation density[2] close to or above 10^{21} m^{-3}.

Costeux (2014) reviewed the large amount of experimental studies focusing on the effect of solid-state foaming conditions and the choice of polymer precursor on the final morphology of the foam (i.e. cell nucleation density N_d, average void size l, and porosity f). The various polymer precursor material systems used to produce nanofoams in the literature are plotted on a porosity f versus void size l map shown in Fig. 2.2. Key references per material system are summarised in Table 2.1. Idealising the foam as a regular array of equisized spherical voids within the polymer matrix, the porosity f is related to the diameter l of the voids via (Kumar and Suh, 1990):

$$f = \left(1 + \frac{6}{\pi l^3 N_d}\right)^{-1} \tag{2.2}$$

The predicted f versus l curves via Eq. 2.2 for nucleation densities ranging from $N_d = 10^{20}$ m^{-3} to $N_d = 10^{26}$ m^{-3} are plotted in Fig. 2.2. The review by Costeux (2014) on experimental studies

[2] The cell nucleation density N_d is defined as the amount of voids per unit volume of unfoamed material.

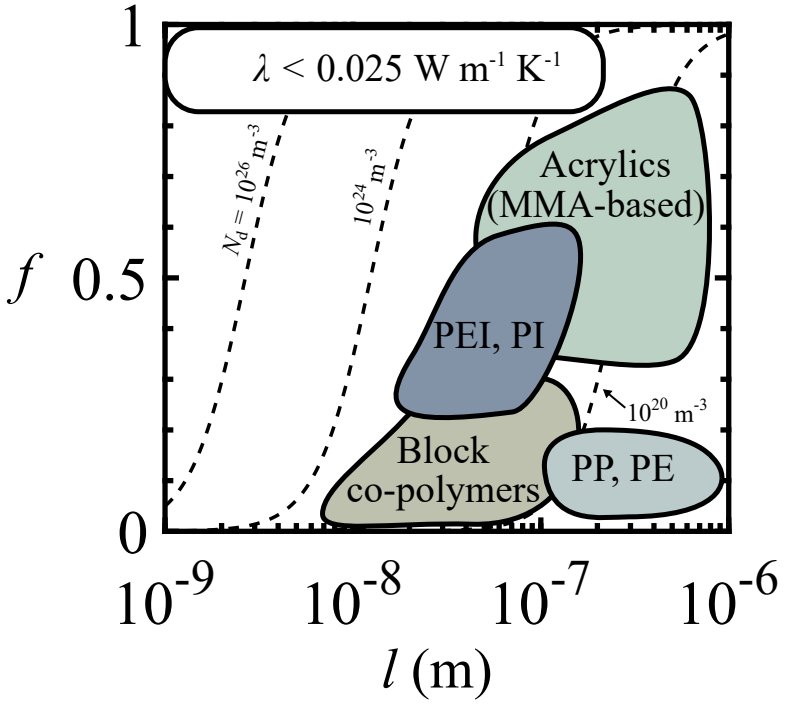

Figure 2.2 Map of porosity f versus average void size l of polymeric nanofoams produced by solid-state foaming in the literature, grouped per polymer precursor material system. The predicted f versus l curves via Eq. 2.2 for various values of nucleation density N_d are included. The plot is an updated version of Fig. 5 in the review of Costeux (2014). References for each material system are given in Table 2.1.

of solid-state nanofoaming dicusses the trade-off between porosity and cell size of a polymeric nanofoam. Polymeric nanofoams of $l < 200$ nm are reported for a nucleation density above 10^{21} m^{-3}, but their porosity is limited to close to 0.85: see, for example, Aher et al. (2013) and Costeux and Zhu (2013). The observed porosity limit for nanofoams with a nucleation density above 10^{21} m^{-3} may be due to the fact that the walls between the nano-sized cells are limited to the end-to-end distance of the individual polymer chains (Pinto et al., 2017; Bernardo et al., 2019). Polymeric nanofoams of porosity on the order of 0.8 to 0.9 have been produced, but their cell size is well above 200 nm (and $N_\mathrm{d} \ll 10^{21}$ m^{-3}) (Costeux, 2014; Martin-de León et al., 2016). The microstructural requirement for polymeric nanofoams with a thermal conductivity lower than the thermal conductivity of air is currently beyond the practical limit of the state-of-the-art solid-state nanofoaming process (Okolieocha et al., 2015; Wang et al., 2017).

Some studies have been conducted to characterise the mechanical properties of polymeric nanofoams, often in comparison with those of macrocellular or microcellular foams made of

Table 2.1 Key references for the different precursor material groups in Fig. 2.2. The highest observed value for the porosity f_{max}, and the associated values for the cell size l and nucleation density N_d in each reference are reported.

Material system	Reference	f_{max}	l (nm)	N_d (m^{-3})
Acrylics (PMMA, PMMA-MAM, ...)	(Reglero Ruiz et al., 2011)	0.7	300	7.6×10^{19}
	(Costeux and Zhu, 2013)	0.82	180	1.5×10^{21}
	(Martin-de León et al., 2016)	0.73	204	3.4×10^{20}
	(Martín-de León et al., 2017)	0.6	14	6.9×10^{22}
PEI, PI	(Miller and Kumar, 2011)	0.54	80	2×10^{20}
	(Aher et al., 2013)	0.62	50	$>10^{21}$
Block co-polymers	(Dutriez et al., 2012)	0.3	20-70	$\sim 10^{21}$
PP, PE	(Lee et al., 2005)	0.16	$\sim$200	2.9×10^{19}
	(Ameli et al., 2014)	0.4	200	$\sim 10^{19}$

the same parent polymer. Miller and Kumar (2011) performed unaxial tensile tests on nanocellular and microcellular PEI foams of identical porosities. Miller and Kumar (2011) found that PEI nanofoams have an increased tensile failure strain and tensile failure strength compared to their microcellular counterparts, whereas the measured Young's modulus was found to be independent of void size. Sharudin and Ohshima (2011) reported that the tensile yield strength of polypropylene-based nanofoams is close to the yield strength of the solid parent polymer, though the tensile failure strain of the nanofoam was found to be lower than the tensile failure strain of the solid polymer. Notario et al. (2015) found that the material performance index for a light, stiff beam in bending $E^{1/2}/\rho$ (where E is the Young's modulus and ρ is the density) and the impact resistance measured by Charpy tests for an PMMA nanofoam exceeded that for a microcellular PMMA foam. They attributed this stiffening to the fact that the average size of the cell walls between the nano-sized voids is in the order of the size of the individual PMMA chains.

It is clear that polymeric nanofoams are attractive material candidates for a wide range of applications where polymeric foams are currently used for: e.g. construction, packaging, automotive, aerospace, and microelectronics (Eaves, 2004; Ashby, 2010; Costeux, 2014). Especially PMMA (and other MMA-based) nanofoams, exhibiting some of the highest porosities and lowest cell sizes reported in the literature, have a potential to be used in applications where materials of low density and low thermal conductivity are required. The use of PMMA nanofoams for industrial purposes is, however, still impeded by the practical issue of making homogeneous, defect-free

polymeric foams with nano-sized voids and of high porosity via the solid-state foaming route. The solid-state nanofoaming process is reviewed in detail in the next section.

2.1.2 The solid-state nanofoaming process

Several processing techniques are available to produce polymeric foams with nano-sized pores including but not limited to sol-gel techniques to produce organic aerogels (Lu et al., 1992, 1995), the use of block co-polymers with sacrificial blocks (Hedrick et al., 1995; Hamley, 2003), and the solid-state foaming process (or gas dissolution process) by saturating a polymer precursor with a a physical blowing agent such as CO_2 (Costeux, 2014; Martin-de León et al., 2016). The solid-state foaming route is explored in this thesis.

2.1.2.1 Processing steps

As reviewed above, the solid-state nanofoaming process is based on the batch foaming process originally developed by Suh and co-workers to manufacture microcellular foams (Martini, 1981; Youn and Suh, 1985; Kumar and Suh, 1990). The process typically consists of three distinct phases (Costeux, 2014; Forest et al., 2015; Martin-de León et al., 2016):

1. **The saturation phase**
   An inert gas is dissolved into a polymer precursor in a pressure vessel. The gas pressure p_{sat} and temperature T_{sat} within the vessel are maintained until the polymer is saturated. For a given combination of polymer precursor and blowing agent, p_{sat} and T_{sat} dictate the equilibrium or saturation concentration of dissolved gas molecules into the polymer.

2. **The nucleation phase**
   Once the polymer is saturated, the pressure in the vessel is rapidly decreased to supersaturate the polymer-gas system. Consequently, voids of gas molecules nucleate within the polymer-gas mixture. If the temperature of the precursor is close to or above the effective glass transition temperature of the solid upon depressurisation, simultaneous nucleation and growth of the voids takes place, this is known as a ‘one step process’. On the other hand, if the precursor’s temperature is below the effective glass transition temperature of the solid, a separate void growth phase is required, this is known as the ‘two step process’.

3. **The void growth and stabilisation phase**

   The nucleated polymer-gas system is heated in a thermal bath to a temperature close to or above the polymer-gas solid's effective glass transition temperature to induce growth of the pressurised nucleated voids. Gas molecules diffuse out of the polymer melt into the expanding voids until their growth is terminated, for instance, by quenching of the foams.

Various processing conditions and material properties play a convoluted role during the solid-state nanofoaming process outlined above. Consider the case of solid-state nanofoaming of an PMMA precursor using CO_2, as detailed in the work of Martin-de León et al. (2016). Some of the key processing variables are traced as a function of time to gain a more detailed understand-

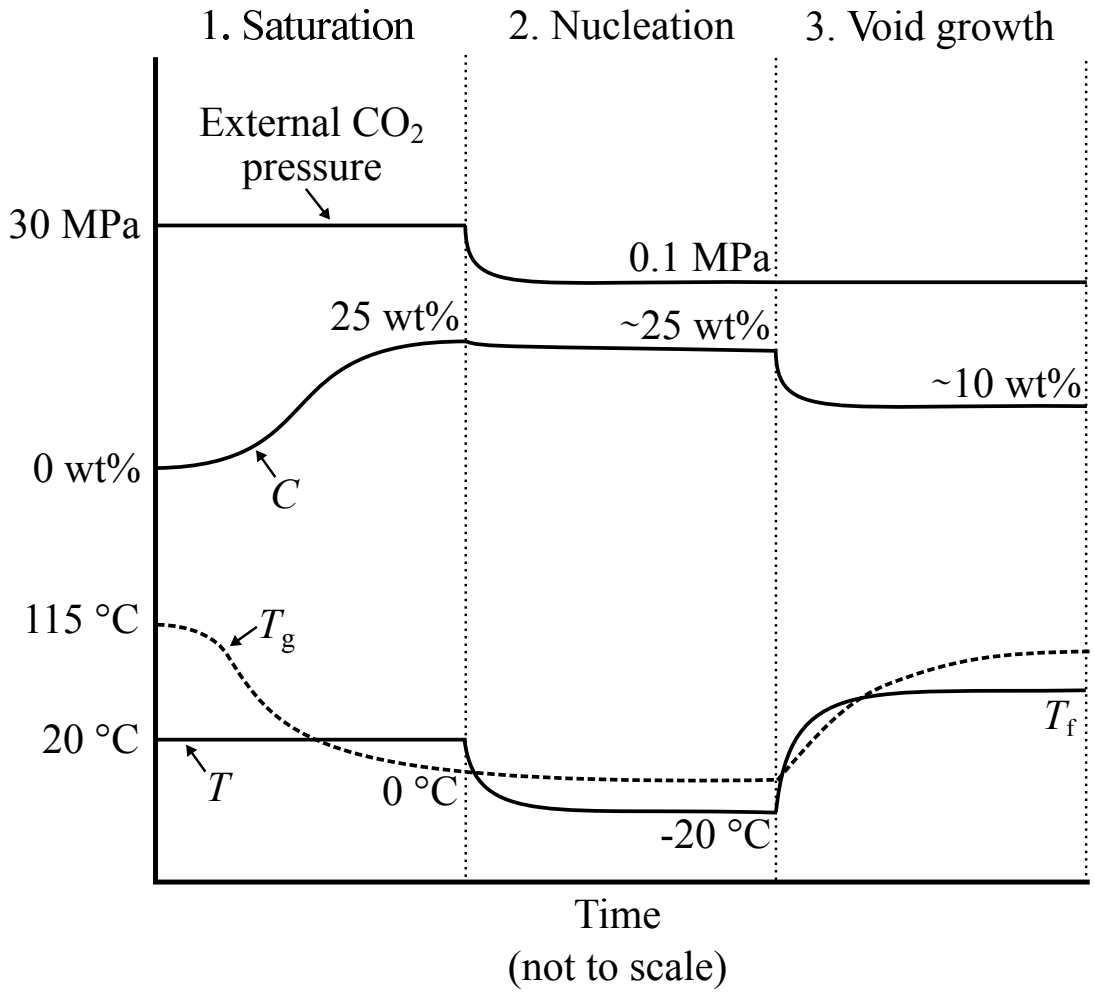

Figure 2.3 The typical change of key process variables (ambient pressure, dissolved gas concentration C, the effective glass transition temperature T_g and temperature T of the polymer-gas solid) as a function of time for a two-step solid-state nanofoaming process of PMMA by CO_2. Figures are approximate and based on data reported by Pinto (2014) and Martin-de León et al. (2016).

ing on how processing conditions affect void nucleation and growth, see Fig. 2.3.

As illustrated in Fig. 2.3, an PMMA precursor is first saturated with CO_2 by subjecting it to a relatively high gas pressure, i.e. p_{sat} = 30 MPa, corresponding to a equilibrium weight concentration[3] C of dissolved CO_2 close to 25 wt% at a saturation temperature close to room temperature. Note that, in general, the higher the equilibrium concentration, the higher the cell nucleation density, which is critical to obtain polymeric foams of high porosity with nano-sized voids as shown in Fig. 2.2 (Costeux, 2014; Martín-de León et al., 2017). Dissolving CO_2 into a linear, amorphous polymer lowers its effective glass transition temperature, as shown in Fig. 2.3. The solubility of CO_2 into PMMA, as well as the dependence of the glass transition temperature upon CO_2 concentration, is reviewed in detail below. The saturation phase typically takes place at a maintained temperature[4]. When the effective glass transition temperature of the PMMA-CO_2 solid decreases to a value below the chosen saturation temperature, the resulting polymer-gas solid may transition from a glassy constitutive state to a glass transition or rubbery constitutive state.

Once the precursor is saturated, the CO_2 pressure is rapidly decreased at an instantaneous pressure release rate ranging from 1 MPa s^{-1} to 100 MPa s^{-1} (Khan et al., 2015; Martin-de León et al., 2016). The fast pressure release induces void nucleation and also adiabatic cooling of the expanding gas as a result of the Joule-Thomson effect (Costeux, 2014). Therefore, the nucleated sample's temperature decreases and the polymer-gas solid may transition back to the glassy state. If this is the case, expansion of the nucleated cavities is impeded and a third growth phase is required to foam the nucleated solid.

A distinct void growth phase is often preferred to have an improved control of the final morphology of the foam (Costeux, 2014). To that end, the nucleated sample is heated in a thermal (water or oil) bath with a maintained foaming temperature T_f. Consequently, the solid material between the voids softens and the nucleated voids expand as a result of the pressure difference between

[3] The weight concentration C is defined with respect to the total mass of the PMMA-CO_2 solid.

[4] The saturation temperature is often set to room temperature for practical convenience. However, the CO_2 solubility of a linear, amorphous polymer such as PMMA typically increases with decreasing temperature. This effect has successfully been exploited by Martín-de León et al. (2017) to produce the first transparent polymeric nanofoams.

the ambient pressure and gas pressure in the bubble. Simultaneously, dissolved CO_2 molecules diffuse out of the solid into the growing cavities. The decreasing CO_2 concentration increases the effective glass transition temperature of the solid phase. During the resulting vitrification process, the void growth rate slows down and the final morphology of the foam may be attained. In some cases, void growth is terminated by quenching the foamed sample in a water bath at a temperature much lower than than the foaming temperature T_f.

2.1.2.2 Solubility of CO_2 in PMMA

The equilibrium concentration of CO_2 in PMMA is governed by the CO_2 pressure and by the temperature (Pantoula and Panayiotou, 2006). Various experimental methods have been employed in the literature to measure the dependence of the CO_2 equilibrium concentration in PMMA upon pressure and upon temperature for pressure and temperature regimes relevant for solid-state nanofoaming of PMMA by CO_2 (i.e. p ranges between 0.1 MPa and 30 MPa and T ranges from 20 °C to 100 °C). Liau and McHugh (1985) used an in-situ barometric technique to measure the dependence of CO_2 weight concentration C upon CO_2 pressure p. Shieh and Liu (2002) measured C as a function of p by measuring the mass of the saturated PMMA-CO_2 samples with a weight balance after depressurisation. Rajendran et al. (2005) used an in-situ gravimetric analysis to report the dependence of C upon p. The measured data for C as a function of p for an PMMA-CO_2 mixture, as reported by Liau and McHugh (1985), Shieh and Liu (2002), and Rajendran et al. (2005) are plotted in Fig. 2.4. There is some scatter between the C versus p curves reported by the different references for close to identical temperatures. This scatter is attributed to the use of different measurement methods and different PMMA grades which may have been subjected to different thermal histories.

The C versus p curve for a glassy polymer may be predicted by the use of a dual-sorption model comprising an idealised linear dissolution term and a Langmuir (void filling) sorption term: (Barrer et al., 1958):

$$C = k_D p + \frac{k_S b p}{1 + b p} \tag{2.3}$$

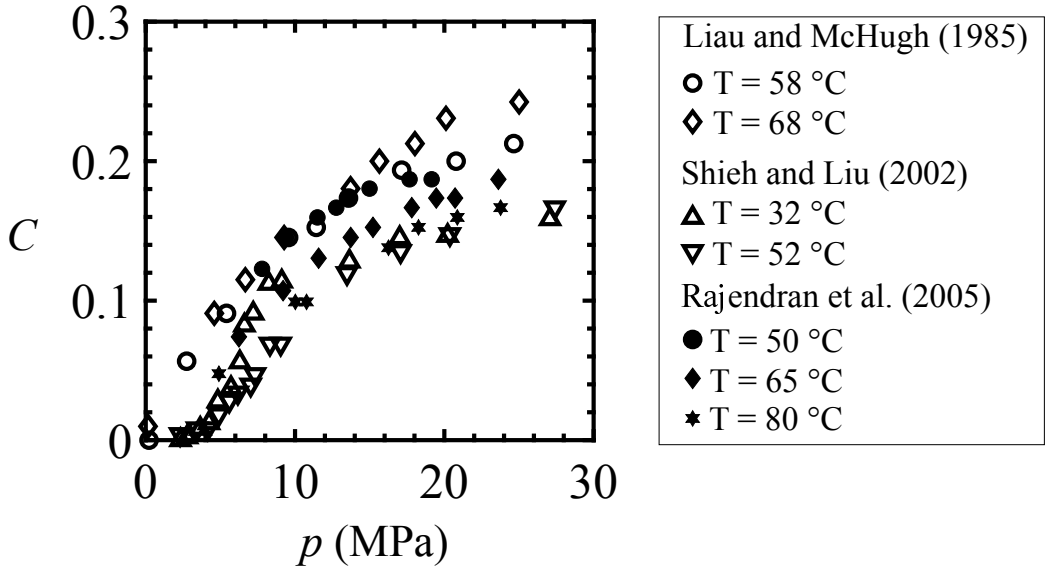

Figure 2.4 Measured equilibrium weight concentration C of CO_2 into PMMA as a function of CO_2 pressure p as reported by Liau and McHugh (1985), Shieh and Liu (2002), and Rajendran et al. (2005) for selected temperatures.

where k_D is a solubility coefficient, b is a gas affinity parameter, and k_S is a saturation coefficient. These coefficients[5] have to be calibrated to measured concentration versus pressure and temperature data for a given polymer-gas system. The Langmuir sorption term becomes close to independent[6] of gas pressure at an elevated gas pressure and the C versus p trend is dominated by the linear dissolution term. The C versus p trend of polymers in the glass transition or rubbery state (i.e. T/T_g close to or above unity) is commonly approximated by Henry's law (Van Krevelen and Te Nijenhuis, 2009):

$$C = k_H p \tag{2.4}$$

A linear and temperature-independent concentration versus pressure curve, as predicted by Eq. 2.4, is a reasonable approximation when predicting void growth during solid-state nanofoaming of PMMA by CO_2 (i.e. p ranges from 0.1 MPa to 30 MPa and T ranges from 20 °C to 100 °C), see Fig. 2.4.

[5] The coefficients of Eq. 2.3 may be assumed to be sensitive to temperature when a strong dependence of the solubility isotherms upon temperature is observed.

[6] $\lim_{p\to\infty} \frac{k_S b p}{1+bp} = k_S$.

2.1.2.3 The dependence of the effective glass transition temperature of PMMA upon CO_2 concentration

The dissolution of CO_2 into a linear, amorphous polymer such as PMMA reduces the glass transition temperature T_g of the PMMA-CO2 solid. This plasticisation effect is attributed to the increased mobility of PMMA chains due to lubrication by the CO_2 molecules, and the decrease of the intermolecular bond strength as the CO_2 molecules increase the spacing between the PMMA chains (Alessi et al., 2003; Verreck et al., 2006). A range of experimental techniques have been used in the literature to determine the value of T_g of PMMA as a function of CO_2 weight concentration C. Chiou et al. (1985) made use of differential scanning calorimetry to measure T_g/T_g^0 as a function of C, where T_g^0 is the glass transition temperature of the polymer absent the dissolved gas. Likewise, Wissinger and Paulaitis (1991) measured the dependence of T_g/T_g^0 upon C based on creep compliance measurements. Guo and Kumar (2015) made use of solid-state foaming experiments to observe the relation between T_g/T_g^0 and CO_2 concentration for an PMMA-CO_2 mixture. The reported T_g/T_g^0 versus C curves for PMMA-CO_2, as reported by Chiou et al. (1985), Wissinger and Paulaitis (1991), and Guo and Kumar (2015) are shown in Fig. 2.5.

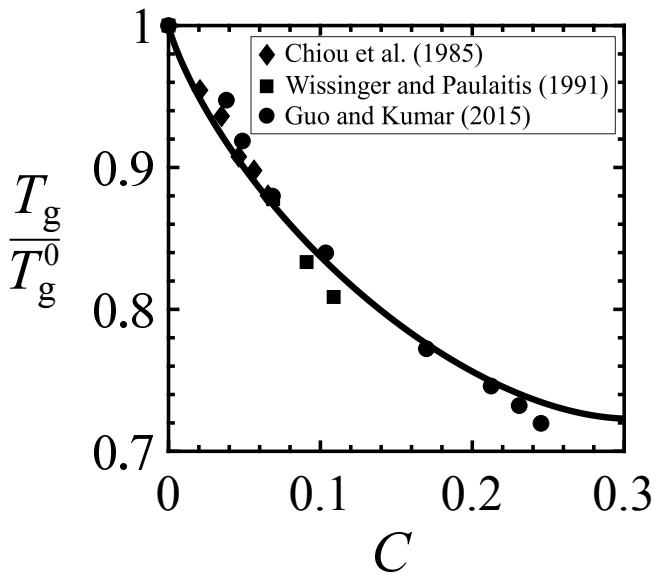

Figure 2.5 Normalised effective glass transition temperature T_g/T_g^0 of the PMMA-CO_2 solid as a function of CO_2 weight concentration C as reported by Chiou et al. (1985), Wissinger and Paulaitis (1991), and Guo and Kumar (2015), and the T_g/T_g^0 versus C curve predicted by the fitted version of Eq. 2.7 to the plotted experimental data.

Chow (1980) used statistical thermodynamics to predict T_g/T_g^0 as a function of C and introduces a parameter θ:

$$\theta = \frac{M_w^p}{zM_w^g}\frac{C}{1-C} \tag{2.5}$$

where M_w^p is the molecular weight of the polymer repeat unit (M_w^p = 110.12 g mol^{-1} for a methyl methacrylate monomer), M_w^g is the molecular weight of the gas (M_w^g = 44.01 g mol^{-1} for CO_2), and z is a lattice coordination number equal to 2 as suggested by Chow (1980). In addition, Chow (1980) defines a parameter β:

$$\beta = \frac{zR}{M_w^p \Delta C_p} \tag{2.6}$$

where R is the universal gas constant and ΔC_p is the change in specific heat capacity of the polymer absent the dissolved gas at the glass transition at constant pressure. According to Chow (1980), the normalised glass transition temperature T_g/T_g^0 is predicted as a function of dissolved gas weight concentration C by:

$$\frac{T_g}{T_g^0} = \exp\Big[\beta\Big((1-\theta)\ln(1-\theta)+\theta\ln\theta\Big)\Big] \tag{2.7}$$

Equation 2.7 is curve fitted to the measured T_g/T_g^0 versus C for PMMA-CO_2 data shown in Fig. 2.5. The fitted value for ΔC_p equals 355 J kg^{-1} K^{-1} which is slightly higher than the measured value of ΔC_p (= 312 J kg^{-1} K^{-1}) by DSC for PMMA as reported by Chiou et al. (1985).

More insight into the role of processing conditions and materials properties on void growth during solid-state nanofoaming is obtained by predicting void growth during the growth phase of the solid-sate foaming process. A selection of void growth models for foaming processes reported in the literature are reviewed in the next section.

2.1.3 Void growth models for foaming processes

The prediction of the growth of a pressurised spherical void in a viscous liquid has been a topic of research long before the invention of synthetic polymeric foams. Amongst others, Lord

Rayleigh contributed to the theory on this subject, leading to the well-known Rayleigh–Plesset equation. This ordinary differential equation can be solved to predict the radius of a pressurised void in an infinite, viscous liquid in time (Lord Rayleigh, 1917; Plesset, 1949).

2.1.3.1 Single void models

A more accurate model to predict void growth during a liquid (or viscous) polymer foaming process was developed by Barlow and Langlois (1962) based on the work of Epstein and Plesset (1950) who reported solutions for the rate of growth of a void in an oversaturated liquid-gas mixture. Barlow and Langlois (1962) considered the growth of a single void in an infinite linear, viscous polymer melt. Emphasis was placed on incorporating the diffusion of dissolved gas molecules from the polymer melt into the expanding void. The resulting governing equations of the single void growth model are (i) an equilibrium equation, (ii) a mass conservation statement, and (iii) a mass diffusion equation. Moreover, Henry's law (Eq. 2.4) is used to relate the pressure p in the void to the concentration of gas in the melt at the surface of the void. A simplified solution for this coupled system of non-linear ordinary differential equations is obtained by assuming that the concentration gradient at the interface between the void and melt develops over a thin boundary layer as suggested by Patel (1980). Favelukis et al. (2000) explored the effect of non-ideal gas assumptions by extending the model of Patel (1980) with a van der Waals equation of state combined with the more sophisticated Flory-Huggins theory (instead of Henry's law) to relate p to C at the surface of the void. Favelukis et al. (2000) reported some minor differences between the predicted void growth curves obtained by either ideal or non-ideal assumptions in the context of polymer devolatilisation processes.

Extensive research has also been conducted on the effect of the choice of the viscous or viscoelastic constitutive law of the polymer melt on void growth. Street (1968) extended the single void model by treating the polymer melt as a viscoelastic fluid (three constant Odroyd fluid). The calculations of Street (1968) demonstrated that the initial rate of growth of a void in an infinite, viscoelastic melt can be an order of magnitude higher compared to the void growth rate in a linear, viscous (Newtonian) melt of identical shear viscosity. Street (1968) attributed this to the lower effective stresses that occur far away from the surface of the growing void in the case

of a viscoelastic melt in comparison to void growth in a linear, viscous melt. In a subsequent work Street et al. (1971) also predicted the growth of the void in a melt which is assumed to be non-Newtonian by use of a power law. The numerical work of Street and co-workers stipulates the significance of the choice of the constitutive law(s) of the polymer on void growth (Street, 1968; Street et al., 1971).

2.1.3.2 Multiple void models

Single void growth models allow one to study the effect of various processing parameters and material properties on void growth during foaming processes. Amon and Denson (1984) argued, however, that the simultaneous growth of multiple voids in a polymer melt should be considered for a more realistic idealisation of cavity expansion during the foaming process. Consequently, Amon and Denson (1984) developed a multiple void growth model whereby the virtual envelope of melt surrounding each nucleated void has a limited amount of dissolved gas. Arefmanesh and Advani (1991) used the model of Amon and Denson (1984) to predict void growth in a viscoelastic melt by using the upper-convected Maxwell constitutive equation. In a subsequent work, Arefmanesh and Advani (1995) reported predicted void growth curves by taking non-isothermal foaming conditions into account. Arefmenesh and co-workers concluded that primarily the initial void growth stage depends on the assumption for the constitutive behaviour.

2.1.3.3 Influence volume based models

Shafi et al. (1996) developed a more sophisticated void growth model taking into account the fact that void nucleation and growth may take place at the same time[7]. To that end, Shafi et al. (1996) assumed a lowered nucleation probability in the influence region surrounding an as-nucleated void and assumed the nucleation of voids to stop once the total volume of the influence spheres assigned to each nucleated void is equal to the volume of the melt. The void growth rate was found to increase as a function of (i) increasing diffusion coefficient of the gas in the polymer and (ii) increasing solubility of the gas in the polymer. The influence volume model of Shafi et al.

[7] This assumption is applicable for conventional (e.g. extrusion) liquid foaming processes as well as the one-step solid-state foaming process detailed above, though not appropriate for a two-step solid-state foaming process for which void nucleation and growth may be analysed separately.

(1996) was extended by Feng and Bertelo (2004) by incorporating a heterogeneous nucleation model and a viscoelastic Oldroyd-B law for the melt. The computed void growth curves by Feng and Bertelo (2004) were found to be in reasonable agreement with the outcomes reported by Han and Yoo (1981) who performed a series of injection foaming experiments on polystyrene. In addition, the predicted final void size distributions by Feng and Bertelo (2004) were found to be close to the measured void size distributions by Kieken (2001) who conducted extrusion foaming tests on polystyrene.

2.1.3.4 Predicting void growth during solid-state nanofoaming

In contrast to the substantial body of experimental work on polymeric nanofoams produced by solid-state foaming, as reviewed by Costeux (2014), and the development of cell growth models for liquid state foaming processes as reviewed above, theoretical studies on cell growth during solid-state nanofoaming are limited. Costeux and co-workers (Costeux et al., 2014; Khan et al., 2015) simulated void nucleation and void growth during solid-state nanofoaming of acrylate co-polymers by making use of the model of Shafi et al. (1996). They conducted a series of nanofoaming experiments and obtained good agreement between the predicted and measured cell size and cell size distributions. However, this model overestimates the measured final porosity of the nanofoams. The mismatch between the simulated and the measured porosity of acrylic nanofoams may be due to (i) the assumption that cell growth terminates when the glass transition temperature of the polymer-gas solid is equal to the foaming temperature and/or (ii) the assumption that the polymer-gas solid surrounding the cell is in a liquid (viscous) state throughout the solid-state foaming process. In reality, void growth occurs at a temperature close to the glass transition temperature of the solid surrounding the void.

2.1.4 Constitutive laws for PMMA in uniaxial tension

The review on void growth models in the literature revealed (i) the importance of the choice of the constitutive law of the polymer-gas solid in which the voids grow and (ii) that no attempts, to the author's knowledge, have been done to predict void growth during the growth stage of a solid-state nanofoaming process focusing on the appropriate constitutive laws for the (bi-axially extended) solid surrounding the growing voids. The focus in this thesis is on solid-state nanofoaming of PMMA by CO_2; a brief review of the regimes of deformation and failure for

a linear, amorphous polymer such as PMMA in unaxial tension close to the glass transition temperature is presented below.

Gilbert et al. (1986) identified four constitutive regimes for a linear, amorphous polymers deformed in uniaxial tension. These regimes are the (i) glassy, (ii) glass transition, (iii) rubbery, and (iv) viscous flow regimes in sequence of increasing temperature T or of decreasing strain rate $\dot{\varepsilon}$, see Fig. 2.6a. The typical stress versus strain response associated with each regime is illustrated in Fig. 2.7a (nominal tensile stress S versus nominal tensile strain e) and Fig. 2.7b (true tensile stress σ versus true (logarithmic) tensile strain ε). In a subsequent study, Bin Ahmad and Ashby (1988) reported similar plots for the rate and temperature dependent flow strength σ_y by an analogous approach, see Fig. 2.6b. Little data exists in the literature on the true tensile failure strain ε_f of PMMA as a function of temperature and strain rate. A possible trend is depicted in Fig. 2.6c, as based on the studies of Cheng et al. (1990), Smith (1963) and Vinogradov (1975). Cheng et al. (1990) measured ε_f in the glassy regime, Smith (1963) elucidated the effect of rate and temperature on ε_f for cross-linked elastomers near the glass transition temperature, and Vinogradov (1975) investigated the effect of strain rate on ε_f for monodisperse, amorphous polymer melts.

The regimes of deformation and failure for PMMA are reviewed in more detail in this section. For each regime, the mechanisms of molecular deformation and failure are discussed and constitutive laws used to describe the small strain, viscoelastic and the large strain, viscoplastic behaviour are summarised.

2.1.4.1 The glassy regime and the glass transition regime

The small strain, viscoelastic response

The glassy regime exists at temperatures below the glass transition, $T/T_g < 1$. Yannas and Luise (1982) developed an analytical model predicting the dependence of the the glassy modulus E_g on T/T_g by considering rotation of polymer chain segments restricted by intramolecular and intermolecular energy barriers. A first order approximation of this model predicts E_g to decrease

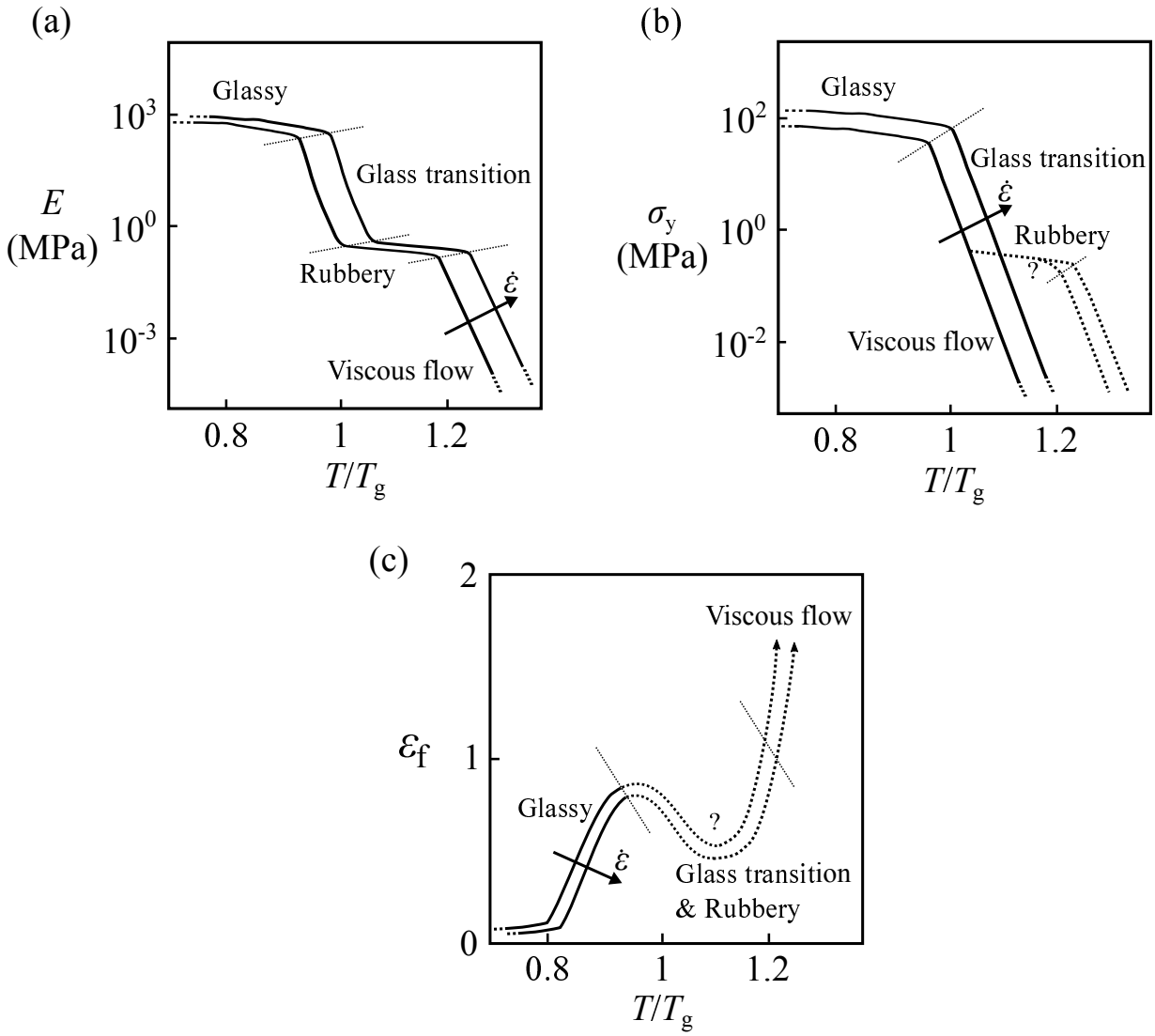

Figure 2.6 Constitutive trends from the literature for a linear, amorphous polymer of high molecular weight in uniaxial tension at temperatures close to its glass transition: (a) vanishing strain modulus E as a function of T/T_g for two distinct strain rates (Gilbert et al., 1986), (b) flow strength σ_y as a function of T/T_g for two distinct strain rates (Bin Ahmad and Ashby, 1988), and (c) true tensile failure strain ε_f as a function of T/T_g for two distinct strain rates (Smith, 1963; Vinogradov, 1975; Cheng et al., 1990).

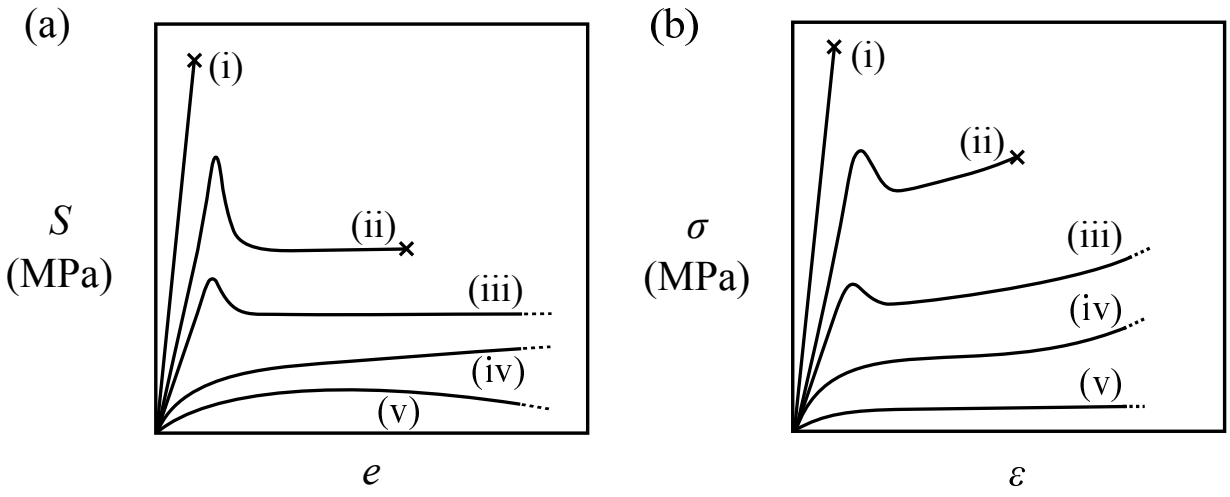

Figure 2.7 Illustration of the typical stress versus strain response of PMMA in uniaxial tension, around and above the glass transition temperature for identical strain rates: (a) nominal stress S versus nominal strain e at constant nominal strain rate $\dot{e}$ and (b) true stress σ versus true strain ε at constant true strain rate $\dot{\varepsilon}$. As the temperature increases for a fixed rate, the response evolves through the following constitutive regimes: (i) the brittle (elastic) glassy, (ii) the plastic yielding glassy, (iii) the glass transition, (iv) the rubbery, and (v) the viscous flow regime. Crosses at the end of the curves denote failure.

in an almost linear fashion with increasing temperature due to the increase in vibrational energy of chain segments to give (Yannas and Luise, 1982; Gilbert et al., 1986):

$$E_{\mathrm{g}} = E_0\left(1 - \alpha_{\mathrm{m}}\frac{T}{T_{\mathrm{g}}}\right) \tag{2.8}$$

in terms of a coefficient α_{m} related to size of the conformational segments and the magnitude of the energy barriers, and modulus E_0 at absolute zero.

Near the glass transition temperature ($T/T_{\mathrm{g}} \approx 1$) the small strain response is viscoelastic in nature. Gilbert et al. (1986) treated the polymer at $T/T_{\mathrm{g}} \approx 1$ as a parallel array of a large number of one dimensional Maxwell units; each unit comprises a linear dashpot and a linear spring in series, such that the array has a spectrum of relaxation time to mimic the macroscopic, observed relaxation in modulus around the glass transition. The non-linear dependence of the viscosity of the dashpot on T/T_{g} can be modelled by WLF theory (Williams et al., 1955):

$$\eta_{\mathrm{WLF}} = 3\eta_0 \exp\left(\frac{-C_1(T/T_{\mathrm{g}} - 1)}{C_2/T_{\mathrm{g}} + T/T_{\mathrm{g}} - 1}\right) \tag{2.9}$$

where η_0 is a reference viscosity at $T/T_g = 1$, and C_1 and C_2 are fitting constants. The constant C_1 can be related to the free volume fraction of the polymer at $T/T_g = 1$, while C_2 can be related to the free volume expansion coefficient of the polymer (Young and Lovell, 2011). Williams et al. (1955) demonstrated that the values of C_1 and C_2 are independent of the choice of polymer system, although more recent studies on amorphous polymers report tailored values for C_1 and C_2 as summarised by Ferry (1980) and Mark (2003). The magnitude of the reference viscosity η_0 may be governed by the molecular weight of the polymer as detailed below.

The large strain, viscoplastic response

The dependence of the plastic response in the glassy regime upon temperature is more complex, and can roughly be subdivided into two regimes, $T/T_g < 0.8$, and $0.8 < T/T_g < 1$. Typically, when a linear, amorphous polymer is subjected to uniaxial tension at $T/T_g < 0.8$, the stress versus strain response is almost linear and brittle fracture intervenes (at a true tensile strain below 0.1) by the formation of an unstable craze or by fast fracture from a pre-existing flaw (Bin Ahmad and Ashby, 1988; Mark, 2003).

For $0.8 < T/T_g < 1$, shear yielding follows an initial elastic response. Typically, yield is accompanied by a load drop and by the development of a neck (Melick et al., 1999). High strain rate sensitivity reduces the degree of neck formation and orientation hardening leads to neck propagation along the length of the specimen, as measured and described in detail by G'Sell and co-workers (G'Sell and Jonas, 1979; G'Sell et al., 1992) and analysed by finite element simulations by Wu and van der Giessen (1995). After the neck has propagated along the entire length of the sample, the load increases again until failure intervenes. Wu and Van Der Giessen (1993) reviewed the use of chain network models to predict the orientation hardening found in the stress-strain response of cross-linked rubbers and linear, amorphous polymers. Near the glass transition temperature ($T/T_g \approx 1$), the secondary (van der Waals) bonds between the chains melt and polymer chain segments can reptate past each other. The stress versus strain response becomes highly rate and temperature sensitive at temperatures near the glass transition temperature. At temperatures above T_g, there ceases to be a load drop at yield, and no neck is formed (G'Sell and Souahi, 1997; Dooling et al., 2002).

It is widely accepted that plastic yielding of linear, amorphous polymers is governed by the thermally activated motion of molecular chain segments (Fleck et al., 1990). The time and tem-

perature dependence of the flow strength may be described by a modified version of the Eyring model which was originally developed for the viscous flow of liquids (Eyring, 1936; Ree and Eyring, 1955). The Ree-Eyring model assumes that an applied stress $\bar{\sigma}$ reduces the energy barrier for vibrating chain segments to jump forward and increases the barrier to jump backwards. Between the secondary (β-) transition and the (α-) glass transition temperature, the von Mises, effective plastic strain rate $\dot{\varepsilon}_{\mathrm{e}}$ is related to $\bar{\sigma}$ via a single transition process such that (Ree and Eyring, 1955):

$$\frac{\dot{\varepsilon}_{\mathrm{e}}}{\dot{\varepsilon}_0} = \sinh\left(\frac{\bar{\sigma} v}{kT}\right) \exp\left(\frac{-q}{kT}\right) \tag{2.10}$$

where $\dot{\varepsilon}_0$ is a reference strain rate, q is an activation energy, v is an activation volume, and k is Boltzmann's constant. Linear, amorphous polymers are typically pressure-dependent in their flow response, such that yield is activated by both the von Mises effective stress σ_{e} and the hydrostatic (mean) stress σ_{h}, where[8]:

$$\sigma_{\mathrm{e}}{}^2 = \frac{3}{2} S_{ij} S_{ij} \tag{2.11}$$

in terms of the deviatioric stress tensor S_{ij} ($= \sigma_{ij} - \delta_{ij}\sigma_{\mathrm{h}}$), and:

$$\sigma_{\mathrm{h}} = \frac{\sigma_{kk}}{3} \tag{2.12}$$

Note that the hydrostatic stress σ_{h} is equal in magnitude but opposite in sign to the pressure p. A common assumption is to assume that the stress measure $\bar{\sigma}$, activating plastic flow (see Eq. 2.10), is given by:

$$\bar{\sigma} = \sigma_{\mathrm{e}} + \alpha \sigma_{\mathrm{h}} \tag{2.13}$$

where α is a pressure sensitivity index taken to be a material constant. Hence, the ratio between the yield strength in compression ($\sigma_{\mathrm{yc}} < 0$) and the yield strength in tension ($\sigma_{\mathrm{yt}} > 0$), when deformed at identical effective plastic strain rate $\dot{\varepsilon}_{\mathrm{e}}$ and temperature T, is (Van Loock and Fleck, 2018):

[8] A repeated suffix denotes summation over 1 to 3 following the usual Einstein notation.

$$\frac{\sigma_{yc}}{\sigma_{yt}} = \frac{3+\alpha}{3-\alpha} \tag{2.14}$$

Measurements of the ratio σ_{yc}/σ_{yt} imply $\alpha \approx 0.4$ for PMMA (Bauwens-Crowet, 1973; Bin Ahmad and Ashby, 1988; Dooling et al., 2002).

Failure strain

Within the plastic yielding regime, $0.8 < T/T_g < 1$, large plastic strains are achievable prior to ductile fracture. Failure is by the stable growth of cavities (known as 'diamonds') originating from surface defects or crazes until they reach a critical size (Cornes and Haward, 1974; Kinloch and Young, 1983). A few experimental studies in the literature report the brittle and ductile tensile failure strain ε_f of PMMA as a function of temperature and strain rate in the glassy regime (Cheng et al., 1990; Fleck et al., 1990; Abdel-Wahab et al., 2016). To a first approximation, the dependence upon T/T_g is governed by two linear relations, one for brittle elastic behaviour (small slope) and one for failure at large plastic strains (large slope), see Fig. 2.6c. The measured values for ε_f by Cheng et al. (1990) suggest that the ductility of PMMA is relatively insensitive to strain rate in the glassy regime.

2.1.4.2 The rubbery regime

The small strain, visco-elastic response

Linear, amorphous polymers of moderate to high molecular weight (i.e. > 150 000 g mol^{-1} typically exhibit a rubbery plateau at a temperature regime just above the glass transition; the extent of the rubbery plateau depends on the molecular weight (distribution) of the polymer (McLoughlin and Tobolsky, 1952; Gilbert et al., 1986). Within this rubbery regime, most of the secondary bonds are broken and long range sliding of polymer chains is prevented by chain entanglements. The entanglement points act as physical cross-links governing the polymer's constitutive state in a similar fashion to chemical cross-links of rubbers. The rubbery modulus at vanishing strain can be related to temperature by a Gaussian statistical analysis of a cross-linked network, i.e. the stiffness of the network changes as the entropy of the network chains changes, see (Treloar, 1975; Treloar et al., 1976; Gilbert et al., 1986):

$$E = \frac{3\rho RT}{M_e} \tag{2.15}$$

where ρ is the (temperature-dependent) density of the rubber and M_e is the number average molecular weight between the entanglement points (or cross-links).

The large strain, visco-plastic response

Bin Ahmad and Ashby (1988) omit the presence of the rubbery plateau between the glassy regime and the viscous flow regime in their description of σ_y as a function of rate and temperature. As the width of the rubbery plateau is governed by the average molecular weight (and the molecular weight distribution), this approach may suffice for grades of low molecular weight. In contrast, most commercial linear amorphous polymers typically possess a relatively high molecular weight (i.e. $> 150\,000$ g mol^{-1}), and an extensive rubbery regime on a σ_y versus T/T_g curve is anticipated above the glass transition as sketched in Fig. 2.6b.

Only a limited set of complete stress versus strain curves for PMMA in uniaxial tension are reported in the literature for testing temperatures close to and just above the glass transition temperature (G'Sell and Souahi, 1997; Dooling et al., 2002). Characterisation of the dependence of the large strain, visco-plastic response of PMMA in uniaxial tension upon temperature, rate, and molecular weight at temperatures close to or just above T_g is therefore challenging.

Failure strain

Experimental data on the effect of rate and temperature on the tensile failure strain ε_f of linear, amorphous polymers in the glass transition and rubbery regime are scarce. Smith (1963) investigated the ultimate tensile strength and failure strain of cross-linked, amorphous elastomers such as styrene-butadiene rubbers (SBR) near their glass transition and demonstrated the applicability of time-temperature superposition for the tensile failure strain. Vinogradov (1975) found that the tensile failure strain ε_f of polymer melts went through a minimum at a temperature above T_g and then underwent a steep increase as the viscous flow regime is reached. The dependence of ε_f upon T/T_g for a commercial linear, amorphous polymer may exhibit a similar trend: a local maximum is attained in the rubbery regime, followed by a dip as the polymer transitions from the rubbery to the viscous state, see Fig. 2.6c. However, insufficient measurements are reported in the literature for firm conclusions to be drawn. For instance, tensile tests on some commercial grades of PMMA and polystyrene melts performed by Pearson and Connelly (1982) show

that the failure strain of molten PMMA is independent of strain rate. The reviews of Malkin and Petrie (1997) and Joshi and Denn (2004) point out that fundamental models on the dependence of failure strain upon molecular weight (distribution) in the rubbery state also appear to be lacking.

2.1.4.3 The viscous regime

The small strain, visco-elastic response

At temperatures just above the glass transition temperature (i.e. $T/T_g > 1.15$), molecular entanglement points slip and the macroscopic constitutive behaviour can be treated as a viscous melt. Flow occurs by the reptation of individual polymer chains that are confined in tubes as defined by their surrounding environment (Rouse, 1953; De Gennes, 1976; Doi and Edwards, 1986). Simple models exist for this behaviour. For example, Gilbert et al. (1986) modelled the rate and temperature dependent small strain modulus in the viscous regime by means of a Maxwell unit consisting of a WLF or Arrhenius governed dashpot and a linear spring with a temperature-dependent modulus.

The large strain, visco-plastic response

Bin Ahmad and Ashby (1988) suggest a straightforward view of the rate and temperature dependent flow strength σ_y for a polymer melt in the viscous flow regime. They assume that the flow strength σ_y versus strain rate $\dot{\varepsilon}$ relation is linear with slope 3η, where η is the shear viscosity. They assert that the temperature dependence of η is given by WLF theory, see Eq. 2.9, for temperatures close to T_g, and by an Arrhenius relation for higher temperatures. A reptation model for viscous flow was developed by Doi and Edwards (Doi and Edwards, 1978a,b), showing that the shear viscosity has a power law dependence upon molecular weight, with an exponent of 3 in good agreement with experimental observations for polymer melts (O'Connor and Ball, 1992).

Failure strain

It is broadly accepted that the rupture strain of a viscous melt is governed by the surface tension-driven instability of Rayleigh–Plateau (Plateau, 1873; Lord Rayleigh, 1878).

2.1.4.4 Large strain, three dimensional models

Boyce and co-workers (Boyce et al., 1988; Boyce and Arruda, 1990; Arruda and Boyce, 1993) developed a sophisticated three dimensional theoretical framework to simulate the stress-strain response of linear, amorphous polymers over the entire glass-to-rubber transition regime. Based on the one-dimensional model of Haward and Thackray (1968), they assume that the polymer has a parallel combination of intermolecular and molecular network resistances. The framework of Boyce et al. (2000) was originally developed for polyethylene terephthalate glycol (PETG), but, more recently, Palm et al. (2006) have used it to describe the constitutive behaviour of PMMA around T_g for uniaxial compression. The three dimensional model of Dooling et al. (2002) focuses on the constitutive response of PMMA loaded in uniaxial tension around and above its glass transition. The three-dimensional large strain constitutive models of Dooling et al. (2002) and Palm et al. (2006) give good curve fits to uniaxial compressive and some tensile test data. However, they make use of a large number of fitting constants and there are few non-proportional, multi-axial tests available to calibrate the full three-dimensional response. Moreover, these models were developed to predict the deformation response, but give little insight into failure. The constitutive laws summarised in the deformation mechanism maps of Gilbert et al. (1986) and Bin Ahmad and Ashby (1988) provide a less sophisticated one dimensional description of the deformation of PMMA in uniaxial tension close to the glass transition. They rely, however, on less fitting constants and are readily implemented in analytical or numerical frameworks aiming to predict the deformation of PMMA in tension close to the glass transition for processes such as hot embossing or solid-state foaming.

2.1.5 Concluding remarks

The following remarks are summarised to conclude the literature review on polymeric nanofoams and the solid-state nanofoaming process:

- Polymeric nanofoams produced by solid-state foaming have attracted a lot of interest during the last decade due to their potentially unique combination of mass-rationalised properties. One of those highly cited properties is their thermal conductivity which may be lower than that of air due to the Knudsen effect.

- The microstructural requirement (porosity above 0.85 and void size below 200 nm) for polymeric nanofoams to have a thermal conductivity lower than that of air is, however, currently beyond the practical limit of the state-of-the-art solid-state nanofoaming process (Okolieocha et al., 2015; Wang et al., 2017). Methyl methacrylate-based nanofoams (such as PMMA nanofoams) have some of the highest porosities and lowest cell sizes reported in the literature.

- The solid-state nanofoaming process typically comprises three steps. First, a polymer precursor is saturated with a physical blowing agent during the saturation. Second, nucleation is induced by supersaturating the polymer-gas mixture. Third, the sample is foamed by allowing the as-nucleated voids to expand.

- Void growth prediction models in the literature predominantly focus on cavity expansion during liquid (e.g. extrusion foaming) rather than solid-state foaming routes. The relatively recent model of Khan et al. (2015) focuses on the prediction of void nucleation and growth during a solid-state nanofoaming process but makes use of a viscous constitutive law. The latter assumption is arguably not appropriate as, during solid-state foaming, cavity expansion occurs at temperatures close to the effective glass transition temperature of the solid surrounding the void.

- Gilbert et al. (1986) and Bin Ahmad and Ashby (1988) employed a set of constitutive laws to construct deformation maps for PMMA in uniaxial tension close to the glass transition. The use of these constitutive equations to simulate void growth during solid-state foaming of PMMA is attractive given the need of only a few fitting constants and the relatively low computational power required to solve them within a void growth framework. Accurate void growth simulations for solid-state (nano)foaming with an PMMA grade of interest require the calibration of these constitutive equations to measured stress-strain curves of the PMMA grade (or of a grade with a similar average molecular weight and molecular weight distribution). However, tensile stress-strain curves for commercial PMMA grades at temperatures close to the glass transition are scarce in the literature.

2.2 Adhesive joints

Adhesive joints are, just like polymeric foams, one of the countless applications of synthetic polymers. Adhesive bonding is more and more frequently being used to join load-bearing structural components as it offers many advantages compared to traditional joining methods such as mechanical fastening (riveting, bolting, ...) or welding (Adams et al., 1997; da Silva et al., 2018). These advantages include:

- Good damping properties.
- More uniform stress distribution along the bond.
- Improved fatigue strength.
- Reduced weight.
- Improved corrosion resistance.
- Ability to join dissimilar materials to produce hybrid material systems and structures.

Some drawbacks are associated with the use of adhesive bonding methods. Adhesive joints have a limited service temperature range dictated by the nature of the synthetic polymeric constituent. In addition, substrate materials may require extensive pretreatment and curing of the adhesive may require excessive time and an external heat source. Despite these disadvantages, adhesive bonding has become common place in the aerospace, automotive, and wind turbine industries to join lightweight materials such as aluminium and CFRP or GFRP composites (Higgins, 2000; Davies et al., 2009; Loureiro et al., 2010; Carlberger and Stigh, 2010; da Silva et al., 2018).

2.2.1 Adhesive joint design

The design of a bonded joint may be governed by many aspects, including, but not limited to, the substrate material, the anticipated operational conditions, and the manufacturing and operational costs. Many adhesive joint designs are available to the engineer, some common designs are presented in Fig. 2.8. Failure of the joint may occur by (i) cohesive failure in the adhesive,

(ii) failure at the adhesive-substrate interface, known as adhesive failure, or (iii) failure in the substrate (Davis and Bond, 2010). Mixed failure modes are possible. The experimental and theoretical results in this thesis are limited to the case of cohesive failure.

Many structural adhesives exist. The choice of the adhesive may depend on the nature of the substrate materials, the joint design, the anticipated loading conditions, the operational environment, adhesive layer height restrictions, and the end-of-life requirements. Common structural adhesives are (i) epoxy-based adhesives, (ii) polyurethane (PUR) adhesives, and (iii) acrylic adhesives (Dillard, 2010). Epoxies are the strongest and stiffest class of structural adhesives, with a Young's modulus close to 1 GPa, and a uniaxial tensile strength close to 50 MPa, but are typically brittle in nature (i.e. their tensile failure strain is limited to close to 0.05). Elastomeric particles are often added to the epoxy to increase the ductility and toughness of the epoxy (Kinloch and Young, 1983; Kinloch et al., 1983; Huang and Kinloch, 1992). These epoxies are known as rubber-modified epoxies. Polyurethane and other elastomeric adhesives exhibit a significantly higher ductility (with a tensile failure strain in the range of 1 to 2), but have a much lower strength and stiffness than epoxy adhesives. Acrylic adhesives such as methyl methacrylate (MMA) adhesives typically exhibit intermediate properties between epoxy and PUR adhesives (Scigrip Europe, 2017; Dillard, 2010). The typical nominal stress versus nominal strain response of an unmodified epoxy adhesive, a rubber-modified epoxy adhesive, a PUR adhesive, and an MMA adhesive in uniaxial tension is shown in Fig. 2.9.

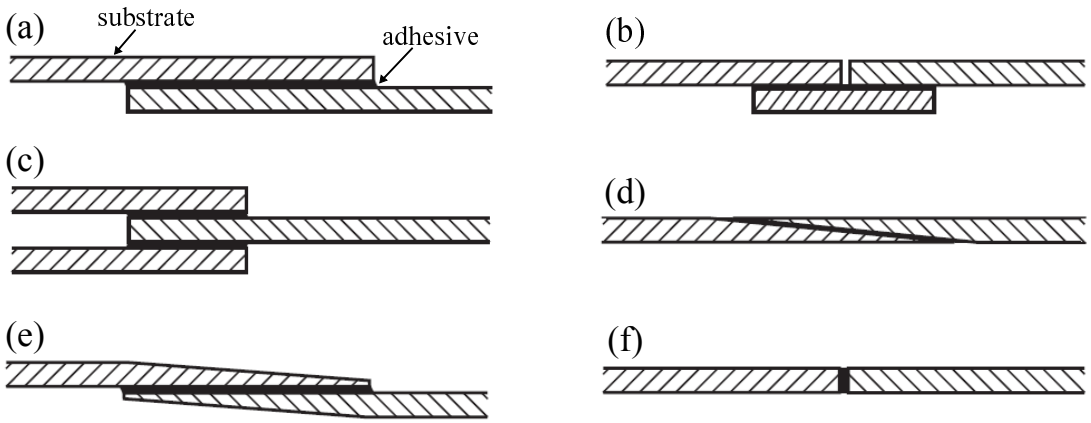

Figure 2.8 Sketches of common adhesive joint designs: (a) simple lap joint, (b) strap joint, (c) double lap joint, (d) scarf joint, (e) tapered lap joint, (f) butt joint. Adapted from (Hexcel, 2003).

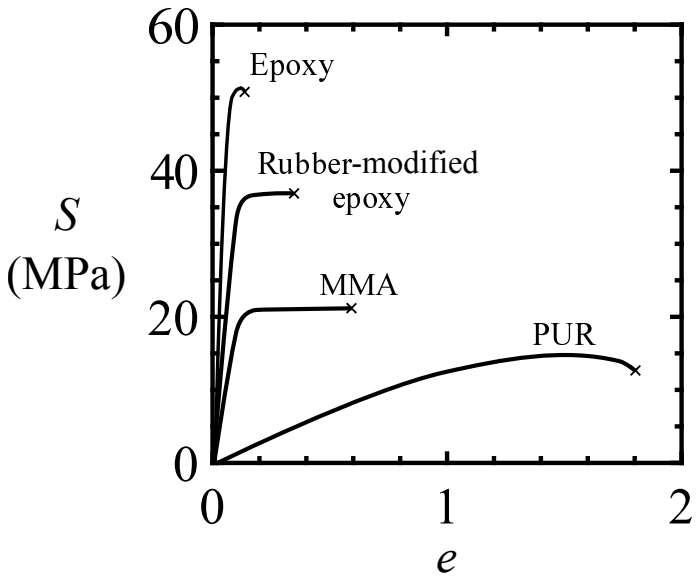

Figure 2.9 Typical nominal stress verus nominal strain curves of common structural adhesives in uniaxial tension: unmodified epoxy (Imanaka et al., 2015), rubber-modified epoxy (Imanaka et al., 2015), acrylic (MMA) (Scigrip Europe, 2017; Kozlowski et al., 2018), polyurethane (PUR) (Dillard, 2010)). The stress-strain curves are representative for tests at room temperature and at a moderate strain rate (close to $\dot{e} = 10^{-3}\ \mathrm{s}^{-1}$). Crosses at the end of the curves denote failure.

The fracture toughness of a structural adhesive is an additional property that may have to be taken into account for the design of an adhesive joint. The critical mode I energy release rate G_c of linear, elastic and brittle adhesives such as unmodified epoxies may be obtained via standard fracture toughness tests, such as compact tension (CT) and single edge notch bending (SENB) tests, on the bulk adhesive (Hunston et al., 1989; da Silva et al., 2018). Ductile elastic-plastic adhesives may have a pronounced crack growth resistance or *R*-curve behaviour. In this case, G_c may be dependent on the length of a stably growing crack due to an extrinsic toughening mechanism (Tvergaard and Hutchinson, 1992). A rise in toughness from the initial critical energy release rate G_c^0 is often observed until a crack length-independent (steady-state) value for the critical energy release rate G_c^ss is attained. Rubber-modified epoxies typically exhibit significant *R*-curve behaviour facilitated by non-linear, irreversible deformation of adhesive material when going through the process zone at the crack tip into the wake of the growing crack (Du et al., 1998, 2000). The non-linear deformation takes place by cavitation of the elastomeric particles and by shear yielding of the epoxy matrix (Evans et al., 1986; Yee and Pearson, 1986; Huang and Kinloch, 1992). Measured *R*-curves of rubber-modified epoxies via SENB tests are shown in Fig. 2.10 (Imanaka et al., 2015). As shown in Fig. 2.10, rubber-modified epoxies may have

pronounced R-curves with G_c^0/G_c^{ss} in the order of 2 to 10 (Du et al., 1998, 2000; Ameli et al., 2010). In contrast, most common structural adhesives such as unmodified or toughened epoxies, acrylic, and polyurethane adhesives exhibit typically flat or moderate ($G_c^0/G_c^{ss} < 1.5$) R-curves (Banea et al., 2014; Monteiro et al., 2015; Sekiguchi et al., 2017; Maloney and Fleck, 2018).

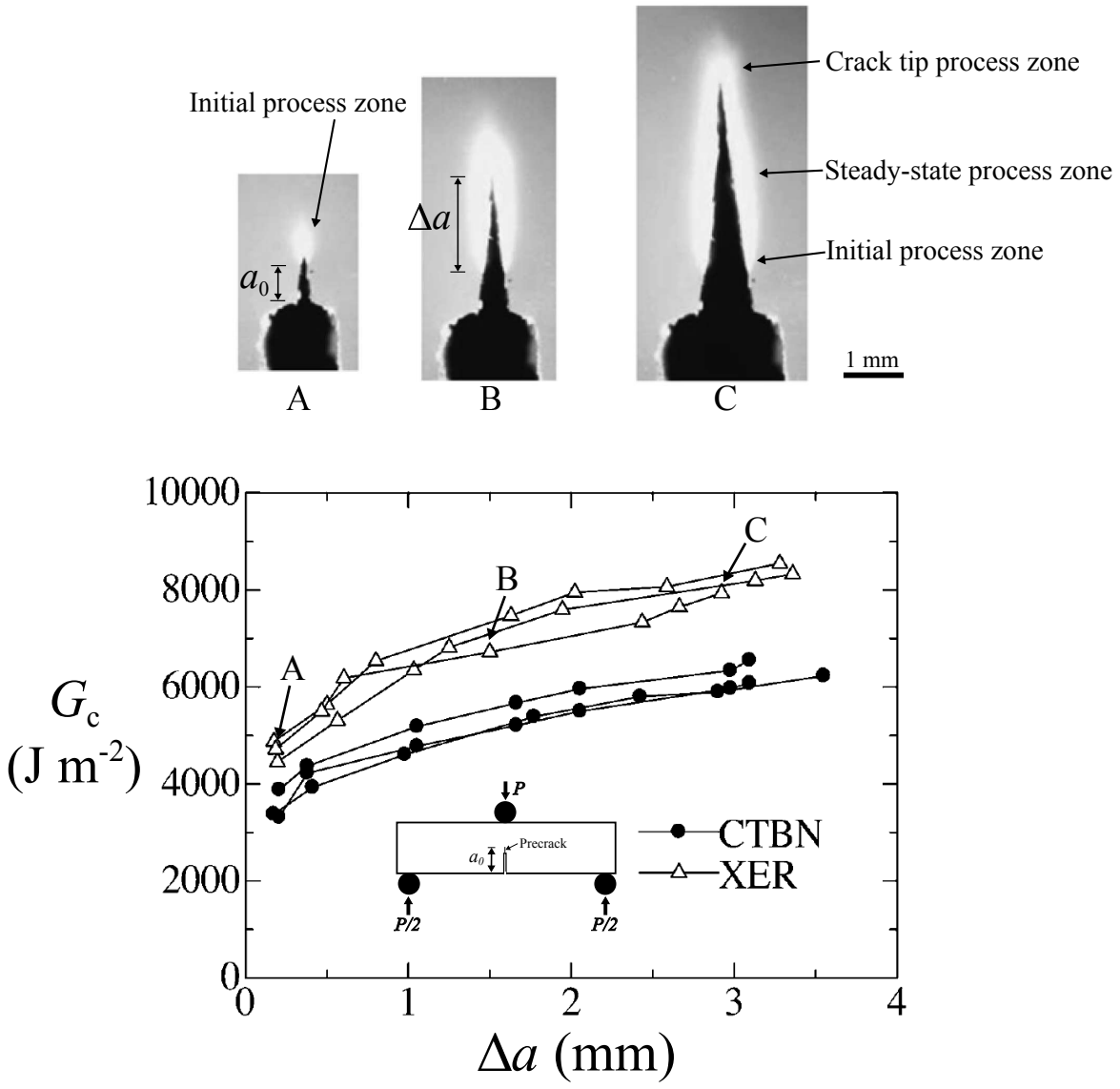

Figure 2.10 Critical mode I energy release rate G_c versus crack growth Δa resistance curves measured for a crack in a rubber-modified epoxy SENB specimen. The two epoxies are modified with carboxy-terminated butadiene-acrylonitrile (CBTN) and cross-linked rubber (XER) particles. The images are taken from the surface during a test with a XER-modified epoxy specimen and show three stages of crack growth and the corresponding development of the surface process zone during the test. Images are adapted from the work of Imanaka et al. (2015).

Most *R*-curve measurements are conducted via joint specimen geometries such as the (tapered) double cantilever specimen comprising two cantilever substrates joined by an adhesive layer with a pre-crack (da Silva et al., 2018). *R*-curves reported via joint specimens may, however, not be representative for the true, geometry-independent *R*-curve of the bulk adhesive given the *R*-curve may be suppressed in the adhesive when constrained in a layer between two stiff substrates (Tvergaard and Hutchinson, 1996). The role of these constraint effects on the strength and toughness of adhesive joints are explored in detail in the coming paragraphs.

2.2.2 Constrained adhesive layers

As mentioned above, the behaviour of a thin adhesive layer when located between two substrates may be different from that of the bulk adhesive. Potential causes for this phenomenon include (i) the presence of defects in the adhesive layer and (ii) the constraint exerted by the stiff substrates on the compliant layer.

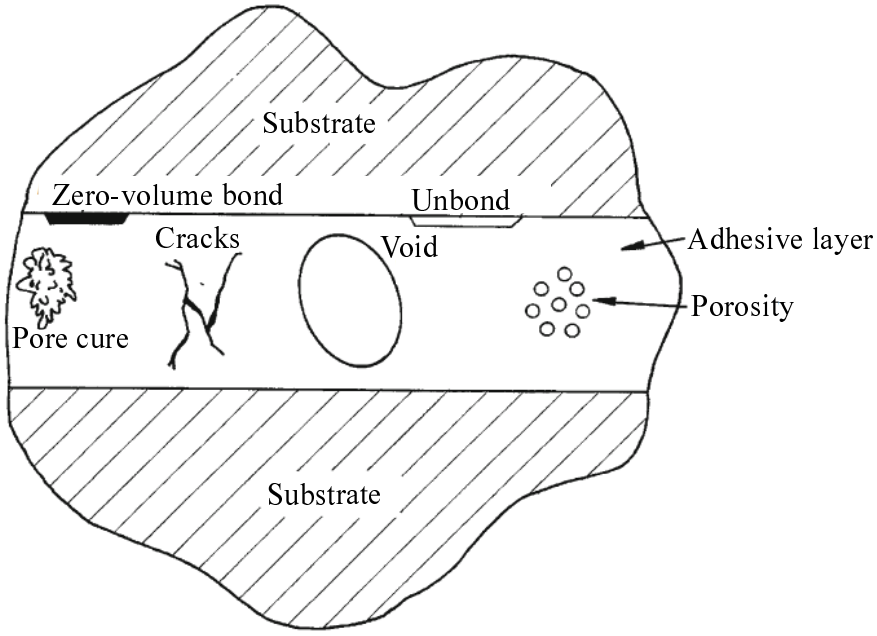

Figure 2.11 Sketch of the various defects which may be present in the adhesive layer of a bonded joint. Adapted from da Silva et al. (2018).

2.2.2.1 The presence of defects

A sketch of the various defects which may be present in an adhesive layer upon curing is given in Fig. 2.11. Porosity in the adhesive layer may be caused by volatiles in the adhesive components or entrapped moisture in the surface of the substrate prior to application of the adhesive (Chester and Roberts, 1989; Pearce et al., 1998; Katnam et al., 2011). These microvoids may coalesce into larger voids prior to the curing of the adhesives. Large voids can also be caused by entrapment of air during the application of the adhesive, insufficient supply of the adhesive, and shrinking of the adhesive during the bonding process (Bascom and Cottington, 1972; da Silva et al., 2018). For instance, MMA adhesives are known to exhibit high levels of volumetric shrinking (in the order of 10% to 30%) during curing (Dillard, 2010; Kwon et al., 2014). Shrinkage may also give rise to the presence of cracks in the adhesive layer and at the adhesive-substrate interface. Some regions in the adhesive layer may also be only partially cured due to, for example, insufficient thermal exposure. The strength and stiffness of the adhesive in these partially cured areas may be significantly reduced. Surface unbonds may also be present when the adhesive is unevenly distributed over the substrate. Zero-volume unbonds (known as kissing bonds) exist where the adhesive and substrate are in contact but the bond is only partial caused by, for example, inappropriate pretreatment of the surface of the substrate (Jeenjitkaew and Guild, 2017; da Silva et al., 2018).

The presence of one or more of the aforementioned forms of defects in an adhesive joint may severely degrade the performance of the joint. In practice, however, it is often impossible to produce defect-free adhesive joints. Non-destructive testing of a joint by, for instance, ultrasonic and spectroscopic methods can be performed to assess the severity of defect formation in the bond (Dillard, 2010; da Silva et al., 2018). Accurate models are required to predict the properties of the joint in the presence of these voids and cracks. Constraint effects of the stiff substrate on the compliant adhesive layer containing these defects may have to be taken into account.

2.2.2.2 Constraint effects on compliant adhesive layers

As mentioned above, the properties of constrained adhesives may differ from those of the adhesive in bulk. The effect of constraint by the substrate depends on the nature of the adhesive

material. For instance, it is well known that the apparent tensile stiffness of butt joints comprising an incompressible elastomeric adhesive, such as a PUR or silicon adhesive, is a function of the shape factor[9] of the joint (Gent and Lindley, 1959). In addition, failure by unstable cavitation of cracks or voids in these elastomeric adhesive layers may may be triggered due to increased triaxial stresses generated in the adhesive as the level of constraint (i.e. magnitude of the shape factor) is increased (Gent and Lindley, 1959; Lindsey, 1967; Ball, 1982). The role of constraint on the fracture behaviour of elastic, brittle (i.e. unmodified epoxy) adhesives and elastic-plastic, ductile (i.e. rubber-modified epoxy and MMA-based) adhesives is discussed in the following paragraphs. Note that most of the experimental evidence on constraint effects in adhesive layers mentioned in this discussion is based on tests with epoxy-based adhesive material systems given they were, and still are, the most prevalent and characterized adhesive materials.

Wang et al. (1978) computed the distribution of the tensile stress component σ_{yy} at the crack tip along the mid-height plane of an adhesive layer in a DCB specimen by making use of a finite element (FE) model. Both the adhesive material and the substrate material were assumed to be linear, elastic (with Young's modulus E_1 for the substrate and Young's modulus E_2 for the adhesive). Wang and co-workers explored the role of constraint by varying the modulus mismatch ratio E_2/E_1 and showed that a local singular stress field field of intensity K^{tip} exists close to the crack tip. Ryvkin (2000) made use of the Wiener-Hopf method to give solutions (in terms of quadratures) for the tensile stress component σ_{yy} at the tip of a semi-infinite crack subjected to mode I loading in an infinite elastic layer sandwiched between two infinite elastic substrates. The solutions of Ryvkin (2000) suggested that for $E_2/E_1 < 0.1$, the size of this local K^{tip} stress field is close to 0.015 times the layer height. Application of the path-independence of the J-integral (Rice, 1968) gives a relationship between the intensity of the remote K^{∞}-field and the intensity of the local K^{tip}-field at the crack tip (Trantina, 1972; Fleck et al., 1991):

$$K^{\text{tip}} = \left(\frac{\bar{E}_2}{\bar{E}_1}\right)^{\frac{1}{2}} K^{\infty} \tag{2.16}$$

where $\bar{E}$ and $\bar{\nu}$ represent the Young's modulus E and Poisson's ratio ν in plane stress, but $E/(1-\nu^2)$ and $\nu/(1-\nu)$ in plane strain. In words, the toughness of a compliant adhesive layer constrained by a stiffer substrate may be higher than the toughness of the bulk adhesive. This is

[9] The shape factor is defined as the loaded cross-sectional area of the joint divided by the area of the free surfaces.

known as the elastic stress-intensity shielding effect (Suo, 1990; Fleck et al., 1991).

Rice (1968) gave a solution for K^{tip} for the case of a semi-infinite crack in a linear, elastic adhesive layer clamped by two rigid substrates (i.e. $\bar{E}_2/\bar{E}_1 \rightarrow 0$) and subjected to a uniform opening displacement orthogonal to the adhesive layer:

$$K^{\text{tip}} = [(1-\bar{\nu}^2)h]^{\frac{1}{2}}\sigma_{yy} \tag{2.17}$$

Note that K^{tip} is independent of crack length. Wang (1997) made use of Eqs. 2.16 and 2.17 and conducted FE simulations to give closed-form (approximate) interpolated solutions for the value of K^{tip} for a crack in an elastic layer sandwiched between two elastic substrates as a function of crack length, adhesive layer height, and modulus mismatch ratio. The physical basis for these equations is limited, however, and they do now allow to explore the role of plasticity at the crack tip and the effect of finite joint width on the strength of the joint.

The role of constraint on the fracture toughness of an adhesive joint was characterized in the experimental study of Bascom et al. (1975). Bascom and co-workers conducted a series of fracture tests on tapered DCB specimens comprising an epoxy adhesive (with a flat R-curve in bulk) and

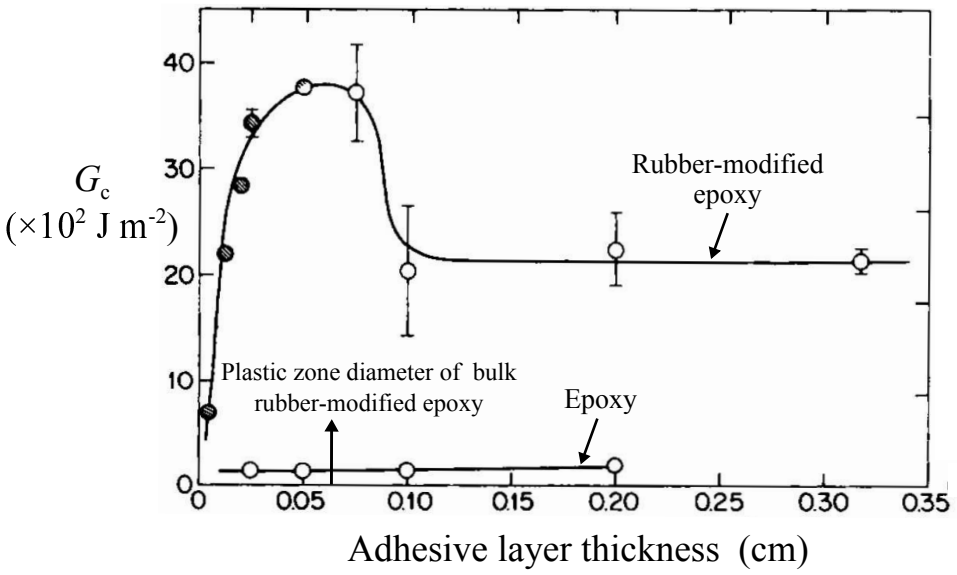

Figure 2.12 The measured toughness G_c of a DCB joint as a function of adhesive layer height for a untoughened epoxy adhesive and a rubber-modified epoxy adhesive. Adapted from the work of Bascom et al. (1975).

a rubber-modified epoxy (with a pronounced *R*-curve in bulk, see Fig. 2.10). The experimental outcomes of Bascom et al. (1975) suggested that the toughness of the epoxy joint was independent of adhesive layer height, see Fig. 2.12. In contrast, a strong dependence of the toughness of the joint comprising the rubber-modified epoxy adhesive upon layer height was observed, see Fig. 2.12. For an increasing adhesive layer height, the toughness increased until a maximum value of joint toughness was observed. The peak in toughness was found to correspond to a layer height close to the estimated diameter of the plastic zone at the tip of a crack in a bulk adhesive. For larger adhesive layer heights, the toughness decreases and eventually reaches a layer-height independent value close to the bulk adhesive toughness. Multiple experimental studies reported a similar relation between the toughness of a rubber-modified epoxy joint and the height of the adhesive layer (Kinloch and Shaw, 1981; Hunston et al., 1989; Daghyani et al., 1995; Yan et al., 2001; Lee and Ramesh, 2004). This non-linear relation is thought to be governed by the complex interaction between plastic dissipation mechanisms in the epoxy adhesives and the effect of constraint due to the presence of the substrates.

A qualitative explanation for the role of constraint (i.e. adhesive layer height) on the measured toughness of a rubber-modified epoxy joint was given by Kinloch and Shaw (1981). Making use of the FE analysis of Wang et al. (1978) introduced above, Kinloch and Shaw suggested that the observed peak in joint toughness corresponded to an adhesive layer height providing enough constraint to enlarge the plastic zone at the crack tip with respect to the magnitude of the plastic zone in the bulk adhesive. According to Kinloch and Shaw (1981), lower adhesive layer heights restrict the formation of the plastic zone and subsequently reduce the plastic dissipation of material at the crack tip, leading to a reduced joint toughness. On the other hand, an adhesive layer height above the optimum height results in a joint toughness close to the bulk adhesive toughness as the role of constraint on the stress distribution at the crack tip becomes negligible (Komatsu et al., 2018).

More insight on the failure of constrained elastic-plastic layers was provided by the work of Ashby et al. (1989). Ashby et al. (1989) observed that the failure strength of a constrained metal wire exceeded the uniaxial yield strength of an unconstrained wire up to a factor of six. Failure of the constrained metal wires was found to be triggered by unstable cavitation instead of failure by necking and cup-and-cone fracture as observed in unconstrained wires. Inspired by the work

of Ashby and co-workers, Varias et al. (1991) conducted FE simulations of an elastic-plastic layer with strain hardening capability sandwiched between two elastic substrates. Varias and co-workers reported that the maximum mean stresses at a distance equal to several layer heights from the crack tip may be four to six times the yield strength of the layer. The competition of failure mechanisms triggered at these elevated levels of stress triaxiality such as cavitation and interfacial debonding was discussed in the work of Varias et al. (1991). In addition, they stipulate that crack tip shielding may take place due to non-proportional stressing associated with the plastic flow in the layer constrained by the substrates. This shielding effect differs from the elastic stress-intensity shielding effect formulated in Eq. 2.16, but may also contribute to a joint toughness exceeding the toughness of the bulk adhesive as shown for the rubber-modified epoxy joint in Fig. 2.12.

Subsequent seminal work on the fracture toughness of constrained elastic-plastic layers was performed by Tvergaard and Hutchinson (Tvergaard and Hutchinson, 1992, 1994, 1996). Tvergaard and Hutchinson made use of an FE model comprising a cohesive zone obeying a traction versus separation law[10] of peak strength $\hat{\sigma}$ and of work of separation Γ at the plane ahead of the crack in an elastic-plastic material constrained by two elastic substrates. Their results suggested that *R*-curve effects vanish when the adhesive layer height is smaller than the size of the plastic zone of the adhesive in bulk. In addition, when $\hat{\sigma}$ is lower than two times the yield strength of the adhesive, the toughness of the joint was found to be independent of layer height.

The work of Hutchinson and co-workers (Varias et al., 1991; Tvergaard and Hutchinson, 1992, 1994, 1996) focused on joints comprising ductile metal layers constrained by ceramic substrates. Pardoen et al. (2005) considered the case of a polymeric-based adhesive joint and used an FE model similar to the one employed by Tvergaard and Hutchinson (1996) to shed light on the role of constraint on the toughness of the adhesive joint. Pardoen et al. (2005) conducted wedge-peel fracture tests on two structural adhesives to infer values for the two characteristic parameters ($\hat{\sigma}$ and Γ) of the traction-separation law for the cohesive zone, and assumed $\hat{\sigma}$ and Γ to be independent of constraint. The computed curves for the toughness of the joint as a function of adhesive layer height for both adhesives were found to be similar to the one shown in Fig. 2.12

[10] The effect of the shape of the traction separation law for the cohesive zone on the computed distributions of stress components at the crack tip was found to be minor compared to the choice for $\hat{\sigma}$ and Γ (Tvergaard and Hutchinson, 1992).

for the rubber-modified epoxy. More insight was obtained in a subsequent study, in which Pardoen and co-workers defined three regimes in the adhesive layer where plastic dissipation may develop: crack tip plasticity, reverse plastic loading at the crack face, plastic shear deformation at the adhesive-substrate interface (Martiny et al., 2012). Each of these energy dissipation mechanisms may contribute to the observed toughness of the joint. Only when the combined toughness contribution via these plastic dissipation mechanisms is of the same order or larger than the constrained-independent intrinsic work of fracture Γ, a dependence of the joint toughness upon layer height is expected. The constraint-induced plastic dissipation contribution to the joint toughness becomes negligible for joints with adhesive layer heights much larger than the plastic zone size of the adhesive in bulk.

2.2.3 Concluding remarks

The following remarks are summarised to conclude the literature review on adhesive joints:

- Adhesive bonding may offer several advantages compared to mechanical fastening joining techniques, including, but not limited to, the ability to join dissimilar materials and the potential to reduce the weight of the joint.
- Constrained adhesive layers are prone to defects including (micro)voids and (micro)cracks introduced during the bonding process. The ability to accurately predict the failure strength of adhesive joints as a function of pore or crack size is essential to manufacture reliable structures making use of bonded joints.
- There is a large literature on the role of constraint on the fracture behaviour of confined adhesive layers. Consider the case of a joint comprising an adhesive layer made of a rubber-modified epoxy, which typically exhibits a pronounced *R*-curve in bulk due to plastic dissipation facilitated by the rubber particles embedded in the epoxy adhesive. There is substantial experimental (Kinloch and Shaw, 1981; Hunston et al., 1989; Daghyani et al., 1995; Yan et al., 2001; Lee et al., 2004) and numerical evidence (Varias et al., 1991; Tvergaard and Hutchinson, 1996; Pardoen et al., 2005; Martiny et al., 2012) in the literature that the toughness of the joint may be reduced when the adhesive layer height is less than the size of the process zone of the modified epoxy in bulk, see Fig. 2.12. On the other

hand, for some structural adhesives such as unmodified epoxies, no such dependence of the toughness upon layer height may be observed, see Fig. 2.12.

- Most numerical studies exploring the role of constraint on the fracture toughness of confined adhesive layers make use of a cohesive zone embedded in the elastic or elastic-plastic adhesive layer. Subtleties aside, the strength $\hat{\sigma}$ and the work of separation Γ assigned to traction-separation law for the cohesive zone, rather than its shape, are found to be of most significance for the numerical outcomes (Tvergaard and Hutchinson, 1992; Stigh et al., 2010). The values for $\hat{\sigma}$ and Γ may be estimated via tests on joints (Yan et al., 2001; Pardoen et al., 2005) but the physical basis for these values is often limited (Stigh et al., 2010). In the case of structural adhesives, $\hat{\sigma}$ may be chosen to equal the uniaxial tensile strength of the adhesive (Blackman et al., 2003; Sun et al., 2008b,a; Carlberger and Stigh, 2010) and Γ may be chosen to equal the toughness G_c^0 of the adhesive in bulk (Pardoen et al., 2005). It is common to assume the two parameters $\hat{\sigma}$ and Γ to be independent of constraint. In this way, the contribution of plastic dissipation in the adhesive layer to the toughness of the joint may be computed by assuming the adhesive layer to be elastic-plastic. For joints comprising unmodified epoxies (Monteiro et al., 2015; Maloney and Fleck, 2018) and polyurethane (Banea et al., 2014; Sekiguchi et al., 2017) structural adhesives, the toughness contribution via plastic dissipation might only be a fraction of Γ. In these cases, one may adopt a pragmatic approach of assuming the toughness of the joint to be independent of constraint (and equal to Γ) (Martiny et al., 2012). This approach may also be applicable for joints with adhesive layer heights much larger than the plastic zone size of the adhesive in bulk as the role of constraint on plastic dissipation mechanism in the adhesive layer is expected to be minimal (Komatsu et al., 2018).

Part I

Void growth during solid-state nanofoaming

Chapter 3

Deformation and failure diagrams for PMMA in uniaxial tension

The first part of this thesis explores the topic of void growth during solid-state nanofoaming of PMMA by CO_2. As stipulated in Section 2.1.3, accurate prediction of void growth during solid-state foaming of a polymer grade of interest requires the use of an appropriate constitutive description for this particular grade. Constitutive laws for PMMA in uniaxial tension close to the glass transition temperature were summarised in Section 2.1.4. These constitutive relations need to be calibrated to measured stress-strain curves. Reported stress-strain responses for commercial PMMA grades in uniaxial tension close to the glass transition temperature are, however, scarce in the literature. To this end, uniaxial tensile tests on an PMMA grade of high molecular weight over a range of temperatures near the glass transition and over two decades of strain rate are conducted. Deformation maps are constructed for Young's modulus, flow strength, and failure strain as a function of temperature for selected strain rates. Constitutive laws are calibrated for the modulus and flow strength within each identified regime of deformation. Additional uniaxial tensile tests are conducted with an PMMA grade of a markedly lower molecular weight for temperatures close to the glass transition temperature for a selected strain rate. The observed differences between the two grades in terms of regimes of deformation and fracture are briefly discussed.

3.1 Theory

The regimes of deformation and failure for PMMA in uniaxial tension were reviewed in detail in Section 2.1.4. A brief summary of the constitutive laws used to describe the small strain, visco-elastic and the large strain, visco-plastic behaviour of the tested PMMA grades in this chapter is given.

3.1.1 The glassy and glass transition regime

The small strain, viscoelastic response of PMMA in the glassy and glass transition regime is predicted by a single Maxwell unit comprising a linear spring of glassy modulus E_g, as defined by Eq. 2.8, in series with a linear dashpot with a viscosity η_{WLF} following WLF theory, see Eq. 2.9. Now, consider a uniaxial tensile test at constant strain rate $\dot{\varepsilon}$. For the small-strain visco-elastic response at time $t > 0$, the secant modulus $E_s = \sigma(\varepsilon_{ref})/\varepsilon_{ref}$ is used, where ε_{ref} is a reference strain, taken to equal 0.05. For the Maxwell unit under consideration E_s reads as:

$$E_s = \frac{\eta_{WLF}\dot{\varepsilon}}{\varepsilon_{ref}}\left[1 - \exp\left(\frac{-\varepsilon_{ref}}{\dot{\varepsilon}}\frac{E_g}{\eta_{WLF}}\right)\right] \tag{3.1}$$

where E_g and η_{WLF} are defined in Eq. 2.8 and Eq. 2.9, respectively.

A single transition process Ree-Eyring equation is used for the large strain, viscoplastic response of PMMA in the glassy and glass transition regime. The flow strength σ_y is related to temperature and rate:

$$\frac{\dot{\varepsilon}_e}{\dot{\varepsilon}_0} = \sinh\left(\frac{\bar{\sigma}v}{kT}\right)\exp\left(\frac{-q}{kT}\right) \tag{3.2}$$

where Eq. 2.10 is re-stated for convenience. Note that the flow strength σ_y is related to the applied stress $\bar{\sigma}$ via Eq. 2.13. The assumed value for α (= 0.4) in this Chapter is based on the experimental outcomes of Bauwens-Crowet (1973), Bin Ahmad and Ashby (1988), and Dooling et al. (2002) who reported that the ratio of the yield strength in compression to yield strength in tension of PMMA is close to 1.3 when deformed at moderate strain rates.

3.1.2 The rubbery regime

Most commercially available grades of PMMA are of relatively high molecular weight (i.e. $M_w > 150\ 000$ g mol^{-1}), and typically exhibit a rubbery plateau at temperatures just above the glass transition temperature. Instead of making use of entropy-based models that relate the rubbery modulus to temperature (Treloar et al., 1976; Wu and Van Der Giessen, 1993), it was found that the following empirical relation is adequate to describe the observed rate sensitivity (and temperature sensitivity) of the modulus of the tested PMMA in the rubbery regime:

$$E_R = E_R^0\left(1 - \alpha_R \frac{T}{T_g}\right)\left(\frac{\dot{\varepsilon}}{\dot{\varepsilon}_R}\right) \tag{3.3}$$

where α_R is a temperature coefficient, n is a rate sensitivity index and E_R^0 and $\dot{\varepsilon}_R$ refer to a reference modulus and strain rate, respectively.

A linear, elastic true stress versus true strain behaviour is assumed to represent the rubbery (large strain) response of PMMA. To describe the flow strength as a function of temperature and rate it is necessary to introduce a reference strain ε_{ref} such that the flow 'strength' is given by:

$$\sigma_y = E_R \varepsilon_{ref} \tag{3.4}$$

with E_R governed by Eq. 3.3.

3.1.3 The viscous flow regime

Polymethyl methacrylate grades of relatively low molecular weight (i.e. $M_w < 150\ 000$ g mol^{-1}) typically have a viscous flow regime at temperatures just above the glass transition (McLoughlin and Tobolsky, 1952). A linear, viscous flow rule can be used to describe the constitutive behavior of these low molecular weight PMMA grades[1]:

$$\sigma_y = \eta_{WLF}\dot{\varepsilon} \tag{3.5}$$

[1] Equation 3.5 may also be used to describe the constitutive response of a high molecular weight PMMA grade at temperatures far above the glass transition (Bin Ahmad and Ashby, 1988).

where η_{WLF} is a temperature-dependent viscosity, see Eq. 2.9.

3.2 Test methods

3.2.1 Test materials

Uniaxial tensile tests were conducted with two PMMA grades[2] of markedly different molecular weight: cast PMMA sheets (Altuglas CN) with sheet thickness close to 3 mm and pelletised PMMA (Altuglas V825T). The molecular weight distribution of the samples was measured via gel permeation chromatography (GPC) with tetrahydrofuran as the eluent and detection by refractive index[3]. The measured molecular weight distribution of the two PMMA grades is shown in Fig. 3.1. The measured weight-average molecular weight M_w of the cast sheet PMMA is equal to 3 580 000 g mol^{-1}, while M_w = 92 500 g mol^{-1} for the V825T PMMA grade. The Altuglas CN and Altuglas V825T grades are respectively referred to as 'high M_w PMMA' and 'low M_w PMMA' in this thesis.

The glass transition temperature[4] (T_g = 114.5 °C) of the low M_w PMMA was found to be close to the the glass transition temperature of the high M_w PMMA (T_g = 116.5 °C) as measured by DSC with a heating rate of 10 °C min^{-1}.

3.2.2 Specimen geometries and testing procedures

Dogbone specimens were machined from the PMMA sheets as shown in Fig. 3.2, and were adhered to aluminum alloy tabs (35 mm x 26 mm x 1.4 mm). The specimens were pin-loaded and dots of diameter equal to 1 mm were painted onto the gauge section of the specimens with white acrylic paint. Their relative displacement was tracked by a video camera during each test. The average nominal strain e in the gauge section of the specimen was measured from the

[2] The PMMA grades were acquired from Altuglas International (Colombes, France).
[3] GPC was performed with an Agilent Technologies PL GPC220 measurement unit (USA) with a nominal flow rate equal to 1.67×10^{-5} l s^{-1} at a testing temperature equal to 30 °C by Smithers Rapra (Shawbury, UK).
[4] The transition half-height of measured flow curves was taken as the value for T_g. The reported value for T_g is the average of two DSC measurements. There was negligible scatter between the two measurements.

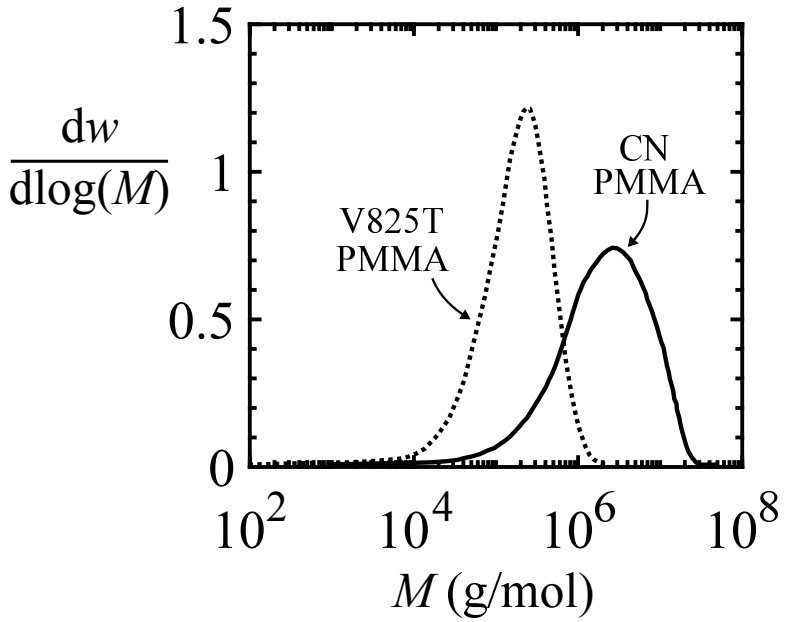

Figure 3.1 The normalised molecular weight distributions of the cast Altuglas CN and pelletised Altuglas V825T PMMA grades as measured by GPC. Note that w is the weight fraction.

axial separation between the two pairs of horizontally aligned white dots. Assuming uniform deformation in the gauge section, the true strain ε is given by:

$$\varepsilon = \ln(1+e) \tag{3.6}$$

The dogbone specimens were tested in a servo-hydraulic test machine [5] in displacement control, and the test temperature was set by making use of an environmental chamber with feedback temperature control and fan-assisted air circulation. The specimen's temperature was independently monitored by a placing a thermocouple against it. The front face of the dogbone specimens was viewed through a transparent window of the environmental chamber. The cross-head displacement, tensile load P, air chamber temperature, and sample temperature were simultaneously monitored and logged. Assuming uniform and incompressible deformation[6] in the gauge section, the true tensile stress σ is computed by:

$$\sigma = \frac{P}{A} = \frac{P}{A_0}(1+e) \tag{3.7}$$

[5] Instron 5500R-6025 test bench (USA).

[6] The validity of the uniform and incompressible deformation assumptions to present the true stress versus true strain curves is discussed in the introduction of Section 3.3 and in Section 3.3.1.

where A and A_0 refer to the current and nominal cross-sectional area of the gauge, respectively.

Tests with the high M_w PMMA were performed for temperatures ranging from 80 °C to 185 °C and for three cross-head speeds (v_{ch} = 5 mm s^{-1}, v_{ch} = 0.5 mm s^{-1} and v_{ch} = 0.05 mm s^{-1}). Additional tests were performed with the low M_w PMMA for temperatures ranging from 80 °C to 170 °C for v_{ch} = 5 mm s^{-1}. The tests were terminated at the point of specimen failure or when the maximum actuator displacement (100 mm) was reached. The latter constraint corresponds to a true strain of approximately unity within the gauge section of the dogbone specimens.

Upon recognising that higher failure strains occur when the test temperature is at or above the glass transition temperature, additional tests were performed using an alternative hourglass-shaped specimen used to probe the failure strain at temperatures near T_g, in the range of 115 °C to 190 °C, following the practice of Hope et al. (1980). The geometry of the hourglass specimen is shown in Fig. 3.3. Recall that the loading direction is aligned with the direction of the z-axis, the thickness direction is aligned with the y-axis, and the transverse direction is aligned with the x-axis. The axial strain can be measured by a longitudinal measurement method, i.e. measuring the change in shape of the dots at the mid-section. However, this method is prone to scatter, and the alternative transverse gauge-based measurement method of Hope et al. (1980) was used in order to reduce this measurement scatter:

i) An average measure for the transverse true strain ε_x at the minimum section of hourglass specimen is obtained from the spacing w between the pair of white marker dots.

ii) Assume that the through-thickness strain ε_y equals the transverse strain ε_x. This was verified by post-failure examination of the thickness and width of the hourglass specimens.

iii) Assume incompressibility, as discussed below, such that $\varepsilon_x + \varepsilon_y + \varepsilon_z = 0$.

Then, the true tensile strain ε_z is related to the current spacing w and initial spacing w_0 by:

$$\varepsilon_z = -2\ln\left(\frac{w}{w_0}\right) \tag{3.8}$$

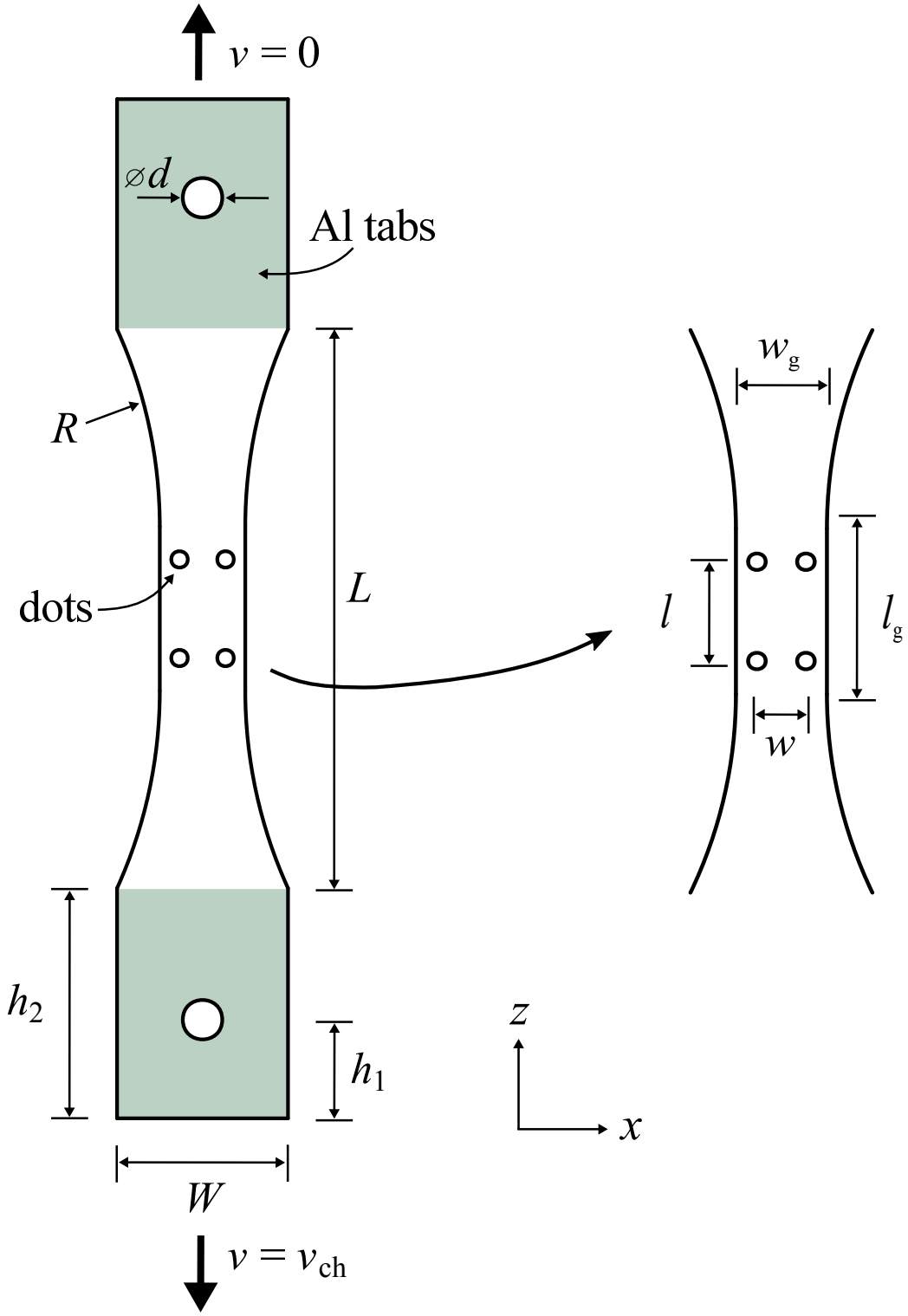

Figure 3.2 Plan view of the dogbone tensile specimen deformed at a cross-head speed v_{ch} with nominal thickness equal to 3 mm, R = 72.5 mm, L = 85 m, d = 6 mm, W = 26 mm, h_1 = 15 mm, h_2 = 35 mm. Nominal dimensions in the gauge area: w_g = 13 mm, l_g = 25 mm, w = 10 mm, l = 15 mm.

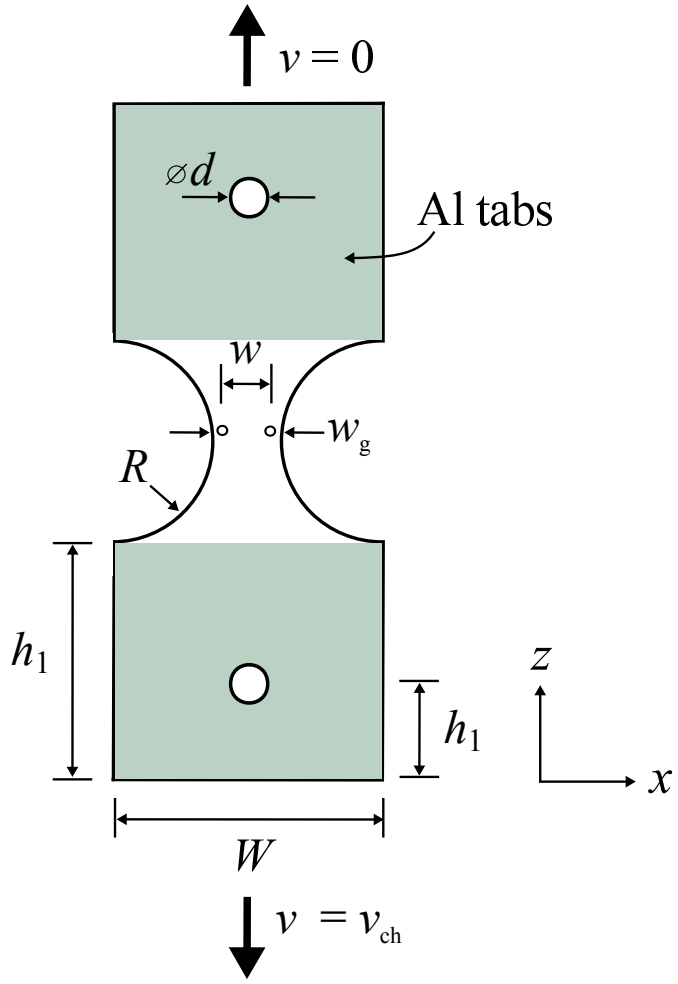

Figure 3.3 Plan view of the hourglass-shaped tensile specimen deformed at a cross-head velocity v_{ch} with nominal thickness equal to 3 mm, R = 15 mm, d = 6 mm, h_1 = 15 mm, h_2 = 35 mm, W = 40 mm. Nominal dimensions in the gauge area: w_g = 10 mm, w = 9 mm.

3.3 Results and discussion

True tensile stress σ versus true tensile strain ε curves are reported for the high M_w PMMA grade for temperatures close to T_g and nominal strain rates in the range $\dot{e} = 5.9 \times 10^{-4}$ s^{-1} to $\dot{e} = 5.9 \times 10^{-2}$ s^{-1}. In addition, the measured σ versus ε curves for the low M_w PMMA grade for temperatures close to the glass transition temperature and a nominal strain rates equal to $\dot{e} = 5.9 \times 10^{-2}$ s^{-1} are given. Values for the modulus, flow strength and failure strain are extracted from each of the curves and used to calibrate the constitutive descriptions summarised in Section 3.1. A series of tests with the high M_w PMMA grade was also performed for temperatures in the range of 25 °C and 80 °C in order to identify the temperature (and strain rate)

at which the behaviour switches from elastic-brittle to elastic-plastic. The transition occurs at close to 70 °C, such that the response is elastic-brittle at the high strain rate and elastic-plastic at the low strain rate (and intermediate rate). The focus in this chapter is on the elastic-plastic response of the PMMA.

In addition, the transverse true strain was measured as a function of axial true strain for a selection of the dogbone specimen tensile tests with the high M_w PMMA. The elastic Poisson's ratio ν was found to increase from $\nu = 0.35$ at T = 80 °C to $\nu = 0.4$ at T = 105 °C, in agreement with the measurements by Gilmour et al. (1979) and Lu et al. (1997). In contrast, the plastic Poisson's ratio ν_p, defined as the ratio of the transverse to axial value of the true plastic strain, was almost constant at 0.45 to 0.5 between T = 80 °C and T = 185 °C, implying that plastic flow is almost incompressible (G'Sell et al., 1992).

3.3.1 Tensile stress-strain curves

The true stress σ versus true strain ε responses of the high M_w PMMA dogbone specimens are plotted in Fig. 3.4a for $0.91 \leq T/T_g \leq 1.01$ and in Fig. 3.4b for $1.04 \leq T/T_g \leq 1.18$ for a nominal strain rate $\dot{e} = 5.9 \times 10^{-3}$ s^{-1} and for $\dot{e} = 5.9 \times 10^{-4}$ s^{-1}. At $T/T_g < 1$, linear, elastic deformation takes place prior to yielding. The yield point is followed by material softening, and by the associated development of a neck. The severity of necking is assessed by measuring by the ratio r of the gauge width in the necked zone over the gauge width in the unnecked zone. The value of r at a true strain equal to 0.55 is shown in Fig. 3.4a for $0.91 \leq T/T_g \leq 1.01$ and $\dot{e} = 5.9 \times 10^{-3}$ s^{-1}. The degree of necking decreases as T/T_g increases and necking ceases around the glass transition. The true stress versus true strain responses, as shown in Fig. 3.4a for $0.91 \leq T/T_g \leq 0.97$, therefore give the overall structural response in the presence of necking rather than the local material response. Values of the modulus and initial peak strength are extracted from the stress-strain curves to calibrate the constitutive laws, and neck development is therefore considered to be beyond the scope of this study[7]. Note that the oscillations on the σ-ε curves for $\dot{e} = 5.9 \times 10^{-4}$ s^{-1} in Fig. 3.4a are caused by the cyclic activation of the fan in the environmental chamber, resulting in a sinusoidal time versus sample temperature variation

[7] See, for example, the studies of Wu and van der Giessen (1995) and Li and Buckley (2009) for a detailed analysis of necking of polymers in the presence of strain softening.

with an amplitude close to 1 °C and time period close to 200 s.

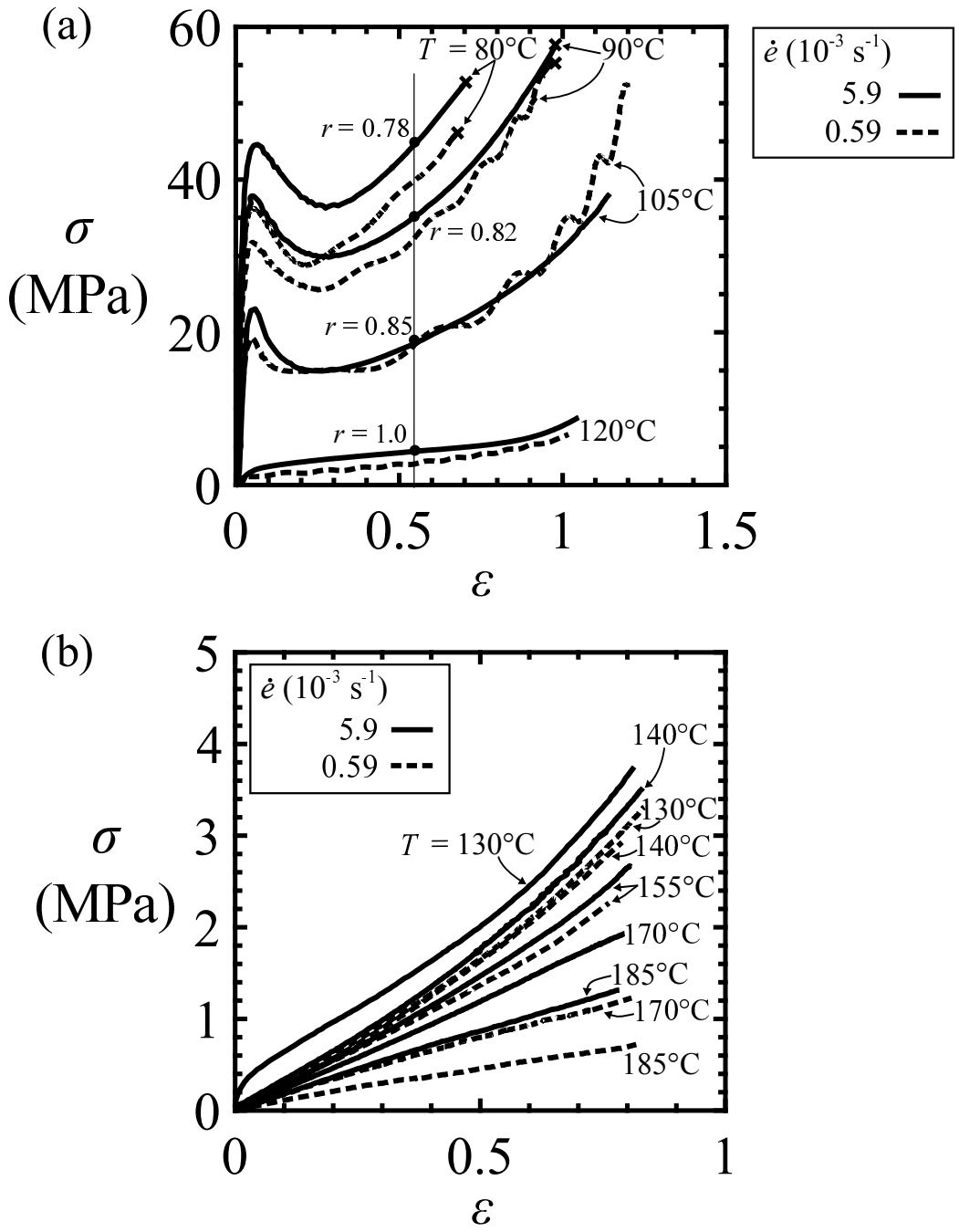

Figure 3.4 Measured true stress versus true strain curves of the high M_w PMMA grade in uniaxial tension for a nominal strain rate $\dot{e} = 5.9 \times 10^{-3}$ s^{-1} and $\dot{e} = 5.9 \times 10^{-4}$ s^{-1} and testing temperatures ranging from (a) T = 80 °C to T = 120 °C and (b) T = 130 °C to T = 185 °C. Tests were terminated when the maximum displacement of the actuator was attained or when the specimen failed (denoted with cross at the end of the curve). The r value in (a) represents the ratio of the measured gauge width in the necked zone over the gauge width in the unnecked zone at a true strain equal to 0.55.

Now consider the response at higher temperatures. In the range of T = 120 °C to T = 155 °C, (corresponding to $1.01 \leq T/T_g \leq 1.1$), the σ versus ε curves are almost independent of temperature and strain rate, and this is characteristic of rubberlike elasticity. The temperature and rate sensitivity increase again at the highest testing temperatures (T = 170 °C and T = 185 °, i.e. $1.14 \leq T/T_g \leq 1.18$), indicating a transition to a viscous deformation regime.

The measured true stress versus true strain responses of the low M_w PMMA and high M_w PMMA dogbone specimens at $\dot{e} = 5.9 \times 10^{-2}$ s^{-1} are plotted in Fig. 3.5a for $0.91 \leq T/T_g \leq 1.01$ and in Fig. 3.5b for $1.04 \leq T/T_g \leq 1.14$. For $T/T_g \leq 1.04$, i.e. in the glassy and glass transition regime, the structural response of the two PMMA grades is similar. The constitutive response is different between the two PMMA grades for $T/T_g > 1.04$: the σ-ε curves of the low M_w PMMA are more sensitive to testing temperature than the σ-ε curves of the high M_w PMMA.

Additional insight is obtained by interrupting selected tensile tests prior to failure, and then by fully unloading them. The measured loading-unloading true stress versus true strain curves for the low M_w and high M_w PMMA at a nominal strain rate $\dot{e} = 5.9 \times 10^{-4}$ s^{-1} are shown in Fig. 3.6. For T/T_g = 0.94 (within the glassy regime), elastic unloading occurs in the manner of an elasto-viscoplastic solid, with a substantial remnant strain at zero load for both PMMA grades. When the temperature is increased to T/T_g = 1.06, the elastic rubbery regime is entered for the high M_w PMMA and the unloading curve is almost coincidental with the loading curve; marginal hysteresis occurs and the remnant strain upon unloading is close to zero. There is no observation of a rubbery regime for the low M_w PMMA above the glass transition temperature. At T/T_g = 1.06 (and T/T_g = 1.12), the S-ε response of the low M_w PMMA resembles that of a linear, viscous liquid (with substantial remnant strain upon unloading). The high M_w PMMA transitions to a viscous regime close to T/T_g = 1.16.

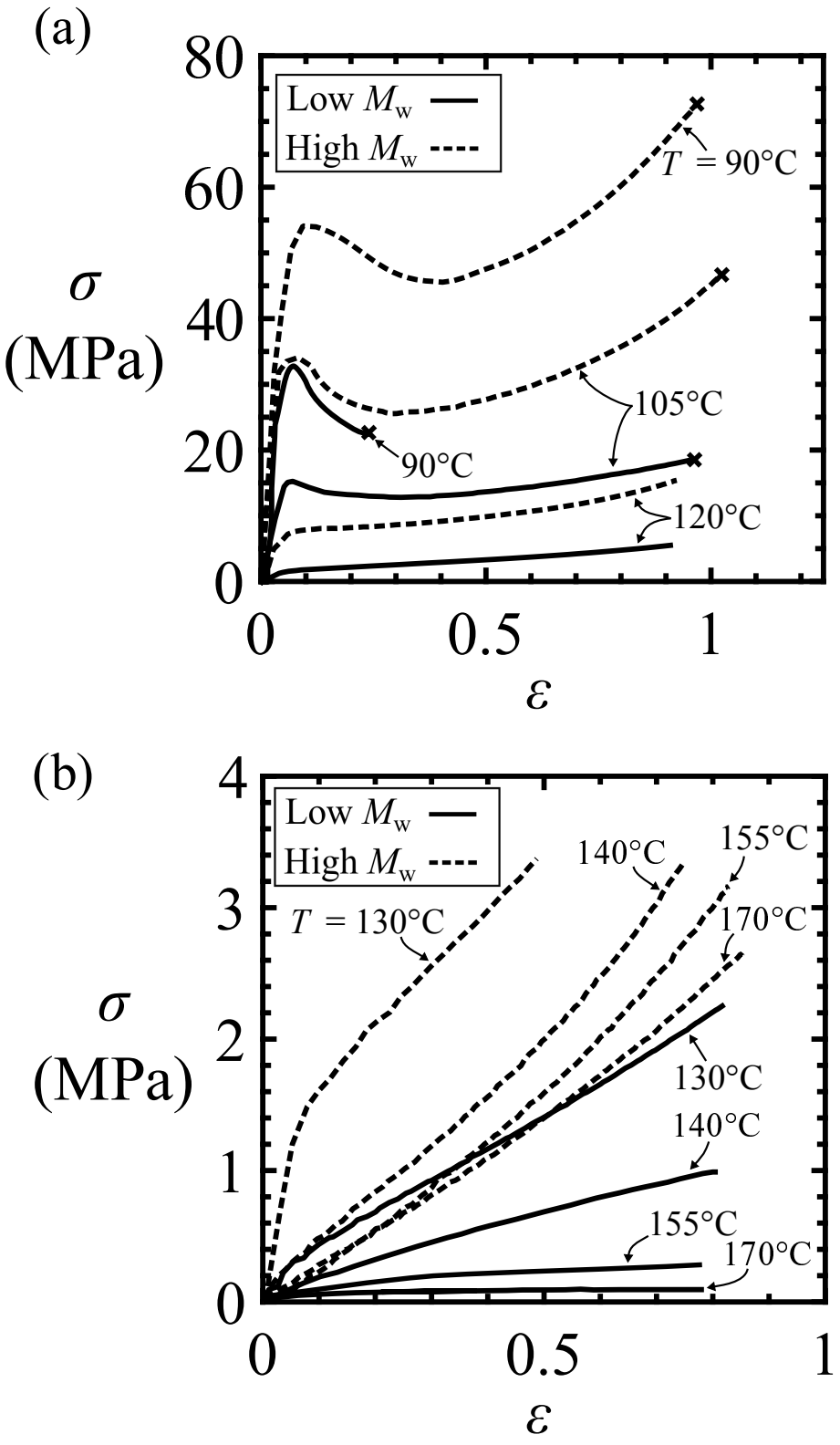

Figure 3.5 Measured true tensile stress versus true tensile strain curves for the low M_w and high M_w PMMA grades in uniaxial tension for a nominal strain rate $\dot{e} = 5.9 \times 10^{-2}$ s^{-1} and for temperatures ranging from (a) T = 90 °C to T = 120 °C and (b) T = 130 °C to T = 170 °C.

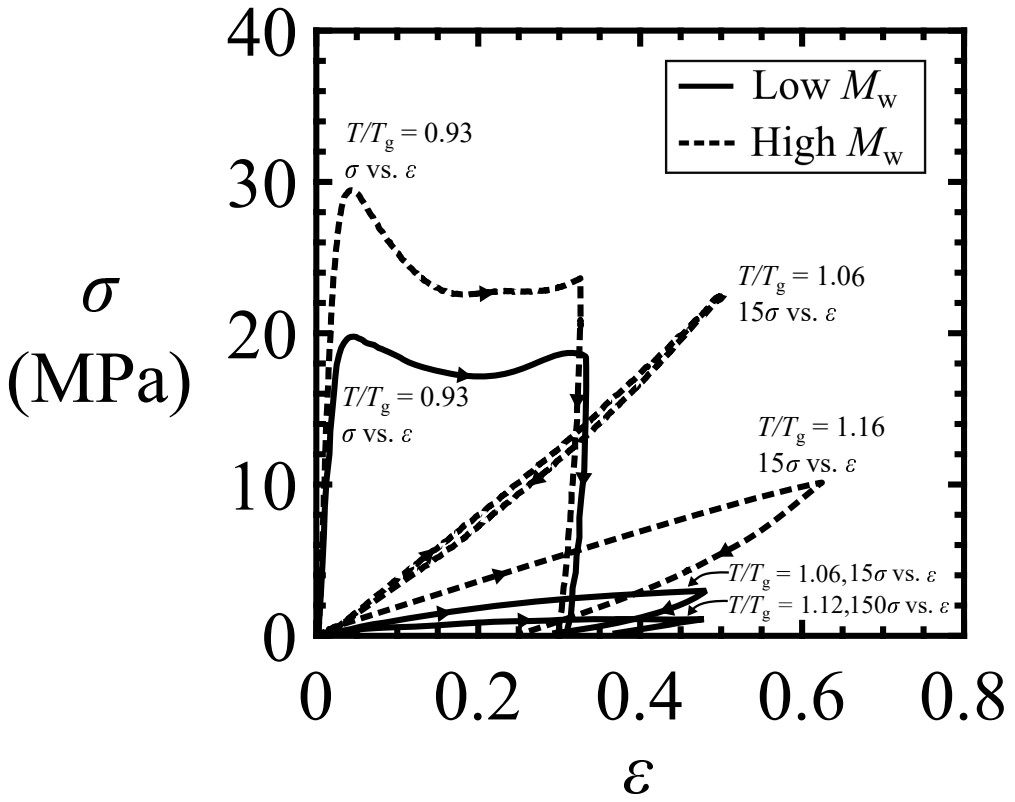

Figure 3.6 Loading-unloading true stress versus true strain curves for the low M_w and high M_w PMMA grades in uniaxial tension at $T/T_g = 0.93$, $T/T_g = 1.06$, and $T/T_g = 1.12$ (low M_w PMMA) or $T/T_g = 1.16$ (high M_w PMMA) for a nominal strain rate $\dot{e} = 5.9 \times 10^{-4}$ s^{-1}.

3.3.2 Deformation maps

The dependence of the modulus E of the high M_w PMMA upon T/T_g is given in Fig. 5.3a for three nominal strain rates. Note that E is measured as the secant modulus based on a true reference strain ε_{ref} equal to 0.05. The dependence of E upon T/T_g and upon strain rate in the glassy and glass transition regime is captured by means of Eq. 3.1. Equation 3.1 is fitted by regression to the measured modulus values corresponding to $0.91 \leq T/T_g \leq 1.04$ for $\varepsilon_{ref} = 0.05$. The fitted parameters (η_0, C_1, C_2, E_0, α_m) are stated in Table 3.1. The dependence of E upon T/T_g in the rubbery regime is assumed to be governed by Eq. 3.3. Equation 3.3 is calibrated by the measured modulus values corresponding to $1.06 \leq T/T_g \leq 1.18$, resulting in $E_R^0 = 65.8$ MPa, $\alpha_R = 0.80$, $\dot{\varepsilon}_R = 1.58$ s^{-1}, and $n = 0.173$. The E versus T/T_g curves, as predicted by the fitted versions of Eqs. 3.1 and 3.3 for the three tested nominal strain rates, are depicted in Fig. 5.3a. The experimental curves are captured to adequate accuracy.

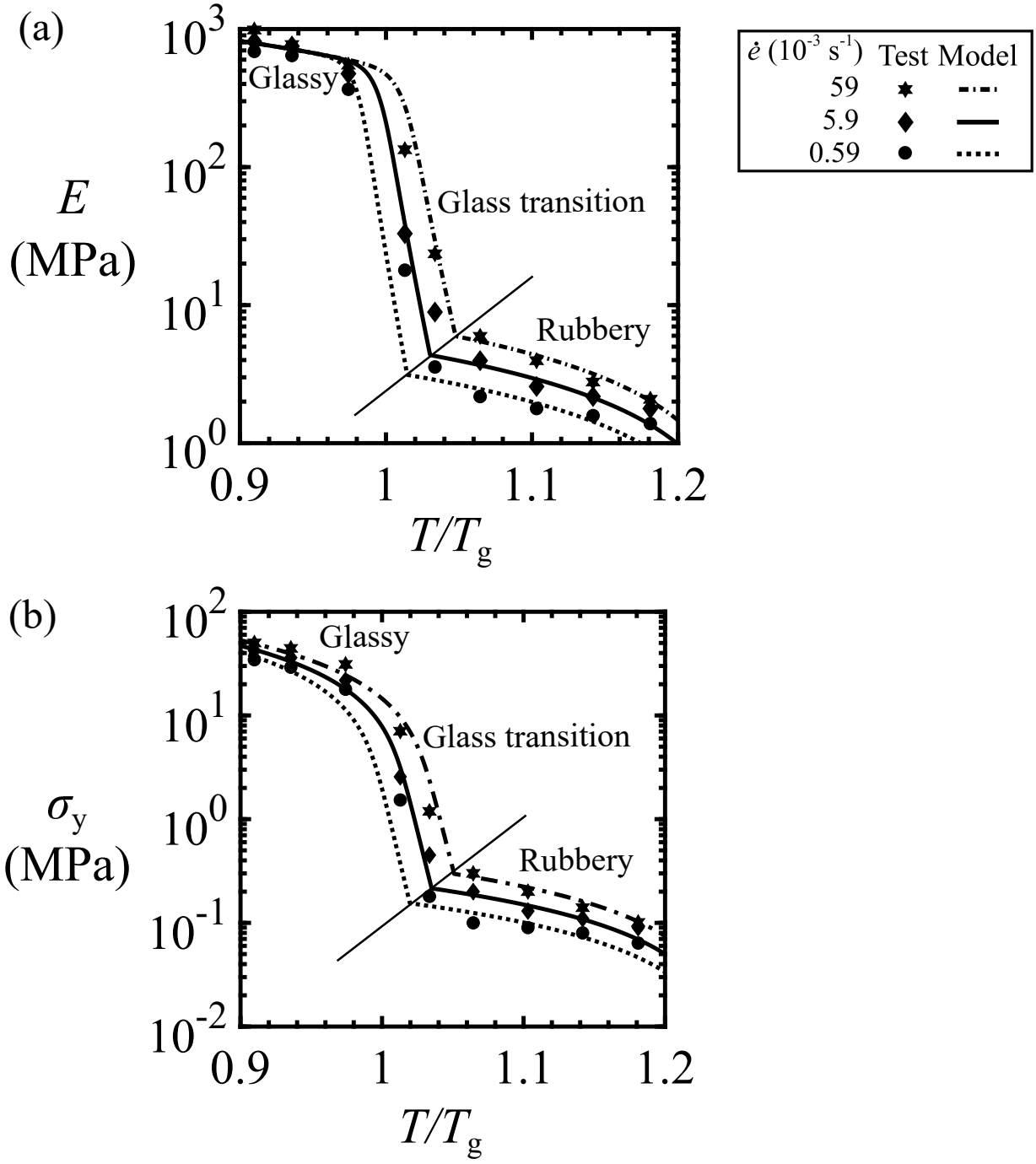

Figure 3.7 Deformation maps for the high M_w PMMA grade in uniaxial tension close to the glass transition for a reference strain equal to 0.05: (a) modulus versus normalised temperature for three nominal strain rates with the predicted curves by the fitted versions of Eq. 3.1 in the glassy and glass transition regime and Eq. 3.3 in the rubbery regime and (b) flow strength versus normalised temperature for three nominal strain rates with the predicted curves by the calibrated versions of Eq. 3.2 in the glassy and glass transition regime and Eq. 3.4 in the rubbery regime.

Table 3.1 Fitted (and initial) parameters for Eq. 3.1 to the measured secant modulus values of the high M_w PMMA gradecorresponding to 80 °C $\leq T \leq$ 130 °C via regression, R^2 = 0.97 for ε_{ref} = 0.05.

Parameter	Fitted value	(Gilbert et al., 1986)
η_0 (Pa·s)	6.7×10^{8}	1.1×10^{16}
C_1	42.7	17.4
C_2 (K)	113.8	143
E_0 (GPa)	3.52	8.6
α_m	0.85	0.28

The measured flow strength σ_y of the high M_w PMMA is plotted as a function of T/T_g for three nominal strain rates, see Fig. 3.7b. The flow strength in the glassy and glass transition regime is assumed to be governed by rate and temperature via a single transition process Ree–Eyring equation, see Eq. 3.2. Equation 3.2 is fitted by regression to the σ_y values corresponding to 0.91 $\leq T/T_g \leq$ 1.04. The fitted values for v, $\dot{\varepsilon}_0$, and q as well as the initial values for the regression, based on the results of Bauwens-Crowet (1973), are summarised in Table 3.2. The fitted value for the activation volume is of the same order of magnitude as the ones reported in the literature (Ward and Sweeney, 2012). This volume is about 5 to 10 times larger than the estimated volume of a monomer unit which is in agreement with the idea that shear yielding is governed by the collective movement of numerous chain segments (Fleck et al., 1990). As depicted in Fig. 3.7b, the measured σ_y versus T/T_g trends in the glassy and glass transition regime are well approximated by the Ree–Eyring fit, while the dependence of the flow strength upon rate and temperature in the rubbery regime is captured with reasonable accuracy by Eq. 3.4 (with ε_{ref} = 0.05 and the fitted version of Eq. 3.3 for the rubbery modulus).

The dependence of the measured flow strength σ_y of the low M_w and high M_w PMMA grades upon T/T_g for $\dot{e} = 5.9\times10^{-2}$ s^{-1} is shown in Fig. 3.8. A single transition Ree–Eyring equation

Table 3.2 Fitted (and initial) parameters for Eq. 3.2 to the measured flow strength values corresponding to 80 °C $\leq T \leq$ 130 °C via regression, R^2 = 0.98.

Parameter	Fitted value	(Bauwens–Crowet, 1973)
v (nm^3)	1.62	2.56
$\dot{\varepsilon}_0$ (s^{-1})	1.5×10^{56}	2×10^{51}
q (J)	7.31×10^{-19}	6.85×10^{-19}

(Eq. 3.2) is fitted by regression to the values of the low M_w PMMA in the glassy and glass transition regime (corresponding to $0.94 \leq T/Tg \leq 1.04$). The values of q and $\dot{\varepsilon}_0$ for the low M_w PMMA are assumed to be equal the fitted values for the high M_w PMMA (see Table 3.2) and Eq. 3.2 is fitted by varying the activation volume v, resulting in v = 2.21 nm^3. The predicted σ_y versus trend for $\dot{e} = 5.9 \times 10^{-2}$ s^{-1} and $\dot{e} = 5.9 \times 10^{-3}$ s^{-1} (low M_w PMMA) and for $\dot{e} = 5.9 \times 10^{-1}$ s^{-1} and $\dot{e} = 5.9 \times 10^{-2}$ s^{-1} (high M_w PMMA) by the calibrated versions of Eq. 3.2 are included in Fig. 3.8.

A linear, viscous constitutive law (Eqs. 2.9 and 3.5) is fitted to the measured σ_y versus T/T_g trend for the low M_w PMMA in the regime of $1.06 \leq T/T_g \leq 1.14$ for $\dot{e} = 5.9 \times 10^{-2}$ s^{-1}, resulting in $\eta_0 = 2.8 \times 10^6$ Pa·s, C_1 = 3.22, and C_2 = 17.3 K. The predicted σ_y versus T/T_g trends for $\dot{e} = 5.9 \times 10^{-2}$ s^{-1} and $\dot{e} = 5.9 \times 10^{-3}$ s^{-1} for the low M_w PMMA by the calibrated versions of Eqs. 2.9 and 3.5 (and for $\dot{e} = 5.9 \times 10^{-2}$ s^{-1} and $\dot{e} = 5.9 \times 10^{-3}$ s^{-1} for the high M_w PMMA by the fitted version of Eq. 3.4) are included in Fig. 3.8.

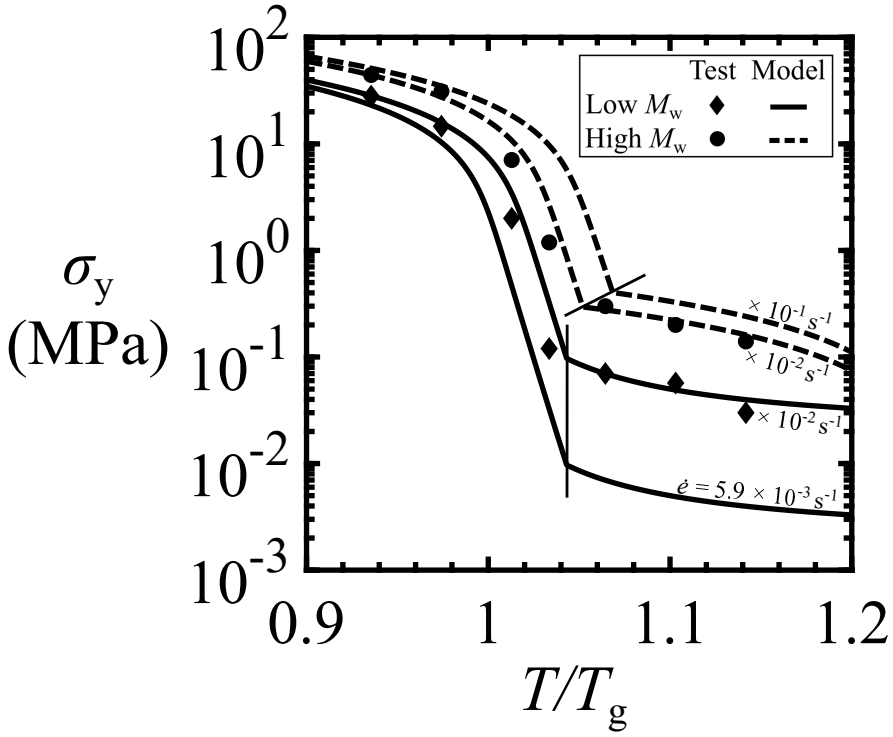

Figure 3.8 The measured flow strength versus normalised temperature for the low M_w and high M_w PMMA grades in uniaxial tension for a nominal strain rate $\dot{e} = 5.9 \times 10^{-2}$ s^{-1}. The predicted σ_y versus T/T_g curves by the fitted versions of Eqs. 3.2 and 3.5 (low M_w) or Eq. 3.4 (high M_w) are included for two selected strain rates with ε_{ref} = 0.05.

3.3.3 Failure diagrams

The measured true tensile failure strain ε_f of the high M_w PMMA grade is plotted as a function of T/T_g in Fig. 3.9a for two nominal strain rates: $\dot{e} = 5.9 \times 10^{-2}$ s^{-1} and $\dot{e} = 5.9 \times 10^{-4}$ s^{-1}. No failure of the hourglass-shaped specimen was observed at T = 190 °C for $\dot{e} = 5.9 \times 10^{-2}$ s^{-1} before reaching the maximum cross-head extension. Recall that the failure strain is measured via a transverse gauge in addition to a longitudinal gauge over the full range of T/T_g employed. The two methods are in good agreement except at $T/T_g \geq 1.1$ for which $\varepsilon_f > 1.5$. In this regime, the reduction in cross-sectional area at the minimum section of the hourglass-shaped specimen is larger than the elongation of the dots.

The transverse gauge-based failure envelope of the high M_w PMMA grade for $\dot{e} = 5.9 \times 10^{-2}$ s^{-1} is fitted by a linear relation (R^2 = 0.92):

$$\varepsilon_f = 7.3\frac{T}{T_g} - 6.3 \tag{3.9}$$

while the transverse gauge-based failure envelope of the high M_w PMMA grade for the lowest explored value of nominal strain rate $\dot{e} = 5.9 \times 10^{-4}$ s^{-1} is captured by a third order polynomial (R^2 = 0.97):

$$\varepsilon_f = -80.8\left(\frac{T}{T_g}\right)^3 + 230.2\left(\frac{T}{T_g}\right)^2 - 211\frac{T}{T_g} + 62.9 \tag{3.10}$$

Equations 3.9 and 3.10 are plotted in Fig. 3.9a along with the observed values of failure strain.

The residual true tensile strain ε_r, measured post-failure, is compared with ε_f in Fig. 3.9b. At temperatures $T/T_g < 1$, there is negligible elastic spring-back and $\varepsilon_r \approx \varepsilon_f$. For $1 < T/T_g < 1.1$, ε_r decreases sharply with increasing temperature, consistent with rubbery behaviour. For $1.1 < T/T_g < 1.18$, ε_r increases with increasing temperature, consistent with a transition to viscous behaviour.

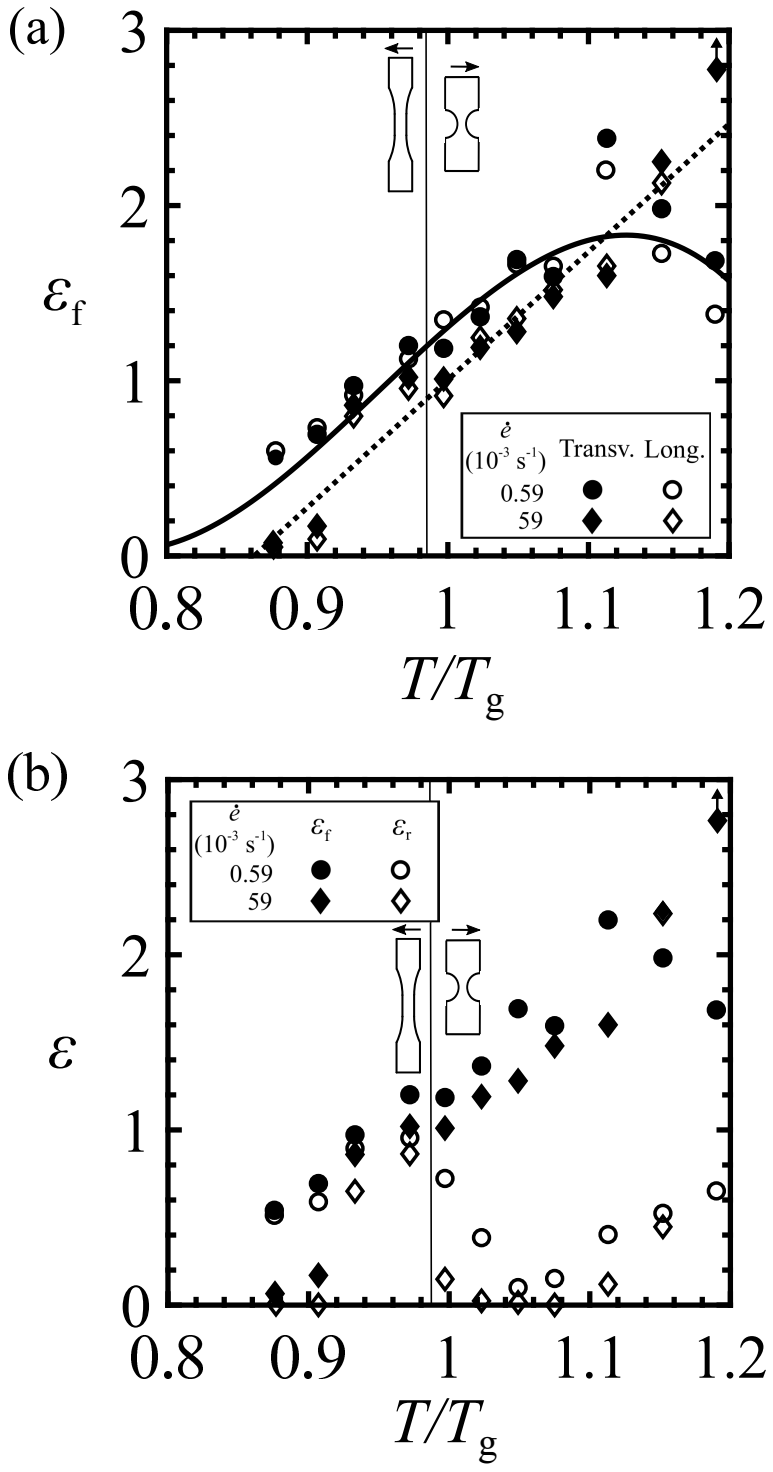

Figure 3.9 Failure diagrams for the high M_w PMMA grade: (a) measured true tensile failure strain ε_f by the transverse (transv.) and longitudinal (long.) method as a function of T/T_g for two nominal strain rates with fitted failure envelopes given in Eqs. 3.9 (dashed line) and 3.10 (solid line) and (b) measured residual true tensile strain ε_r and the measured ε_f as a function of T/T_g for two nominal strain rates.

The curve fits (Eqs. 3.9 and 3.10) from the measured values of ε_f as a function of T/T_g are compared in Fig. 3.10a with the observed failure strains as reported by Cheng et al. (1990) for an PMMA grade with a number-averaged molecular weight M_n close to 500 000 g mol^{-1} in the glassy regime. There is reasonably good agreement between the data of Cheng et al. (1990) and those of the present study. A comparison is made between the failure envelope of the high M_w PMMA in the rubbery regime to that of a lightly cross-linked styrene-butadiene rubber (SBR), as reported by Smith (1958). For the lowest strain rate ($\dot{e} = 5.9 \times 10^{-4}$ s^{-1}), the failure strain envelope above the glass transition temperature of the linear, amorphous, high M_w PMMA is found to be similar to the failure strain envelope above T_g of a chemically cross-linked SBR.

The measured true tensile failure strain ε_f and the residual strain ε_r of the low M_w PMMA is plotted as a function of T/T_g for a nominal strain rate $\dot{e} = 5.9 \times 10^{-2}$ s^{-1} in Fig. 3.10b. No specimen failure was observed at T = 145 °C, T = 160 °C, and T = 175 °C before reaching the maximum cross-head extension. The ε_f versus T/T_g failure envelope at $\dot{e} = 5.9 \times 10^{-2}$ s^{-1} of the low M_w PMMA is captured by a linear relation:

$$\varepsilon_f = 13.3\frac{T}{T_g} - 11.7 \tag{3.11}$$

Equation 3.11 is plotted in Fig. 3.10b. For the sake of comparison, the measured values of ε_f and ε_r of the high M_w PMMA is plotted as a function of T/T_g for $\dot{e} = 5.9 \times 10^{-2}$ s^{-1} in Fig. 3.10b. For $T/T_g < 1$, the ε_f versus T/T_g and the ε_r versus T/T_g curves of the two PMMA grades are similar. In contrast, the value of ε_r at $T/T_g \geq 1$ is close to invariant to temperature. This is consistent with the observation of a transition to a viscous regime (and absence of a rubbery regime) above the glass transition for the low M_w PMMA grade.

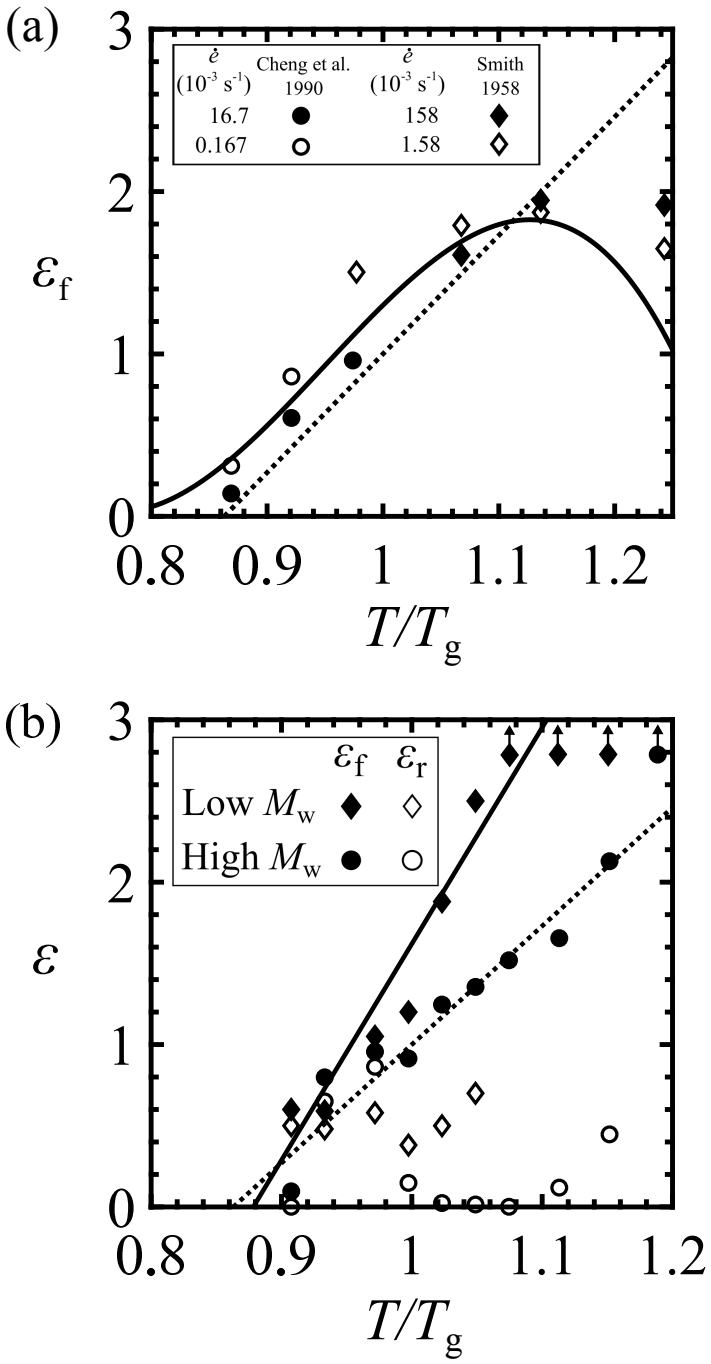

Figure 3.10 Failure diagrams for the low M_w and the high M_w PMMA grades: (a) ε_f versus T/T_g curve fits (Eq. 3.9 (dashed line) and Eq. 3.10 (solid line)) along with the ε_f versus T/T_g data reported by Cheng et al. (1990) for PMMA in the glassy regime and by Smith (1958) for SBR in the glass transition and rubbery regime and (b) the measured true tensile failure strain ε_f and the residual strain ε_r of the low M_w and high M_w PMMA as a function of T/T_g for a nominal strain rate $\dot{e} = 5.9 \times 10^{-2}$ s^{-1} along with the fitted failure envelopes given in Eq. 3.11 for the low M_w PMMA (solid line) and Eq. 3.9 (dashed line) for the high M_w PMMA.

3.4 Concluding remarks

The tensile response of a commercial PMMA grade of high molecular weight (close to 3 500 000 g mol^{-1}) has been characterised over a range of temperatures near the glass transition and over two decades of strain rate via a series of uniaxial tensile tests. Modulus, flow strength and failure strain are plotted as a function of temperature via deformation and failure maps for selected strain rates. Fitted constitutive relations in terms of modulus and flow strength are reported for three identified constitutive regimes: the glassy, glass transition, and rubbery regime. Additional uniaxial tensile tests are conducted with a different grade of PMMA of lower molecular weight (approximately 100 000 g mol^{-1}) though close to identical value of T_g to give insight into the effect of molecular weight on the constitutive response of PMMA in uniaxial tension close to T_g. The response of the low molecular weight PMMA was found to be similar to the high molecular weight PMMA in the glassy and glass transition regime, while viscous (instead of rubbery) behaviour was observed above T_g.

Chapter 4

Solid-state nanofoaming experiments on PMMA

Solid-state nanofoaming experiments are conducted on the two PMMA grades characterized in Chapter 3 by making use of CO_2 as the blowing agent. The dependence of porosity of the nanofoams upon foaming time and foaming temperature is measured. The morphology of the PMMA nanofoams is also characterized in terms of cell size, cell nucleation density, and open cell content.

4.1 Materials and methods

4.1.1 Test materials

Solid-state nanofoaming experiments were conducted on Altuglas V825T PMMA (of molecular weight M_w = 92 500 g mol^{-1}) and Altuglas CN PMMA (M_w = 3 580 000 g mol^{-1}), see Section 3.2.1. The Altuglas V825T PMMA was received in pellets, whereas the Altulgas CN PMMA grades came in cast sheets with thickness close to 3 mm. The Altuglas V825T and Altuglas CN grades are referred to as the 'low M_w PMMA' and 'high M_w PMMA', respectively. Both grades have a density ρ^p equal to 1 190 kg m^{-3} (measured at 23 °C and at 50 % relative humidity). As detailed in Section 3.2.1, the glass transition temperature of the low M_w PMMA

(T_g = 114.5 °C) is approximately equal to the glass transition temperature of the high M_w PMMA (T_g = 116.5 °C).

4.1.2 Nanofoaming experiments

Foaming precursors of the low M_w and high M_w PMMA grades were made as follows. The low M_w PMMA pellets were heated to 250 °C, then compressed between two heated plates with a pressure equal to 17 MPa for 60 s at 250 °C. Then, the resulting low M_w PMMA sheet was allowed to cool down to room temperature with the pressure of 17 MPa maintained. Cuboid precursors with dimensions $20\times10\times3$ mm^3 were machined from the low M_w PMMA sheet and the as-received high M_w PMMA sheet.

Foaming experiments were performed using a pressure vessel[1] with a pressure controller[2] and temperature controller[3]. Medical grade CO_2 (of more than 99.9 % purity) was used as blowing agent for the foaming experiments. A two step solid-state foaming process was employed (Martin-de León et al., 2016). The precursor samples were put into the pressure vessel at a constant CO_2 saturation pressure (p_{sat} = 31 MPa) and at a maintained saturation temperature (T_{sat} = 25 °C). Complete saturation of the PMMA by CO_2 is achieved within 24 hours at these saturation conditions (Martin-de León et al., 2016). The corresponding CO_2 equilibrium weight concentration[4] C was measured as follows. A saturated sample (with p_{sat} = 31 MPa) was placed out of the pressure vessel. Then, the mass of the sample was measured[5] as a function of time. The equilibrium CO_2 concentration was obtained by extrapolating the measured mass-time curve to zero. The value for the equilibrium concentration for p_{sat} = 31 MPa and T_{sat} = 25 °C is close to 24 wt% for both the low and high M_w PMMA.

After the saturation of the precursor was complete, the pressure was progressively released to ambient pressure with a controlled, instantaneous pressure drop rate close to 100 MPa s^{-1}. The

[1] Pressure vessel model PARR 4681 of Parr Instrument Company (USA) with a 10^{-3} m^3 capacity. The maximum pressure and temperature of the pressure vessel corresponds to 350 °C and 41 MPa, respectively.
[2] Pressure controller pump SFT-10 of Supercritical Fluid Technologies Inc (USA).
[3] Temperature controller CAL 3300 of CAL Controls Ltd, UK.
[4] The weight concentration C of CO_2 in PMMA is defined with respect to the total mass of the PMMA-CO_2 mixture. Note that the definition of CO_2 solubility (with respect to the mass of the PMMA absent CO_2) is often used in experimental nanofoaming studies (Martin-de León et al., 2016).
[5] Mass measurements were conducted with an analytical balance AT261 of Mettler-Toledo (USA).

Table 4.1 Overview of the 20 individual foaming experiments conducted on both the low M_w and the high M_w PMMA grades.

p_{sat} (MPa)	T_{sat} (°C)	T_f (°C)	t_f (s)
31	25	25	60, 180, 300, 600
31	25	40	60, 180, 300, 600
31	25	60	60, 180, 300, 600
31	25	80	60, 180, 300, 600
31	25	100	60, 180, 300, 600

samples were subsequently foamed in a thermal bath[6] at a foaming temperature ranging from T_f = 25 °C to T_f = 100 °C and foaming times ranging from t_f = 60 s to t_f = 600 s. Samples were quenched by immersing them in a water bath at a temperature close to 10 °C at the end of the foaming time. An overview of the saturation and foaming conditions used to foam the low M_w and the high M_w PMMA grades is given in Table 4.1.

4.1.3 Characterisation

4.1.3.1 Porosity

The geometric volume V_f of the nanofoams was determined by the water-displacement method and the mass of the nanofoams m_f was measured with a weight balance[7]. A layer of 200 µm from each side of the foamed sample was polished off[8] to ensure the solid skin layer (of thickness below 100 µm) was absent before the mass and volume measurements were made. The mass and volume measurements were conducted at least 24 hours after foaming took place to allow remnant CO_2 to diffuse out of the nanofoams. The porosity of the samples is obtained by:

$$f = 1 - \frac{m_f}{V_f \rho_p} \tag{4.1}$$

[6] Thermal bath J.P. Selecta Model 6000685 of Grupo Selecta (Spain). The thermal bath is filled with water for T_f = 25 °C to T_f = 80 °C. An oil bath was used for T_f = 100 °C.
[7] See footnote 5.
[8] Grinding and polishing system LaboPOl2-LaboForce3 of Struers (USA).

4.1.3.2 Microstructure

The microstructure of the nanofoams was analysed by SEM microscopy. The samples were cooled in liquid nitrogen and subsequently fractured. Fracture surfaces were coated with a layer of gold by sputtering[9]. Micrographs of the coated fracture surfaces were taken by a SEM[10]. The cellular structure of each material was characterised by analysing the micrographs with software based on ImageJ/FIJI developed by Pinto et al. (2013). By analysing over 200 voids obtained from at least 3 micrographs per foamed sample, the average cell size l, the standard deviation s of the observed cell sizes, and the cell nucleation density N_{d}, calculated via (Kumar and Suh, 1990):

$$N_{\mathrm{d}} = \left(1 - f\right)^{-1} \left(\frac{nM^2}{A}\right)^{\frac{3}{2}}, \tag{4.2}$$

is reported for each foamed sample. Note that in Eq. 4.2, n refers to number of voids in the micrograph of area A and magnification factor M.

4.1.3.3 Open cell content

The open cell content of the foamed samples was measured using gas pycnometry with nitrogen according to the ASTM D6226-15 standard (ASTM, 2015a). The open cell content ratio O_{v} is defined as the ratio of the volume of open-celled voids to the total volume of pores and is obtained by[11]:

$$O_{\mathrm{v}} = \left(1 - \frac{V_{\mathrm{pyc}}}{V_{\mathrm{f}}}\right) f^{-1} \tag{4.3}$$

where V_{pyc} is the pycnometer volume[12] obtained by subjecting the foamed samples to a pressure scan from 0.02 MPa to 0.13 MPa in the pycnometer[13]. The pycnometer volume initially decreases as the gas pressure increases until the interconnected open cells are completely filled

[9] Sputter coater SDC 005 of Balzers Union (Liechtenstein).
[10] Scanning electron microscope QUANTA 200 FEG of Thermo Fisher Scientific (USA).
[11] The volume contribution of the nano-sized voids at the surface of the sample is neglected in Eq. 4.3.
[12] The volume of the three-dimensional sample which is inaccessible to the gas.
[13] Gas pycnometer (USA) AccuPyc II 1340 of Micromeritics (USA).

with gas and the pycnometer volume remains constant at increased pressures. This constant volume value is assumed to equal V_{pyc} to calculate O_v via Eq. 4.3.

4.2 Results and discussion of the nanofoaming experiments

A series of representative SEM micrographs of the nanofoams produced with the low M_w and the high M_w PMMA grades are shown in Fig. 4.1. The low M_w and the high M_w nanofoams have distinctly different microstructures when foamed at identical foaming temperatures and foaming times. The measured porosity f, the average observed cell size l, the standard deviation s of the observed cell sizes, and the cell nucleation density N_d of the nanofoams made from the low M_w and the high M_w PMMA grades are reported in Table 4.2 and Table 4.3, respectively.

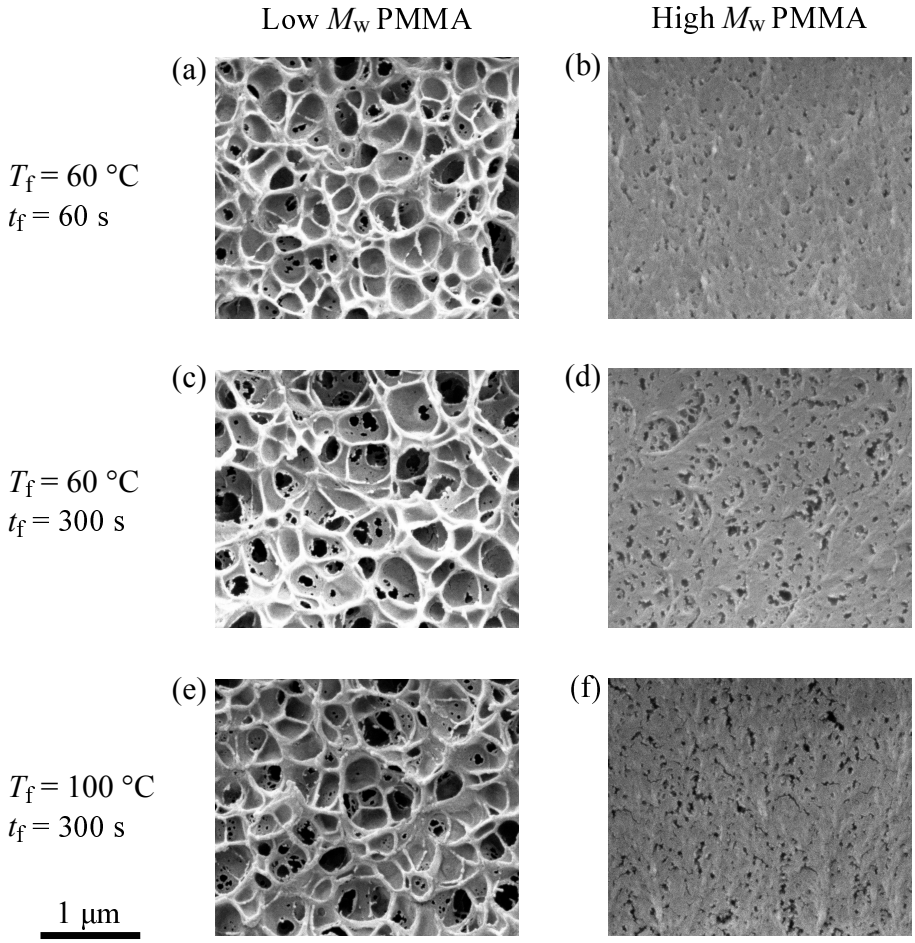

Figure 4.1 SEM micrographs of the low M_w and the high M_w nanofoams for different combinations of foaming temperature T_f and foaming time t_f.

Table 4.2 Measured values for the porosity f, the average observed cell size l, the standard deviation of the observed cell sizes s, the open cell content O_v, and the cell nucleation density N_d of the low M_w nanofoams as a function of foaming time t_f and foaming temperature T_f. Foams collapsed at T_f = 100°C, and so no open cell content values are reported for the nanofoams produced at T_f = 100°C.

t_f (s)	T_f (°C)	f	l (nm)	s (nm)	O_v	N_d ($\times 10^{20}$ m^{-3})
60	25	0.45	219	87	0.12	1.50
180	25	0.47	228	79	0.08	1.50
300	25	0.51	283	112	0.08	0.91
600	25	0.51	235	85	0.08	1.48
60	40	0.52	262	102	0.07	1.22
180	40	0.61	250	125	0.02	1.70
300	40	0.64	254	105	0.15	1.27
600	40	0.66	233	103	0.14	2.11
60	60	0.56	234	89	0.07	2.34
180	60	0.66	297	111	0.33	1.72
300	60	0.68	279	122	0.4	1.76
600	60	0.68	284	109	0.36	1.63
60	80	0.72	333	134	0.63	1.16
180	80	0.74	288	138	0.90	1.83
300	80	0.75	297	125	0.78	1.75
600	80	0.73	274	109	0.93	2.08
60	100	0.64	297	122	-	1.21
180	100	0.68	253	110	-	1.81
300	100	0.62	246	103	-	1.75
600	100	0.51	291	125	-	0.76

The observed cell nucleation density N_d of the low M_w and the high M_w nanofoams is plotted as a function of foaming temperature in Figs. 4.2a and 4.2b, respectively. The cell nucleation density of the low nanofoams ($N_d \approx 2 \times 10^{20}$ m^{-3}) is an order of magnitude lower than that of the high M_w nanofoams ($N_d \approx 2 \times 10^{21}$ m^{-3}). The cell nucleation density of both PMMA grades is found to be independent of foaming time or temperature. The observed average cell size l of the high M_w nanofoams ranges between 20 nm to 50 nm, which is an order of magnitude lower than that of the low M_w nanofoams (l = 200 nm to l = 350 nm), see Tables 4.2 and 4.3. The observed range of N_d and l for the low M_w nanofoams is consistent with the results of Martin-de León et al. (2016) who conducted foaming experiments with an identical low M_w PMMA grade.

Table 4.3 Measured values for the porosity f, the average observed cell size l, the standard deviation of the observed cell sizes s, the open cell content O_v, and the cell nucleation density N_d of the high M_w nanofoams as a function of foaming time t_f and foaming temperature T_f. Foams collapsed at T_f = 100°C, and so no open cell content values are reported for the nanofoams produced at T_f = 100°C.

t_f (s)	T_f (°C)	f	l (nm)	s (nm)	O_v	N_d ($\times 10^{20}$ m^{-3})
60	25	0.22	36	14	0.30	14.9
180	25	0.28	23	10	0.22	40.0
300	25	0.29	30	12	0.28	9.0
600	25	0.31	36	18	0.21	6.9
60	40	0.33	28	13	0.19	54.2
180	40	0.42	32	16	0.07	32.3
300	40	0.45	37	14	0.08	7.8
600	40	0.47	45	29	0.09	26.0
60	60	0.45	37	14	0.08	20.4
180	60	0.55	39	17	0.03	24.0
300	60	0.57	40	17	0.28	31.8
600	60	0.57	41	19	0.03	25.8
60	80	0.58	39	20	0.51	21.8
180	80	0.6	39	19	0.73	27.8
300	80	0.6	38	19	0.95	36.6
600	80	0.59	44	22	0.88	46.6
60	100	0.59	34	15	-	35.4
180	100	0.53	27	14	-	80.4
300	100	0.50	37	18	-	24.9
600	100	0.45	34	12	-	32.6

The measured average cell size l of the low M_w and the high M_w nanofoams is plotted as a function of foaming time for a selected foaming temperature equal to 60 °C, see Fig. 4.2c. Void growth typically occurs over a foaming time period of 60 s to 180 s, after which cell growth slows down and a stable (foaming time-independent) value for l is attained. The sensitivity of the final value for l to foaming temperature is small, see Table 4.2 and Table 4.3.

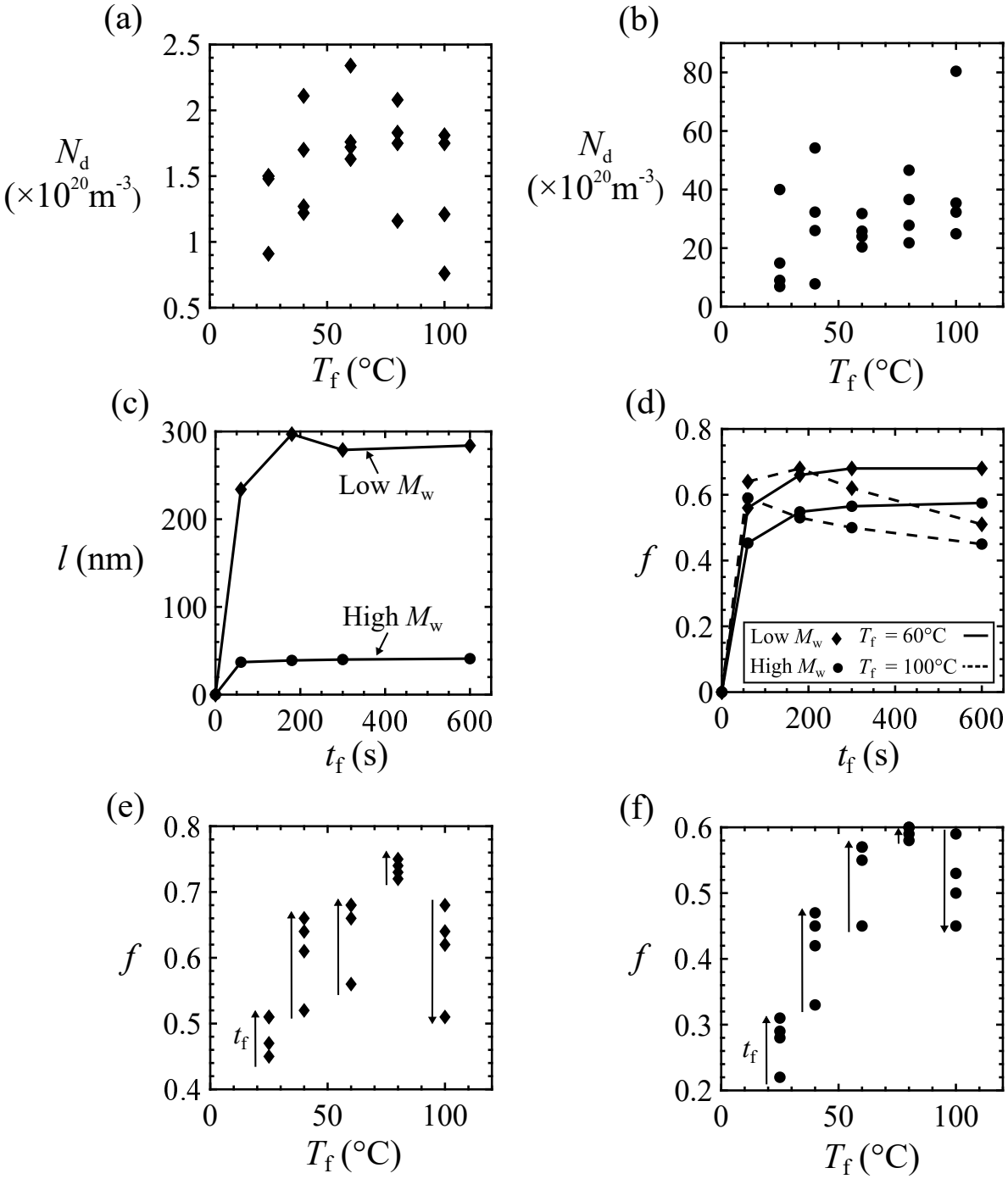

Figure 4.2 Nanofoaming experiments with the low M_w and high M_w PMMA grades: (a) nucleation density N_d versus foaming temperature T_f for the low M_w nanofoams, (b) nucleation density N_d versus foaming temperature T_f for the high M_w nanofoams, (c) average cell size l versus foaming time t_f at T_f = 60 °C, (d) porosity f versus foaming time t_f at T_f = 60 °C and T_f = 100 °C, (e) porosity f versus foaming temperature T_f for the low M_w nanofoams, (f) porosity f versus foaming temperature T_f for the high M_w nanofoams.

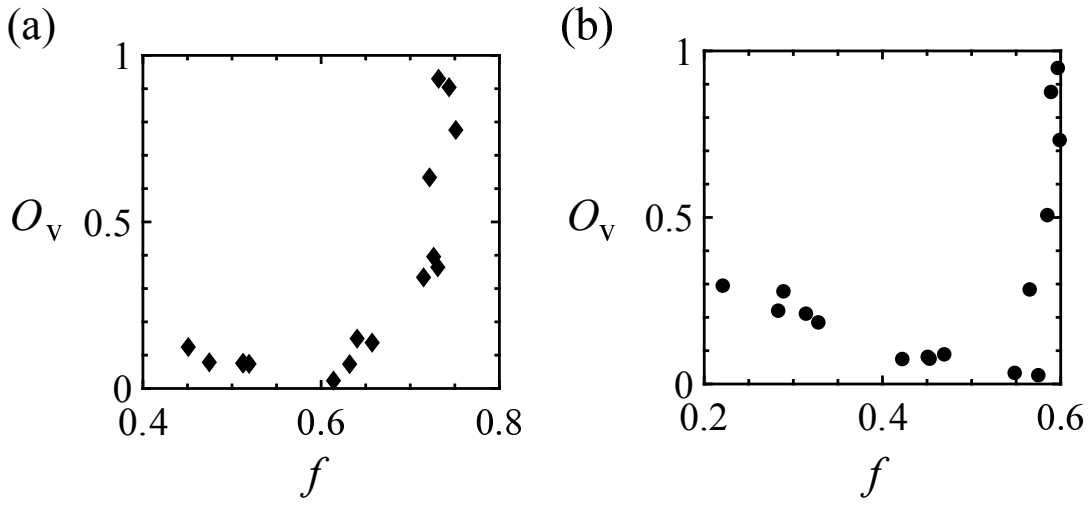

Figure 4.3 Measured open cell content O_v versus porosity f: (a) low M_w nanofoams and (b) high M_w nanofoams.

The measured porosity f of the low M_w and the high M_w nanofoams is plotted as a function of foaming time for T_f = 60 °C and for T_f = 100 °C in Fig. 4.1d. In agreement with the l versus T_f curves for T_f = 60 °C shown in Fig. 4.1c, the porosity increases over a foaming period of 60 s to 180 s until a stable (t_f-independent) value for the final porosity is achieved.

The highest observed porosity for the low M_w nanofoams (f_{max} = 0.75) is approximately 25% higher than the highest observed porosity for the high M_w nanofoams (f_{max} = 0.6). At a foaming temperature equal to 100 °C, the porosity decreases with increasing foaming time beyond t_f = 60 s, and this is due to collapse of the foamed structure. This behaviour is also illustrated in Figs. 4.2e and 4.2d where f is plotted as a function of T_f for the explored range of foaming times for the low M_w nanofoams and the high M_w nanofoams, respectively.

The measured open cell content O_v is plotted as a function of the measured porosity f in Figs. 4.3a (low M_w PMMA) and 4.3b (high M_w PMMA) for foaming temperatures ranging from 25°C to 80 °C. Nanofoams with porosities well below the highest observed porosity f_{max} are closed-celled in nature. An abrupt transition to an open-celled structure occurs close to f_{max}. The observed collapse of the foam at T = 100 °C is preceded by cell wall tearing for the low M_w nanofoams (see Fig. 4.4a) and by the formation of cracks interconnecting the nano-sized pores in the high M_w nanofoams (see Fig. 4.4b).

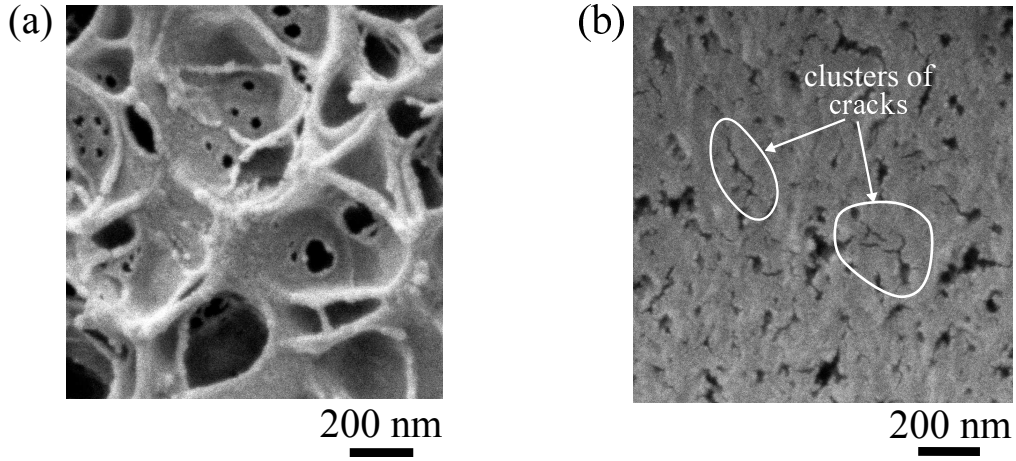

Figure 4.4 SEM micrographs of open-celled nanofoams: (a) cell wall tearing in the low M_w nanofoam for t_f = 300 s and T_f = 100 °C and (b) the nucleation and growth of cracks from the nano-size voids in the high M_w nanofoam for t_f = 300 s and T_f = 100 °C.

4.3 Concluding remarks

Solid-state nanofoaming experiments are performed on two grades of PMMA of markedly different molecular weight (M_w = 92 500 g mol^{-1} and M_w = 3 580 000 g mol^{-1}). It was found that molecular weight of the PMMA has a profound effect upon the final morphology of the PMMA nanofoams. When subjected to identical foaming conditions, the observed cell size l ($\approx$ 35 nm) of the high molecular weight PMMA nanofoams is an order of magnitude less than the cell size of the low molecular weight PMMA nanofoams ($\approx$ 205 nm). This is consistent with the observation that the nucleation density N_d ($\approx 2\times10^{21}$ m^{-3}) of the high molecular weight PMMA nanofoams is an order of magnitude higher than that of the low molecular weight PMMA nanofoams N_d ($\approx 2\times10^{20}$ m^{-3}). In addition, a limit in attainable porosity f_{max} was observed: f_{max} equals 0.6 for the high molecular weight PMMA and f_{max} equals 0.75 for the low molecular weight PMMA. The microstructure of the PMMA nanofoams transitions from closed-celled to open-celled at a porosity close to f_{max}.

Chapter 5

Prediction of void growth during solid-state nanofoaming

A one dimensional numerical model is developed to predict the growth of spherical, gas-filled voids during the solid-state foaming process. Emphasis is placed on void growth during solid-state nanofoaming of PMMA by making use of CO_2 as the blowing agent. The foaming model makes use of the experimentally calibrated constitutive laws for the PMMA grades tested in Chapter 3. The effect of dissolved CO_2 is accounted for by a shift in the glass transition temperature of the PMMA. Predicted curves for the porosity as a function of foaming time and foaming temperature are compared to those measured in Chapter 4. In addition, cell wall tearing mechanisms are explored to investigate the observed limit in final porosity.

5.1 The void growth model

A void growth model is developed to predict the porosity of an PMMA nanofoam as a function of foaming time and foaming temperature. The expansion of a pre-existing, as-nucleated cavity during the growth phase of the solid-state nanofoaming process is simulated by means of a one dimensional 'multiple void' growth model (Amon and Denson, 1984), see Section 2.1.3.2. Consider a polymer-gas solid with equisized spherical voids. A cross-section of the undeformed configuration of a spherical void, with initial radius a_0 and initial outer radius b_0 along with the spherical (r, θ, ϕ)-coordinate system is shown in Fig. 5.1. Assume that the initial gas pressure p_0 in the as-nucleated void equals the saturation pressure during the saturation phase prior to

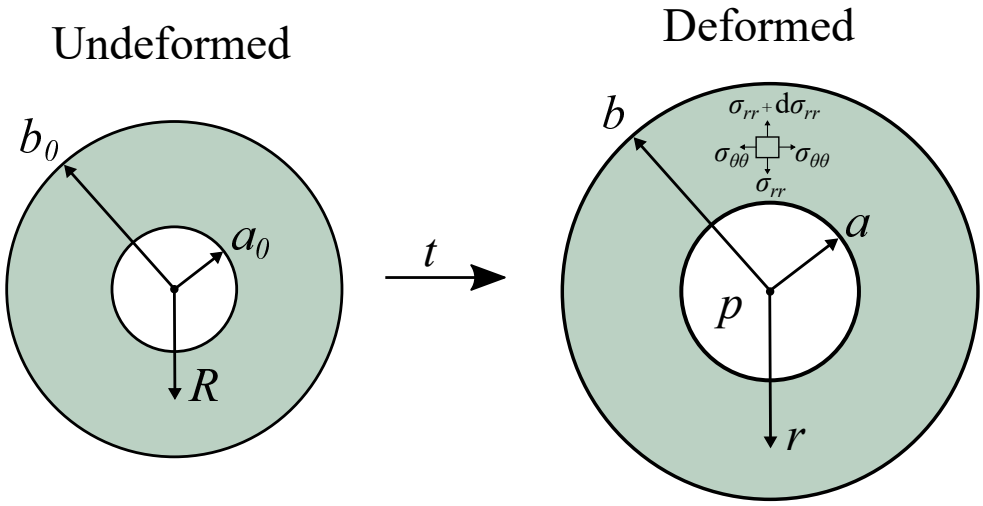

Figure 5.1 Spherical void in (a) the undeformed configuration with initial radius a_0 and initial outer radius b_0 and (b) the deformed configuration at time t of the void with radius a, outer radius b and gas pressure p.

nucleation of the voids. The deformed configuration for the void of inner radius a and outer radius b at time t is shown in Fig. 5.1.

5.1.1 Kinematics

Assume that the void remains spherical during growth and that the solid surrounding the void is incompressible. Then a material point, initially at radius R, is displaced to a radius r such that:

$$r^3 - a^3 = R^3 - {a_0}^3 \tag{5.1}$$

For later used, this relation is re-arranged to the form:

$$\left(\frac{r}{R}\right)^3 = 1 + \left(\frac{a_0}{R}\right)^3 \left[\left(\frac{a}{a_0}\right)^3 - 1\right] \tag{5.2}$$

Note that r/R is a function of a time-like variable a/a_0 and of the Lagrangian position variable R/a_0. The von Mises strain ε_e is defined in the usual manner, and for the void problem it reads:

$$\varepsilon_e = |2\varepsilon_{\theta\theta}| = 2\ln\left(\frac{r}{R}\right) \tag{5.3}$$

where $\varepsilon_{\theta\theta}$ is the hoop strain. Now insert Eq. 5.2 into Eq. 5.3 to obtain:

$$\varepsilon_{\mathrm{e}} = \frac{2}{3}\ln\left[1+\left(\frac{a_0}{R}\right)^3\left(\left(\frac{a}{a_0}\right)^3-1\right)\right] \tag{5.4}$$

and take the time derivative of r in Eq. 5.1:

$$\dot{r} = v_r = \left(\frac{a}{r}\right)^2 \dot{a} \tag{5.5}$$

where v_r is the radial velocity of a material element at r. Consequently, the effective strain rate $\dot{\varepsilon}_{\mathrm{e}}$ reads:

$$\dot{\varepsilon}_{\mathrm{e}} = |\frac{\partial v_r}{\partial r}| = \frac{2a^2}{R^3}\left(\frac{r}{R}\right)^{-3}\dot{a} \tag{5.6}$$

where r/R scales with the current void size a in accordance with Eq. 5.2.

5.1.2 Equilibrium

Now, write (σ_{rr}, $\sigma_{\theta\theta}$, $\sigma_{\phi\phi}$) as the active stress components in the spherical coordinate system. Radial equilibrium dictates that (Timoshenko and Goodier, 1970):

$$\frac{\partial \sigma_{rr}}{\partial r} + \frac{1}{r}\Big(2\sigma_{rr} - \sigma_{\theta\theta} - \sigma_{\phi\phi}\Big) = 0 \tag{5.7}$$

Due to symmetry, $\sigma_{\theta\theta} = \sigma_{\phi\phi}$ and Eq. 5.7 reduces to:

$$\frac{\partial \sigma_{rr}}{\partial r} = \frac{2(\sigma_{\theta\theta} - \sigma_{rr})}{r} = \frac{2\sigma_{\mathrm{e}}}{r} \tag{5.8}$$

where $\sigma_{\mathrm{e}} = \sigma_{\theta\theta} - \sigma_{rr}$ is the von Mises effective stress (Hill, 1950). Integration of Eq. 5.8 leads to:

$$p - p_a = \int_{r=a}^{r=b} \frac{2\sigma_{\mathrm{e}}}{r}\mathrm{d}r \tag{5.9}$$

where p is the gas pressure inside the cavity for a given radius a and p_a is the ambient pressure. In addition, incompressibility dictates:

$$dr = \left(\frac{R}{r}\right)^2 dR \tag{5.10}$$

and Eq. 5.9 can be re-phrased in the Lagrangian form:

$$p - p_a = \int_{R=a_0}^{R=b_0} \frac{2}{R}\left(\frac{R}{r}\right)^3 \sigma_e dR \tag{5.11}$$

Now, the effective stress σ_e is a function of the effective strain ε_e (Eq. 5.4), the effective strain rate $\dot{\varepsilon}_e$ (Eq. 5.6) and the normalised temperature T/T_g via the constitutive law for an PMMA-CO_2 solid of the functional form:

$$\sigma_e = F\left(\varepsilon_e, \dot{\varepsilon}_e, \frac{T}{T_g}\right) \tag{5.12}$$

The choice of the function F is based on the findings presented in Section 3.3.2 and is detailed below. It is emphasised that the glass transition temperature T_g is a function of CO_2 concentration.

5.1.3 Mass conservation

At the start of the foaming process, the chemical potential of CO_2 molecules in the as-nucleated voids is lower than chemical potential of CO_2 molecules in the PMMA-CO_2 solid. Consequently, CO_2 molecules migrate from the PMMA-CO_2 solid to the growing cavity. The weight concentration of CO_2 gas molecules $C(R,t)$ at time t and position R (for $a_0 < R < b_0$) can be obtained by solving Fick's second law of diffusion (Crank, 1975):

$$\frac{\partial C(R,t)}{\partial t} = \frac{D}{R^2}\frac{\partial}{\partial R}\left[R^2\left(\frac{r}{R}\right)^4 \frac{\partial C(R,t)}{\partial R}\right] \tag{5.13}$$

where D refers to the diffusion coefficient for CO_2 in PMMA. Measurements of D at temperatures and pressures typical for solid-state nanofoaming of PMMA by CO_2 are available in the literature as follows. Guo and Kumar (2015) measured D based on desorption measurements and

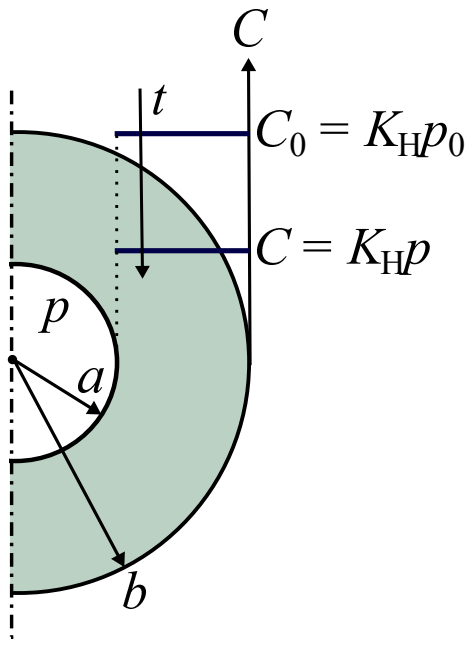

Figure 5.2 Sketch of the spatially uniform CO_2 concentration in the PMMA-CO_2 solid surrounding the void.

found D to range between 2.5×10^{-12} m^2 s^{-1} and 3.65×10^{-11} m^2 s^{-1}for temperatures ranging from -30 °C to 100 °C at a CO_2 pressure equal to 5 MPa. Li et al. (2018) measured D based on sorption measurements and found D to vary between 6×10^{-11} m^2 s^{-1} and 9.5×10^{-11} m^2 s^{-1} for temperatures ranging from 30 °C to 70 °C and pressures ranging from 6 MPa to 18 MPa. Now, consider a characteristic diffusion time τ_D:

$$\tau_D = \frac{(L_\mathrm{D})^2}{D} \tag{5.14}$$

where L_D is a diffusion length which may be approximated for the void growth problem by:

$$L_\mathrm{D} \approx 2b_0 \approx \left(\frac{6}{\pi N_\mathrm{d}}\right)^{\frac{1}{3}} \tag{5.15}$$

where it is assumed that the nucleation density N_d is approximated by $3/(4\pi b_0^3)$. Observation of cell nucleation densities of PMMA nanofoams ($N_\mathrm{d} > 10^{20}$ m^{-3}) imply a value for L_D lower than 250 nm. Upon adopting a low value of D equal to 10^{-12} m^2 s^{-1}, we obtain $\tau_D \approx 60$ ms via Eq. 5.14, which is at least two orders of magnitude lower than typical observed cell growth times for solid-state nanofoaming of PMMA by CO_2 as discussed in Section 4.2 and in the work of Martin-de León et al. (2016). The CO_2 concentration profile $C(R,t)$ may therefore assumed

to be spatially uniform at all times: $C(R,t) = C(t)$, see Fig. 5.2. Consequently, one does not need to solve the diffusion equation (Eq. 5.13) to predict void growth during solid-state nanofoaming of PMMA by CO_2.

Furthermore, the mass of gas molecules in the void and in the surrounding solid is assumed to be constant; leakage of gas molecules to neighbouring voids or the sample's environment is neglected. The resulting mass conservation statement reads:

$$C\rho^{\mathrm{p}}(b^3 - a^3) + \rho^{\mathrm{g}}a^3 = C_0\rho^{\mathrm{p}}(b_0^3 - a_0^3) + \rho_0^{\mathrm{g}}a_0^3 \tag{5.16}$$

where ρ^{g} is the density of the gas in the void, and ρ^{p} is the density of the PMMA-CO_2 solid. The value for ρ^{p} is, as a first order approximation, assumed[1] to be equal to the density of the PMMA solid absent CO_2, i.e. $\rho^{\mathrm{p}} = 1\,190$ kg m^{-3}.

5.1.4 Additional assumptions for the solid-state foaming of PMMA by CO_2

The relations in Eqs. 5.11 and 5.16 form a coupled pair of equations which can be solved to obtain p as a function of cavity expansion a/a_0. Additional assumptions for solid-state foaming of PMMA by CO_2 are detailed below.

5.1.4.1 Dependence of the PMMA-CO_2 glass transition temperature upon CO_2 concentration

The dissolution of CO_2 into a linear, amorphous polymer such as PMMA reduces the glass transition temperature T_{g} of the PMMA-CO_2 solid. The dependence of the glass transition temperature of PMMA upon CO_2 concentration was reviewed in Section 2.1.2.3. The T/T_{g}^0 versus CO_2 concentration C curve is assumed to be predicted by the Chow equation (Eq. 2.7):

[1] This assumption is based on the findings of Pantoula and co-workers (Pantoula and Panayiotou, 2006; Pantoula et al., 2007) who reported that the relative increase in volume of an PMMA-CO_2 mixture is close to the relative increase of the mass of the PMMA-CO_2 for a CO_2 pressure up to 30 MPa.

$$\frac{T_g}{T_g^0} = \exp\Big[\beta\Big((1-\theta)\ln(1-\theta)+\theta\ln\theta\Big)\Big] \tag{5.17}$$

where θ is defined as:

$$\theta = \frac{M_w^p}{zM_w^g}\frac{C}{1-C} \tag{5.18}$$

where M_w^p is the molecular weight of the polymer repeat unit (M_w^p = 110.12 g mol^{-1} for a methyl methacrylate monomer), and z is the lattice coordination number assumed to be equal to 2 as suggested by Chow (1980). The parameter β in Eq. 5.17 reads:

$$\beta = \frac{zR}{M_w^p \Delta C_p} \tag{5.19}$$

where R is the universal gas constant and ΔC_p is the change in specific heat capacity of the PMMA absent the CO_2, assumed to be equal to 355 J kg^{-1} K^{-1}, based on the curve fit to the data of Chiou et al. (1985), Wissinger and Paulaitis (1991), and Guo and Kumar (2015) as detailed in Section 2.1.2.3.

5.1.4.2 Constitutive laws for the PMMA-CO_2 solid

The effective stress σ_e of the PMMA-CO_2 solid at a given strain ε_e, strain rate $\dot{\varepsilon}_e$, and temperature T_g/T_g^0 is assumed to be the same as that given by PMMA in the absence of CO_2: the effect of CO_2 is accounted for by a shift in the value for T_g as detailed above. Deformation mechanisms for PMMA in uniaxial tension close to the glass transition temperature were reviewed in Section 2.1.4. A series of uniaxial tension tests with a low M_w and a high M_w PMMA grade over a range of temperatures near the glass transition and over two decades of strain rate were conducted to construct deformation and failure maps for the two PMMA grades in Section 3.3.2. A single transition process Ree–Eyring equation was calibrated to relate the flow strength σ_e of the PMMA grades in the glass and glassy regime to the normalised temperature T_g/T_g^0 and strain rate $\dot{\varepsilon}_e$:

$$\frac{\dot{\varepsilon}_e}{\dot{\varepsilon}_0} = \sinh\left(\frac{\sigma_e v}{kT}\right)\exp\left(\frac{-q}{kT}\right) \tag{5.20}$$

where Eq. 2.10 is re-stated for convenience. Note that, as a first order assumption, the dependence of the strength of the PMMA-CO_2 solid on hydrostatic stress is neglected, i.e. $\bar{\sigma} = \sigma_e$, given the dependence of CO_2 concentration upon the pressure dependence of the yield strength of PMMA is not known.

An empirical equation was used in Section 3.3.2 to relate σ_e to ε_e, $\dot{\varepsilon}_e$ and T_g/T_g^0 in the rubbery regime observed above the glass transition for the high M_w PMMA:

$$\sigma_e = E_R^0\left(1 - \alpha_R \frac{T}{T_g}\right)\left(\frac{\dot{\varepsilon}}{\dot{\varepsilon}_e}\right)\varepsilon_e \tag{5.21}$$

where Eq. 3.3 is re-stated for convenience. A linear, viscous regime was observed for the low M_w PMMA at temperatures above the glass transition:

$$\sigma_e = \eta_{WLF}\dot{\varepsilon}_e \tag{5.22}$$

where η_{WLF} is a temperature-dependent viscosity, see Eq. 2.9.

The dependence of the effective stress σ_e of the PMMA-CO_2 solid upon strain, strain rate and normalised temperature is assumed to be governed by Eq. 5.20 and Eq. 5.22 (low M_w PMMA) or Eq. 5.21 (high M_w PMMA). A summary of the fitted parameters for the constitutive laws employed for the PMMA-CO_2 solid, as discussed in Section 4.2, is given in Table 5.1.

5.1.4.3 Gas laws

The dependence of the equilibrium concentration C of CO_2 into PMMA upon CO_2 pressure p was reviewed in Section 2.1.2.2 for pressure and temperature regimes relevant for the solid-state foaming process employed for the foaming experiments detailed in Section 4.1.2. Here, it is assumed that Henry's law suffices to predict the dependence of C upon p such that (Rajendran et al., 2005; Pantoula and Panayiotou, 2006; Pantoula et al., 2007; Van Krevelen and Te Nijenhuis, 2009):

$$C = k_H p \tag{5.23}$$

Table 5.1 Fitted parameters for the constitutive laws for the low M_w PMMA (Eqs. 5.20 and 5.22) and the high M_w PMMA (Eqs. 5.20 and 5.21), see Section 3.3.2.

Parameter	low M_w PMMA	high M_w PMMA
v (nm^{-3})	2.5	1.8
q (J)	7.31×10^{-19}	7.31×10^{-19}
$\dot{\varepsilon}_0$ (s^{-1})	1.5×10^{56}	1.5×10^{56}
η_0 (Pa·s)	2.8×10^{6}	-
C_1	3.2	-
C_2 (K)	17.3	-
E_R^0 (MPa)	-	65.8
α_R	-	0.8
$\dot{\varepsilon}_R$ (s^{-1})	-	1.58
n	-	0.173

where k_H is Henry's law coefficient which is assumed to be independent of temperature and of pressure. Based on the measured 24 wt% equilibrium concentration of CO_2 in PMMA at a pressure p equal to 31 MPa and temperature T = 25 °C (see Section 4.1.2), the value for k_H equals 7.7×10^{-9} Pa^{-1} for both PMMA grades.

Recall that during the growth phase of a typical solid-state nanofoaming process the gas saturation pressure ranges from 10 MPa to 30 MPa and the foaming temperatures typically varies from 20 °C to 100 °C. Empirical (non-ideal) equations of state for CO_2 in these temperature and pressure regimes are available (Huang et al., 1985; Span and Wagner, 1996). In this study, however, an ideal gas law for the CO_2 in the void is assumed as a first order approximation to predict the expansion of the void:

$$p = \frac{\rho^g RT}{M_w^g} \tag{5.24}$$

This simplifying assumption for the equation of state of the CO_2 gas is found to be adequate to predict the porosity of the PMMA nanofoams as a function of foaming time and foaming temperature as detailed in the next section.

5.1.4.4 Temperature-time profile during void growth

During the rapid release of pressure at the end of the saturation phase, the samples cool down from the saturation temperature (T = 25 °C) to a temperature[2] close to T_0 = -15 °C due to adiabatic cooling of the expanding gas. The samples are subsequently placed in a thermal bath at a maintained foaming temperature T_f. Upon submersion in the foaming bath, assume that the temperature profile $T(t)$ is of the form:

$$T = T_0 + (T_f - T_0)(1 - \exp(-t/\tau)) \tag{5.25}$$

where τ is a time constant associated with the heat conduction into the PMMA, as measured by a thermocouple.

5.1.5 Input for the void growth simulations

Void growth during solid-state foaming of PMMA by CO_2 is simulated by solving the equilibrium equation (Eq. 5.11) and the mass conservation statement (Eq. 5.16) simultaneously, with due account of the dependence of the effective glass transition temperature T_g of the PMMA-CO_2 solid upon CO_2 concentration (Eq. 5.17), the dependence of the effective stress σ_e of the PMMA-CO_2 solid on strain, strain rate and normalised temperature (Eq. 5.20 and 5.22 (low M_w PMMA) or Eq. 5.21 (high M_w PMMA)), the gas laws (Eqs. 5.23 and 5.24), and the time-temperature profile of the PMMA-CO_2 solid (Eq. 5.25). The resulting system of equations is solved by numerical integration[3]. The values for the processing parameters and the material properties (those not explicitly stated before) are summarised in Table 5.2. Note that the initial porosity f_0 is defined as:

$$f_0 = \left(\frac{a_0}{b_0}\right)^3 \tag{5.26}$$

[2] The temperature T_0 was measured by placing a thermocouple on the sample after the pressure release at the end of the saturation phase.

[3] The numerical integration was conducted within the Matlab computing environment by means of the ode15s function.

and is estimated[4] to be close to 10^{-3} for the low M_w and high M_w PMMA grades. Moreover, the initial void radius a_0 is estimated by assuming:

$$a_0 \approx \left(\frac{3f_0}{4\pi N_d}\right)^{\frac{1}{3}} \tag{5.27}$$

where the cell nucleation density N_d is equal to 2×10^{20} m^{-3} for the low M_w PMMA nanofoams and $N_d = 20 \times 10^{20}$ m^{-3} for the high M_w PMMA nanofoams, see Section 4.2.

Table 5.2 Input parameters for the void growth simulations during solid-state nanofoaming of PMMA by CO_2.

	low M_w PMMA	high M_w PMMA
p_0 (MPa)	31	31
p_a (MPa)	0.1	0.1
τ (s)	20	20
T_g (°C)	114.5	116.5
f_0	10^{-3}	10^{-3}
a_0 (nm)	10.5	5

5.2 Results and discussion of the void growth predictions

Consider the deformation mechanism maps of the low M_w PMMA (see Fig. 5.3a) and the high M_w PMMA (see Fig. 5.3b) grades. The predicted trajectory of the effective stress at the surface of the cavity σ_e by the void growth model is plotted as a function of T/T_g for foaming temperatures T_f = 25 °C and T_f = 80 °C and for a foaming time up to 600 s. Note that, both the temperature T and the glass transition temperature T_g evolve in time during void growth. For the both the low M_w and high M_w, at the start of foaming, $T = T_0$ and T/T_g is close to 0.9, with σ_e close to 0.8 MPa for the low M_w PMMA and σ_e is close to 0.3 MPa for the high M_w PMMA. When the temperature increases from $T = T_0$ to $T = T_f$, T/T_g rises to close to unity and σ_e increases steeply. The void growth simulations suggest that during solid-state foaming of PMMA, the normalised temperature T/T_g remains predominantly between 0.9 and 1 and,

[4] The initial porosity f_0 is measured by saturating low M_w and high M_w PMMA precursors with CO_2 at p = 31 MPa and T = 25 °C. Upon release of the pressure to atmospheric pressure, the samples were immediately immersed in liquid nitrogen (T = -196 °C) to prevent growth of the nucleated voids. The porosity of the samples was measured by the method detailed in Section 4.1.3.1 via Eq. 4.1 after the CO_2 was completely desorbed. The measured porosity was assumed to be representative for the value of f_0.

consequently, void growth does not occur within either the viscous regime (low M_w PMMA) or within the rubbery regime (high M_w PMMA).

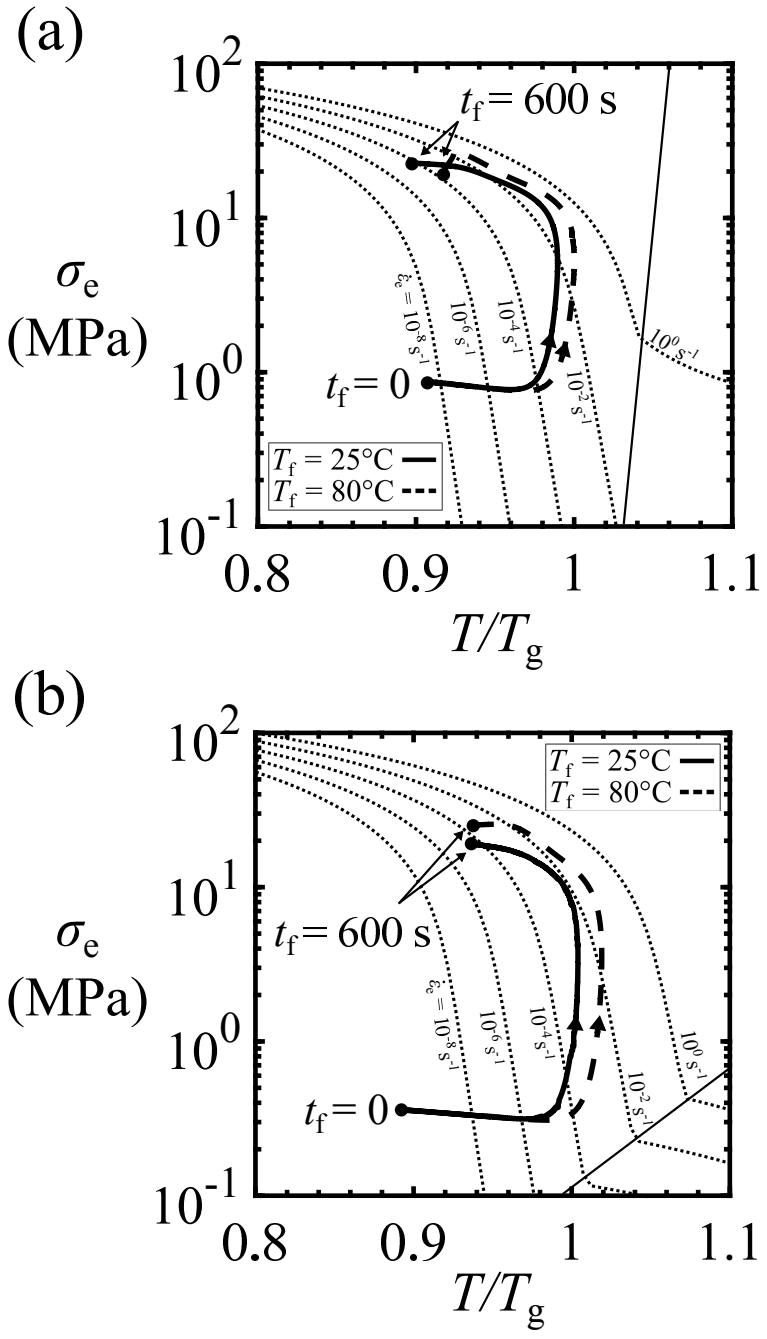

Figure 5.3 Deformation mechanism maps of (a) the low M_w PMMA grade and (b) the high M_w PMMA grade (for a reference strain ε_f equal to 0.05) with contours of effective strain rate $\dot{\varepsilon}_e$ as a function of T/T_g for foaming temperatures T_f = 25 °C and T_f = 80 °C and for a foaming time up to 600 s.

The predicted normalised gas pressure p/p_0 in the cavity is plotted during void growth in the low M_w and the high M_w PMMA grades as a function of foaming time t_f (up to 600 s, corresponding to the maximum foaming time explored for the nanofoaming experiments as detailed in Section 4.1.2) for T_f = 25 °C and T_f = 80 °C, see Fig. 5.4. For T_f = 25 °C, the predicted gas pressure in the cavity at the end of the foaming process at t_f = 600 s is two orders of magnitude higher than the ambient pressure, and the remnant weight concentration of CO_2 in the PMMA matrix C is in the order of 0.1. In contrast, for T_f = 80 °C, the gas pressure is close to the ambient pressure at t_f = 600 s, and negligible remnant CO_2 is present in the PMMA.

The predicted porosity f is plotted as a function of foaming temperature T_f for foaming times t_f = 180 s and t_f = 600 s in Fig. 5.5 for the low M_w and the high M_w nanofoams. The measured values of final porosity of the low M_w and high M_w nanofoams for t_f = 180 s and t_f = 600 s for T_f = 25 °C to T_f = 80 °C are included in Fig. 5.5. The void growth model predicts the observed increase in porosity of the low M_w nanofoam with respect to the high M_w nanofoam (at an identical foaming time and foaming temperature). As detailed in Section 3.3.2 (and shown in Fig. 5.3), the effective stress of the low M_w PMMA when deformed in uniaxial tension close to the glass transition is lower than that of the high M_w PMMA at an identical rate $\dot{\varepsilon}_e$ and temperature T/T_g. The void growth simulations suggest that this difference in constitutive response causes the

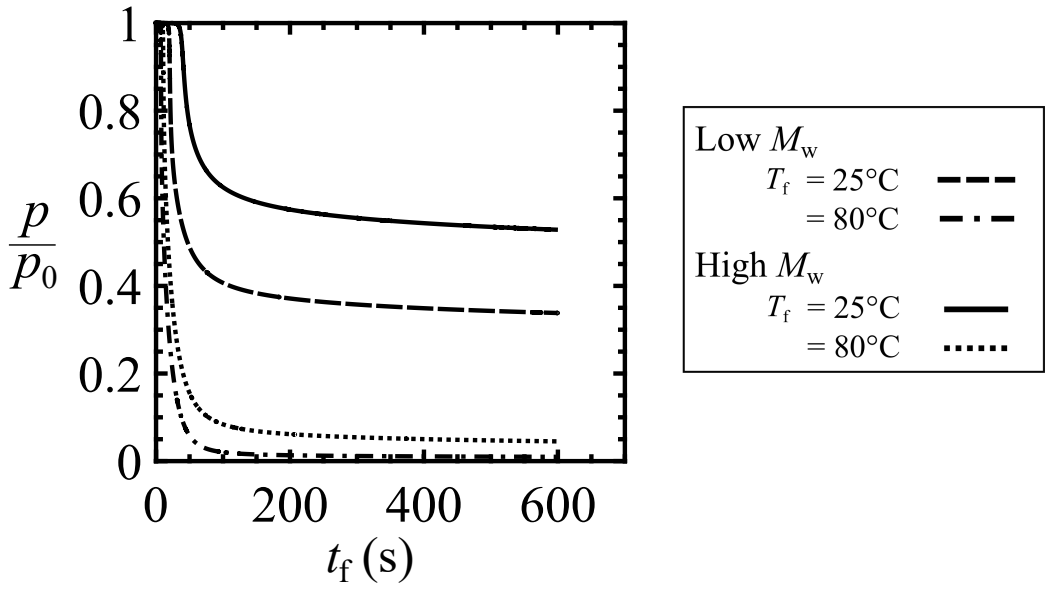

Figure 5.4 The predicted normalised gas pressure p/p_0 as a function of foaming time t_f during solid-state nanofoaming of the low M_w and the high M_w PMMA grades for foaming temperatures T_f = 25 °C and T_f = 80 °C and for a foaming time up to 600 s.

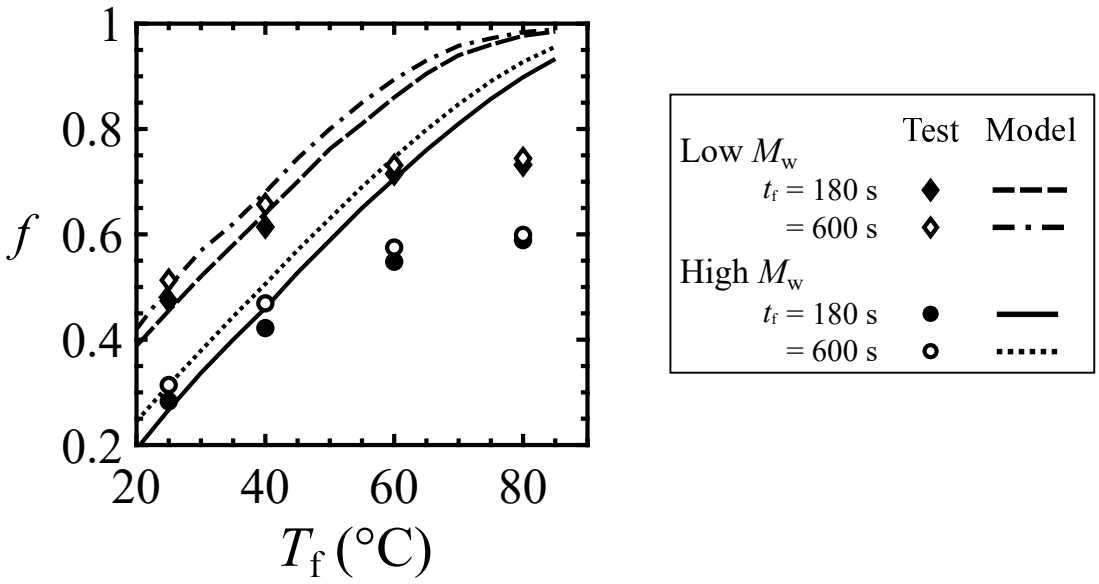

Figure 5.5 The predicted porosity f plotted as a function of foaming temperature T_f for foaming times t_f = 180 s and t_f = 600 s for the low M_w and the high M_w nanofoams. The measured values of f for the low M_w and high M_w nanofoams for t_f = 180 s and t_f = 600 s for T_f = 25 °C to T_f = 80 °C are included.

difference between the observed final porosity between the low M_w and high M_w nanofoams. Moreover, there is a reasonably close agreement between the predicted and measured porosities for T_f = 25 °C to T_f = 40 °C for both the low M_w and high M_w nanofoams. For $T_f > 40$ °C, the cell growth model overestimates the observed porosity. Observations of SEM micrographs suggest that cell walls tear (low M_w PMMA) and cracks nucleate and grow between the voids (high M_w PMMA) at T_f = 60 °C and T_f = 80 °C, leading to open-celled microstructures (see Fig. 4.4). This is also confirmed by open cell content measurements by gas pycnometry: nanofoams with the highest observed porosities have predominantly open-celled microstructures, see Fig. 4.3. At increased foaming temperatures (i.e. T_f = 100 °C) collapse of the foamed open-celled microstructure is observed leading to measured porosities below the maximum observed porosities at T_f = 80 °C, as shown in Figs. 4.2e and 4.2f.

Two alternative hypotheses are now explored for cell wall failure which could lead to open-celled microstructures as observed for the PMMA nanofoams: (i) achievement of a critical hoop strain at the void, or (ii) achievement of a minimum (critical) value of ligament thickness between neighbouring voids.

(i) Critical hoop strain

Assume that the solid surrounding the expanding void is incompressible:

$$b^3 - a^3 = b_0^3 - a_0^3 \tag{5.28}$$

Recall that the initial (as-nucleated) porosity f_0 equals $(a_0/b_0)^3$ as defined in Eq. 5.26 and the current porosity f equals $(a/b)^3$. Now, rearrange Eq. 5.28, to express f as a function of f_0 and the true hoop strain ε_s at the surface of the void, where $\varepsilon_s = \varepsilon_{\theta\theta}(r = a) = \ln(a/a_0)$:

$$f^{-1} = 1 + \exp\big(-3\varepsilon_s\big)\big(f_0^{-1} - 1\big) \tag{5.29}$$

Tearing of the cell wall occurs when ε_s equals the T/T_g-dependent true tensile failure strain ε_f. The critical porosity f_f corresponding to this ductility-governed failure criterion reads:

$$f_f^{-1} = 1 + \exp\big(-3\varepsilon_f\big)\big(f_0^{-1} - 1\big) \tag{5.30}$$

(ii) Critical ligament size

The alternative failure hypothesis assumes that there is a minimum number of confined polymer chains separating individual cells to prevent rupture of the solid between the cells. Define the smallest distance between two neighbouring cells h as:

$$h = 2(b - a) \tag{5.31}$$

Dividing by a_0 and making use of the expression $\varepsilon_s = \ln(a/a_0)$, Eq. 5.31 can be rearranged to:

$$\frac{h}{a_0} = 2\exp\big(\varepsilon_s\big)\big(f^{-\frac{1}{3}} - 1\big) \tag{5.32}$$

The true hoop strain at the surface of the cavity ε_s is related to the initial and current porosity via Eq. 5.29:

$$\exp\big(\varepsilon_s\big) = \left(\frac{f_0^{-1} - 1}{f^{-1} - 1}\right)^{\frac{1}{3}} \tag{5.33}$$

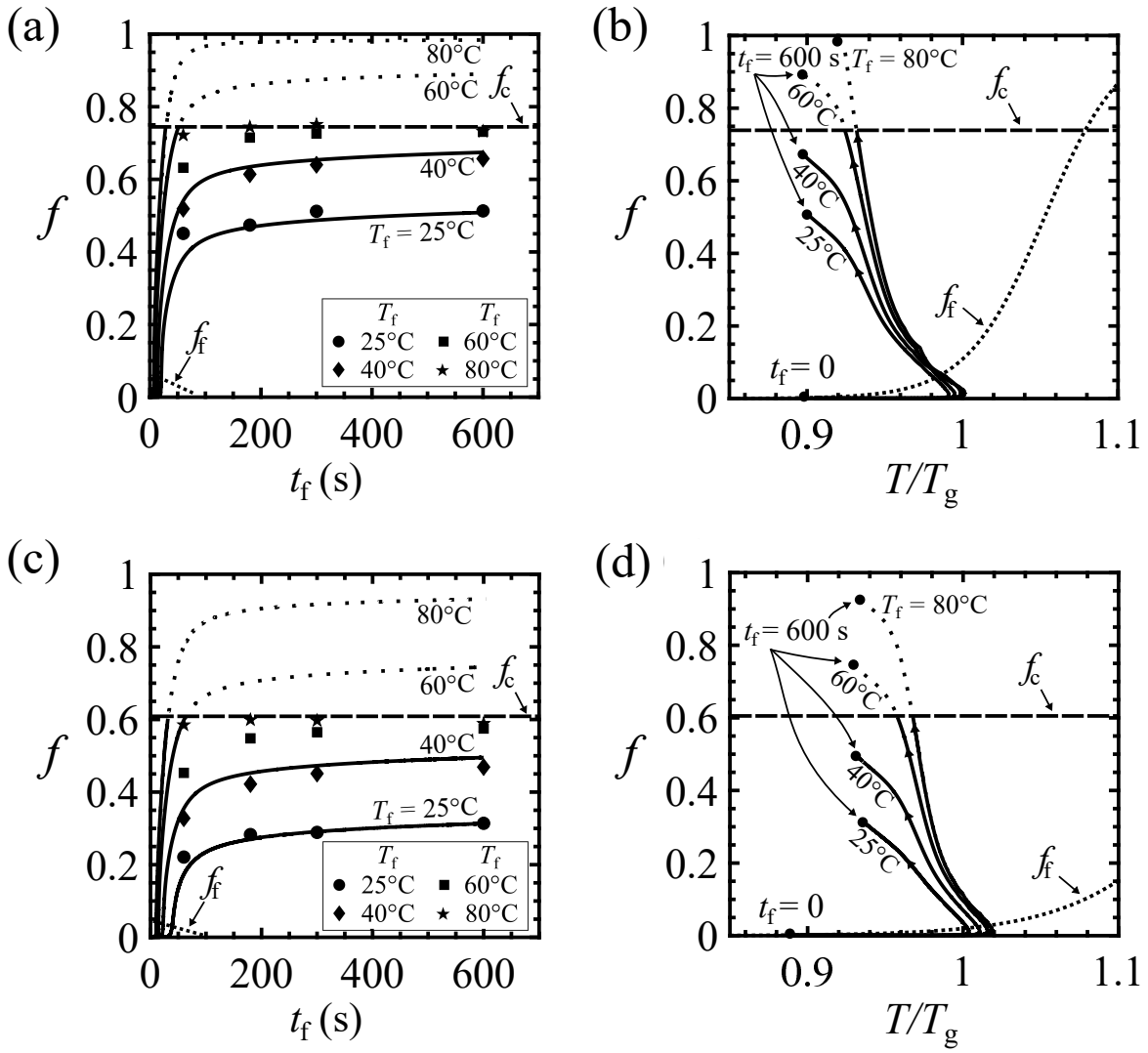

Figure 5.6 The predicted porosity f versus foaming time t_f and versus normalised temperature T/T_g: (a) f versus t_f for the low M_w nanofoams, (b) f versus T/T_g for the low M_w nanofoams, (c) f versus t_f for the high M_w nanofoams, and (d) f versus T/T_g for the high M_w nanofoams. Symbols refer to measurements in (a) and (c).

Then, upon making use of Eqs. 5.32 and 5.33:

$$\frac{h}{a_0} = 2\left(f^{-\frac{1}{3}} - 1\right)\left(\frac{f_0^{-1} - 1}{f^{-1} - 1}\right)^{\frac{1}{3}} \tag{5.34}$$

Write h_c as the critical cell wall thickness, and assume that it is independent of the value of T/T_g. The corresponding critical value of porosity f_c is given by Eq. 5.34 with $h = h_c$.

The predicted porosity f is plotted as a function of foaming time t_f (up to 600 s) for foaming temperatures ranging from T_f = 25 °C to T_f = 80 °C in in Figs. 5.6a and 5.6c for the low M_w

and high M_w nanofoams, respectively. The measured values of porosity f for T_f = 25 °C to T_f = 80 °C are included. The predicted f versus T/T_g curves are shown in Figs. 5.6b and 5.6d for the low M_w and high M_w nanofoams, respectively. The ductility-governed porosity limit f_f as given by Eq. 5.30 is plotted in Figs. 5.6a to 5.6d based on the predicted hoop strain ε_s during void growth and by making use of the measured response of ε_f versus T/T_g (Eq. 3.11 for the low M_w PMMA and Eq. 3.9 for the high M_w PMMA). Note that the initial porosity f_0 is assumed to equal 10^{-3}, see Table 5.2. The maximum attainable porosity f_f is close to 0.1 and 0.05 for the low and high M_w nanofoams, respectively. These values for final porosity are much lower than the observed values of final porosity f_{max}. The alternative porosity limit f_c is plotted in Figs. 5.6a to 5.6d via Eq. 5.34 for $f_0 = 10^{-3}$ by taking $h_c/a_0 = 3$ (low M_w PMMA) and $h_c/a_0 = 4.2$ (high M_w PMMA) in order to match the observed value of the maximum observed porosity f_{max} on the nanofoams. This analysis suggests that the critical ligament length limits achievable porosity.

Recall that the initial void size a_0 of the low M_w nanofoams is estimated to be close to 10.5 nm, whereas a_0 = 5 nm for the high M_w nanofoams. Consequently, the estimated corresponding critical cell wall dimension equals 32 nm for the low M_w nanofoams, whereas h_c equals 21 nm for the high M_w nanofoams. The values for h_c may be compared with respect to the root-mean-square end-to-end distance R_{ee} of an idealised polymer chain comprising n monomers[5] of length l (Rubinstein and Colby, 2003; Young and Lovell, 2011):

$$R_{ee} = \sqrt{C_\infty n} l \tag{5.35}$$

where C_∞ is the characteristic ratio accounting for steric interactions and restriction in bond angles between neighbouring monomers. Alternatively, the polymer chain may be idealised by an equivalent freely-jointed chain with N (= n/C_∞) links of length b (= lC_∞) with, such that:

$$R_{ee} = \sqrt{N} b \tag{5.36}$$

Assuming that b = 1.7 nm and C_∞ = 9 for PMMA, as reported by Rubinstein and Colby (2003), the value for R_{ee} is close to 20 nm for the low M_w PMMA, whereas $R_{ee} \approx 110$ nm for the high

[5] The amount of monomers n in the chain is approximated by the degree of polymerisation $x_p = M_w/M_w^p$, where M_w^p is the molecular weight of the monomer (M_w^p = 100.2 g mol^{-1} for PMMA).

M_w PMMA. Thus, the values for h_c are of the same order of magnitude as the root-mean-square end-to-end distance R_{ee} of the PMMA chains. This is in agreement with the results of Crosby and co-workers (Liu et al., 2015; Bay et al., 2018) who conducted a series of uniaxial tensile tests on thin polystyrene films with M_w = 136 000 g mol^{-1}. They found that the tensile failure strain decreases with decreasing film thickness t_s in the regime t_s = 15 nm to t_s = 77 nm; these values are close to the estimated value for R_{ee} = 25 nm of the PS chains.

5.3 The limits of solid-state nanofoaming

One of the aims of current research on polymeric nanofoams is to produce foams of high porosity ($f > 0.85$) and comprising small voids ($l < 200$ nm). The void growth model and the cell wall tearing analysis discussed above may be used to shed light on the limitations of the solid-state nanofoaming process when attempting to manufacture nanofoams with such a morphology.

Recall Fig. 2.2, in which the final porosity f of various polymeric nanofoams reported in the literature, grouped per polymer precursor material system, is plotted as a function of final void size l. Contours of cell nucleation densities N_D are plotted in Fig. 2.2 via Eq. 2.2. In order to produce nanofoams with $f > 0.85$ and $l < 200$ nm, it is necessary for the cell nucleation density to be close or above 10^{21} m^{-3}. As detailed in Section 2.1.1, nanofoams with a cell nucleation density close to 10^{21} m^{-3} have been reported. For foaming systems relying on a homogeneous nucleation strategy[6], this is achieved by dissolving a critical concentration of blowing agent into the polymer precursor during the saturation phase. The value of this critical gas concentration depends upon the nature of the polymer precursor. For acrylic-based polymers such as PMMA, a CO_2 concentration exceeding 20 wt% is required (this is achieved, for instance, at $p_{sat} > 30$ MPa for T_{sat} close to room temperature) to produce nanofoams with $N_d \approx 10^{21}$ m^{-3} (Martin-de León et al., 2016), whereas for polyphenylsulfone (PPSU) only 13 wt% of CO_2 (achieved, for instance, at p_{sat} = 15 MPa for $t_f = -15$ °C) needs to be dissolved during the saturation phase to produce nanofoams with $N_d \approx 10^{21}$ m^{-3} (Guo et al., 2015a), and for polyetherimide (PEI)

[6] Heterogeneous nucleation strategies, such as the use of polymeric blends with nano-sized particles or the use of miscible polymeric blends, may also be used to produce nanofoams with $N_d \approx 10^{21}$ m^{-3} (Costeux, 2014; Martín-de León et al., 2019).

close to 16 wt% of CO_2 (achieved at p_{sat} = 5 MPa for t_f close to room temperature) has to be dissolved for $N_d \approx 10^{21}$ m^{-3} (Krause et al., 2001; Miller and Kumar, 2009).

Hence, many polymeric material systems (besides MMA-based polymers) can be used to produced nanofoams with nucleation densities sufficiently high to potentially attain a morphology of $f > 0.85$ and $l < 200$ nm, see Fig. 2.2. However, it is clear from Fig. 2.2, that only MMA-based nanofoams with $N_d \approx 10^{21}$ m^{-3} have been reported with $f > 0.7$ and $l < 200$ nm. The highest reported porosity for polyetherimide (PEI) nanofoams, for example, is close to 0.6 (with $N_d \approx 10^{21}$ m^{-3}) (Krause et al., 2001; Miller and Kumar, 2009; Aher et al., 2013). The observed 'porosity limit' for PEI nanofoams is explored in the coming paragraphs based on the combined experimental and theoretical analysis on solid-state nanofoaming of PMMA outlined in Chapter 4 and the present chapter. It is emphasised that the discussion in the coming paragraphs focuses on PEI nanofoams produced via solid-state foaming with CO_2. However, the arguments should be valid for any polymer precursor-blowing agent system for which foams with a sufficiently high cell nucleation density ($N_d \approx 10^{21}$ m^{-3}) can be achieved at the end of the saturation phase of the solid-state foaming process.

The line of reasoning is as follows. PEI nanofoams with a porosity above 0.6 may be produced by using a saturation pressure p_{sat} above the typically employed values for p_{sat} for solid-state nanofoaming of PEI in the literature. Most studies on PEI nanofoams focus on producing nanofoams with a sufficiently high cell nucleation density to produce foams with nano-sized voids. The critical concentration of CO_2 in PEI to achieve $N_d \approx 10^{21}$ m^{-3} is attained at saturation pressures much lower ($p_{sat} \approx 5$ MPa for T_{sat} close to room temperature) than that for PMMA (p_{sat} = 30 MPa for T_{sat} close to room temperature) (Krause et al., 2001; Costeux, 2014; Miller and Kumar, 2009; Zhou et al., 2012). To illustrate the effect of saturation pressure on final porosity, void growth simulations are conducted with the void growth model detailed in Section 5.1, using the input parameters[7] for the high M_w PMMA. Void growth predictions are conducted for a saturation pressure ranging from p_{sat} = 5 MPa to p_{sat} = 25 MPa and for T_f/T_g^0, where T_g^0 is the glass transition temperature of the polymer precursor absent CO_2, ranging from

[7] The assumed set of material properties and processing conditions are identical to the ones detailed in Section 5.1 for the high M_w PMMA void growth simulations unless otherwise stated. Note that the simulations are conducted for a value of the nucleation density $N_d = 2 \times 10^{21}$ m^{-3} independent of p_{sat}, whereas in reality N_d is dependent upon p_{sat}.

T_f/T_g^0 = 0.77 to T_f/T_g^0 = 0.98. The predicted porosity at t_f = 150 s for selected values of p_{sat} is plotted as a function of T_f/T_g^0. In addition, the measured values for f at t_f = 150 s for PEI nanofoams produced by Miller and Kumar (2009) with p_{sat} = 5 MPa are plotted as function of T_f/T_g^0 ($T_g^0 \approx 210$ °C for PEI). There is a mismatch between the predicted and measured porosity versus normalised foaming temperature curves for $T_f/T_g^0 < 0.95$, which may be attributed to the invalidity of the assumption that the predicted porosity values for the high M_w PMMA nanofoams may be compared with those for the PEI nanofoams[8]. Remarkably, however, the highest measured and predicted value of porosity of the PEI nanofoams is close to 0.6 at T_f/T_g^0 just below unity. Based on the predicted f versus T_f/T_g^0 curves at elevated values of the saturation pressure (p_{sat} = 15 MPa and p_{sat} = 25 MPa), it is hypothesised that PEI nanofoams of $f > 0.6$ may be produced by employing a saturation pressures well above 5 MPa.

Based on the cell wall failure analysis detailed in Section 5.2, it is expected that the maximum achievable porosity f_c for the PEI nanofoams (attained by using a sufficiently high value of p_{sat}) is governed by a minimum value of cell wall thickness h_c, as predicted by Eq. 5.34. The value of h_c is close to the estimated end-to-end distance of the individual polymer chains and may depend on the nature of the polymer too. To illustrate, Eq. 5.31 is re-written as:

$$f = \left(\frac{h}{l} + 1\right)^{-3} \tag{5.37}$$

The value of f_c is predicted via Eq. 5.37 as a function of void size l for a given value of minimum ligament thickness h_c. Predicted f_c versus l curves for selected values of h_c may be superimposed on the f versus l map shown in Fig. 2.2; this is done in Fig. 5.8. To produce nanofoams of $f > 0.85$ and $l < 200$ nm, h_c has to be close to 5 nm. Assuming an individual polymer chain diameter close to 0.5 nm (Roiter and Minko, 2005), the condition h_c = 5 nm would correspond to a minimum of 10 aligned polymer chains separating the void to prevent rupture of the cell wall.

[8] Differences between PMMA and PEI nanofoams may include: (i) the fitted equations for the constitutive description of the linear, amorphous PEI (of unkown molecular weight) close to the glass transition temperature may differ from those assumed for the high M_w PMMA, (ii) the solubility of CO_2 into PEI differs from CO_2 into PMMA, (iii) the dependence of T_g/T_g^0 upon CO_2 concentration for PEI may differ from that of PMMA, (iv) the assumed temperature time profile for the PEI nanofoaming experiments may be different than the one assumed for the PMMA nanofoaming experiments, and (v) the assumption that N_d is independent of p_{sat}. For accurate void growth predictions for solid-state nanofoaming of PEI one has to (i) have information about the nucleated state of the material prior to void growth by conducting a series of foaming experiments and (ii) calibrate the governing equations of the void growth model as done for the two PMMA grades in Chapter 3 to 5.

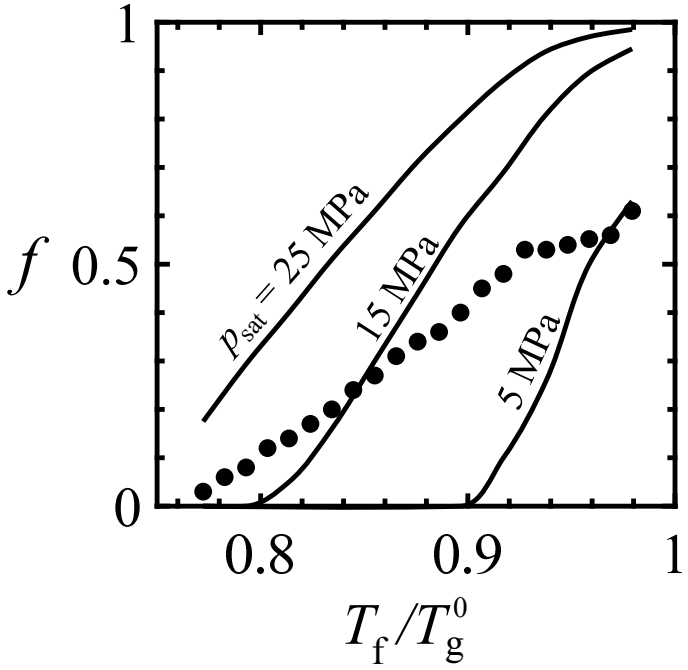

Figure 5.7 Foaming diagram in which the predicted porosity f at t_f = 150 s is plotted as a function of normalised foaming temperature T_f/T_g^0 for the high M_w PMMA nanofoams for selected values of the saturation pressure (solid lines). The measured values for the porosity of PEI nanofoams (p_{sat} = 5 MPa) at t_f = 150 s as reported by Miller and Kumar (2009) are plotted as a function of T_f/T_g^0. The experimental data points reported by Miller and Kumar (2009) are plotted with filled circle markers.

This level of confinement might be too high for conventional, linear amorphous polymers, and this may explain why polymeric nanofoams of $f > 0.85$ and $l < 200$ nm produced via solid-state foaming have not been reported so far.

It is concluded that, in theory, solid-state foaming may be used to produce nanofoams of $f > 0.85$ and $l < 200$ nm when two necessary conditions are fulfilled. The first condition requires a cell nucleation density close to or above 10^{21} m^{-3}. As detailed above, there are many experimental studies, using a wide range of polymeric precursor materials and nucleation strategies, reporting on the production of nanofoams with $N_d \approx 10^{21}$ m^{-3}. The second condition requires a polymeric precursor material allowing a minimum cell wall thickness close to 5 nm to prevent rupture of the cell walls separating the nano-sized voids. Experimental studies, such as those by Bay et al. (2018), complemented by numerical analyses (i.e. molecular dynamics simulations) may be useful to identify appropriate polymeric precursor material systems which would allow a minimum

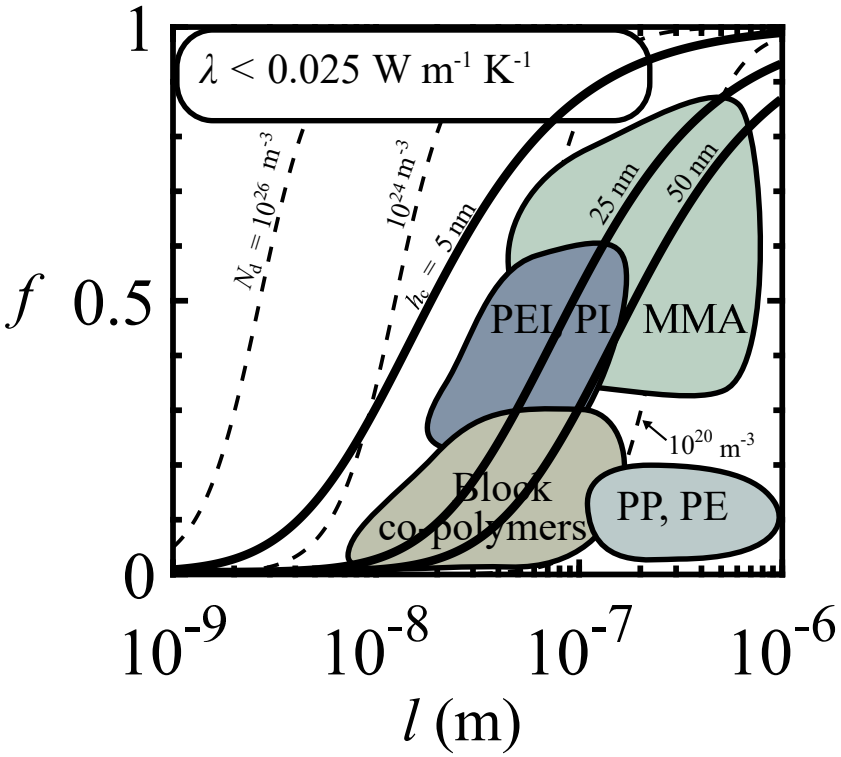

Figure 5.8 The porosity f versus void size l map shown in Fig. 2.2 with superimposed critical porosity f_c curves predicted via Eq. 5.37 for selected values of h_c (solid lines). The nucleation density contours via Eq. 2.2 for selected values of N_d are included (dashed lines).

ligament length in the order of 5 to 10 nm.

5.4 Concluding remarks

A void growth model has been developed to simulate cavity expansion during solid-state nanofoaming of PMMA by CO_2. Experimentally calibrated constitutive laws for the PMMA grades close to the glass transition temperature are used in the simulations. The effect of dissolved CO_2 is accounted for by a shift in the glass transition temperature of the PMMA. Diffusion of CO_2 within the PMMA matrix is sufficiently rapid for the concentration of CO_2 to remain almost uniform spatially.

The predicted porosity versus foaming time curves, at selected foaming temperatures, are in good agreement with those measured, as reported in Section 4.2, for porosities well below the maximum observed porosity. There is also close agreement between the predicted and observed sensitivity to molecular weight. This suggests that the observed difference in constitutive response close to the glass transition between the two PMMA grades leads to the measured difference in porosity. Moreover, cell wall tearing accounts for the observed limit in final porosity. The existence of a limiting minimum cell wall thickness of magnitude close to that of the end-to-end distance of the polymer chains is suggested. When the cell wall thickness approaches this minimum value during foaming, rupture of the cell walls occurs; this leads to an open-celled structure, and to a limit on foam expansion.

The void growth model may be used to construct foaming diagrams (i.e. porosity as a function of foaming temperature and saturation pressure) for a given combination of polymer precursor and blowing agent, given the governing equations are calibrated to the polymer-blowing agent system (and sufficient information about the nucleated state of the material prior to the growth phase is known). The practical foaming window, however, is constrained by tearing of the cell walls separating the nano-sized voids. The analysis in this chapter suggests that a polymer-blowing agent system that allows to produce nanofoams with a cell nucleation density close to or above 10^{21} m^{-3}, may be used to produce nanofoams with a thermal conductivity lower than that of air (i.e. with porosity above 0.85 and average void size below 200 nm), provided that the minimum cell wall thickness to prevent cell wall tearing is in the order of 5 nm.

Part II

Tensile fracture of an adhesive layer

Chapter 6

Case study: failure of an MMA adhesive layer in a butt joint from pre-existing voids

An introductory experimental case study is presented on the fracture of a methyl methacrylate (MMA) adhesive layer from pre-existing voids. First, uniaxial tensile tests and single edge notch bending tests are conducted to characterise the bulk properties of the MMA adhesive. Second, tensile tests are conducted on butt joints comprising an MMA adhesive layer and two aluminium alloy substrates. Emphasis is placed on the dependence of the tensile strength of the joint upon void content, layer height, and joint width.

6.1 Materials and methods

6.1.1 Adhesive material

Butt joint specimens are manufactured using a two-component MMA adhesive[1]. The adhesive component contains a mixture of methyl methacrylate (MMA), methacrylic acid (MAA), and elastomeric and metallic toughening particles. The activating component is based on benzoyl peroxide. The adhesive and activator component are mixed by a 10 to 1 volume ratio according to the manufacturer's recommendation (Scigrip Europe, 2017); the adhesive mixture is cured via an exothermic reaction at room temperature.

[1] Methyl methacrylate adhesive SG300-40 acquired from Scigrip (UK).

6.1.2 Uniaxial tensile tests

Dogbone specimens with the MMA adhesive were produced using a custom polytetrafluoroethylene (PTFE) mould. The geometry of the dogbones with nominal thickness t equal to 4.3 mm is defined in Fig. 6.1a. A manual applicator gun was used with a static-mixing nozzle to fill the mould with the uncured adhesive mixture. Excess adhesive was removed with a PFTE strip to smoothen the top surface. The specimens were cured at room temperature for at least one week prior to testing.

Uniaxial tensile tests were conducted at room temperature with the dogbone specimens on a screw-driven test bench[2]. The tensile load was measured by the machine's load cell and the relative displacement of the material in the gauge area was measured via a laser extensometer[3]; the gauge length is equal to 25 mm. Tests were performed for cross-head velocities equal to v_{ch} = 0.027 mm s^{-1} and v_{ch} = 0.27 mm s^{-1}, corresponding to nominal strain rates equal to $\dot{e} = 10^{-3}$ s^{-1} and $\dot{e} = 10^{-2}$ s^{-1}, respectively. Three tensile tests were conducted per strain rate. The specimens fractured in the gauge area and the resulting fracture surfaces were examined with an optical and a scanning electron microscope (SEM).

6.1.3 Fracture toughness tests

Single edge notch bending (SENB) specimens were manufactured with the MMA adhesive using a PFTE mould according to the method detailed above. The dimensions of the SENB specimens are in agreement with the ASTM D5045 standard, see Fig. 6.1b (ASTM, 2014). An initial notch of length equal to 6 mm was made with a saw. A sharp pre-crack of length close to 1.5 mm was made at the end of the sawed notch by tapping with a razor blade such that the initial notch length a_0 is close to 7.5 mm.

Fracture tests were performed at room temperature on a screw-driven test bench at a cross-head displacement equal to 0.167 mm s^{-1}. The crack length a (= a_0 + Δa), where Δa is the length of

[2] Instron 5500R-6025 test bench (USA).
[3] LE-05 Electronic Instrument Research laser extensometer (USA).

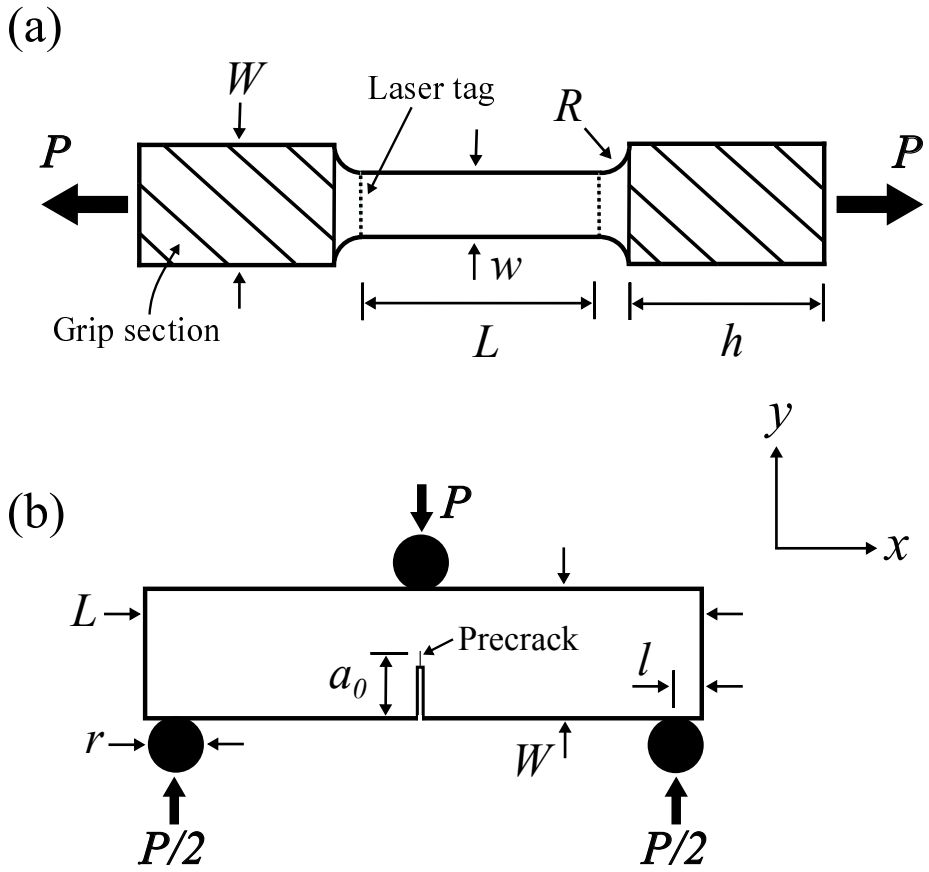

Figure 6.1 Plan view of (a) the dogbone tensile specimen of nominal thickness t = 4.3 mm, L = 27 mm, W = 14 mm, h = 22.4 mm, w = 6.3 mm, R = 3.5 mm and (b) the single edge notch bending (SENB) specimen of thickness t = 3.6 mm, L = 67.5 mm, l = 4 mm, W = 15 mm, and $a_0 \approx 7.5$ mm. The radius r of the cylindrical supporting rollers and indenter is equal to 4 mm.

the grown crack during the bending test, was monitored with a traveling microscope and loading-unloading cycles were conducted at different stages prior to ($\Delta a = 0$) and during crack growth ($\Delta a > 0$). The SENB test was terminated when the observed crack length is close to $0.25 b_0$, where b_0 is the nominal length of the ligament (= W - a_0) as prescribed in the ASTM D5045 standard. The indentation load P was measured by the load cell of the test bench. The displacement u of the indenter was measured via a laser extensometer. The J-integral value J was measured as a function of crack growth Δa according to the ASTM E1820-18 standard (ASTM, 2015b). The elastic component J_e of the J-integral at a given observed crack length a is obtained via:

$$J_e = \frac{(1-\nu^2)(L-2l)^2 F^2 P^2}{t^2 W^3 E} \tag{6.1}$$

where t is the thickness of the SENB specimen, E the Young's modulus of the adhesive, ν the Poisson's ratio of the adhesive, and $F(a/W)$ a finite width correction factor:

$$F = \frac{3\left(\frac{a}{W}\right)^{\frac{1}{2}}\left[1.99 - \left(\frac{a}{W}\right)\left(1-\frac{a}{W}\right)\left(2.15 - 3.93\frac{a}{W} + 2.7\left(\frac{a}{W}\right)^2\right)\right]}{2\left(1+2\frac{a}{W}\right)\left(1-\frac{a}{W}\right)^{\frac{3}{2}}} \tag{6.2}$$

The plastic component J_p is measured via (ASTM, 2015b):

$$J_\mathrm{p} = \frac{1.9A_\mathrm{p}}{t(W-a_0)} \tag{6.3}$$

where $A_\mathrm{p}(a/W)$ is the plastic part of the area under the load P versus indenter displacement u curve. The measured value for J as a function of crack growth length Δa is then calculated by use of Eqs. 6.1 and 6.3:

$$J = J_\mathrm{e} + J_\mathrm{p} \tag{6.4}$$

6.1.4 Butt joint tests

Butt joint specimens with circular cross-sections were manufactured by bonding two aluminium alloy (grade 6082) adherends to each other with the MMA adhesive. The geometry of the butt joint is detailed in Fig. 6.2. The joints were made as follows. The adhesion surface of the aluminium alloy adherends was manually polished using 60 grit emery paper. The surfaces were subsequently cleaned and degreased with acetone. An excess amount of adhesive was injected in the bond gap, the adhesive layer height $2h$ was adjusted by placing the adherends into a custom-made rig. The adhesive was allowed to cure for at least a week before the excess adhesive was machined from the joint.

The tensile response of butt joints with four different geometries was measured, see Table 6.1. A shape factor κ was introduced to quantify the level of constraint by the substrates on the adhesive layer. The value for κ is equal to the ratio of the loaded cross-sectional area of the joint and the area of the free surfaces of the adhesive layer (Hattori and Takei, 1950). For the butt joint geometry defined in Fig. 6.2, κ reads:

$$\kappa = \frac{r}{4h} \tag{6.5}$$

Void growth in the constrained adhesive layer was observed during the curing stage. The voids result from entrapped air during the application of the adhesive, and are thought to grow during the curing stage due to shrinkage of the MMA adhesive. The distribution and size of the voids was quantified using computed tomography (CT) imaging for a selected number of butt joints prior to testing. The butt joints were mounted in a screw-driven mechanical test bench by pins and loaded in tension at room temperature. The relative displacement Δu between the two adhesive-adherend interfaces was measured during the tensile test with a clip gauge. The tensile load P was monitored by the machine's load cell. A global nominal strain measure e for the material elements in the adhesive layer is defined as:

$$e = \frac{\Delta u}{2h} \tag{6.6}$$

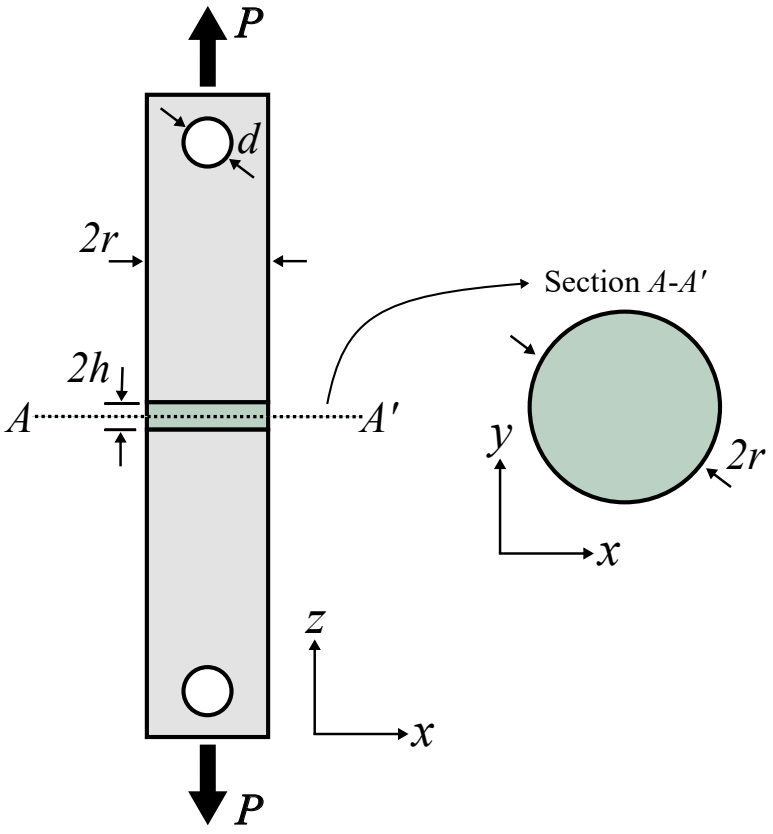

Figure 6.2 The geometry of the butt joint of radius r, adhesive layer height $2h$, and hole diameter d = 13.4 mm for Geometry I to III and d = 10.6 mm for Geometry IV (see Table 6.1).

and the nominal stress σ^{∞} reads:

$$\sigma^{\infty} = \frac{P}{\pi r^2} \tag{6.7}$$

The cross-head speed v_{ch} of the test bench was adjusted to the nominal adhesive layer height of the joint, such that the normalised displacement rate $v_{\mathrm{ch}}/2h$ is equal to 10^{-2} s^{-1} for all joint geometries. Tensile tests were conducted until failure of the joints is observed, the failure surfaces were examined with an optical microscope.

Table 6.1 The explored butt joint geometries in terms of shape factor κ, cross-sectional radius r, and adhesive layer half-height h.

Geometry	κ	r (mm)	h (mm)
I	1	20	5
II	2	20	2.5
III	10	20	0.5
IV	1	10	2.5

6.2 Results and discussion

6.2.1 Uniaxial tensile response

A selection of the measured nominal stress S versus nominal strain e curves obtained via uniaxial tensile tests on the MMA adhesive is shown in Fig. 8.3a. The S-e response is elastic-plastic and sensitive to strain rate. The measured values for the Young's modulus[4] E, the yield strength[5] σ_{y}, and the nominal tensile failure strain e_{f} are reported in Table 6.2 for the two nominal strain rates and compared with the manufacturer's reported values for E, σ_{y}, and e_{f} (Scigrip Europe, 2017). The measured values of E and σ_{y} are close to those reported by the manufacturer, whereas the tensile ductility of the MMA adhesive was found to be significantly lower. An SEM micrograph of the failure surface of a dogbone specimen (deformed at $\dot{e} = 10^{-2}$ s^{-1}) is shown in Fig. 6.3b. Ruptured elastomeric particles are observed. The size of the particles ranges from close to 5 µm to 100 µm and the particles are found to be evenly distributed within the MMA matrix.

[4] The value for the Young's modulus is based on the slope of the initial linear part of the S-e curve.
[5] The yield strength corresponds to the plateau value for S subsequent to the initial elastic regime of the S-e curve.

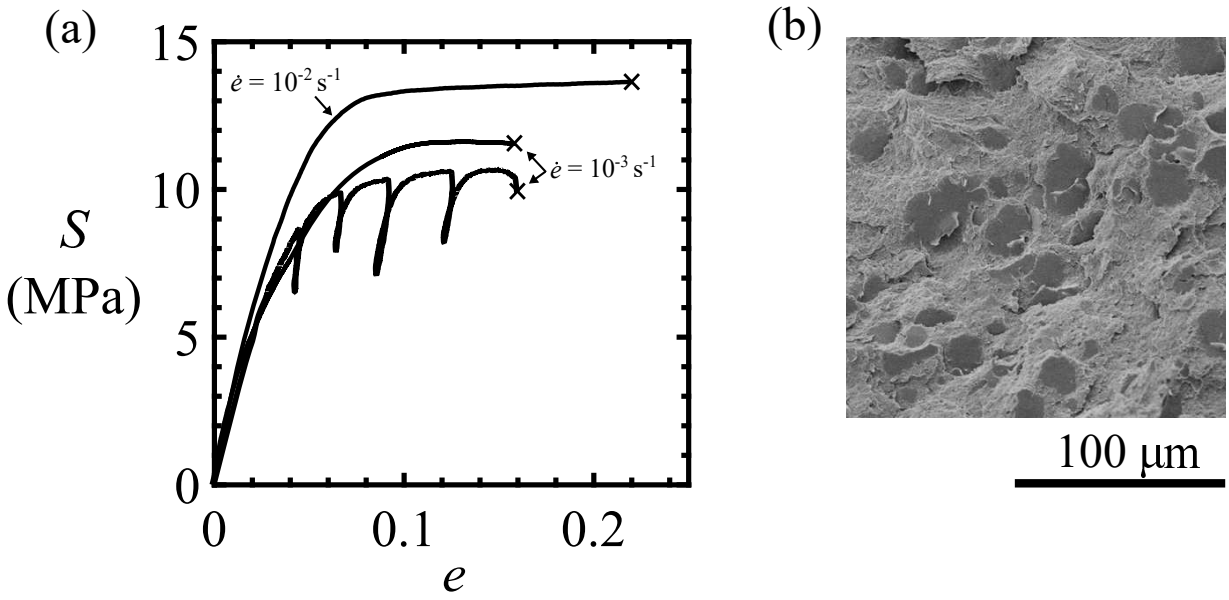

Figure 6.3 Results of the uniaxial tensile tests on the MMA adhesive. (a) measured nominal stress S versus nominal strain e curves in uniaxial tension for a nominal strain rate equal to $\dot{e} = 10^{-3}$ s^{-1} and $\dot{e} = 10^{-2}$ s^{-1}. An additional S versus e curve for $\dot{e} = 10^{-3}$ s^{-1} with a series of loading-unloading cycles is shown too. A cross at the end of the S-e curve denotes specimen failure. (b) SEM micrograph of the dogbone specimen's failure surface (for $\dot{e} = 10^{-2}$ s^{-1}) showing ruptured elastomeric particles.

Table 6.2 The measured Young's modulus E, yield strength σ_y, and nominal tensile failure strain e_f of the MMA adhesive in uniaxial tension. The average values for E, σ_y, and e_f are based on three tensile tests per strain rate. The reported values for E, σ_y, and e_f by the manufacturer (measured at an unspecified nominal strain rate) are included (Scigrip Europe, 2017).

$\dot{e}$ (s^{-1})	E (MPa)	σ_y (MPa)	e_f	Source
10^{-3}	263	10.9	0.16	This work
10^{-2}	311	12.9	0.2	This work
Unknown	207-276	12-15	0.4-0.6	Manufacturer

6.2.2 Single edge notch bending measurements

The measured indentation load P versus indenter displacement u response during a SENB test is shown in Fig. 6.4. Four stages of crack growth and process zone development are identified on the P-u curve. Images from the surface of the loaded SENB specimen at each of these four stages are included in Fig. 6.4, the corresponding location on the P-u curve is shown too. No crack growth or development of a process zone on the travelling microscope image is observed during the initial part of the linear, elastic regime of the P-u curve as shown on the image for position 'A'. A process zone is observed at the tip of the pre-crack on the surface of the SENB specimen at the onset of the non-linear part of the P-u curve, see the image corresponding to position 'B'. Crack growth is observed close to the peak value of P as shown on the position 'C' image. Beyond the peak value of P, the crack continues to grow and the process zone length reaches a steady-state value. The steady-state value[6] of the process zone at the surface of the specimen is close to 1.2 mm when the crack growth length exeeds 0.5 mm, see the image corresponding to position 'D'.

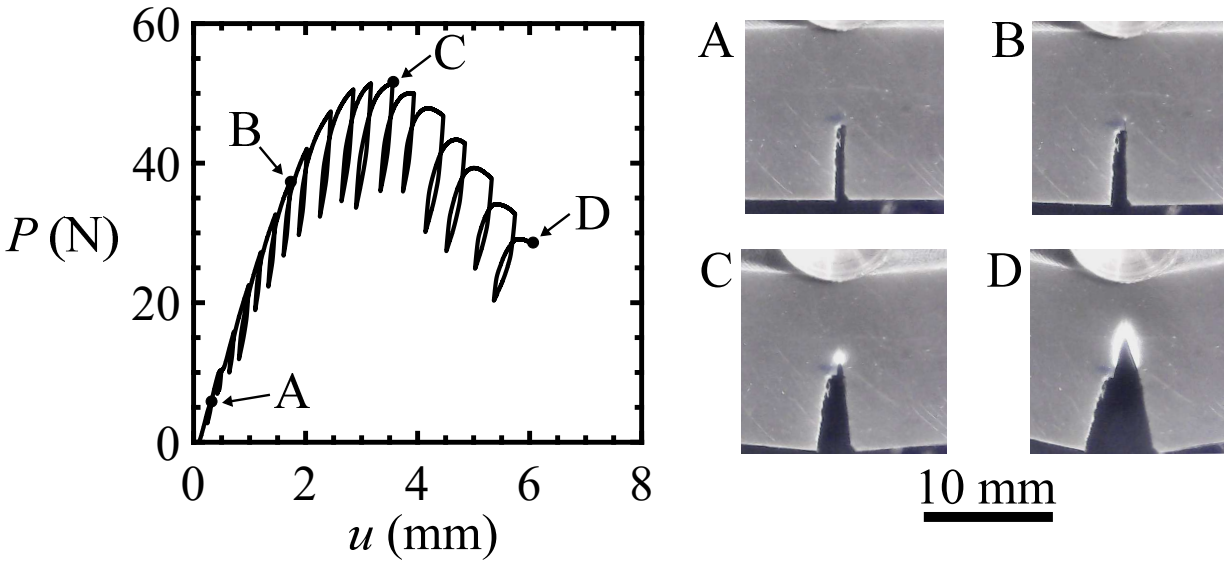

Figure 6.4 The measured indentation load P versus indenter displacement u and images of the crack tip process zone and the growing crack at the surface of the SENB specimen during different stages of the SENB test.

[6] Note that the reported value of l_S is the average of the measured process lengths on the surface of the SENB specimens for $\Delta a > 0.5$ mm based on two SENB tests.

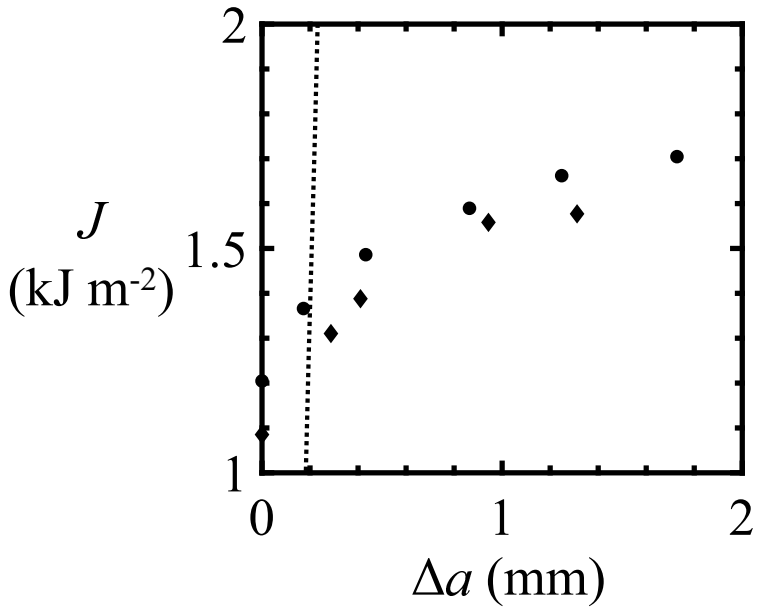

Figure 6.5 The measured J versus crack growth Δa (=a - a_0) resistance curves for two SENB tests on the MMA adhesive. A dashed crack tip blunting offset line is plotted via Eq. 6.8.

A crack growth resistance curve of the MMA adhesive is obtained by measuring the crack length on the surface of the SENB specimen based on the images of the travelling microscope and by computing J at each crack length measurement via Eq. 6.4. The Young's modulus E is assumed to equal 311 MPa, see Table 6.2, and the Poisson's ratio ν is taken as 0.38 (Moller et al., 2015). The measured J versus crack growth Δa resistance curves (or R-curves) based on two SENB tests are shown in Fig. 6.5. Moderate R-curve behaviour is observed for the MMA adhesive. To account for initial crack tip blunting, a 0.15 mm offset line is drawn on Fig. 6.5 (ASTM, 2015b; Anderson, 2005):

$$J = 2(\Delta a - 1.5 \times 10^{-4})\sigma_y \tag{6.8}$$

where σ_y is assumed to equal 12.9 MPa, see Table 6.2. The critical mode I energy release rate of the MMA adhesive $G_c^0 = J_c^0$, can be estimated via the intersection point of Eq. 6.8 and the measured J versus Δa curve of the MMA adhesive: $G_c^0 \approx 1.32$ kJ m^{-2}. The value of the process zone length l_S is estimated via (Anderson, 2005):

$$l_S = \frac{EG_c^0}{\pi(1-\nu^2)\sigma_y^2} \tag{6.9}$$

where it is assumed that the critical stress to trigger non-linear deformation at the crack tip corresponds to the uniaxial tensile yield strength σ_y. Taking E = 311 MPa, ν = 0.38 and σ_y = 12.9 MPa, l_S is estimated to equal 0.9 mm, reasonably close to the observed value of $l_S \approx 1.2$ mm based on the images taken of the surface of the SENB specimen by the travelling microscope.

A steady-state value of J is attained ($G_c^{ss} = J^{ss} \approx 1.6$ kJ m^{-2}) when the crack has grown to close to 1 mm. The observed R-curve behaviour of the MMA adhesive may be attributed to non-linear, irreversible deformation of material when going through the process zone into the wake of the growing crack, see Fig. 6.4. This mechanism has been discussed in Section 2.2.1 for rubber-modified epoxies, which typically exhibit much more pronounced R-curves, i.e. G_c^{ss}/G_c^0 in the range of 2 to 10 (Du et al., 1998, 2000; Imanaka et al., 2015).

6.2.3 Tensile strength of the butt joints

The nominal remote tensile stress σ^∞ of the MMA-aluminium alloy butt joint shown in Fig. 6.2 is plotted as a function of nominal tensile strain e for a normalised displacement rate $v_{ch}/2h = 10^{-2}$ s^{-1} in Fig. 6.6. The σ^∞ versus e curves for the Geometry II and III butt joints are shown in Fig. 6.6a, whereas the σ^∞-e curves of the Geometry I and IV butt joints are shown in Fig. 6.6b, see Table 6.1. The measured S-e curve for the MMA adhesive in uniaxial tension for $\dot{e} = 10^{-2}$ s^{-1} is included in Figs. 6.6a and 6.6b.

The butt joints failed by cohesive failure. The nominal tensile strain at failure e_f of the joints was found to be subject to scatter and ranges from e_f = 0.01 to 0.05. The values for e_f are lower than the observed value for the tensile ductility of the MMA adhesive (e_f^0 = 0.2, see Table 6.2) and the tensile ductility reported by the manufacturer (see Table 6.2). The observed reduction in failure strain may be caused by the presence of voids in the adhesive layer. These voids are thought to originate from entrapped air bubbles during the application of the adhesive. Further void growth may be induced by shrinkage of the adhesive during the curing process.

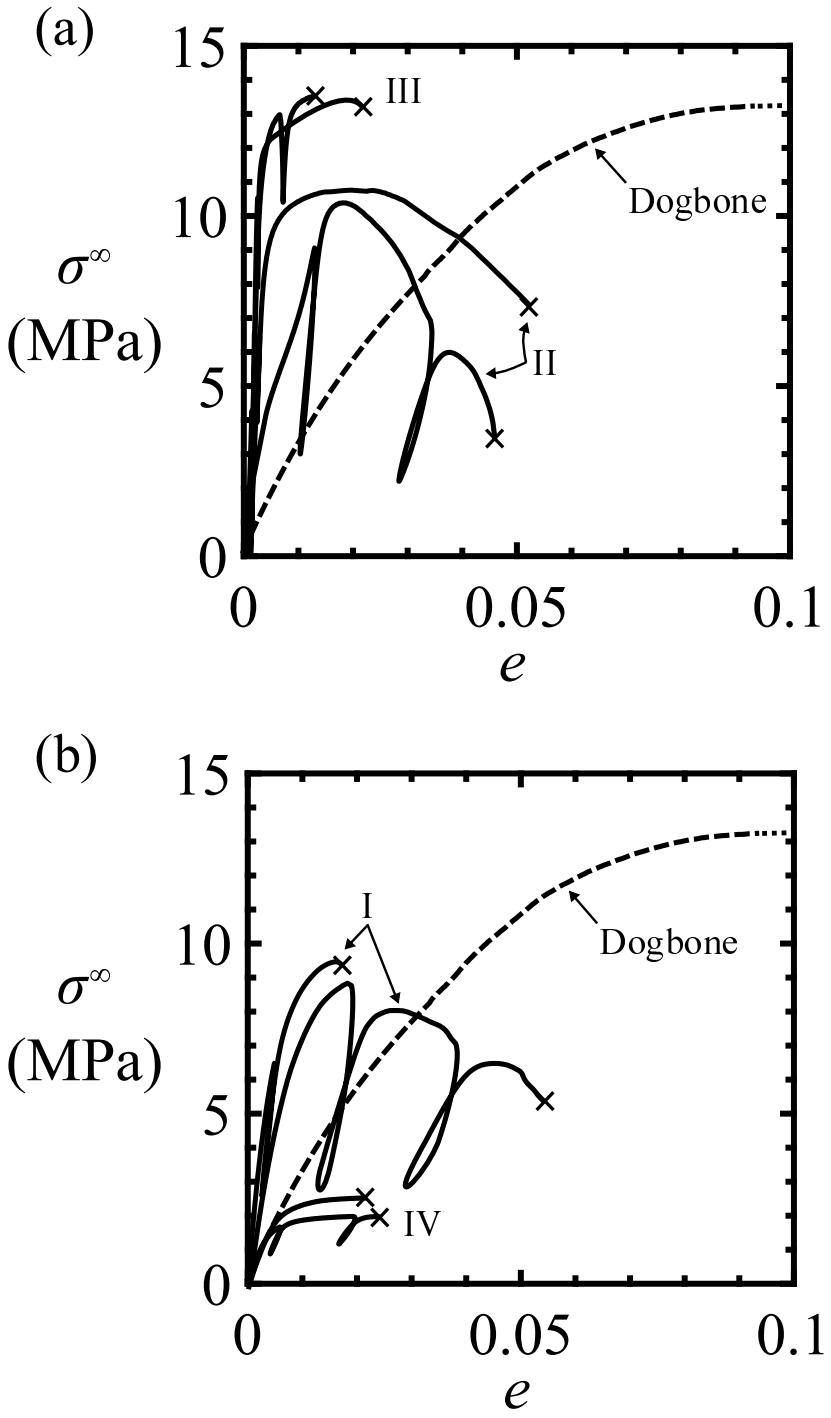

Figure 6.6 Nominal stress σ^∞ versus nominal strain e for the butt joints in uniaxial tension for a normalised displacement rate $v_{ch}/2h = 10^{-2}$ s^{-1} for (a) the Geometry II and III and (b) the Geometry I and Geometry IV butt joints. The σ^∞-e response of a repeat test with a series of loading-unloading cycles is shown for each geometry. A cross at the end of the curve denotes specimen failure. The measured S-e response of the MMA dogbone in uniaxial tension for $\dot{e} = 10^{-2}$ s^{-1} is included.

The distribution and size of the voids in the adhesive layer was examined by CT prior to the tensile tests for a selected number of butt joints. An example of a cross-sectional CT image of the adhesive layer (at the adhesive layer mid-height plane) of a Geometry IV butt joint is shown in Fig. 6.7a. The failure surfaces of the tested butt joints were examined with an optical microscope, see Fig. 6.7b. Comparison of the optical images of the failure surface and the CT images suggested that there was no void growth in the adhesive layer during the tensile tests. The total surface area of the voids A_f is measured based on the optical images of the failure surfaces.

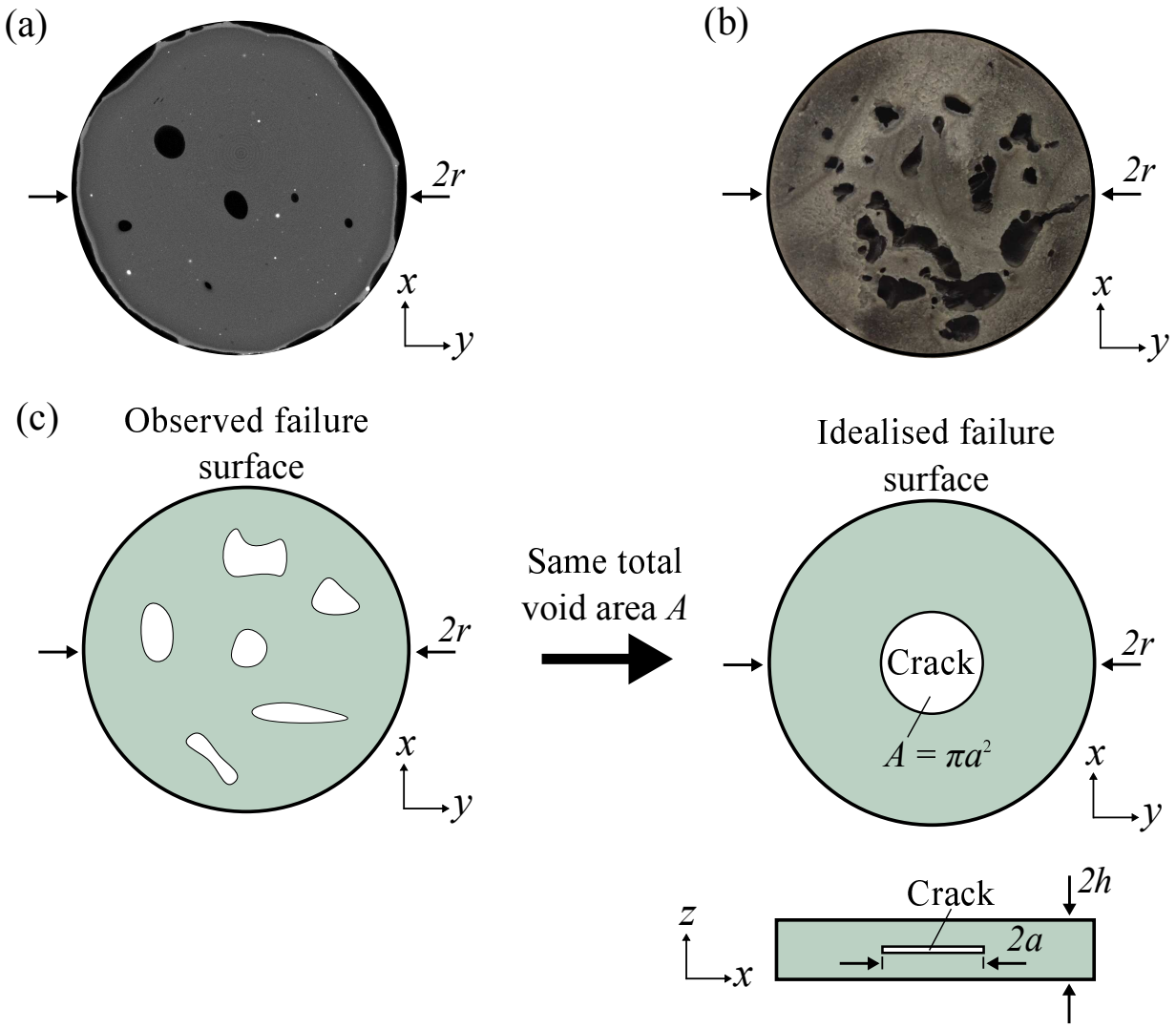

Figure 6.7 Void size and distribution analysis: (a) computed tomography image of the cross-section of the adhesive layer in the undeformed state (Geometry IV butt joint, r = 10 mm), (b) optical image of the failure surface of a failed butt joint (Geometry I, r = 20 mm), (c) sketch illustrating the idealisation of the cluster of voids on the failure surface (observed with an optical microscope) as one penny-shaped circular crack of A_f equal to the sum of the measured areas of the individual observed voids on the failure surface.

The cluster of voids on the failure surface is idealised as one penny-shaped circular crack of radius a and area A_f:

$$a = \left(\frac{A_f}{\pi}\right)^{\frac{1}{2}} \tag{6.10}$$

This idealisation is sketched in Fig. 6.7c.

The normalised ductility of the butt joint e_f/e_f^0, the apparent modulus E/E^0 of the butt joint, where E corresponds to the slope of the initial linear part of the measured σ^∞-e curves of the butt joints in tension and E^0 (= 311 MPa) is the measured Young's modulus of the adhesive (see Table 6.2), and the normalised failure strength σ_f^∞/σ_y, where σ_f^∞ is the measured nominal failure strength of the joint and σ_y (= 12.9 MPa) the measured tensile yield strength of the adhesive (see Table 6.2), are reported in Table 6.3 for one tensile test per butt joint geometry. The normalised estimated process zone length of the bulk adhesive l_S/h and the measured normalised idealised void radius a/h are included in Table 6.3. The normalised apparent modulus E/E^0 of the butt joint is found to increase with increasing level of constraint, i.e. with an increasing value for the shape factor κ. A failure map is constructed in which σ_f^∞/σ_y is plotted as a function of a/h for each joint geometry based on the values reported in Table 6.3, see Fig. 6.8. A theoretical framework is developed in the next chapter with the aim to predict σ_f^∞/σ_y as a function of the normalised void size a/h, the normalised process zone length of the adhesive l_S/h, and the joint width h/r for a given modulus mismatch ratio E_2/E_1, where E_1 is the Young's modulus of the substrate material and E_2 is the Young's modulus of the adhesive material.

Table 6.3 Results of the tensile tests on the MMA-aluminium alloy butt joints. The measured normalised failure strain e_f/e_f^0, the measured normalised apparent modulus E/E^0, the measured normalised remote strength σ_y^∞/σ_y, the normalised process zone length of the unconstrained, bulk adhesive l_S/h, and the normalised idealised void radius a/h are reported for one test per geometry (see Table 6.1).

Geometry	κ	e_f/e_f^0	E/E^0	σ_f^∞/σ_y	l_S/h	a/h
I	1	0.1	3.2	0.72	0.18	1.4
II	2	0.25	6.4	0.81	0.36	2.5
III	10	0.1	20.1	0.99	1.82	8.4
IV	1	0.1	1.0	0.17	0.36	2.6

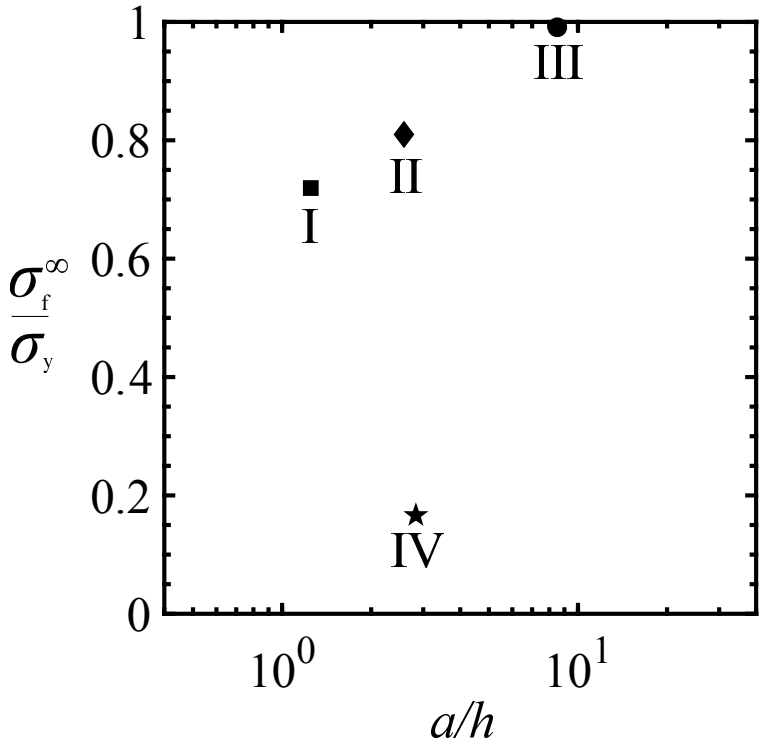

Figure 6.8 The normalised failure strength σ_f^∞/σ_y as a function of the observed normalised idealised void size a/h for the four MMA-aluminium alloy butt joint geometries explored in this study, see Tables 6.1 and 6.3.

6.3 Concluding remarks

The bulk properties of a methyl methacrylate adhesive are measured via a series of uniaxial tensile tests and single edge notch bending (SENB) tests. A mild strain rate sensitivity is observed for the measured elastic-plastic tensile stress versus tensile strain response. For a nominal strain rate equal to $\dot{e} = 10^{-2}$ s^{-1}, the Young's modulus E is found to be close to 311 MPa and the tensile yield strength σ_y is close to 12.9 MPa. A mild crack growth resistance curve is observed on the measured J versus crack growth Δa response via the SENB tests: the toughness G_c^0 at crack initiation is estimated to be close to 1.3 kJ m^{-2}, while the steady-state (crack length independent) value of G_c^{ss} is close to 1.6 kJ m^{-2}. The length of the process zone l_S at the tip of a crack in an unconstrained volume of adhesive material is estimated to be equal to 0.9 mm.

Tensile butt joints comprising two aluminium alloy cylindrical substrates and a layer of methyl methacrylate adhesive are manufactured. The level of constraint of the adhesive layer is varied by

making joints of different adhesive layer heights. The distribution and the size of voids present in the adhesive layer after curing are quantified via computed tomography and via optical images of the failure surfaces after testing. The measured tensile ductility of the adhesive layer in the butt joints was found to be significantly lower than the tensile ductility obtained via the uniaxial tensile tests on the methyl methacrylate dogbones. In addition, the normalised failure strength failure strength σ_f^∞/σ_y, where σ_f^∞ is the nominal failure strength of the butt joint and σ_y the uniaxial tensile yield strength of the adhesive, is found to be sensitive to geometry of the joint and to the normalised area of voids on the fracture surface. An analytical framework is developed in the next chapter to predict the dependence of the normalised failure strength of the butt joint upon crack or void size.

Chapter 7

Prediction of the tensile strength of a centre-cracked adhesive joint

The tensile strength of an adhesive joint is predicted for a centre-cracked elastic layer, sandwiched between elastic substrates, and subjected to a remote tensile stress. A tensile cohesive plastic zone, of Dugdale type, is placed at each crack tip, and the cohesive zone is characterised by a finite strength and a finite toughness. An analytical theory of the fracture strength is developed to determine the macroscopic strength of the adhesive joint as a function of the relative magnitude of crack length, layer thickness, plastic zone size, specimen width and elastic modulus mismatch between layer and substrates. Fracture maps are constructed to reveal competing regimes of behaviour. The maps span the full range of behaviour from a perfectly brittle response (with no crack tip plasticity) to full plastic collapse. Finite element calculations are conducted to verify the developed analytical framework.

7.1 Introduction

The tensile strength of an adhesive joint is predicted for the geometry of a centre-cracked elastic layer of height $2h$, sandwiched between elastic substrates, and subjected to remote tensile stress σ^{∞}, as shown in Fig. 7.1. The idealisation of the adhesive by a linear, elastic solid of Young's modulus E_2, which differs from the value E_1 for the substrates, allows for the role of material mismatch upon the stress state (and fracture strength) to be explored. Initially, the crack, of length $2a$, is treated as a Griffith crack of finite crack tip toughness Γ but with no cohesive zone.

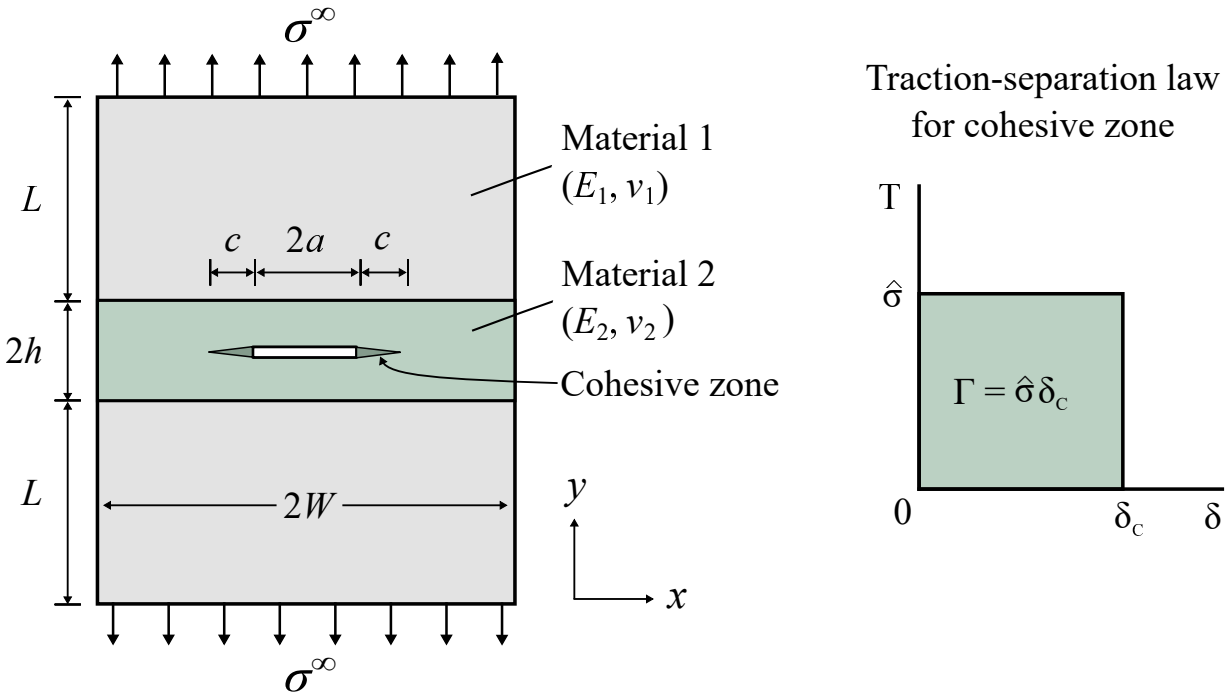

Figure 7.1 Cross-sectional view of a sandwich joint consisting of an adhesive layer of thickness $2h$, with a through-thickness crack of length $2a$, and loaded by a remote tensile stress σ^∞. The traction-separation law for the cohesive zone in the adhesive is shown on the right, and results in a cohesive zone of length c at the crack tip.

Subsequently, a tensile cohesive plastic zone is placed at each crack tip, and the cohesive zone is characterised by a finite strength $\hat{\sigma}$ and a finite toughness Γ. This two-parameter description ($\hat{\sigma}$, Γ) allows for a prediction of failure strength over a wide range of crack length.

As reviewed in Section 2.2.2, the strength $\hat{\sigma}$ and toughness Γ of an adhesive layer may depend upon the thickness of the layer (Kinloch and Shaw, 1981; Hunston et al., 1989; Daghyani et al., 1995; Yan et al., 2001; Lee and Ramesh, 2004; Pardoen et al., 2005; Martiny et al., 2012) but the details of this dependence are beyond the scope of the present study. The pragmatic approach adopted here is to assume that values of $\hat{\sigma}$ and Γ have been measured for an adhesive layer of given thickness, and the aim of the study is to explore the sensitivity of the macroscopic strength upon the normalised crack length a/h and upon the material mismatch ratio E_2/E_1. Commonly, the measured value of $\hat{\sigma}$ is adequately approximated by the uniaxial tensile strength of the bulk adhesive (Blackman et al., 2003; Salomonsson and Andersson, 2008; Sun et al., 2008b,a; Carlberger and Stigh, 2010; Stigh et al., 2010) but it may depend upon the degree of plastic constraint (Varias et al., 1991). In addition, the magnitude of Γ will depend upon the degree of crack ex-

tension if the adhesive material displays a pronounced *R*-curve. However, polymeric adhesives commonly display a negligible *R*-curve particularly in the form of a thin layer between substrates (Tvergaard and Hutchinson, 1996). As detailed in Section 2.2.1, most common structural adhesives[1] such as unmodified or toughened epoxies, acrylic, and polyurethane adhesives exhibit typically flat or moderate ($\Gamma^0/\Gamma^{ss} < 1.5$) *R*-curves in bulk (Monteiro et al., 2015; Maloney and Fleck, 2018; Banea et al., 2014; Sekiguchi et al., 2017). Consequently, the effect of an *R*-curve on crack growth in an adhesive layer is ignored.

The semi-infinite crack in adhesive layer

Consider first the asymptotic problem of an elastic adhesive layer of height $2h$ sandwiched between two elastic substrates, and containing a semi-infinite crack, as shown in Fig. 7.2. The crack is placed along the mid-plane of the adhesive layer. Assume that the substrate (material 1) and the adhesive (material 2) are isotropic, homogeneous and linear elastic solids. The Young's modulus and Poisson's ratio of the substrate and adhesive are (E_1, ν_1) and (E_2, ν_2),

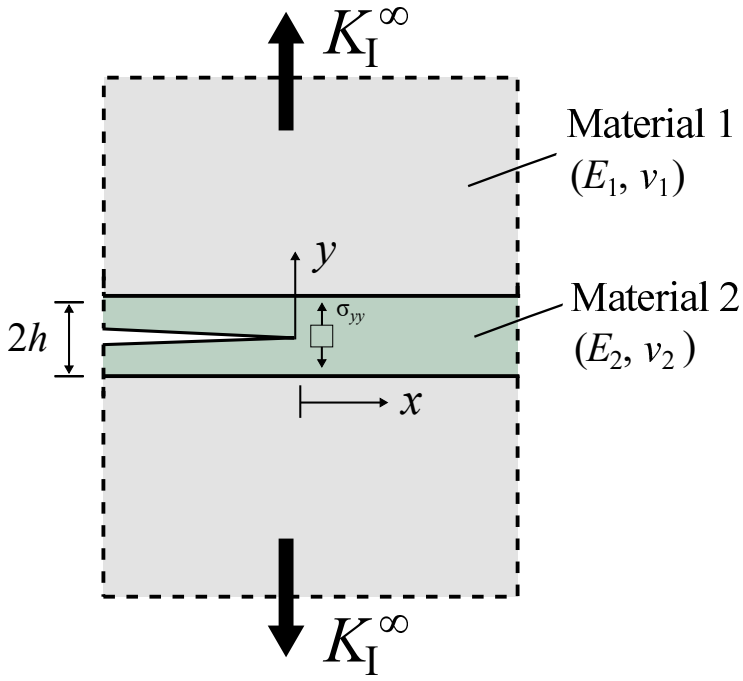

Figure 7.2 A linear, elastic adhesive layer (material 2) of height $2h$ is sandwiched between two linear, elastic substrates (material 1). A semi-infinite crack in the adhesive layer exists on the mid-plane of the adhesive layer, parallel to the interfaces. The joint is subjected to a remote mode I loading of magnitude K^∞.

[1] Rubber-modified epoxies are an exception as they may exhibit a pronounced *R*-curve in bulk, see Fig. 2.10 (Du et al., 1998; Imanaka et al., 2015).

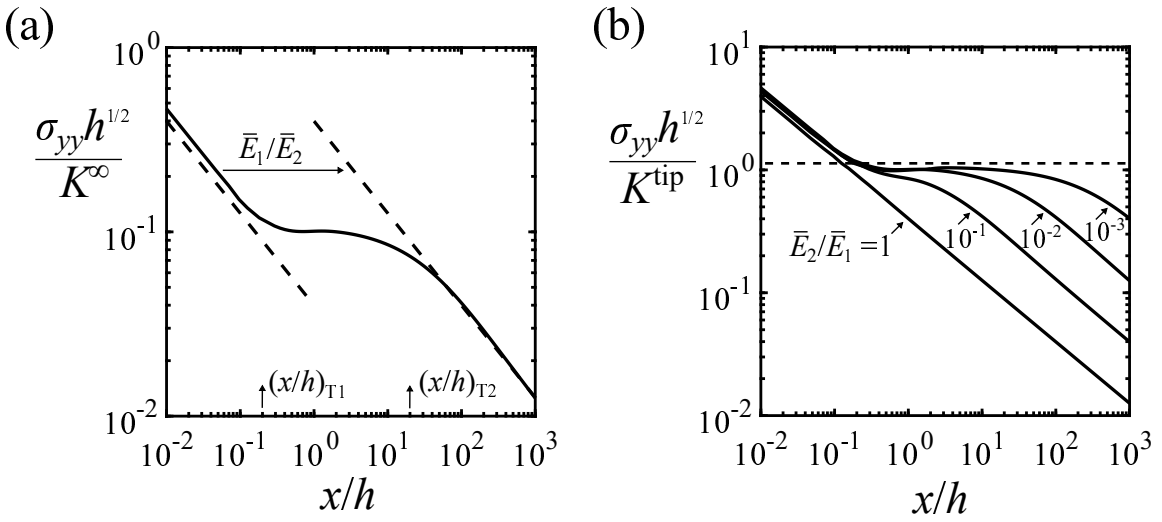

Figure 7.3 The tensile stress distribution directly ahead of a semi-infinite crack in a sandwich layer, see Fig. 7.2, for $\bar{\nu} = 3/7$: (a) tensile stress is normalised by K^{∞} for $\bar{E}_2/\bar{E}_1 = 10^{-2}$, the left and right asymptotes are plotted via Eqs. 7.2 and 7.3, respectively; (b) The tensile stress is normalised by K^{tip} with the horizontal asymptote predicted via Eq. 7.5.

respectively. A general, plane problem is considered in the present study, where $\bar{E}$ and $\bar{\nu}$ represent E and ν in plane stress, but $\bar{E} = E/(1-\nu^2)$ and $\bar{\nu} = \nu/(1-\nu)$ in plane strain. In this introductory problem under consideration, the adhesive joint is subjected to a remote mode-I K field of magnitude K^{∞}. The normal stress component σ_{yy}, perpendicular to the crack plane and directly ahead of the crack tip, has been calculated by finite element (FE) analysis, for selected values of the modulus-mismatch ratio $\bar{E}_2/\bar{E}_1$ and $\bar{\nu} = 3/7$; the details of this calculation are reported in Appendix A. The normalised stress component, $\sigma_{yy}\sqrt{h}/K^{\infty}$, is plotted in Fig. 7.3a as a function of normalised distance from the crack tip x/h for the representative case $\bar{E}_2/\bar{E}_1 = 10^{-2}$.

Path-independence of the J-integral (Rice, 1968) implies that the remote K^{∞}-field and the local K^{tip}-field at the crack tip are related by (Trantina, 1972; Wang et al., 1978; Fleck et al., 1991):

$$K^{\text{tip}} = \left(\frac{\bar{E}_2}{\bar{E}_1}\right)^{\frac{1}{2}} K^{\infty} \tag{7.1}$$

where Eq. 2.16 is re-stated for convenience. Hence, as can be seen in Fig. 7.3a, the stress at the crack tip within the adhesive layer is shielded by the presence of stiffer substrate material. Adjacent to the crack tip, the stresses are given by the leading term of the William's singularity analysis (Williams, 1957), with σ_{yy} given by:

$$\frac{\sigma_{yy}\sqrt{h}}{K^{\infty}} = \left(\frac{1}{2\pi}\frac{\bar{E}_2}{\bar{E}_1}\frac{h}{x}\right)^{\frac{1}{2}} \tag{7.2}$$

Consistent with the requirement given in Eq. 7.1, the stress component σ_{yy} remote from the crack tip scales as:

$$\frac{\sigma_{yy}\sqrt{h}}{K^{\infty}} = \left(\frac{1}{2\pi}\frac{h}{x}\right)^{\frac{1}{2}} \tag{7.3}$$

Relations 7.2 and 7.3 provide asymptotes to the stress distribution ahead of the crack in Fig. 7.3a. The stress follows the local K^{tip} field close to the crack tip provided x/h is less than a transition value designated by $(x/h)_{\text{T1}}$. Alternatively, at sufficiently large values of x/h, above a second transition value $(x/h)_{\text{T2}}$, the stress state satisfies the remote K^{∞} field. Equations 7.2 and 7.3 imply that:

$$\left(\frac{x}{h}\right)_{\text{T2}} = \frac{\bar{E}_1}{\bar{E}_2}\left(\frac{x}{h}\right)_{\text{T1}} \tag{7.4}$$

The stress distribution is plotted as a function of x/h along the crack plane for selected values of modulus mismatch ratio in the range $\bar{E}_2/\bar{E}_1 = 1$ to $\bar{E}_2/\bar{E}_1 = 10^{-3}$ in Fig. 7.3b. The normalised tensile stress displays a plateau value for x/h values between $(x/h)_{\text{T1}}$ and $(x/h)_{\text{T2}}$. For a decreasing value of modulus mismatch ratio, the plateau stress tends to the asymptotic limit of:

$$\frac{\sigma_{yy}\sqrt{h}}{K^{\text{tip}}} = \left(1-\bar{\nu}^2\right)^{-\frac{1}{2}} \tag{7.5}$$

which is the solution for the case of a semi-infinite crack in an adhesive layer clamped by two rigid substrates and subjected to a uniform opening displacement as introduced in Section 2.2.2 via Eq. 2.17.

Note from Fig. 7.3b that the value of $(x/h)_{\text{T1}}$ equals approximately 0.2 independent of the magnitude of the modulus mismatch ratio over the range considered. Consequently, Eq. 7.4 reduces to $(x/h)_{\text{T2}} = 0.2\bar{E}_1/\bar{E}_2$, with the immediate implication that a remote K^{∞} field can only exist in a specimen of characteristic in-plane dimensions (such as crack length, height and ligament width)

that significantly exceed the value of $0.2h\bar{E}_1/\bar{E}_2$. Assume that an in-plane dimension on the order of $h\bar{E}_1/\bar{E}_2$ is required to meet this condition. This places a severe restriction on the relevance of a remote stress intensity factor for thick polymeric adhesive joints between metallic or composite substrates. For example, consider an epoxy adhesive of thickness 1 mm and Young's modulus $\bar{E}_2$ = 1 GPa sandwiched between steel substrates of modulus $\bar{E}_1$ = 210 GPa. Then, an in-plane structural dimension of h
$barE_1/\bar{E}_2$ = 210 mm is required in order for a remote K-field to exist. This requirement is significantly more restrictive for the choice of a thick elastomeric adhesive between steel substrates (as used, for example, in shipbuilding) such that h = 10 mm and $\bar{E}_2$ = 0.1 GPa; the minimum in-plane dimension then becomes 21 m. For such applications, it is necessary to consider a prototypical specimen of finite crack length and subjected to a remote stress, such as the centre-cracked sandwich panel shown in Fig. 7.1, and recognise the fact that a remote K-field may not exist for this specimen. This is the main geometry under consideration in the present study.

7.2 Theory

Consider the finite sandwich joint shown in Fig. 7.1. The joint consists of an adhesive layer of height $2h$ and width $2W$ sandwiched between two substrates, each of length L. A through-thickness centre-crack of length $2a$ lies parallel to the interface at mid-height of the adhesive layer. The substrate is identified as material 1, and the adhesive is identified as material 2, each being isotropic, homogeneous and linear elastic, with elastic properties $\bar{E}_1$, $\bar{\nu}_1$ and $\bar{E}_2$, $\bar{\nu}_2$ as defined above. The sandwich layer is loaded by a remote tensile stress σ^∞ parallel to the y-axis. It is assumed that the adhesive has a crack-tip cohesive zone that obeys a tensile traction versus separation law of the form shown on the right-hand side of Fig. 7.1, with a finite cohesive strength $\hat{\sigma}$ and toughness Γ. Now introduce a reference length scale, following Tvergaard and Hutchinson (1992), as:

$$l_S = \frac{\bar{E}_2\Gamma}{\pi\hat{\sigma}^2} \tag{7.6}$$

The strength of the sandwich joint σ_f^∞ is a function of the normalised crack length a/h, modulus mismatch ratio $\bar{E}_2/\bar{E}_1$, and the normalised reference length scale l_S/h, and can be written in non-dimensional form as:

$$\bar{\sigma} = \frac{\sigma_{\mathrm{f}}^{\infty}\sqrt{h}}{\sqrt{\bar{E}_2\Gamma}} = f\left(\frac{a}{h}, \frac{W}{h}, \frac{\bar{E}_2}{\bar{E}_1}, \frac{l_{\mathrm{S}}}{h}, \bar{\nu}_1, \bar{\nu}_2\right) \tag{7.7}$$

The role of Poisson's ratio is minor and neglected in the present study. The sensitivity of the strength of the joint upon the other non-dimensionless groups is explored. First, the limiting case of a Griffith crack in an elastic layer of finite toughness but unbounded cohesive strength ($l_{\mathrm{S}} \to 0$) is considered. Then, a finite cohesive strength is taken into account.

7.2.1 Griffith crack in an elastic layer

Consider first the extreme cases of a very short crack and a very long crack in an elastic, brittle adhesive (of unbounded cohesive strength $\hat{\sigma}$). Then, the more involved case of an intermediate crack length is analysed. The terms 'short','long', and 'intermediate' are made precise below.

7.2.1.1 Asymptotic analysis for a very short or very long crack

In the limit of a very short crack length $a/h \ll 1$, the presence of the substrate can be ignored, and the crack tip stress intensity factor is given by:

$$K^{\mathrm{tip}} = \sigma^{\infty}\sqrt{\pi a} \tag{7.8}$$

Crack growth occurs when the energy release rate G attains the toughness Γ of the adhesive, such that

$$G = \frac{(K^{\mathrm{tip}})^2}{\bar{E}_2} = \Gamma \tag{7.9}$$

and the macroscopic fracture strength is then given by:

$$\bar{\sigma} = \frac{\sigma_{\mathrm{f}}^{\infty}\sqrt{h}}{\sqrt{\bar{E}_2\Gamma}} = \left(\frac{h}{\pi a}\right)^{\frac{1}{2}} \tag{7.10}$$

Alternatively, for a very long crack for which $a/h \gg 1$, the presence of the adhesive can be ignored. For $a/W \ll 1$, the stress intensity factor reads:

$$K^{\infty} = \sigma^{\infty}\sqrt{\pi a} \tag{7.11}$$

Then, from Eqs. 7.1 and 7.9, the strength of the joint is:

$$\bar{\sigma} = \frac{\sigma_{\mathrm{f}}^{\infty}\sqrt{h}}{\sqrt{\bar{E}_2\Gamma}} = \left(\frac{\bar{E}_1}{\bar{E}_2}\frac{h}{\pi a}\right)^{\frac{1}{2}} \tag{7.12}$$

7.2.1.2 General analysis for an intermediate length of crack

An analytical expression for the strength $\bar{\sigma}$ is derived for the case of an intermediate crack length with respect to the adhesive layer height and joint width. Consider the joint shown in Fig. 7.4, and write Δu as the extra displacement of the ends of the specimen due to the presence of a crack of length $2a$ and an end load P per unit thickness. Thus, Δu is equal to $P\Delta C$, where $\Delta C(a) \equiv C(a) - C(0)$ is the extra compliance due to the presence of the crack. For the center-cracked joint, one may write (Tada et al., 2000):

$$G = \frac{P^2}{4}\frac{\partial(\Delta C)}{\partial a} \tag{7.13}$$

Note that for a specimen of infinite height as shown in Fig. 7.4, C is unbounded but ΔC is infinite. The adhesive joint on the left hand side of Fig. 7.4 is idealised by the summation of two problems on the right hand side, case (1) and case (2), such that:

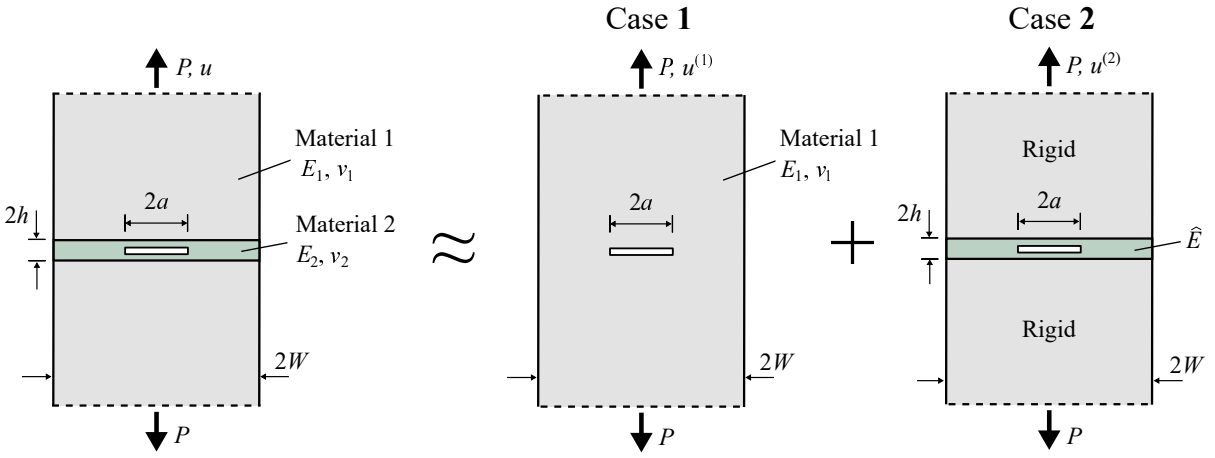

Figure 7.4 Superposition procedure to determine the K-calibration for a Griffith crack in an elastic layer.

$$\frac{\partial(\Delta C)}{\partial a} = \frac{\partial(\Delta C^{(1)})}{\partial a} + \frac{\partial(\Delta C^{(2)})}{\partial a} \tag{7.14}$$

Note that case (1) neglects the presence of the adhesive layer in the determination of the additional compliance due to the presence of the crack and that case (2) is an approximate analysis for the additional compliance due to the presence of the crack when a strip of height $2h$ and made from material 1 is replaced by a strip of material 2. Thus, in case (2), the substrate is treated as rigid and the replacement strip is of effective modulus such that:

$$\frac{1}{\hat{E}} = \frac{1-\bar{\nu}_2^2}{\bar{E}_2} - \frac{1-\bar{\nu}_1^2}{\bar{E}_1} \tag{7.15}$$

The constraint factors $(1-\bar{\nu}_1^2)$ and $(1-\bar{\nu}_2^2)$ arise from the fact that the strain component in the replacement layer vanishes in the tangential direction.

Expressions are now derived for $\partial(\Delta C^{(1)})/\partial a$ and $\partial(\Delta C^{(2)})/\partial a$. For case (1), the material 1 center-cracked panel of finite width (Tada et al., 2000):

$$\frac{\partial(\Delta C^{(1)})}{\partial a} = \frac{\pi a F^2}{W^2 \bar{E}_1} \tag{7.16}$$

where the finite width correction factor F is a function of a/W (Tada et al., 2000; Federsen, 1966):

$$F = \left[1 - 0.025\left(\frac{a}{W}\right)^2 + 0.06\left(\frac{a}{W}\right)^4\right]\left[\sec\left(\frac{\pi}{2}\frac{a}{W}\right)\right]^{\frac{1}{2}} \tag{7.17}$$

Now, consider case (2). The net section stress σ^{net} reads:

$$\sigma^{\text{net}} = \frac{P}{2W}\left(1 - \frac{a}{W}\right)^{-1} \tag{7.18}$$

Moreover, for the linear, elastic adhesive layer of case (2), one may write:

$$\sigma^{\text{net}} = \frac{\hat{E}\Delta u}{2h} \tag{7.19}$$

Equating Eqs. 7.18 and 7.19, and making use of the definition for ΔC (=Δu/P) as introduced above, gives:

$$\Delta C^{(2)}(a) = C^{(2)}(a) = \frac{h}{W\hat{E}\left(1-\frac{a}{W}\right)} \tag{7.20}$$

and therefore:

$$\frac{\partial(\Delta C^{(2)})}{\partial a} = \frac{h}{W^2\hat{E}\left(1-\frac{a}{W}\right)^2} \tag{7.21}$$

Now, make use of the Irwin relation, $K^{\text{tip}} = \sqrt{\bar{E}_2 G}$, and Eq. 7.13 to obtain for the joint on the left-hand side of Fig. 7.4:

$$K^{\text{tip}} = \frac{P}{2}\left(\bar{E}_2\frac{\partial(\Delta C)}{\partial a}\right)^{\frac{1}{2}} \tag{7.22}$$

The normalised strength $\bar{\sigma}$, as defined in Eq. 7.7, is related to P and K^{tip} upon noting that $\sigma^{\infty} = P/2W$:

$$\bar{\sigma} = \frac{P\sqrt{h}}{2WK^{\text{tip}}} \tag{7.23}$$

Upon making use of Eqs. 7.14, 7.16, 7.21, 7.22 and 7.23, the general formula:

$$\bar{\sigma} = \left[\frac{\bar{E}_2}{\bar{E}_1}\frac{a}{h}\pi F^2 + \left((1-\bar{\nu}_2^2) - (1-\bar{\nu}_1^2)\frac{\bar{E}_2}{\bar{E}_1}\right)\left(1-\frac{a}{W}\right)^{-2}\right]^{-\frac{1}{2}} \tag{7.24}$$

is obtained. For $\nu = \bar{\nu}_1 = \bar{\nu}_2$, this relation reduces to:

$$\bar{\sigma} = \left[\frac{\bar{E}_2}{\bar{E}_1}\frac{a}{h}\pi F^2 + (1-\bar{\nu}^2)\left(1-\frac{\bar{E}_2}{\bar{E}_1}\right)\left(1-\frac{a}{W}\right)^{-2}\right]^{-\frac{1}{2}} \tag{7.25}$$

Note that according to Eq. 7.25 there is a plateau value in strength for intermediate values of a/h, this plateau value reduces to the following limit for $\bar{E}_2/\bar{E}_1 \to 0$:

$$\bar{\sigma} = (1-\bar{\nu}_2^2)^{-\frac{1}{2}} \tag{7.26}$$

The strength plateau value given in Eq. 7.26 is consistent with the Rice (1967) solution given in Eq. 7.5 upon noting $K^{\text{tip}} = \sqrt{\bar{E}_2\Gamma}$ and $\sigma_{yy} = \sigma_{\text{f}}^{\infty}$. For very small cracks, Eq. 7.10 is valid. The transition between the adhesive-governed regime (short cracks) and the substrate-governed regime (intermediate and long cracks) is obtained by equating the strengths from Eqs. 7.10 and Eq. 7.26. The resulting transition value of normalised crack length reads:

$$\frac{a}{h} = \frac{1 - \bar{\nu}_2^2}{\pi} \tag{7.27}$$

Equations 7.10 and 7.25 for the strength $\bar{\sigma}$ are plotted as a function of a/h in Fig. 7.5a for the case of an infinitely wide joint ($h/W = 0$) and for selected values of modulus mismatch ratio $\bar{E}_2/\bar{E}_1$ in the range of 0 (rigid substrate case) to 1 (homogeneous case). The short crack asymptote, Eq. 7.10, exists in the region identified[2] as regime B in Fig. 7.5a, whereas the case of intermediate to long cracks is termed regime C. The long crack asymptote given by Eq. 7.12 is included in Fig. 7.5a. The failure strength $\bar{\sigma}$ of the joint with a Griffith crack decreases with increasing value of modulus mismatch ratio $\bar{E}_2/\bar{E}_1$ in regime C, but is independent of the magnitude of $\bar{E}_2/\bar{E}_1$ in the short crack regime B. The sensitivity of the strength $\bar{\sigma}$ to joint width is shown in Fig. 7.5b, in which $\bar{\sigma}$ is plotted for selected values of h/W ranging from 0 to 0.1 and for a modulus mismatch ratio $\bar{E}_2/\bar{E}_1 = 10^{-2}$. As the crack length a approaches the joint width W, the strength $\bar{\sigma}$ drops sharply. This is consistent with the usual form of the K-calibration for a specimen of finite dimensions (Tada et al., 2000).

7.2.2 Plasticity at the crack tip

7.2.2.1 Asymptotic analysis for a very short crack

The effect of a finite length cohesive zone at the crack tip on the strength of the joint shown in Fig. 7.1 is now taken into account. It is emphasised that the cohesive zone has a uniform strength $\hat{\sigma}$ and toughness Γ, and the material length scale l_{S} is a derived material property via Eq. 7.6. Note that, in general, the value of l_{S} is not equal to the length of the cohesive zone c (see Fig. 7.1). This is only the case for a semi-infinite crack in an infinite solid made from the adhesive material.

[2] A more precise definition will be given for regimes B and C in Section 7.2.2.

Consider first the case for which $a + l_S \ll h$. The crack and cohesive zone exist within a much larger layer of adhesive; the strength of the joint $\bar{\sigma}$ can be predicted by ignoring the presence of the substrate. The strip yield model of Dugdale (1960) and Barenblatt (1962) may be em-

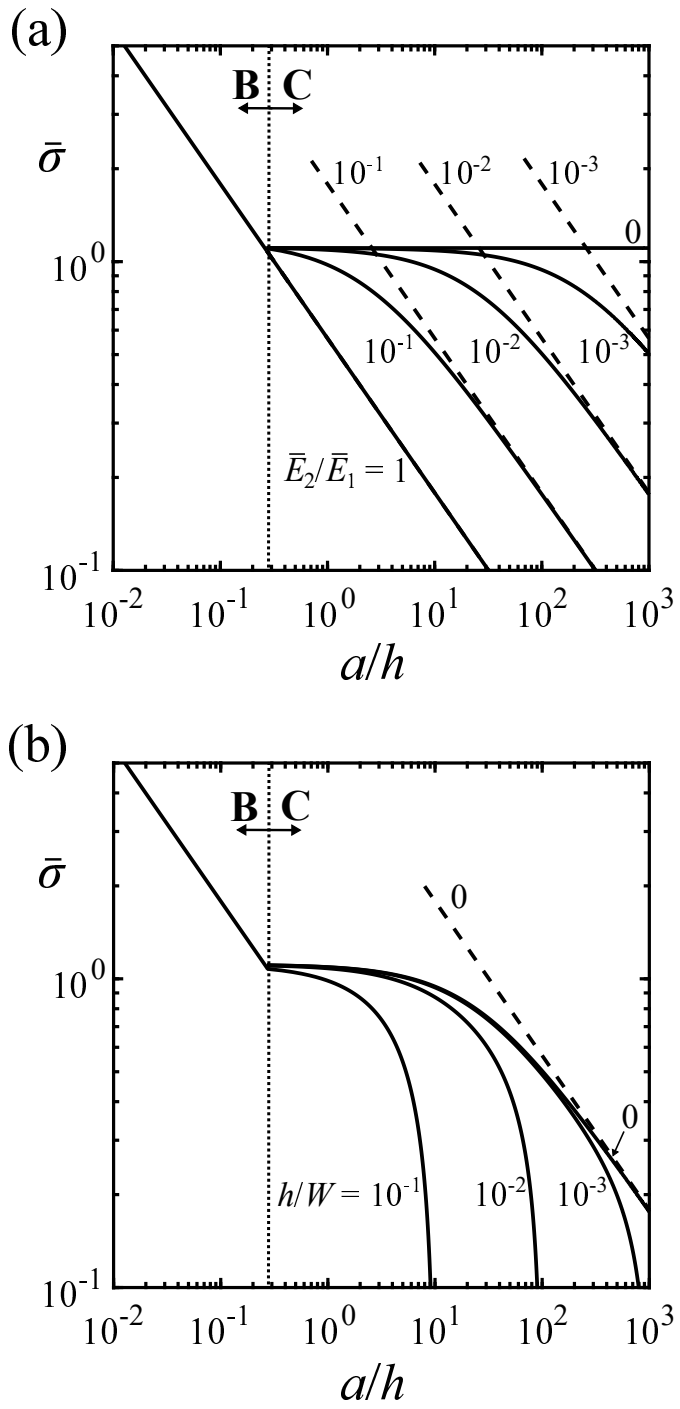

Figure 7.5 Strength $\bar{\sigma}$ versus normalised crack length a/h for an elastic, brittle Griffith crack, (a) for $h/W = 0$ and (b) for $\bar{E}_2/\bar{E}_1 = 10^{-2}$. The dotted lines are plotted via Eq. 7.12 for the long crack asymptote, while the solid lines are predicted via Eq. 7.25 in regime C and via Eq. 7.10 in regime B.

ployed, as is appropriate for the assumed traction-separation law defined on the right-hand side of Fig. 7.1. In the Dugdale strip yield model, the crack tip opening displacement δ^{tip} for a through crack of length $2a$ in a linear, elastic and infinite sheet under a remote uniaxial tensile stress σ^{∞} reads:

$$\delta^{\text{tip}} = \frac{8\hat{\sigma}a}{\pi\bar{E}_2}\ln\left[\sec\left(\frac{\pi\sigma^{\infty}}{2\hat{\sigma}}\right)\right] \tag{7.28}$$

Upon recognising that $\Gamma = \hat{\sigma}\delta_{\text{C}}$, where the critical crack tip opening displacement δ_{C} is the value of δ^{tip} when the remote tensile stress $\hat{\sigma}^{\infty}$ is equal to the remote tensile failure strength of the joint $\sigma_{\text{f}}^{\infty}$, Eq. 7.28 is re-expressed as:

$$\frac{l_{\text{S}}}{h} = \frac{\bar{E}_2\delta_{\text{C}}}{\pi\hat{\sigma}h} = \frac{8a}{\pi^2 h}\ln\left[\sec\left(\frac{\pi\sigma^{\infty}}{2\hat{\sigma}}\right)\right] \tag{7.29}$$

Equation 7.29 is valid provided that $a + l_{\text{S}} \ll h$ and $h \leq W$. Moreover, Eq. 7.29 can be employed to predict $\bar{\sigma}$ as a function of a/h, making use of the direct connection between $\bar{\sigma}$ and $\sigma_{\text{f}}^{\infty}/\hat{\sigma}$ via the definition for the material reference length scale l_{S} given in Eq. 7.6:

$$\bar{\sigma} \equiv \frac{\sigma_{\text{f}}^{\infty}\sqrt{h}}{\sqrt{\bar{E}_2\Gamma}} = \frac{\sigma_{\text{f}}^{\infty}}{\hat{\sigma}}\frac{\hat{\sigma}\sqrt{h}}{\sqrt{\bar{E}_2\Gamma}} = \frac{\sigma_{\text{f}}^{\infty}}{\hat{\sigma}}\left(\frac{h}{\pi l_{\text{S}}}\right)^{\frac{1}{2}} \tag{7.30}$$

7.2.2.2 General analysis for an intermediate and long crack length

Consider the case where the combined length of a and l_{S} are on the order of, or larger than, h. Again, an approximate analytical derivation is performed for the cohesive zone problem, as shown on the left-hand side of Fig. 7.6.

The present analytical method assumes that the crack tip displacement δ^{tip} for the full problem (as given in the left-hand side of Fig. 7.6) is adequately given by the superposition of the crack tip opening displacement for problems (1) and (2) as stated on the right hand side of Fig. 7.6:

$$\delta^{\text{tip}} = \delta^{(1)} + \delta^{(2)} \tag{7.31}$$

Here, $\delta^{(1)}$ is the crack tip opening displacement for a crack of length $2a$ in a linear, elastic sheet of infinite width of material 1 under a remote tensile stress of σ^{∞} (see case 1 of Fig. 7.6), and

$\delta^{(2)}$ is the crack tip opening displacement for a crack of length $2a$ in a linear, elastic sandwich layer with Young's modulus equal to $\hat{E}$, defined earlier in Eq. 7.15, and clamped between two rigid substrates of finite width subjected to a remote tensile stress σ^{∞} (see case 2 of Fig. 7.6). This approximation is exact in the limit of a joint comprising rigid substrates, i.e. $\bar{E}_2/\bar{E}_1 = 0$, and for the homogeneous case for which $\bar{E}_2/\bar{E}_1 = 1$.

Expressions are now derived for $\delta^{(1)}$ and $\delta^{(2)}$. Consider first case 1 of Fig. 7.6. Making use of Eq. 7.28, the crack tip opening displacement $\delta^{(1)}$ reads:

$$\delta^{(1)} = \frac{8\hat{\sigma}a}{\pi\bar{E}_1}\ln\left[\sec\left(\frac{\pi\sigma^{\infty}}{2\hat{\sigma}}\right)\right] \tag{7.32}$$

For case 2, the value of the J-integral taken around the crack tip is given by:

$$J^{\text{tip}} = \hat{\sigma}\delta^{(2)} \tag{7.33}$$

In addition, for a linear, elastic system the value of the J-integral taken around a remote contour J^{∞} equals the energy release rate, and J^{∞} can be deduced from the expression for the derivative of the compliance as given in Eq. 7.21, such that, via Eq. 7.13:

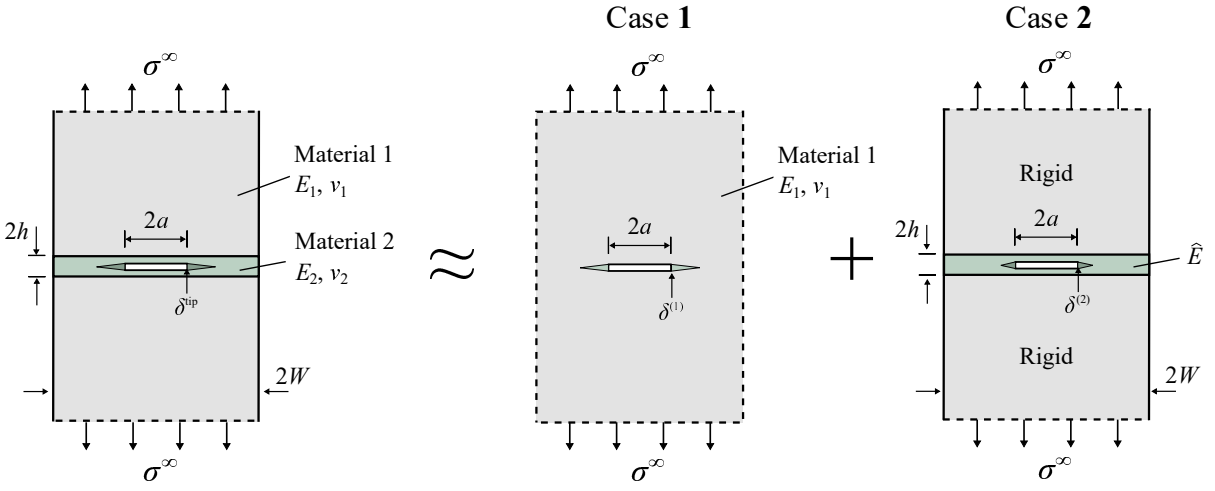

Figure 7.6 Superposition procedure to calculate the macroscopic tensile strength of a centre-cracked sandwich layer, for finite values of l_S, and a is comparable to, or larger than h.

$$J^{\infty} = \frac{h(\sigma^{\infty})^2}{\hat{E}}\left(1-\frac{a}{W}\right)^{-2} \tag{7.34}$$

Making use of the path-independence of the J-integral, Eqs. 7.33 and 7.34 can be combined to give:

$$\delta^{(2)} = \frac{h(\sigma^{\infty})^2}{\hat{E}\hat{\sigma}}\left(1-\frac{a}{W}\right)^{-2} \tag{7.35}$$

Hence, the relation 7.31 becomes, via Eqs. 7.32 and 7.35:

$$\frac{\delta^{\text{tip}}}{h} = \frac{8\hat{\sigma}}{\pi\bar{E}_1}\frac{a}{h}\ln\left[\sec\left(\frac{\pi\sigma^{\infty}}{2\hat{\sigma}}\right)\right] + \frac{(\sigma^{\infty})^2}{\hat{E}\hat{\sigma}}\left(1-\frac{a}{W}\right)^{-2} \tag{7.36}$$

Upon recalling the definition of l_{S} in Eq. 7.6, one may write it as $l_{\text{S}} \equiv \delta_{\text{C}}\bar{E}_2/\pi\hat{\sigma}$. At fracture, $\sigma^{\infty} = \sigma_{\text{f}}^{\infty}$ and $\delta^{\text{tip}} = \delta_{\text{C}}$. Therefore, by making use of Eq. 7.36, the ratio of material length scale l_{S} to adhesive layer half-height h reads:

$$\frac{l_{\text{S}}}{h} = \frac{8}{\pi^2}\frac{\bar{E}_2}{\bar{E}_1}\frac{a}{h}\ln\left[\sec\left(\frac{\pi\sigma_{\text{f}}^{\infty}}{2\hat{\sigma}}\right)\right] + \frac{1}{\pi}\left(\frac{\sigma_{\text{f}}^{\infty}}{\hat{\sigma}}\right)^2\left[(1-\bar{\nu}_2^2)-(1-\bar{\nu}_1^2)\frac{\bar{E}_2}{\bar{E}_1}\right]\left(1-\frac{a}{W}\right)^{-2} \tag{7.37}$$

For the case $\bar{\nu} = \bar{\nu}_1 = \bar{\nu}_2$, Eq. 7.37 reduces to:

$$\frac{l_{\text{S}}}{h} = \frac{8}{\pi^2}\frac{\bar{E}_2}{\bar{E}_1}\frac{a}{h}\ln\left[\sec\left(\frac{\pi\sigma_{\text{f}}^{\infty}}{2\hat{\sigma}}\right)\right] + \frac{1-\bar{\nu}^2}{\pi}\left(\frac{\sigma_{\text{f}}^{\infty}}{\hat{\sigma}}\right)^2\left(1-\frac{\bar{E}_2}{\bar{E}_1}\right)\left(1-\frac{a}{W}\right)^{-2} \tag{7.38}$$

7.2.3 Regimes of behaviour

There are four regimes of behaviour for the joint problem defined in Fig. 7.1. First, there is a broad division into whether the behaviour can be described by an asymptotic limit where the effect of the substrate can be ignored. This condition is found to be approximated by the geometric relation:

$$l_{\text{S}} + a < 0.3h \tag{7.39}$$

The division between the adhesive- and substrate-governed regimes of fracture given by Eq. 7.39 is illustrated in the l_S/h versus a/h failure map shown in Fig. 7.7 as a solid line separating regions A and B from regions C and D. Within the adhesive-governed regime, where the inequality given in Eq. 7.39 holds, there is a subdivision between toughness-controlled fracture and strength-controlled fracture. A strength criterion is adopted, assuming that fracture is strength-controlled when $\sigma_f^\infty/\hat{\sigma} > 0.99$, which implies from Eq. 7.29 that:

$$\frac{l_S}{a} < 3.37 \tag{7.40}$$

This criterion has been added to Fig. 7.7 to distinguish between regime A, where fracture is controlled by strength, and regime B, where fracture is controlled by toughness. It is emphasised that this boundary is independent of the value of the modulus mismatch ratio.

Now consider the geometries satisfying $(l_S + a) > 0.3h$ such that the presence of the substrate needs to be accounted for. Again, there exists two sub-regions: regime C for the toughness-controlled fracture regime and regime D for the strength-controlled fracture regime. It is convenient to use a strength criterion $\sigma_f^\infty/\hat{\sigma} = 0.99$ for the division between regimes C and D. The resulting trajectory on the l_S/h versus a/h failure map follows directly from Eq. 7.38 and reads:

$$\frac{l_S}{h} = 3.37\frac{\bar{E}_2}{\bar{E}_1}\frac{a}{h} + 0.31(1-\bar{\nu}^2)\left(1-\frac{\bar{E}_2}{\bar{E}_1}\right)\left(1-\frac{a}{W}\right)^{-2} \tag{7.41}$$

for the case where $\bar{\nu} = \bar{\nu}_1 = \bar{\nu}_2$. The C to D boundary, as given by Eq. 7.41, is plotted in Fig. 7.7 for $\bar{\nu} = 3/7$, $h/W = 0$, and for two selected values of the modulus mismatch ratio: $\bar{E}_2/\bar{E}_1 = 0$ and $\bar{E}_2/\bar{E}_1 = 10^{-2}$. Sketches of different joint geometries are included in Fig. 7.7 to illustrate the relative magnitude of the normalised length scales l_S/h and a/h in the regimes A to D. In addition, contours of strength are plotted in Fig. 7.7 via Eqs. 7.29 (regime B) and 7.38 (regime C) for selected values of strength ratios: $\sigma_f^\infty/\hat{\sigma} = 0.1$ and $\sigma_f^\infty/\hat{\sigma} = 0.35$.

It is instructive to cross-plot $\sigma_f^\infty/\hat{\sigma}$ as a function of a/h. This is done in Fig. 7.8a for selected values of l_S/h and for $\bar{E}_2/\bar{E}_1 = 10^{-2}$, $\bar{\nu} = 3/7$, and $h/W = 0$. The curves are again plotted by making use of Eqs. 7.29 and 7.38. Predictions for $\sigma_f^\infty/\hat{\sigma}$ are included for the limit or a rigid substrate, i. e. $\bar{E}_2/\bar{E}_1 = 0$, shown as dashed lines in Fig. 7.8a. Moreover, it is insightful to rescale

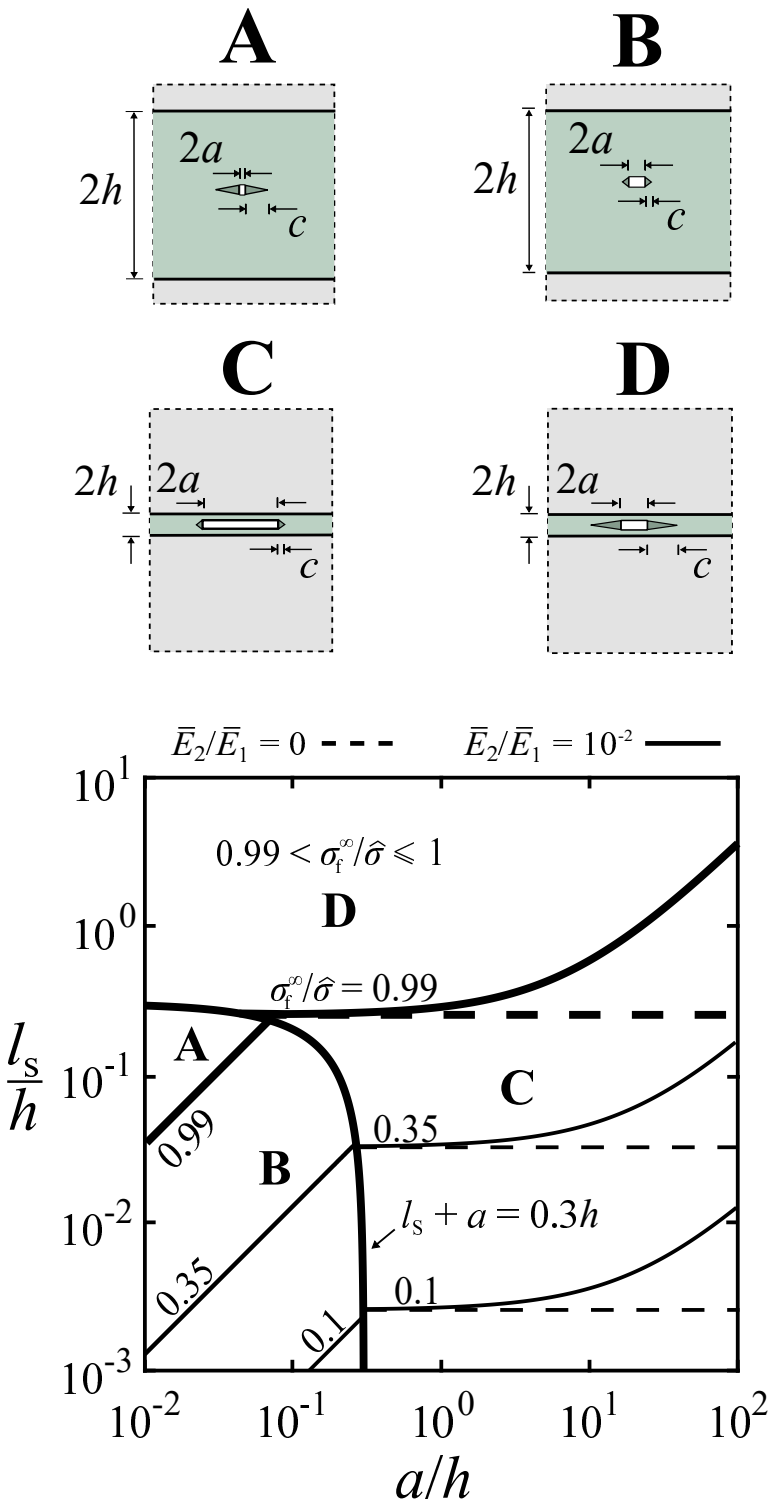

Figure 7.7 Failure mechanism map for centre-cracked sandwich specimen for $h/W = 0$, $\bar{\nu} = 3/7$, and two choices for the modulus mismatch ratio $\bar{E}_2/\bar{E}_1 = 10^{-2}$ (solid line) and $\bar{E}_2/\bar{E}_1 = 0$ (dashed line). The contours of strength are given by Eq. 7.38 in regimes C and D, and by 7.29 in regimes A and B.

the strength values $\sigma_f^\infty/\hat{\sigma}$ into the form $\bar{\sigma}$ by making use of the identity given in Eq. 7.30. Note that, in the limit of an elastic, brittle Griffith crack, such that $\hat{\sigma}$ is unbounded, the strength ratio $\bar{\sigma}$ remains finite whereas the strength ratio $\sigma_f^\infty/\hat{\sigma}$ vanishes. Thus, $\bar{\sigma}$ has been plotted as a function of a/h in Fig. 7.8b in order to make contact with the results for the Griffith crack, recall Fig. 7.5.

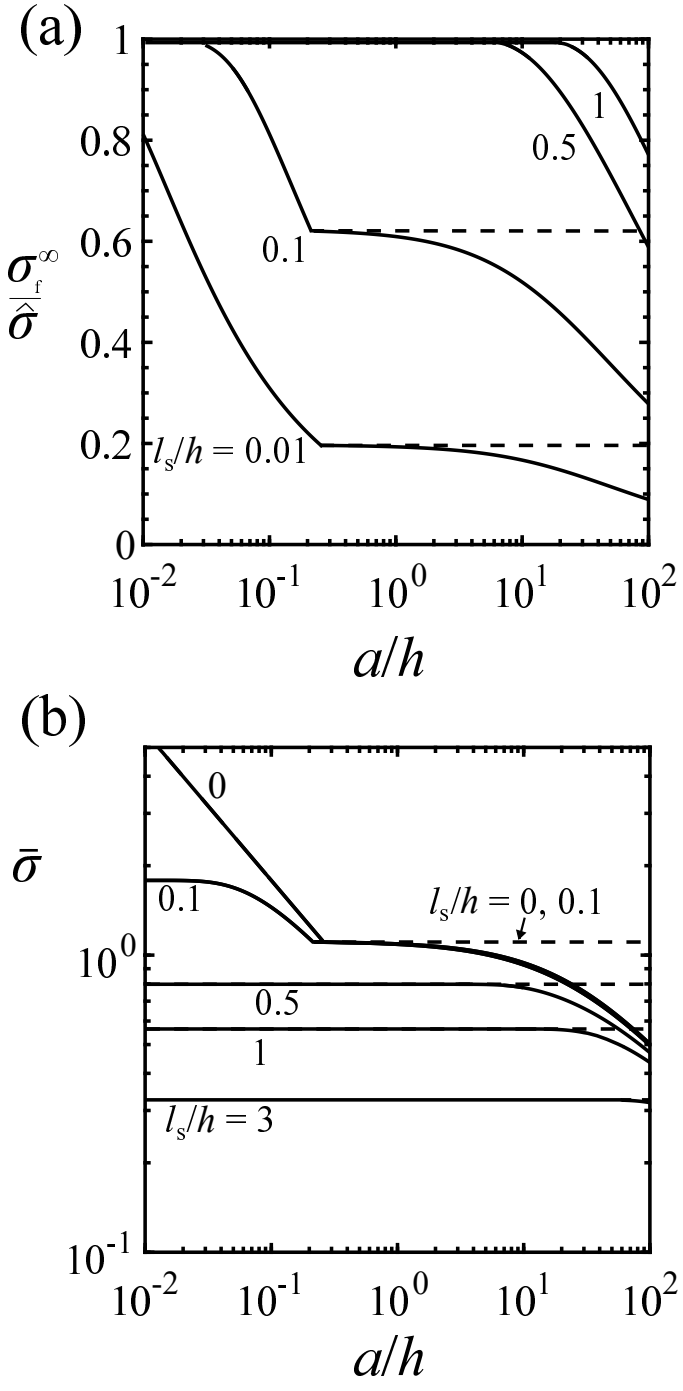

Figure 7.8 Strength predictions for $h/W = 0$, $\bar{E}_2/\bar{E}_1 = 0$ (dashed line) and $\bar{E}_2/\bar{E}_1 = 10^{-2}$ (solid line) (a) $\sigma_f^\infty/\hat{\sigma}$ versus a/h; (b) $\bar{\sigma}$ versus a/h. In both figures, strength predictions are given by Eq. 7.29 for $l_S/h \leq 0.1$ and $a/h < 0.3$. Otherwise, Eq. 7.38 is used.

Inspection of Fig. 7.7 shows that for an infinitesimal cohesive zone length at the crack tip, i.e. $l_S/h \rightarrow 0$, the active fracture mode switches from the adhesive-governed regime B to the substrate-governed regime C. Both regimes are toughness-controlled. The plot of $\bar{\sigma}$ versus a/h for $\bar{E}_2/\bar{E}_1 = 0$ in Fig. 7.8b is indistinguishable from that for $\bar{E}_2/\bar{E}_1 = 10^{-2}$ in regime B, but the strength predictions become sensitive to the value of the modulus mismatch ratio with increasing values of a/h in regime C.

Second, assume a relatively small plastic zone length, as parametrised by $l_S/h = 0.1$. In the failure mechanism map of Fig. 7.7, with increasing a/h, there is a transition from strength-control (regime A) to toughness-control, regimes B and C. In regime A, the ratio $\sigma_f^\infty/\hat{\sigma}$ is equal to unity, and this is shown in Fig. 7.8a. Then, for $0.03 < a/h < 0.25$, regime B is active, such that the crack and its cohesive zone are shorter than the adhesive height ($l_S + a < 0.3h$) and $\sigma_f^\infty/\hat{\sigma}$ decreases with increasing a/h, see Fig. 7.8a. At longer crack lengths, i.e. $a/h > 0.25$, regime C is entered and the strength ratio $\sigma_f^\infty/\hat{\sigma}$ is below the yield value of unity and independent of a/h for $\bar{E}_2/\bar{E}_1 = 0$ as shown in Fig. 7.8a. In contrast, for a finite value of the modulus mismatch, the value of $\sigma_f^\infty/\hat{\sigma}$ decreases with increasing a/h due to the fact that the crack (and cohesive zone) are embedded within the remote K^∞-field of the substrate, and the long crack asymptote predicted by Eq. 7.12 is approached.

Third, consider the case where $l_S/h = 1$ in the failure map shown in Fig. 7.7. The response is in the strength-controlled regime D such that $\sigma_f^\infty/\hat{\sigma}$ is equal to the yield value of unity for the choice $\bar{E}_2/\bar{E}_1 = 0$ for all values of a/h. However, for $\bar{E}_2/\bar{E}_1 = 10^{-2}$, the fracture response switches from strength-controlled (regime D) to toughness- controlled (regime C) close to $a/h = 15$, and for normalised crack lengths that exceed this transition value, the strength ratio $\sigma_f^\infty/\hat{\sigma}$ decreases with crack extension. Again, this is due to the crack and cohesive zone being embedded within the remote K^∞-field of the substrate in a similar manner to that discussed for $l_S/h = 0.1$.

The transition from strength control (regime D) to toughness control (regime C) in the failure map of Fig. 7.7 occurs at a value of a/h that depends upon both the modulus mismatch $\bar{E}_2/\bar{E}_1$ and the value of the normalised material reference scale l_S/h. The C to D boundary is plotted in Fig. 7.9 using axes of ($\bar{E}_2/\bar{E}_1$,l_S/h), for the choice of $\bar{\nu} = 3/7$ and $h/W = 0$. The map shown

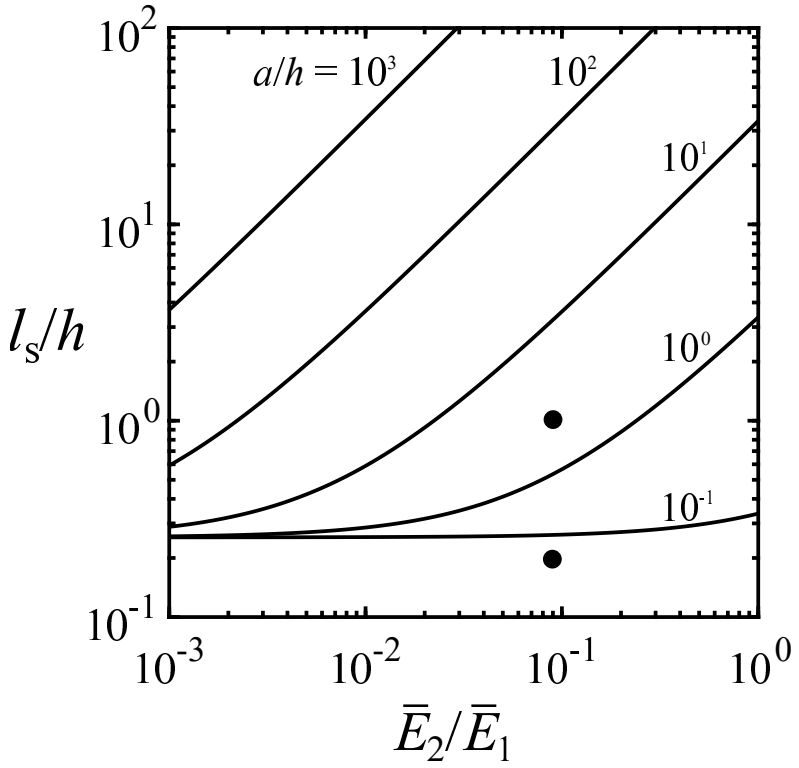

Figure 7.9 Boundary between regimes C and D on a map of l_S/h versus $\bar{E}_2/\bar{E}_1$, for selected values of a/h, for $h/W = 0$. The two data points denote the experimental parameters that are measured for the cellulose acetate-aluminium alloy sandwich layer considered in the experimental study presented in Chapter 8.

in Fig. 7.9 has the following useful interpretation: for any given adhesive-substrate combination, the values for l_S/h and $\bar{E}_2/\bar{E}_1$ are known. This combination of properties and geometry can be plotted as a point on Fig. 7.9. In addition, it is notable that the C to D transition value of a/h is close to 0.1 for the choice of $l_S/h = 0.3$ for a wide range of modulus mismatch values.

7.3 Verification of the analytical framework

Two-dimensional (plane strain) FE simulations are performed using the implicit solver of ABAQUS (version 6.14) to verify the analytical framework derived above. First, the macroscopic strength of the sandwich layer shown in Fig. 7.1 is computed as a function of crack length for the case where the cohesive zone at the crack tip is of vanishing length, i.e. $l_S \to 0$. The effect of modulus mismatch and adhesive layer height on the strength of the joint is explored.

Second, a layer of tensile cohesive elements is added directly ahead of the crack tip to account for both yield and fracture in the process zone ahead of the crack tip.

7.3.1 Finite element simulations for a crack in an elastic sandwich layer absent a cohesive zone

The sandwich layer depicted in Fig. 7.1 is modeled by treating both the adhesive and the substrate as isotropic, elastic solids. The length of the cohesive zone c equals zero. Simulations are performed for normalised crack lengths ranging from $a/h = 0.1$ to $a/h = 30$, with $h/W = 10^{-2}$ and $h/W = 10^{-1}$. The ratio of Young's modulus of the adhesive E_2 to that of the substrate E_1 ranges from 10^{-3} to 0.1, with $\nu = \nu_1 = \nu_2 = 0.3$. Only a quarter of the sandwich specimen is modelled due to the symmetry of the problem, see Fig. 7.10a. The substrate and the adhesive layer are discretised by 8-noded bi-quadratic plane strain elements (CPE8). A quarter point element is located at the crack tip and the mesh is refined close to the crack tip. The total number of elements is a function of the crack half-length a and lies in the range of 100 000 to 200 000. A finite value of remote tensile stress σ^∞ is applied, and the J-integral is evaluated at the crack tip. Upon writing $J = \Gamma$ and $\sigma^\infty = \sigma_f^\infty$, the predicted normalised strength $\bar{\sigma}$ (as defined in Eq. 7.7) is computed and plotted as a function of normalised crack length a/h, see Fig. 7.11a for a modulus mismatch ratio $\bar{E}_2/\bar{E}_1 = 10^{-1}$.

The analytical predictions for the adhesive-governed strength regime are plotted via Eq. 7.10, and via Eq. 7.25 for the substrate-governed strength regime in Fig. 7.11a, and good agreement is noted between the FE predictions and the analytical theory. Equation 7.25 slightly overestimates $\bar{\sigma}$ as obtained by the FE simulations in the regime where the crack length is comparable to the adhesive layer height. Recall that the prediction for a long crack ($a/h \gg 1$) neglects the presence of the adhesive layer in the Irwin relation, i.e. Eq. 7.9. This asymptote is included in Fig. 7.11a: Eq. 7.25 converges to the long crack asymptote (Eq. 7.12) for $a/h > 10$.

The computed $\bar{\sigma}$ versus a/h curves, as obtained by FE simulations, are plotted in Fig. 7.11b for $\bar{E}_2/\bar{E}_1 = 10^{-2}$ and in Fig. 7.11c for $\bar{E}_2/\bar{E}_1 = 10^{-3}$. The strength predictions via Eq. 7.10 in the adhesive-governed regime and via Eq. 7.25 for the substrate-governed regime are included in both figures. Excellent agreement is noted between the predicted values for $\bar{\sigma}$ by the analytical

theory and by the FE model for the explored range of a/h and $\bar{E}_2/\bar{E}_1$ values. Recall that the remote K^{∞}-field only exists for a sufficient long crack, as discussed in relation to Eq. 7.27. The long crack asymptote governed by Eq. 7.12 has been added to Figs. 7.11b and 7.11c, and it is expected to align with the strength prediction by Eq. 7.25 for values a/h beyond the range plotted.

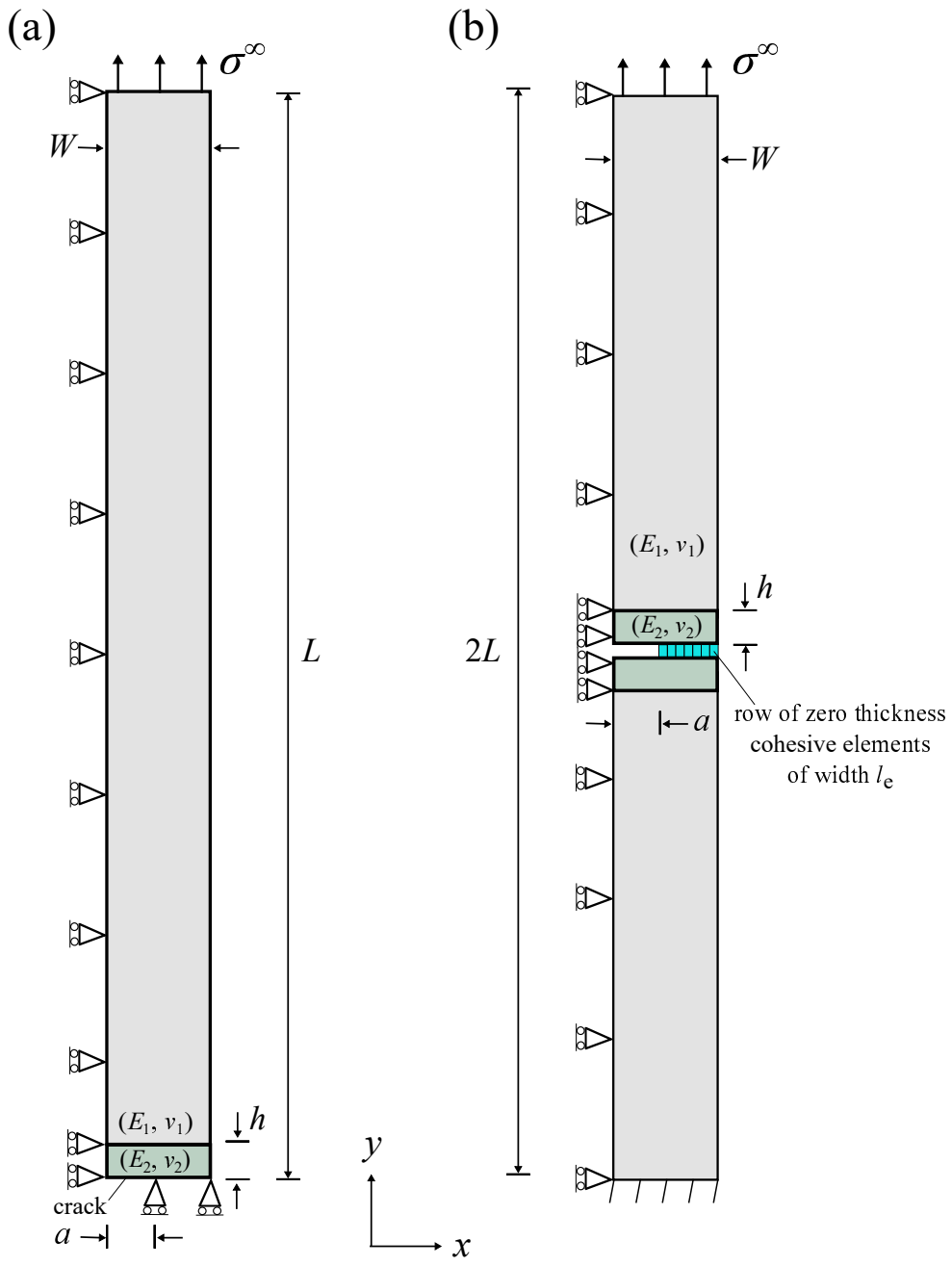

Figure 7.10 The geometries of the two-dimensional FE models for a crack in an elastic sandwich layer (a) absent a cohesive zone and (b) with a cohesive zone. $L = 10h$.

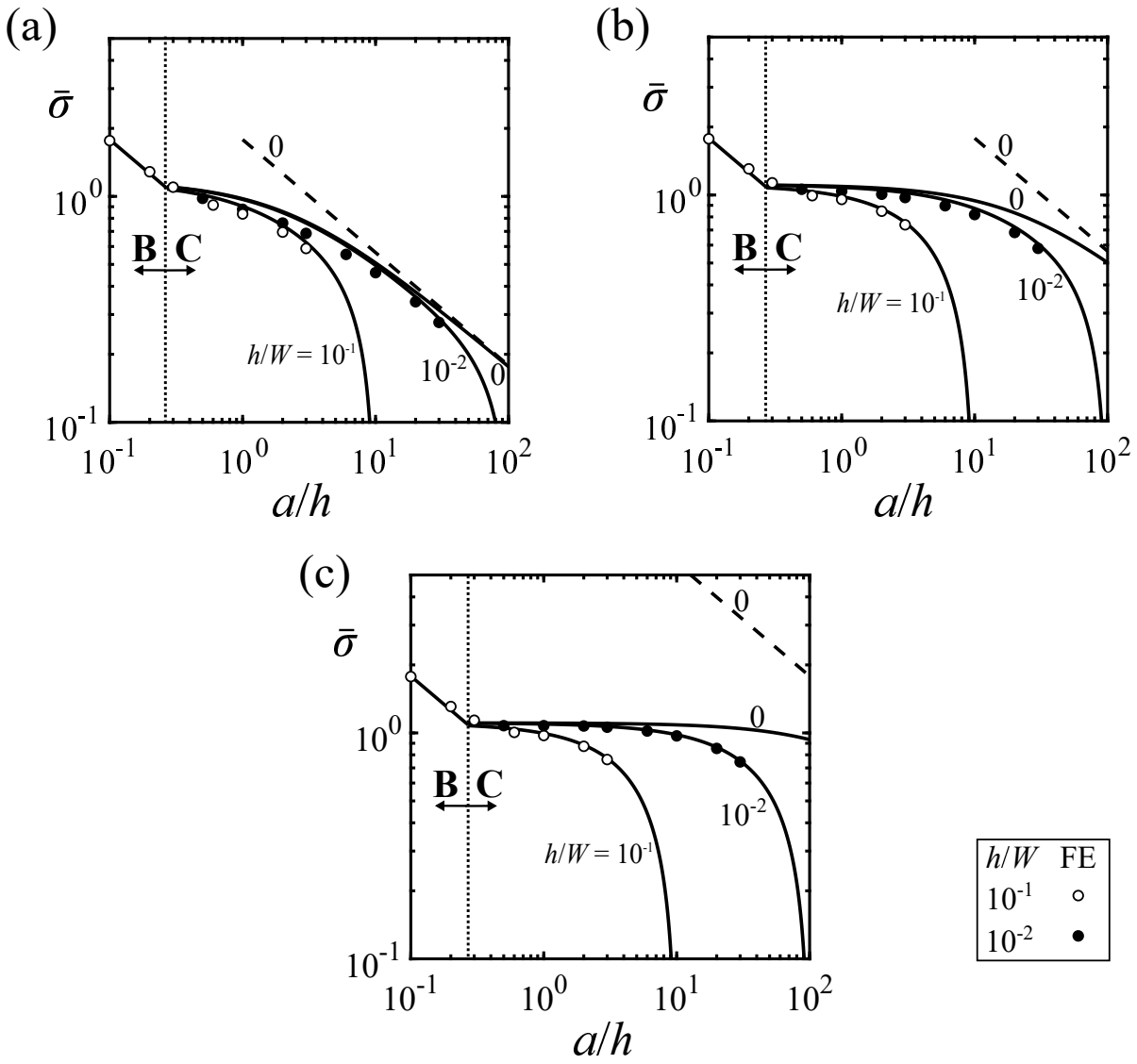

Figure 7.11 Predicted $\bar{\sigma}$ versus a/h data by the FE model shown in Fig. 7.10a for $h/W = 10^{-2}$ and $h/W = 10^{-1}$ for (a) $\bar{E}_2/\bar{E}_1 = 10^{-1}$, (b) $\bar{E}_2/\bar{E}_1 = 10^{-2}$, and (c) $\bar{E}_2/\bar{E}_1 = 10^{-3}$. In regime B, the strength is predicted by Eq. 7.10. In regime C, the strength is predicted via Eq. 7.25. The dashed asymptotic limit lines in regime C are given by Eq. 7.12.

7.3.2 Finite element simulations for a crack in an elastic sandwich layer with a cohesive zone

The strength of the sandwich specimen, as defined in Fig. 7.1, has also been computed by accounting for the presence of a cohesive zone at the crack tip. A layer of tensile cohesive elements is now included in the FE model of the previous section, see Fig. 7.10b. The tensile cohesive zone extends along the x-axis from the crack tip to the free surface at the right-hand side of the sandwich layer. The traction T versus separation δ law of the cohesive elements is linear with slope k until T attains the cohesive strength $\hat{\sigma}$, beyond which $T = \hat{\sigma}$. The adhesive and the substrate materials are treated as isotropic, homogeneous and linear, elastic solids. Simulations are performed for normalised crack lengths ranging from $a/h = 0.03$ to $a/h = 30$, with $h/W = 10^{-2}$ and $h/W = 10^{-1}$. As for the FE simulations absent a cohesive zone, the Young's modulus of the substrate material E_1 is held fixed while a range of values are assumed for the Young's modulus of the adhesive layer; the Poisson's ratios of substrate and layer are held fixed at $\nu = \nu_1 = \nu_2 = 0.3$.

The substrate and the adhesive layer are meshed by 8-noded bi-quadratic plane strain elements (CPE8), and 4-noded cohesive elements (COH2D4) are used for the cohesive elements. Define l_e as the characteristic cohesive element size. Then, an accurate numerical solution requires:

$$\frac{l_e k}{E_2} \gg 1 \tag{7.42}$$

Additionally, l_e has to be sufficiently small to resolve the cohesive zone at the crack tip: $l_e/l_S \leq 1$ (Betegón and Martínez-Pañeda, 2017). A mesh sensitivity study led to the choice $l_e k/E_2 = 100$. The total number of elements depends upon the choice of a and lies between 150 000 and 250 000. For each simulated geometry, the remote tensile stress σ^∞ is incremented in the range $\sigma^\infty/\hat{\sigma} = 0.1$ to $\sigma^\infty/\hat{\sigma} = 0.99$, and the associated value of cohesive zone opening at the crack tip δ^{tip} is determined. Upon writing $\sigma^\infty = \sigma_f^\infty$, the toughness Γ, corresponding to any imposed value of σ^∞, is obtained by:

$$\Gamma = \hat{\sigma}\delta^{\text{tip}} - \frac{\hat{\sigma}^2}{2k} \tag{7.43}$$

and thereby the value of l_S is obtained via Eq. 7.6. The FE predictions are presented in the form of failure maps with axes (l_S/h, a/h) for a modulus mismatch ratio $\bar{E}_2/\bar{E}_1 = 10^{-1}$, $\bar{E}_2/\bar{E}_1 = 10^{-2}$ and $\bar{E}_2/\bar{E}_1 = 10^{-3}$, in Figs. 7.12a, 7.12b, 7.12c, respectively. In each plot, contours of the normalised strength ratio are presented for $h/W = 10^{-2}$ and $h/W = 10^{-1}$, and the analytical Eqs. 7.29 (adhesive-governed regime) and 7.38 (substrate-governed regimes) are included, along with the active failure regime, as implied by the analytical formulae. The analytical predictions are in close alignment with the FE results.

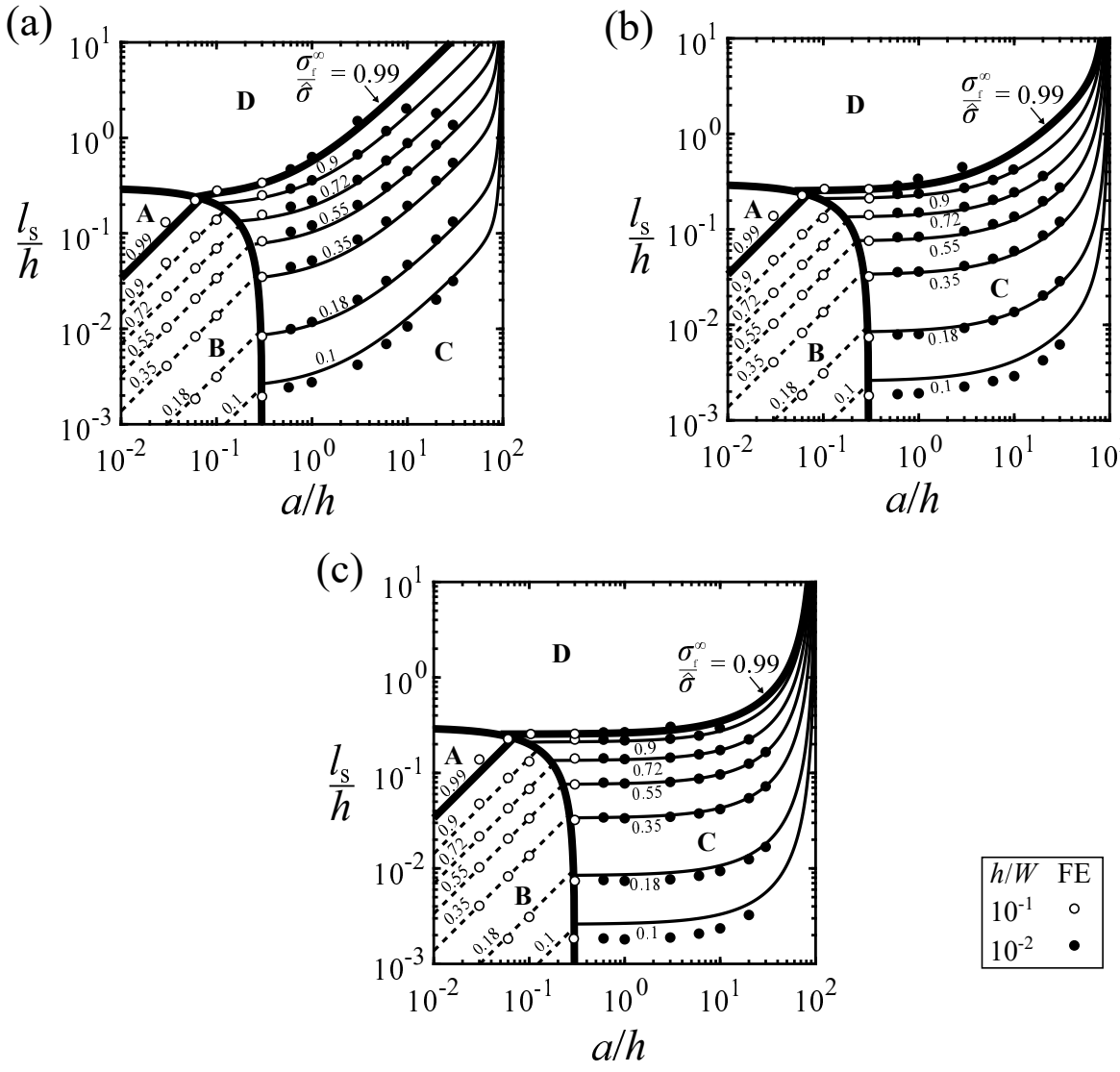

Figure 7.12 Failure map of l_S/h versus normalised crack length a/h for (a) $\bar{E}_2/\bar{E}_1 = 10^{-1}$; (b) $\bar{E}_2/\bar{E}_1 = 10^{-2}$; and (c) $\bar{E}_2/\bar{E}_1 = 10^{-3}$. The strength contours in the adhesive-governed region (regimes A and B) and the substrate-governed region (regimes C and D) are predicted via analytical Eqs. 7.29 and 7.38, respectively.

7.4 Concluding remarks

The tensile strength of an adhesive joint, comprising an adhesive layer made of a linear, elastic material of Young's modulus E_2 and two substrates made from a linear, elastic material of modulus E_1, is predicted as a function of crack length and material mismatch ratio E_2/E_1.

Consider first the case of an elastic, brittle response for a Griffith crack. The relation between the normalised tensile strength and normalised crack length switches from an adhesive-governed strength regime for the case where the crack is much smaller than the adhesive layer height to a substrate-governed strength regime for the case where the crack is much longer than the adhesive layer height. The normalised strength of the joint is independent of normalised crack length for intermediate crack lengths up to a value on the order of a structural length scale hE_2/E_1. This scale is on the order of 1 metre when the layer height equals one millimetre and the elastic modulus of the substrate is one thousand times that of the adhesive layer. The in-plane structural dimensions (including crack length) must exceed this structural dimension in order for a remote K-field to exist within the substrate.

The role of crack tip plasticity on the normalised strength versus normalised crack length curve is explored by the use of a strip yield model. Comprehensive joint design maps are presented to show fracture mechanism maps as a function of modulus mismatch ratio and material non-linearity. When the sum of crack length and cohesive zone length is less than 0.3 times the layer height, the effect of elastic mismatch between substrate and adhesive layer has only a minor influence upon the macroscopic fracture strength of the joint. For this case, the cracked adhesive layer behaves as a centre-crack in an infinite solid made from adhesive, and a transition from toughness control to strength control occurs when the crack length is comparable to that of the cohesive zone length. Alternatively, when the sum of crack length and cohesive zone length exceeds 0.3 times the layer height, the elastic mismatch plays a major role; again there is a transition from toughness control to strength control, but it occurs at a ratio of crack length to layer thickness that depends upon both the elastic mismatch and the ratio of cohesive zone length to layer height.

Finite element simulations are conducted to verify the analytical framework. Excellent agreement between the finite element results and the analytical predictions is obtained. An experimental validation is performed in the subsequent chapter by conducting tensile tests on a sandwich layer comprising a centre-cracked cellulose acetate strip adhered to two aluminium alloy substrates.

Chapter 8

Case study: tensile fracture of a cellulose acetate-aluminium alloy sandwich layer

Experimental support is presented for the analytical framework constructed in the previous chapter. Emphasis is placed on the confirmation of the existence of the competing failure regimes of the failure maps. This is done for the choice of a joint comprising an 'adhesive layer' made from a centre-cracked cellulose acetate strip and substrates made from an aluminium alloy. The tensile strength of the cellulose acetate-aluminium sandwich joint is measured as a function of crack length. The experimental results are compared with the analytical predictions. Additional uniaxial tensile tests and fracture toughness tests are conducted to characterise the cellulose acetate tape.

8.1 Materials and methods

8.1.1 Uniaxial tensile and fracture toughness tests

The cellulose aceate tape[1] is characterised via uniaxial tensile tests and fracture toughness tests. A flat dogbone geometry, as shown in Fig. 8.1a, with the longitudinal direction of the tape aligned along the loading direction, was used to determine the nominal stress S versus nominal

[1] Scotch Magic 810 tape from 3M (Maplewood, US). The tape comprises a backing of cellulose acetate and an acrylic adhesive layer. The thickness of the backing absent the adhesive layer is close to 0.04 mm as measured with a micrometer.

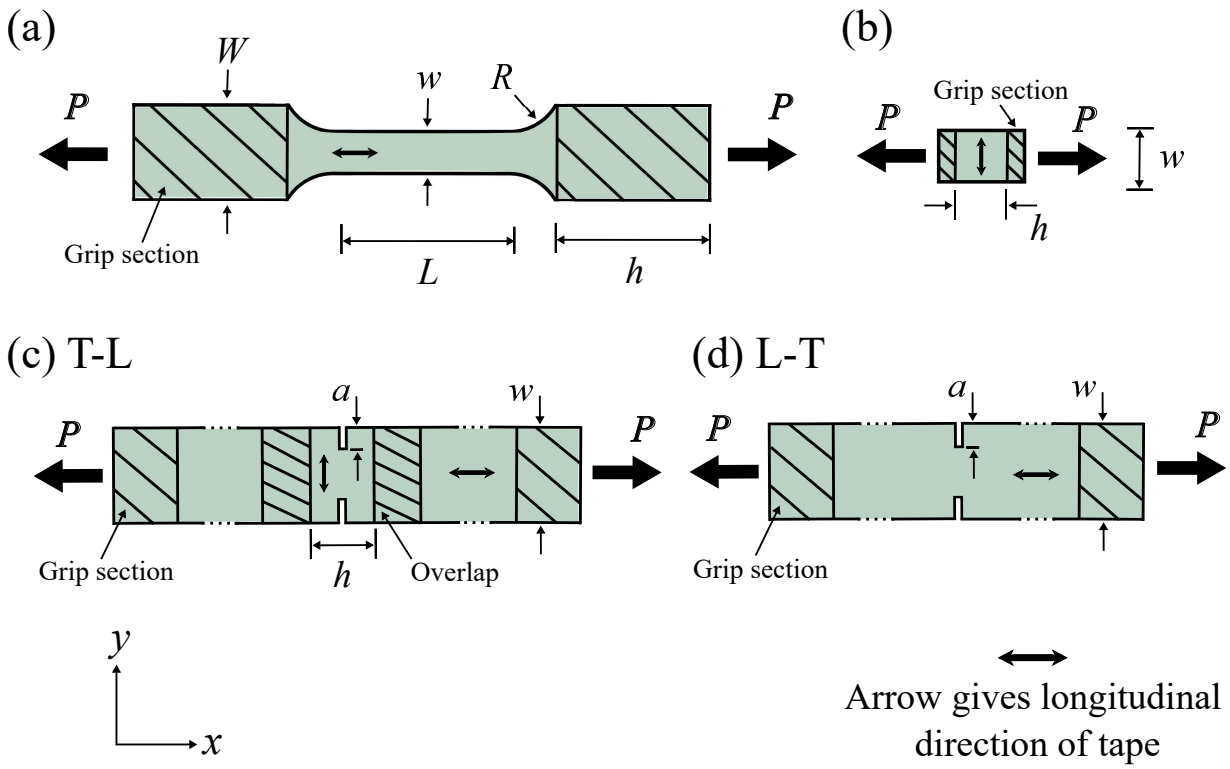

Figure 8.1 Specimen geometries for the uniaxial tensile and fracture toughness tests on the cellulose acetate tape. (a) Dogbone geometry with the tensile load applied along the longitudinal direction of the tape (W = 24 mm, w = 6.4 mm, h = 40 mm, L = 50 mm, R = 15.6 mm). (b) A strip geometry with the tensile load applied along the transverse direction of the tape (w = 10 mm, h = 14 mm). (c) A T-L DENT specimen with w = 24 mm, h = 10 mm, and (d) a L-T DENT specimen with w = 24 mm.

strain e curve. Tensile tests are conducted over two decades of nominal strain rate; at least three uniaxial tensile tests were conducted for each strain rate. The nominal stress-strain curve was also measured in uniaxial tension at a nominal strain rate of 10^{-1} s^{-1} using the strip specimen shown in Fig. 8.1b, for which the longitudinal direction of the tape was orthogonal to the loading direction. The nominal strain during the uniaxial tensile tests was measured using a laser extensometer with a gauge length of 10 mm.

The critical mode I (plane stress) stress-intensity factor K_c of the cellulose acetate tape was measured using a double edge-notched tension (DENT) specimen. The T-L DENT specimen (defined in Fig. 8.1c) contained an initial pre-crack aligned with the longitudinal direction of the tape, whereas the L-T DENT specimen (defined in Fig. 8.1d) contained an initial pre-crack

aligned with the transverse direction of the tape. The pre-cracks were cut with a sharp razor blade, and the plane-stress, mode I fracture toughness K_c was calculated by:

$$K_c = F\sigma_f^{\infty}\sqrt{\pi a} \tag{8.1}$$

where σ_f^{∞} is the tensile fracture strength of the specimen corresponding to the peak load, and the finite width correction factor F reads (Tada et al., 2000; Benthem and Koiter, 1972):

$$\left[1.122 - 0.561\frac{a}{W} - 0.205\left(\frac{a}{W}\right)^2 + 0.471\left(\frac{a}{W}\right)^3 - 0.19\left(\frac{a}{W}\right)^4\right]\left(1-\frac{a}{W}\right)^{-\frac{1}{2}} \tag{8.2}$$

The length a of the pre-crack ranged from a = 1 mm to a = 6 mm for both the T-L and the L-T DENT specimens. Two tests were conducted for each value of a and for each geometry, using a cross-head speed of 1 mm s^{-1}.

Now, write the $\dot{P}$ and $\dot{K}^{\infty}$ as the time rate change of the load and remote stress intensity factor, respectively. Consequently, $\dot{K}^{\infty}$ is given by:

$$\dot{K}^{\infty} = \dot{P}\frac{(\pi a)^{\frac{1}{2}}}{wt} \tag{8.3}$$

where w and t refer to the nominal width and thickness, respectively, of the DENT specimens. The dependence of K_c upon $\dot{K}^{\infty}$ for the T-L DENT specimen geometry of Fig. 8.1c was investigated by selected values of the cross-head speed from 0.3 mm s^{-1} to 6 mm s^{-1} for an initial crack length a = 2 mm.

In addition, uniaxial tensile tests are conducted on the aluminium foil with flat dogbone geometries (shown in Fig. 8.1a) at a strain rate equal to 10^{-2} s^{-1}. The tensile tests were conducted via a dogbone geometry with the longitudinal direction of the tape orthogonal to the loading direction and via a dogbone geometry with the longitudinal direction of the tape aligned with the loading direction.

8.1.2 Tensile tests on cellulose acetate-aluminium sandwich specimens

Consider a centre-cracked sandwich specimen, with a cellulose acetate strip sandwiched between aluminum alloy substrates as shown in Fig. 8.2. The sandwich layer comprises a cellulose acetate strip adhered to two aluminum alloy substrates[2] of identical thickness to that of the cellulose acetate strip. In turn, the aluminium alloy substrates are adhered to aluminium alloy extension sheets of thickness 1.5 mm, which are loaded in tension by the loading pins of a screw-driven test machine as shown in Fig. 8.2.

The direction of the cellulose acetate tape is aligned with a centre-crack of length $2a$ as shown in Fig. 8.2. The tensile failure strength σ_f^∞ of the sandwich layer was measured as a function of crack length $2a$. The remote tensile stress σ^∞ was deduced from the applied load as follows:

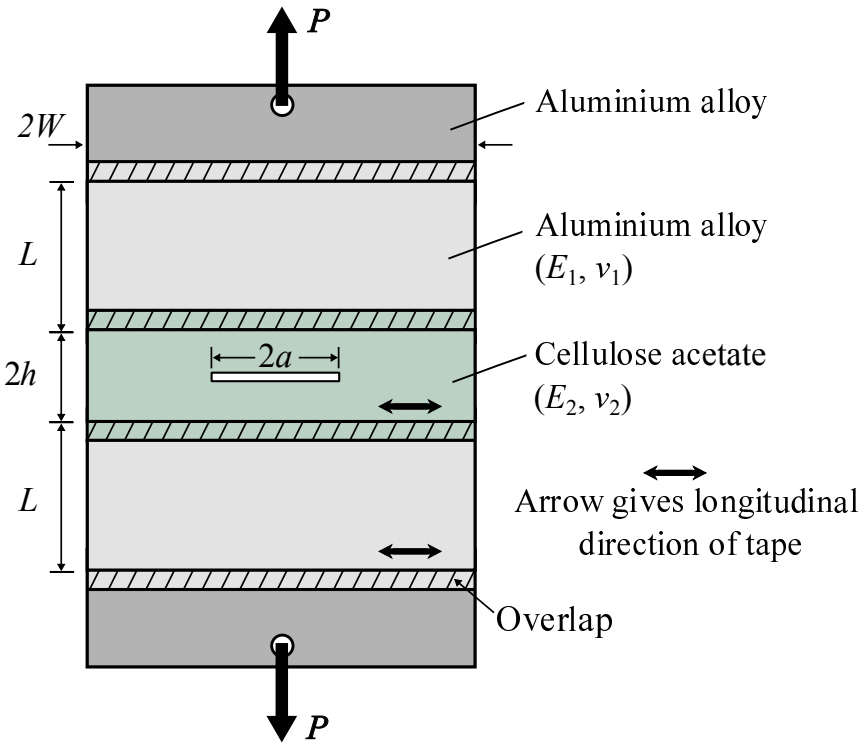

Figure 8.2 Sandwich specimen made from cellulose acetate tape containing a centre-crack of length adhered to a tape of an aluminium alloy. $L \approx 35$ mm and $W = 50$ mm.

[2] AT500 aluminium alloy (grade 8011) tape from Advance Tapes Int. Ltd. (UK). The tape comprises of a an aluminium alloy backing and an acrylic adhesive layer. The thickness of the aluminium layer absent the adhesive layer is close to 0.04 mm as measured with a micrometer.

$$\sigma^{\infty} = \frac{P}{2Wt} \tag{8.4}$$

Tensile tests with the sandwich specimens were performed for two selected values of adhesive layer height (h = 1 mm and h = 5 mm) and for a range of crack lengths between a = 1 mm to a = 25 mm, for both values for h. The tests were conducted at a displacement rate of 1 mm s^{-1} for the specimens with h = 5 mm, and at a rate of 0.2 mm s^{-1} for the specimens with h = 1 mm, to ensure a constant value of strain rate within the cellulose acetate tape (remote from the crack tip). At least three tests per joint geometry were conducted.

8.2 Results and discussion

The nominal stress S is plotted as a function of nominal strain e in Fig. 8.3 for both tensile geometries for the cellulose acetate. A small degree of anisotropy is evident. The measured values of Young's modulus E and yield strength σ_y of the cellulose acetate for each strain rate are reported in Table 8.1.

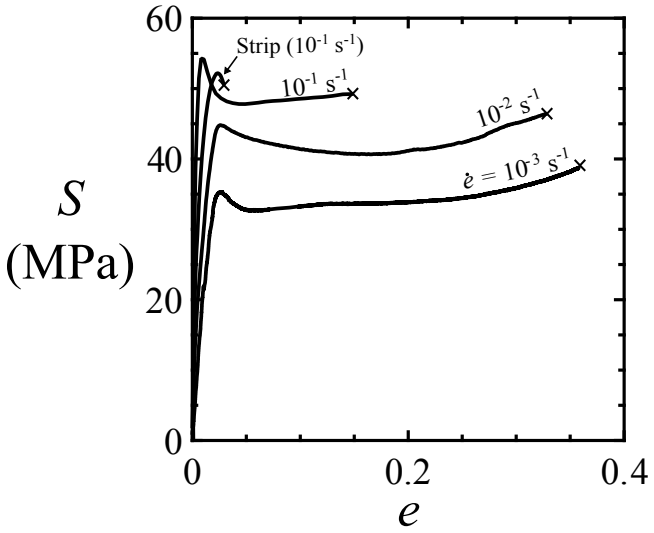

Figure 8.3 Nominal stress S plotted as a function of nominal strain e for the cellulose acetate tape in uniaxial tension at three nominal strain rates using the dogbone specimen of Fig. 8.1a, and at a nominal strain rate of 10^{-1} s^{-1} for the strip specimen of Fig. 8.1b. Crosses at the end of the curve denote failure of the specimen.

Table 8.1 Measured Young's modulus E and yield strength σ_y of the cellulose acetate tape. The uncertainty corresponds to a 95% confidence level of two standard deviations. The dogbone geometry is sketched in Fig. 8.1a, and the strip geometry is sketched in Fig. 8.1b.

$\dot{e}$ (s^{-1})	E (GPa)	σ_y (MPa)	Geometry
10^{-3}	1.7 ± 0.6	36.1 ± 2.8	Dogbone
10^{-2}	3.2 ± 0.9	45.3 ± 3.0	Dogbone
10^{-1}	7.1 ± 0.8	56.1 ± 4.4	Dogbone
10^{-1}	6.4 ± 1.0	53.9 ± 4.8	Strip

The nominal stress S is plotted as a function of nominal strain e in Fig. 8.4 for both tensile aluminium alloy geometries. A small degree of anisotropy is evident. The yield strength[3] of the aluminium alloy at a nominal strain rate equal to 10^{-2} s^{-1} is close to 70 MPa.

The measured load versus cross-head displacement curves of the cellulose acetate DENT specimens were linear in nature, and the maximum load corresponded to brittle fracture with unstable crack propagation from the tip of the pre-crack. The measured values for the plane-stress fracture toughness K_c of the cellulose acetate tape are plotted as a function of initial crack length a/W in

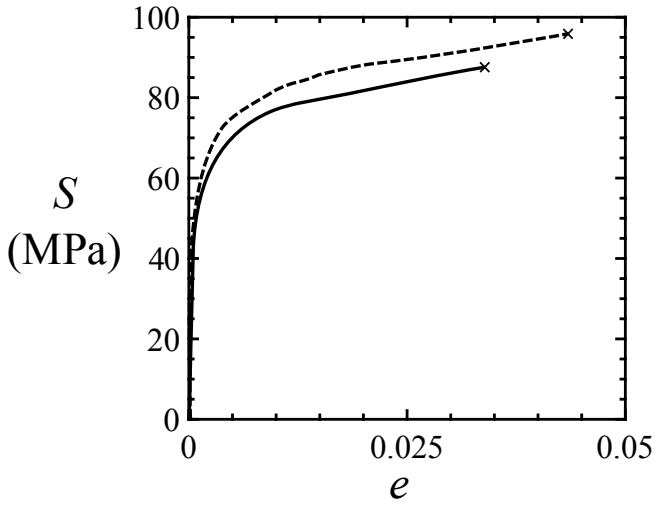

Figure 8.4 Nominal stress S plotted as a function of nominal strain e for the aluminium alloy tape in uniaxial tension at a nominal strain rate equal to 10^{-2} s^{-1}. The tensile tests are conducted with a dogbone geometry (see Fig. 8.1a) with the longitudinal direction of the tape orthogonal to the loading direction (dashed) and with a dogbone geometry (see Fig. 8.1a) with the longitudinal direction of the tape aligned with the loading direction (solid line).

[3] Determined via the 0.002 strain offset method.

Fig. 8.5a. The effect of loading rate upon K_c is reported in Fig. 8.5b. As shown in Figs. 8.5a and 8.5b, the value of K_c is independent of crack length, crack orientation and loading rate (within the range explored). Based upon a total of 34 individual measurements, K_c = 3.0 $\pm$ 0.4 MPa (where the uncertainty corresponds to 95% confidence level of two standard deviations).

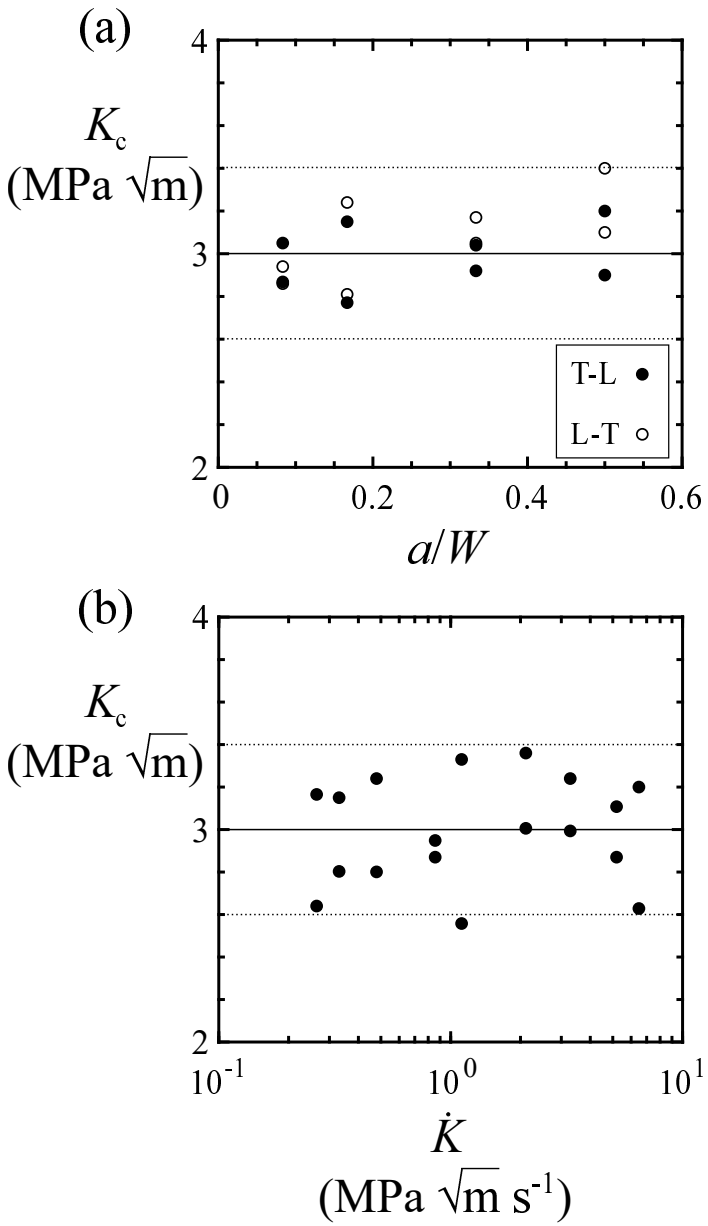

Figure 8.5 Plane stress, fracture toughness measurements for the cellulose acetate tape: (a) fracture toughness K_c versus normalised pre-crack length a/W, for the geometries shown in Figs. 8.1c and 8.1d; (b) fracture toughness K_c versus time derivative of the remote K-field $\dot{K}$. Crack length a is measured to an accuracy of 0.2 mm. The mean and range of fracture toughness values are included in each figure as a solid line and dotted lines, respectively.

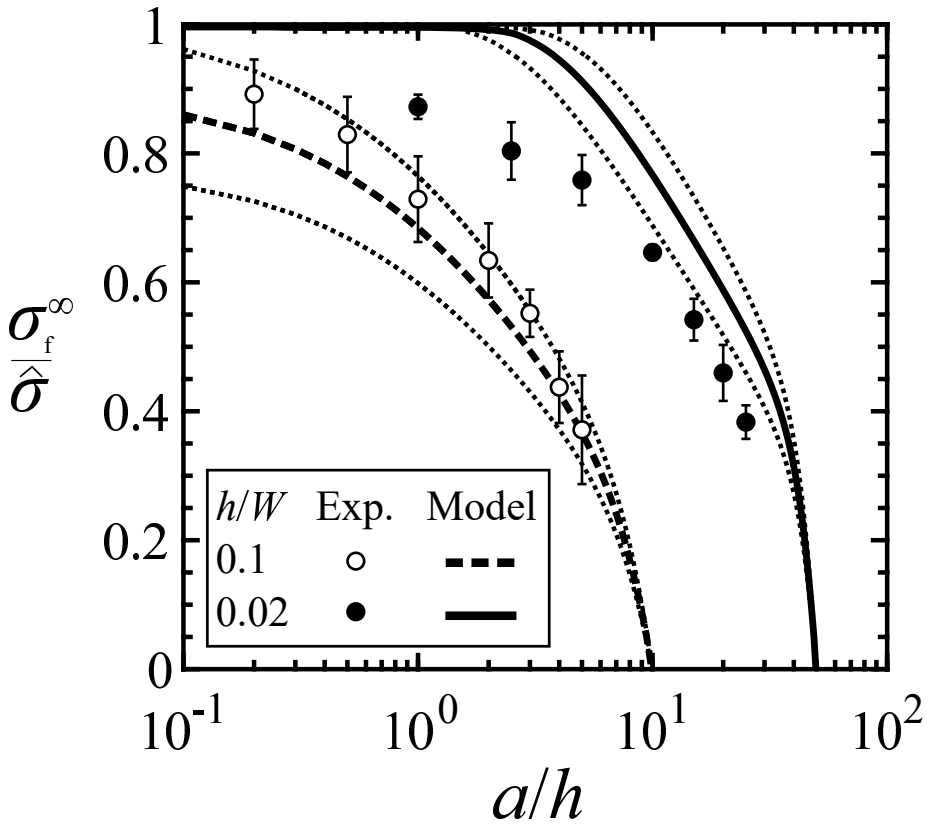

Figure 8.6 Measured and predicted strength $\sigma_f^\infty/\hat{\sigma}$ of the cellulose acetate-aluminium alloy sandwich specimens versus normalised crack length a/h for two selected values of joint adhesive layer height: $h/W = 0.1$ and $h/W = 0.02$. The values of l_S/h are 0.2 and 1 for h/W equal to 0.1 and 0.02, respectively.

The measured normalised failure strength $\sigma_f^\infty/\hat{\sigma}$ of the centre-cracked cellulose acetate-aluminium alloy sandwich layer is reported in Fig. 8.6 as a function of crack length a/h for $h/W = 0.1$ and $h/W = 0.02$. For this plot, it is assumed that $\hat{\sigma}$ equals 54 MPa, corresponding to the average tensile yield strength of the strip specimen (see Fig. 8.3) at a strain rate of 10^{-1} s^{-1}.

In order to include predictions according to the analytical model derived in Section 7.2.2 in Fig. 8.6, it is first necessary to deduce the value of the material reference scale l_S. This, and other pertinent material properties, were estimated as follows. The elastic constants, $\bar{E}$ and $\bar{\nu}$ are simply taken as their plane stress values of E and ν. At the appropriate strain rate, $E = 6.4$ GPa, ν_2 is taken to be 0.38 based on the work of Tsou et al. (1995). Moreover, $K_c = \sqrt{E_2\Gamma} = 3.0 \pm 0.4$ MPa$\sqrt{\text{m}}$, the reference length scale for the cellulose acetate material is calculated via Eq. 7.6: $l_S = 0.98 \pm 0.28$ mm. The Young's modulus of the aluminum alloy

E_1 is 70 GPa and $\nu_1 = 0.33$ (Callister, 2007), implying a modulus mismatch ratio of $E_2/E_1 = 0.09$.

The strength predictions via Eq. 7.37 are shown in Fig. 8.6 for three assumed values of l_S as follows. The solid line and dotted lines for $h/W = 0.02$ are for the mean value $l_S = 0.98$ mm and the upper and lower limits (l_S equals 1.26 mm and 0.70 mm, respectively). Note that the mean value of l_S/h equals 1 for this choice of $h/W = 0.02$, and this implies that regime D is active for $a/h < 3$ while regime C is active for $a/h > 3$, see Fig. 7.9 in Section 7.2.3. The measured strengths broadly support this: the strength drops with increasing a/h in the regime C of toughness control. The strength ratio σ_f^∞ is close to 0.9 at $a/h < 0.3$, which is within 10% of the plastic collapse load, $\sigma_f^\infty/\hat{\sigma} = 1$. The source of this minor discrepancy is unclear, but might be related to the uncertainty of the local strain rate of the material elements at the crack tip.

Now consider the case $h/W = 0.1$. The thick dashed line and associated dotted lines for $h/W = 0.1$ assume a mean value $l_S = 0.98$ mm and the upper and lower limiting values of l_S equal to 1.26 mm and 0.70 mm, respectively. Note that the mean value of l_S/h equals 0.2 for this choice of $h/W = 0.1$. Examination of the maps of Figs. 7.7 and 7.9 of Section 7.2.3 reveals that regime C (toughness control) dominates over strength control, regime D, and the measurements support this: the strength drops with increasing a/h as predicted by Eq. 7.37, to within scatter. In summary, the analytical model, with the attendant maps presented in Section 7.2.3, is supported by the series of experiments.

8.3 Concluding remarks

Experimental validation of the analytical framework in Chapter 7 is achieved by measuring the sensitivity of fracture strength to crack length and layer height for a centre-cracked strip made from cellulose acetate layer, sandwiched between aluminium alloy substrates. Uniaxial tensile tests and fracture toughness tests are conducted to characterise the cellulose acetate tape. The measured value of the material reference length scale l_S is found to equal 1 mm for the cellulose acetate, and two values of layer thickness are employed, $h = 1$ mm and $h = 5$ mm. Thus, l_S/h equals 0.2 and $l_S/h = 1$, along with a modulus mismatch ratio $E_2/E_1 = 0.09$; these values have been added to the map of Fig. 7.9 in Section 7.2.3, and values of crack length a/h are employed

to ensure that failure is by plastic collapse within regime D (sufficiently small a/h) or within regime C (toughness controlled at a sufficiently large a/h) for the choice of $l_S/h = 1$.

In addition, it is instructive to re-visit the tensile strength measurements of the MMA-aluminium alloy butt joints presented in Chapter 6, see Fig. 6.8. Based on the characterisation of the MMA adhesive, the material length scale l_S is estimated to be close to 0.9 mm, the modulus mismatch ratio $\bar{E}_2/\bar{E}_1$ is close to 4.5×10^{-3}. Assuming[4] $\bar{\nu}_1 = 0.49$ for the aluminium alloy and $\bar{\nu}_2 = 0.6$ for the MMA based on the work of Moller et al. (2015), the normalised strength σ_f^∞/σ_y of the four butt joint geometries, see Table 6.1, is predicted as a function of 'crack' length a/h via Eq. 7.37 in Fig. 8.7. The measured combination of σ_f^∞/σ_y and a/h values is included in Fig. 8.7

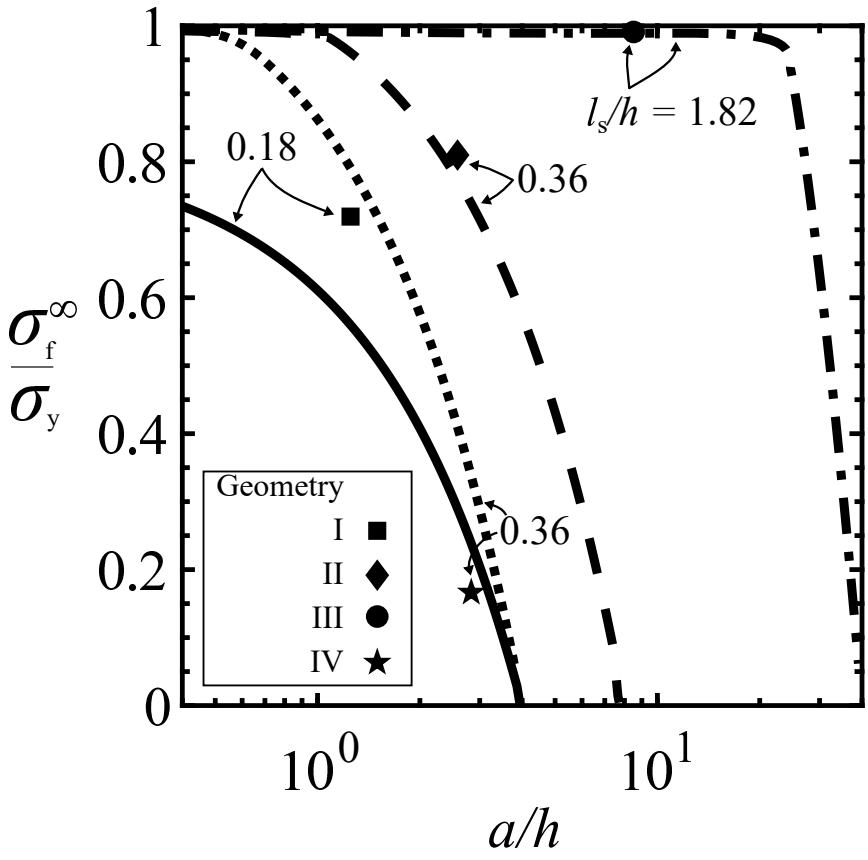

Figure 8.7 Measured and predicted strength of the MMA-aluminium alloy butt joints as a function of normalised 'crack' length a/h for the four butt joint geometries tested in Chaper 6, see Table 6.1 and Fig. 6.8. Predictions are made via Eq. 7.37 assuming $\bar{E}_2/\bar{E}_1 = 4.5 \times 10^{-3}$, $\bar{\nu}_1 = 0.49$, $\bar{\nu}_2 = 0.6$ and the values for l_S/h summarised in Table 6.3.

[4] Plane strain conditions are assumed, see the plane strain definition for $\bar{\nu}$ and $\bar{E}$ in Section 7.1.

for each geometry. The predicted values for σ_f^∞/σ_y via the analytical formula are close to the observed values for σ_f^∞/σ_y (within scatter[5]). The existence of competing fracture regimes (as shown in the Fig. 6.8 failure map presented in Section 7.2.3) is also supported by the results of the MMA-aluminium alloy case study: toughness-controlled fracture (regime C) takes place for the Geometry I, II, and IV butt joints, whereas plastic collapse (regime D) is observed for the Geometry III butt joint.

[5] This scatter may be attributed to (i) the uncertainty of the strain rate of the material elements close to the 'crack' tips and to (ii) the assumption that the cluster of three-dimensional voids and cracks on the fracture surface is idealised by one centre penny-shaped crack, see Fig. 6.7c.

Chapter 9

Conclusions and future work

The focus of this thesis is on the deformation and fracture of MMA-based polymers in the context of void growth. Two applications of interest were considered. Void growth during solid-state nanofoaming was analysed in Part I of the thesis, and fracture of an adhesive layer from a pre-existing void or crack was explored in Part II. The main findings of each part are summarised in the following two sections. Suggestions for future work in the field are outlined too.

9.1 Conclusions and future work for Part I

The first part of the thesis focused on the prediction of void growth during solid-state nanofoaming of PMMA by CO_2. First, uniaxial tensile tests were conducted on two PMMA grades of relatively low and high molecular weight, but with a close to identical glass transition temperature, to obtain calibrated constitutive equations for the void growth predictions. The tensile tests were performed close to the glass transition temperature of the PMMA grades, and over two decades of nominal strain rate. The modulus, flow strength, and failure strain were plotted as a function of temperature via deformation and failure maps for selected strain rates. Three constitutive or deformation regimes were identified for the high molecular weight PMMA: the glassy, glass transition, and rubbery regime. The rubbery regime was found to be absent for the low molecular weight PMMA: a transition to a viscous regime takes place at temperature above the glass transition temperature.

Second, PMMA nanofoams were manufactured from the two PMMA grades via solid-state foaming using CO_2 as the blowing agent. The PMMA grades were subjected to identical saturation conditions, and foaming tests were conducted at selected foaming times and foaming temperatures. It was found that the molecular weight of the PMMA has a profound effect on the final morphology of the PMMA nanofoams. When subjected to identical saturation and foaming conditions, the observed average void size of the high molecular weight PMMA nanofoams is an order of magnitude less than that of the low molecular weight PMMA nanofoams. A limit in attainable porosity was also observed. The limit porosity was found to be close to 0.6 for the high molecular weight PMMA grade and equal to 0.75 for the PMMA grade of low molecular weight. A transition from a closed-cell to an open-celled microstructure at a porosity close to this limit porosity was observed.

Third, a one-dimensional cavity expansion model was developed to predict void growth during solid-state nanofoaming of the two PMMA grades with CO_2. The model makes use of the calibrated constitutive equations for each grade, and the effect of dissolved CO_2 is accounted for by a shift in the glass transition temperature of the PMMA. In addition, a spatially uniform CO_2 concentration was assumed, as the diffusion of CO_2 from the PMMA-CO_2 matrix to the embedded, as-nucleated voids is sufficiently fast. The predicted porosity versus foaming time curves by the void growth model were found to be in good agreement with those measured for porosities well below the maximum observed porosity. Moreover, a close agreement between the predicted and observed sensitivity to molecular weight was obtained. This result suggested that the observed difference in constitutive response close to the glass transition temperature between the PMMA grades leads to the measured difference in final porosity. The outcomes of the void growth simulations also indicated that void growth does not occur within either the rubbery or the viscous regime of the PMMA grades of high and low molecular weight, respectively. Moreover, hypotheses for cell wall tearing were explored to explain the transition from closed-celled to open-celled microstructures at porosities close to the maximum observed porosity. It was found that cell wall rupture is sensitive to the thickness of the cell wall and that the minimum value of ligament thickness to prevent cell wall tearing is of the same order of magnitude as the end-to-end distance of the polymer chains. The analysis suggests that when the cell wall thickness becomes close to this minimum value, a transition from a closed-celled to an open-celled microstructure takes place, and further expansion of the foam is impeded.

The void growth model and the insights from the cell wall tearing analysis were used to discuss the limits of the solid-state foaming process when attempting to produce foams with a thermal conductivity close to or lower than air, i.e. nanofoams of high porosity (> 0.85) comprising nano-sized voids. It was recognised that many polymer precursors (besides MMA-based polymers) may be used to produce nanofoams with a sufficiently high nucleation density to potentially attain such a morphology. However, the reported final porosities of nanofoams made from these polymeric material systems is close to or below 0.6. Void growth simulations suggest, using the example of PEI nanofoams, that higher porosities may be achieved by a more extensive exploration of the saturation and foaming conditions, than currently done in the experimental nanofoaming literature. The practical foaming window, however, is anticipated to be limited by the existence of a minimum cell wall thickness to prevent rupture of the cell walls. In order to produce nanofoams with porosities close to or above 0.85, the value of the critical ligament thickness is estimated to be close to 5 nm.

There is substantial potential for future work in the field of solid-state nanofoaming. Further studies might include:

- The experimental validation of the void growth model for other polymer precursor materials systems than PMMA. These polymeric materials may include block copolymers, long chain branched polymers, and semi-crystalline polymers. To that end, constitutive equations need to be calibrated to measured stress-strain curves of the material systems of interest. In addition, the dependence of the glass transition temperature of the polymer upon the concentration of dissolved blowing agent may have to be measured as these measurements are typically scarce in the literature (for pressures above 5 MPa).

- Further development of the void growth model: (i) the development of a two- or three-dimensional (finite element) void growth model to explore the interaction of neighbouring voids at elevated porosities and/or the nucleation of voids simultaneously with void growth, and (ii) an improved formulation of the interaction of the polymer and the blowing agent by making use, for example, of more sophisticated, non-ideal gas laws such as the Sanchez-Lacombe equation of state (Sanchez and Lacombe, 1974; Von Konigslow et al., 2017).

- The realisation of an improved understanding of the effect of molecular weight on the solid-state nanofoaming foaming window of a linear, amorphous polymer. A combined experimental and numerical approach such as done in this thesis is recommended.

- A more detailed investigation of cell wall tearing during solid-state nanofoaming. Cell wall rupture is thought to limit the practical foaming window of a polymer material system when attempting to produce nanocellular foams of high porosity. The analysis in this thesis suggested that cell walls rupture when the cell wall thickness is close to the estimated length of the individual polymer chains. An improved understanding of which factors govern cell wall tearing is needed to identify potential polymer material systems which may be used to produce nanofoams with porosity close to or above 0.85. This may be accomplished by a combination of theoretical and experimental work. For instance, studies making use of molecular dynamic simulations (Xia and Keten, 2014) combined with tensile tests on thin polymeric films (Liu et al., 2015; Bay et al., 2018) may lead to new insights. The effect of strain rate and normalised temperature on the magnitude of the the minimum cell wall thickness may be explored too. These insights may lead to novel foaming strategies when combined with void growth simulation outcomes.

9.2 Conclusions and future work for Part II

The second part of the thesis focused on the fracture of a structural adhesive (e.g. MMA) layer from pre-existing voids or cracks. First, tensile tests were conducted on butt joints comprising an MMA adhesive layer (containing macroscopic voids) and two aluminium alloy substrates. The properties of the MMA adhesive were measured by performing additional uniaxial tensile and fracture toughness tests on the bulk MMA adhesive. The outcomes of this preliminary case study demonstrated that the tensile strength of the butt joint is sensitive to the geometry of the joint and the normalised area of the pre-existing voids on the failure surface.

Second, an analytic framework is constructed to predict the tensile strength of a butt joint, comprising a linear, elastic adhesive layer and two linear, elastic substrates, as a function of crack length. Two cases were explored: the case of a Griffith crack where the adhesive layer material has a finite toughness but unbounded cohesive strength, and the case where the adhesive layer

material has both a finite toughness and a finite cohesive strength. The toughness and strength were assumed to be independent of layer height for both cases. For the case of a Griffith crack, the relation between the normalised tensile strength and the normalised crack length switches from an adhesive-governed strength regime, when the crack is much smaller than the adhesive layer height, to a substrate-governed strength regime, when the crack is of the same order as, or much larger than, the adhesive layer height. It was demonstrated that the normalised strength of the joint is independent of normalised crack length for intermediate crack lengths up to a value on the order of a structural length scale which is governed by the magnitude of the adhesive layer height and the magnitude of the elastic modulus mismatch ratio (between substrate and adhesive).

The case of crack tip plasticity was explored by constructing an approximate analytical model by making use of a strip yield model. Comprehensive joint design maps are constructed, illustrating how fracture is governed by modulus mismatch ratio and material non-linearity (i.e. the estimated size of the plastic zone at the crack tip in the bulk adhesive). It was found that when the sum of the crack length and the cohesive zone length is less than 0.3 times the layer height, the effect of the elastic mismatch between substrate and adhesive layer upon the tensile strength of the joint is negligible: the fracture is governed by the adhesive. In this regime, a transition exists between toughness control and strength control when the crack length is of the same order as the adhesive layer height. Alternatively, it was shown that when the sum of the crack length and the cohesive zone length is above 0.3 times the layer height, the elastic mismatch ratio has a major influence on the strength of the joint. Again, there is a transition from toughness- to strength-control, but the ratio of crack length to layer height at which this transition occurs is a function of both the elastic mismatch ratio and the ratio of the cohesive zone length to layer height. Finite element simulations were conducted to verify the analytical theory. Excellent agreement was obtained between the predictions made via the analytical theory and those by the finite element model within the explored range of practical values for modulus mismatch ratio and joint geometry.

Third, experimental support was presented for the analytical framework. The tensile strength of a joint comprising a centre-cracked cellulose acetate ‘layer’ and two aluminium alloy substrates was measured as a function of crack length and adhesive layer height. Additional uniaxial tensile

and fracture toughness tests were conducted to characterise the cellulose acetate. Reasonably close agreement between the predicted and measured strength versus crack length curves was observed.

The following suggestions may be considered for future work:

- A more extensive experimental validation of the analytical theory employing a wider range of elastic mismatch ratios, adhesive materials, and joint geometries.
- A relatively straightforward extension of the analytical framework to mode II fracture to allow strength predictions for common adhesive joint designs such as a simple lap joint. Additional experimental validation is recommended.
- An extension of the analytical model by incorporating (i) the effect of constraint (i.e. the ratio of cohesive zone length to adhesive layer height) on joint toughness and/or (ii) a crack growth resistance (*R*-curve) effect. These extensions might be required for accurate strength predictions of joints comprising a thin layer of a structural adhesive for which these effects are anticipated to be non-negligible (i.e. rubber-modified epoxies).

Appendix A

Finite element simulations of a semi-infinite crack in a sandwich layer

The stress state ahead of the tip of a semi-infinite crack in a sandwich layer, under a remote stress intensity factor K^{∞} is determined by (plane strain) finite element calculations using the implicit solver of ABAQUS (version 6.14). The crack geometry, absent a cohesive zone, is defined in Fig. 7.2. The displacement field associated with a remote mode I K-field of magnitude K^{∞} is applied on a semi-circular outer boundary of radius R enclosing the crack tip as specified by (Anderson, 2005):

$$u_x = \frac{2(1+\nu_1)K^{\infty}}{E_1}\left(\frac{r}{2\pi}\right)^{\frac{1}{2}}\cos\left(\frac{\theta}{2}\right)\left[1-2\nu_1+\sin^2\left(\frac{\theta}{2}\right)\right] \tag{A.1}$$

and

$$u_y = \frac{2(1+\nu_1)K^{\infty}}{E_1}\left(\frac{r}{2\pi}\right)^{\frac{1}{2}}\sin\left(\frac{\theta}{2}\right)\left[2-2\nu_1-\cos^2\left(\frac{\theta}{2}\right)\right] \tag{A.2}$$

where u_{xx} and u_{yy} are the horizontal and vertical displacements of the nodes of the semi-circular boundary in terms of polar (r, θ) coordinates. The substrate and the adhesive layer are discretised by 8-noded bi-quadratic plane strain elements with reduced integration (CPE8R), and quarter point elements are used at the crack tip. The value of R/h is close to 180 000, and the total number of elements is approximately 10 000. The Young's modulus E_1 of the substrate material is held fixed while a range of values are assumed for the Young's modulus E_2 of the adhesive

layer; the Poisson's ratios of substrate and layer are held fixed at $\nu = \nu_1 = \nu_2 = 0.3$. The predicted distribution of the tensile stress component σ_{yy} along the crack plane is given in Fig. 7.3.

Bibliography

Abdel-Wahab, A. A., Ataya, S., and Silberschmidt, V. V. (2016). Temperature-dependent mechanical behaviour of PMMA: Experimental analysis and modelling. *Polymer Testing*, 58:86–95.

Adams, R., Comyn, J., and Wake, W. (1997). *Structural Adhesive Joints in Engineering*. Springer Netherlands, 2nd edition.

Aher, B., Olson, N. M., and Kumar, V. (2013). Production of bulk solid-state PEI nanofoams using supercritical CO2. *Journal of Materials Research*, 28:2366–2373.

Alessi, P., Cortesi, A., Kikic, I., and Vecchione, F. (2003). Plasticization of polymers with supercritical carbon dioxide: Experimental determination of glass-transition temperatures. *Journal of Applied Polymer Science*, 88(9):2189–2193.

Ameli, A., Nofar, M., Park, C. B., Pötschke, P., and Rizvi, G. (2014). Polypropylene/carbon nanotube nano/microcellular structures with high dielectric permittivity, low dielectric loss, and low percolation threshold. *Carbon*, 71:206–217.

Ameli, A., Papini, M., Schroeder, J. A., and Spelt, J. K. (2010). Fracture R-curve characterization of toughened epoxy adhesives. *Engineering Fracture Mechanics*, 77(3):521–534.

Amon, M. and Denson, C. D. (1984). A study of the dynamics of foam growth: Analysis of the growth of closely spaced spherical bubbles. *Polymer Engineering & Science*, 24(13):1026–1034.

Anderson, T. L. (2005). *Fracture Mechanics: Fundamentals and Applications*. CRC Press, 3rd edition.

Arefmanesh, A. and Advani, S. G. (1991). Diffusion-induced growth of a gas bubble in a viscoelastic fluid. *Rheologica Acta*, 30(3):274–283.

Arefmanesh, A. and Advani, S. G. (1995). Nonisothermal bubble growth in polymeric foams. *Engineering*, 35(3):252–260.

Arruda, E. M. and Boyce, M. C. (1993). A three-dimensional constitutive model for the large stretch behavior of rubber elastic materials. *Journal of the Mechanics and Physics of Solids*, 41(2):389–412.

Ashby, M. F. (2010). *Materials Selection in Mechanical Design*. Butterworth-Heinemann, 4th edition.

Ashby, M. F., Blunt, F. J., and Bannister, M. (1989). Flow characteristics of highly constrained metal wires. *Acta Metallurgica*, 37(7):1847–1857.

ASTM (2014). D5045 Standard Test Methods for Plane-Strain Fracture Toughness and Strain Energy Release of Plastic Materials. *ASTM Book of Standards*.

ASTM (2015a). D6226-15 Standard Test Method for Open Cell Content of Rigid Cellular Plastics. *ASTM Book of Standards*.

ASTM (2015b). E1820-15a Standard Test Method for Measurement of Fracture Toughness. *ASTM Book of Standards*.

Ball, J. M. (1982). Discontinuous equilibrium solutions and cavitation in nonlinear elasticity. *Philosophical Transactions of the Royal Society A: Mathematical, Physical and Engineering Sciences*, 306(1496):557–611.

Banea, M. D., Da Silva, L. F., and Campilho, R. D. (2014). The effect of adhesive thickness on the mechanical behavior of a structural polyurethane adhesive. *Journal of Adhesion*, 91(5):331–346.

Barenblatt, G. I. (1962). The mathematical theory of equilibrium cracks in brittle fracture. *Advances in Applied Mechanics*, 7:55–129.

Barlow, E. J. and Langlois, W. E. (1962). Diffusion of gas from a liquid into an expanding bubble. *IBM Journal of Research and Development*.

Barrer, R. M., Barrie, J. A., and Slater, J. (1958). Sorption and diffusion in ethyl cellulose. Part III. Comparison between ethyl cellulose and rubber. *Journal of Polymer Science*, 27(115):177–197.

Bascom, W. D. and Cottington, R. L. (1972). Air Entrapment in the use of structural adhesive films. *The Journal of Adhesion*, 4(3):193–209.

Bascom, W. D., Cottington, R. L., Jones, R. L., and Peyser, P. (1975). The fracture of epoxy- and elastomer-modified epoxy polymers in bulk and as adhesives. *Journal of Applied Polymer Science*, 19(9):2545–2562.

Bauwens-Crowet, C. (1973). The compression yield behaviour of polymethyl methacrylate over a wide range of temperatures and strain-rates. *Journal of Materials Science*, 8(7):968–979.

Bay, R. K., Shimomura, S., Liu, Y., Ilton, M., and Crosby, A. J. (2018). Confinement effect on strain localizations in glassy polymer films. *Macromolecules*, 51(10):3647–3653.

Benthem, J. and Koiter, W. (1972). Asymptotic approximations to crack problems. In Sih, G. C., editor, *Methods of Analysis of Crack Problems*, chapter 3, pages 131–178. Noordhoff International Publishing.

Bernardo, V., Martin-de Leon, J., Pinto, J., Catelani, T., Athanassiou, A., and Rodriguez-Perez, M. A. (2019). Low-density PMMA/MAM nanocellular polymers using low MAM contents: Production and characterization. *Polymer*, 163:115–124.

Betegón, C. and Martínez-Pañeda, E. (2017). A cohesive zone framework for environmentally assisted fatigue. *Engineering Fracture Mechanics*, 185:210–226.

Bin Ahmad, Z. and Ashby, M. F. (1988). Failure-mechanism maps for engineering polymers. *Journal of Materials Science*, 23(6):2037–2050.

Blackman, B. R., Hadavinia, H., Kinloch, A. J., Paraschi, M., and Williams, J. G. (2003). The calculation of adhesive fracture energies in mode I: Revisiting the tapered double cantilever beam (TDCB) test. *Engineering Fracture Mechanics*, 70(2):233–248.

Boyce, M., Socrate, S., and Llana, P. (2000). Constitutive model for the finite deformation stress–strain behavior of poly(ethylene terephthalate) above the glass transition. *Polymer*, 41(6):2183–2201.

Boyce, M. C. and Arruda, E. M. (1990). An experimental and analytical investigation of the large strain compressive and tensile response of glassy polymers. *Polymer Engineering & Science*, 30(20):1288–1298.

Boyce, M. C., Parks, D. M., and Argon, A. S. (1988). Large inelastic deformation of glassy polymers. part I: Rate dependent constitutive model. *Mechanics of Materials*, 7(1):15–33.

Callister, W. D. (2007). *Materials Science and Engineering - An Introduction*. John Wiley & Sons, 7th edition.

Carlberger, T. and Stigh, U. (2010). Influence of layer thickness on cohesive properties of an epoxy-based adhesive-an experimental study. *Journal of Adhesion*, 86(8):816–835.

Cheng, W. M., Miller, G. A., Manson, J. A., Hertzberg, R. W., and Sperling, L. H. (1990). Mechanical behaviour of poly(methyl methacrylate). *Journal of Materials Science*, 25(4):1931–1938.

Chester, R. J. and Roberts, J. D. (1989). Void minimization in adhesive joints. *International Journal of Adhesion and Adhesives*, 9(3):129–138.

Chiou, J. S., Barlow, J. W., and Paul, D. R. (1985). Plasticization of glassy polymers by CO2. *Journal of Applied Polymer Science*, 30(6):2633–2642.

Chow, S. (1980). Molecular interpretation of the glass transition temperature of polymer-diluent systems. *Macromolecules*, 364(12):362–364.

Colton, J. S. and Suh, N. P. (1987). Nucleation of microcellular foam: Theory and practice. *Polymer Engineering & Science*, 27(7):500–503.

Cornes, P. L. and Haward, R. N. (1974). Ductile fracture of rigid poly (vinyl chloride). *Polymer*, 15:149–156.

Costeux, S. (2014). CO2-blown nanocellular foams. *Journal of Applied Polymer Science*, 131(23).

Costeux, S., Khan, I., Bunker, S. P., and Jeon, H. K. (2014). Experimental study and modeling of nanofoams formation from single phase acrylic copolymers. *Journal of Cellular Plastics*, 51(2):197–221.

Costeux, S. and Zhu, L. (2013). Low density thermoplastic nanofoams nucleated by nanoparticles. *Polymer*, 54(11):2785–2795.

Crank, J. (1975). *The Mathematics of Diffusion*. Clarendon Press Oxford, 2nd edition.

da Silva, L. F., Öchsner, A., and Adams, R. D. (2018). *Handbook of Adhesion Technology*. Springer-Verlag Heidelberg, 2nd edition.

Daghyani, H. R., Ye, L., and Mai, Y. W. (1995). Mode-I fracture behaviour of adhesive joints. Part I. Relationship between fracture energy and bond thickness. *The Journal of Adhesion*, 53(3-4):149–162.

Davies, P., Sohier, L., Cognard, J. Y., Bourmaud, A., Choqueuse, D., Rinnert, E., and Créac'hcadec, R. (2009). Influence of adhesive bond line thickness on joint strength. *International Journal of Adhesion and Adhesives*, 29(7):724–736.

Davis, M. and Bond, D. (2010). The importance of failure mode identification in adhesive bonded aircraft structures and repairs. *ISASI Australian Safety Seminar, Canberra*.

De Gennes, P. G. (1976). Dynamics of entangled polymer solutions. I. the Rouse model. *Macromolecules*, 9(4):587–593.

Dillard, D. A. (2010). *Advances in structural adhesive bonding*. Woodhead Pub.

Doi, M. and Edwards, S. F. (1978a). Dynamics of concentrated polymer systems part 1. *J. Chem. Soc., Faraday Trans. II*, 74:1789–1801.

Doi, M. and Edwards, S. F. (1978b). Dynamics of rod-like macromolecules in concentrated solution. Part 2. *Journal of the Chemical Society, Faraday Transactions 2: Molecular and Chemical Physics*, 74(6):918–932.

Doi, M. and Edwards, S. F. (1986). *The Theory of Polymer Dynamics*. Oxford University Press.

Dooling, P. J., Buckley, C. P., Rostami, S., and Zahlan, N. (2002). Hot-drawing of poly(methyl methacrylate) and simulation using a glass–rubber constitutive model. *Polymer*, 43(8):2451–2465.

Du, J., Thouless, M. D., and Yee, A. F. (1998). Development of a process zone in rubber-modified epoxy polymers. *International Journal of Fracture*, 92(3):271–286.

Du, J., Thouless, M. D., and Yee, A. F. (2000). Effects of rate on crack growth in a rubber-modified epoxy. *Acta Materialia*, 48(13):3581–3592.

Dugdale, D. (1960). Yielding of steel sheets containing slits. *Journal of the Mechanics and Physics of Solids*, 8(2):100–104.

Dutriez, C., Satoh, K., Kamigaito, M., and Yokoyama, H. (2012). Nanocellular foaming of fluorine containing block copolymers in carbon dioxide: The role of glass transition in carbon dioxide. *RSC Advances*, 2(7):2821–2827.

Eaves, D. (2004). *Handbook of polymer foams*. Rapra Technology Limited (UK).

Epstein, P. S. and Plesset, M. S. (1950). On the stability of gas bubbles in liquid-gas solutions. *The Journal of Chemical Physics*, 18(11):1505–1509.

Evans, A. G., Ahmad, Z. B., Gilbert, D. G., and Beaumont, P. W. (1986). Mechanisms of toughening in rubber toughened polymers. *Acta Metallurgica*, 34(1):79–87.

Eyring, H. (1936). Viscosity, plasticity, and diffusion as examples of absolute reaction rates. *The Journal of Chemical Physics*, 4(4):283–291.

Favelukis, M., Zhang, Z., and Pai, V. (2000). On the growth of a non-ideal gas bubble in a solvent-polymer solution. *Engineering*, 40(6):1350–1359.

Federsen, C. (1966). Discussion to 'Plane strain crack toughness testing' ASTM Special Technical Publication.

Feng, J. J. and Bertelo, C. A. (2004). Prediction of bubble growth and size distribution in polymer foaming based on a new heterogeneous nucleation model. *Journal of Rheology*, 48(2):439.

Ferry, J. D. (1980). *Viscoelastic properties of polymers*. John Wiley & Sons.

Fleck, N. A., Hutchsinson, J. W., and Suo, Z. (1991). Crack path selection in a brittle adhesive layer. *International Journal of Solids and Structures*, 27(13):1683–1703.

Fleck, N. A., Stronge, W. J., and Liu, J. H. (1990). High strain-rate shear response of polycarbonate and polymethyl methacrylate. *Proceedings of the Royal Society A: Mathematical, Physical and Engineering Sciences*, 429(1877):459–479.

Forest, C., Chaumont, P., Cassagnau, P., Swoboda, B., and Sonntag, P. (2015). Polymer nanofoams for insulating applications prepared from CO2 foaming. *Progress in Polymer Science*, 41:122–145.

Gent, A. N. and Lindley, P. B. (1959). Internal rupture of bonded rubber cylinders in tension. *Proceedings of the Royal Society A: Mathematical, Physical and Engineering Sciences*, 249(3):195–205.

Gibson, L. J. and Ashby, M. F. (2014). *Cellular solids: Structure and Properties*. Cambridge University Press, 2nd edition.

Gilbert, D. G., Ashby, M. F., and Beaumont, P. W. R. (1986). Modulus-maps for amorphous polymers. *Journal of Materials Science*, 21(9):3194–3210.

Gilmour, I. W., Trainor, A., and Haward, R. (1979). Elastic moduli of glassy polymers at low strains. *Journal of Applied Polymer Science*, 23:3129–3138 (1979).

G'Sell, C., Hiver, J. M., Dahoun, A., and Souahi, A. (1992). Video-controlled tensile testing of polymers and metals beyond the necking point. *Journal of Materials Science*, 27(18):5031–5039.

G'Sell, C. and Jonas, J. J. (1979). Determination of the plastic behaviour of solid polymers at constant true strain rate. *Journal of Materials Science*, 14(155):583–591.

G'Sell, C. and Souahi, A. (1997). Influence of crosslinking on the plastic behavior of amorphous polymers at large strains. *Journal of Engineering Materials and Technology*, 119(3):223.

Guo, H. and Kumar, V. (2015). Solid-state poly(methyl methacrylate) (PMMA) nanofoams. Part I: Low-temperature CO2 sorption, diffusion, and the depression in PMMA glass transition. *Polymer*, 57:157–163.

Guo, H., Nicolae, A., and Kumar, V. (2015a). Solid-state microcellular and nanocellular polysulfone foams. *Journal of Polymer Science Part B: Polymer Physics*, 53(14):975–985.

Guo, H., Nicolae, A., and Kumar, V. (2015b). Solid-state poly(methyl methacrylate) (PMMA) nanofoams. Part II: Low-temperature solid-state process space using CO2 and the resulting morphologies. *Polymer*, 70:231–241.

Hamley, I. W. (2003). Nanostructure fabrication using block copolymers. *Nanotechnology*, 14(10):39–54.

Han, C. D. and Yoo, H. J. (1981). Studies on structural foam processing - 4. Bubble growth during mold filling. *Polymer Engineering and Science*, 21(9):518–533.

Hart-Smith, L. J. and Strindberg, G. (1997). Developments in adhesively bonding the wings of the SAAB 340 and 2000 aircraft. *Proceedings of the Institution of Mechanical Engineers, Part G: Journal of Aerospace Engineering*, 211(3):133–156.

Hattori, R. and Takei, K. (1950). Spring constants of compressive rubber blocks. *J. Soc. Rubber Industry Japan*, 23(7):194–197.

Haward, R. N. and Thackray, G. (1968). The use of a mathematical model to describe isothermal stress-strain curves in glassy thermoplastics. *Proceedings of the Royal Society A: Mathematical, Physical and Engineering Sciences*, 302(1471):453–472.

Hedrick, J. L., Russell, T. P., Labadie, J., Lucas, M., and Swanson, S. (1995). High temperature nanofoams derived from rigid and semi-rigid polyimides. *Polymer*, 36(14):2685–2697.

Hexcel (2003). Redux Bonding Technology Bonding Brochure.

Higgins, A. (2000). Adhesive bonding of aircraft structures. *International Journal of Adhesion and Adhesives*, 20(5):367–376.

Hill, R. (1950). *The Mathematical Theory of Plasticity*. Clarendon Press Oxford.

Hope, P., Ward, I. M., and Gibson, A. G. (1980). The hydrostatic extrusion of polymethyl methacrylate. *Journal of Materials Science*, 15:2207–2220.

Huang, F. H., Li, M. H., Lee, L. L., Starling, K. E., and Chung, F. T. H. (1985). Accurate equation of state for carbon dioxide. *Journal of Chemical Engineering of Japan*, 18(6):490–496.

Huang, Y. and Kinloch, A. J. (1992). Modelling of the toughening mechanisms in rubber-modified epoxy polymers. *Journal of Materials Science*, 27(10):2753–2762.

Hunston, D. L., Kinloch, A. J., and Wang, S. S. (1989). Micromechanics of fracture in structural adhesive bonds. *The Journal of Adhesion*, 28(2-3):103–114.

Imanaka, M., Ikeda, K., Nakamura, Y., and Kimoto, M. (2015). Fracture behaviour of epoxy resins modified with liquid rubber and crosslinked rubber particles under mode I loading. *Polymers and Polymer Composites*, 23(6):399–406.

Jeenjitkaew, C. and Guild, F. J. (2017). The analysis of kissing bonds in adhesive joints. *International Journal of Adhesion and Adhesives*, 75:101–107.

Joshi, Y. M. and Denn, M. M. (2004). Failure and recovery of entangled polymer melts in elongational flow. *Rheology Reviews*, 2004:1–17.

Katnam, K. B., Stevenson, J. P., Stanley, W. F., Buggy, M., and Young, T. M. (2011). Tensile strength of two-part epoxy paste adhesives: Influence of mixing technique and micro-void formation. *International Journal of Adhesion and Adhesives*, 31(7):666–673.

Khan, I., Adrian, D., and Costeux, S. (2015). A model to predict the cell density and cell size distribution in nano-cellular foams. *Chemical Engineering Science*, 138:634–645.

Kieken, B. (2001). Processing and performance of PS foamed with HCFC-142b and HFC-134a. *Technical Report ATOFINA Chemicals, Inc.*

Kinloch, A. J. and Shaw, S. J. (1981). The fracture resistance of a toughened epoxy adhesive. *The Journal of Adhesion*, 12(1):59–77.

Kinloch, A. J., Shaw, S. J., and Hunston, D. L. (1983). Deformation and fracture behaviour of a rubber-toughened epoxy: 2. Failure criteria. *Polymer*.

Kinloch, A. J. and Young, R. J. (1983). *Fracture Behaviour of Polymers*. Applied Science Publishers.

Komatsu, K., Sekiguchi, Y., Ihara, R., Tatsumi, A., and Sato, C. (2018). Experimental investigation of an adhesive fracture energy measurement by preventing plastic deformation of substrates in a double cantilever beam test. *Journal of Adhesion*, pages 1–18.

Kozlowski, M., Bula, A., and Hulimka, J. (2018). Determination of mechanical properties of methyl methacrylate adhesives (MMA). *ACEE Journal*, 3:87–96.

Krause, B., Sijbesma, H. J., Münüklü, P., Van Der Vegt, N. F., and Wessling, M. (2001). Bicontinuous nanoporous polymers by carbon dioxide foaming. *Macromolecules*, 34(25):8792–8801.

Kumar, V. and Suh, N. P. (1990). A process for making microcellular thermoplastic parts. *Polymer Engineering & Science*, 30(20):1323–1329.

Kumar, V., Van der Wel, M., Weller, J., and Seeler, K. A. (1994). Experimental characterization of the tensile behavior of microcellular polycarbonate foams. *Journal of Engineering Materials and Technology*, 116(4):439.

Kwon, T. Y., Ha, J. Y., Chun, J. N., Son, J. S., and Kim, K. H. (2014). Effects of prepolymerized particle size and polymerization kinetics on volumetric shrinkage of dental modeling resins. *BioMed Research International*, page 914739.

Lee, D.-B., Ikeda, T., Miyazaki, N., and Choi, N.-S. (2004). Effect of bond thickness on the fracture toughness of adhesive joints. *Journal of Engineering Materials and Technology*, 126(1):14–18.

Lee, S. and Ramesh, N. (2004). *Polymeric Foams: Mechanisms and Materials*. CRC Press.

Lee, Y. H., Park, C. B., Wang, K. I., and Lee, M. H. (2005). HDPE-clay nanocomposite foams blown with supercritical CO2. *Journal of Cellular Plastics*, 41(5):487–502.

Li, H. X. and Buckley, C. P. (2009). Evolution of strain localization in glassy polymers: A numerical study. *International Journal of Solids and Structures*, 46(7-8):1607–1623.

Li, R., Ye, N., Shaayegan, V., and Fang, T. (2018). Experimental measurement of CO2 diffusion in PMMA and its effect on microcellular foaming. *Journal of Supercritical Fluids*, 135:180–187.

Liau, I. S. and McHugh, M. A. (1985). *Supercritical Fluid Technologies*. Elsevier Science Publishers (New York).

Lindsey, G. H. (1967). Triaxial fracture studies. *Journal of Applied Physics*, 38(12):4843–4852.

Liu, Y., Chen, Y. C., Hutchens, S., Lawrence, J., Emrick, T., and Crosby, A. J. (2015). Directly measuring the complete stress-strain response of ultrathin polymer films. *Macromolecules*, 48(18):6534–6540.

Lord Rayleigh (1878). On the instability of jets. *Proceedings of the London Mathematical Society*, 1-10(1):4–13.

Lord Rayleigh (1917). On the pressure developed in a liquid during the collapse of a spherical cavity. *Philosophical Magazine Series 6*, 34(200):94–98.

Loureiro, A. L., Da Silva, L. F., Sato, C., and Figueiredo, M. A. (2010). Comparison of the mechanical behaviour between stiff and flexible adhesive joints for the automotive industry. *Journal of Adhesion*, 86(7):765–787.

Lu, H., Zhang, X., and Knauss, W. G. (1997). Conversion to bulk relaxation : studies on poly(methyl methacrylate). *Polymer*, 18(2):261–267.

Lu, X., Arduini-Schuster, M. C., Kuhn, J., Nilsson, O., Fricke, J., and Pekala, R. W. (1992). Thermal conductivity of monolithic organic aerogels. *Science*, 255(5047):971–971.

Lu, X., Caps, R., Fricke, J., Alviso, C. T., and Pekala, R. W. (1995). Correlation between structure and thermal conductivity of organic aerogels. *Journal of Non-Crystalline Solids*, 188(3):226–234.

Malkin, A. Y. and Petrie, C. (1997). Some conditions for rupture of polymer liquids in extension. *Journal of Rheology*, 41(1).

Maloney, K. and Fleck, N. (2018). Toughening strategies in adhesive joints. *International Journal of Solids and Structures*, 158:66–75.

Mark, J. E. (2003). *Physical Properties of Polymers Handbook*. Cambridge University Press, 3rd edition.

Martin-de León, J., Bernardo, V., and Rodríguez-Pérez, M. Á. (2016). Low density nanocellular polymers based on PMMA produced by gas dissolution foaming : fabrication and cellular structure characterization. *Polymers*, 8:256.

Martín-de León, J., Bernardo, V., and Rodríguez-Pérez, M. Á. (2017). Key production parameters to obtain transparent nanocellular PMMA. *Macromolecular Materials and Engineering*, 302(12):3–7.

Martín-de León, J., Bernardo, V., and Rodríguez-Pérez, M. Á. (2019). Nanocellular polymers: the challenge of creating cells in the nanoscale. *Materials*, 12(5):797.

Martini, J. E. (1981). *The production and analysis of microcellular foam*. PhD thesis, Massachusetts Institute of Technology., Dept. of Mechanical Engineering. (USA).

Martiny, P., Lani, F., Kinloch, A. J., and Pardoen, T. (2012). A multiscale parametric study of mode I fracture in metal-to-metal low-toughness adhesive joints. *International Journal of Fracture*, 173(2):105–133.

McLoughlin, J. R. and Tobolsky, A. V. (1952). The viscoelastic behavior of polymethyl methacrylate. *Journal of Colloid Science*, 7(6):555–568.

Melick, H. G. H. V., Casteren, I. A. V., Govaert, L. E., and Meijer, H. E. H. (1999). The influence of intrinsic strain softening on the macroscopic deformation behaviour of amorphous polymers. *Polymer Processing Society*, pages 1–10.

Miller, D. and Kumar, V. (2009). Microcellular and nanocellular solid-state polyetherimide (PEI) foams using sub-critical carbon dioxide I. Processing and structure. *Polymer*, 50:5576–5584.

Miller, D. and Kumar, V. (2011). Microcellular and nanocellular solid-state polyetherimide (PEI) foams using sub-critical carbon dioxide II. Tensile and impact properties. *Polymer*, 52(13):2910–2919.

Moller, J., Hunter, R., Molina, J., Vizán, A., Peréz, J., and da Silva, L. F. (2015). Influence of the temperature on the fracture energy of a methacrylate adhesive for mining applications. *Applied Adhesion Science*, 3(14):1–13.

Monteiro, J. P. R., Campilho, R. D. S. G., Marques, E. A. S., and da Silva, L. F. M. (2015). Experimental estimation of the mechanical and fracture properties of a new epoxy adhesive. *Applied Adhesion Science*, 3(1):1–17.

Nait-Ali, B., Haberko, K., Vesteghem, H., Absi, J., and Smith, D. S. (2006). Thermal conductivity of highly porous zirconia. *Journal of the European Ceramic Society*, 26(16):3567–3574.

Notario, B., Ballesteros, A., Pinto, J., and Rodríguez-Pérez, M. Á. (2016a). Nanoporous PMMA: A novel system with different acoustic properties. *Materials Letters*, 168:76–79.

Notario, B., Pinto, J., and Rodríguez-Pérez, M. Á. (2015). Towards a new generation of polymeric foams: PMMA nanocellular foams with enhanced physical properties. *Polymer*, 63:116–126.

Notario, B., Pinto, J., Solorzano, E., de Saja, J., Dumon, M., and Rodríguez-Pérez, M. Á. (2014). Experimental validation of the Knudsen effect in nanocellular polymeric foams. *Polymer*, 56:57–67.

Notario, B., Pinto, J., Verdejo, R., and Rodríguez-Pérez, M. A. (2016b). Dielectric behavior of porous PMMA: From the micrometer to the nanometer scale. *Polymer*, 107:302–305.

O'Connor, N. P. T. and Ball, R. C. (1992). Confirmation of the Doi-Edwards model. *Macromolecules*, 25(21):5677–5682.

Okolieocha, C., Raps, D., Subramaniam, K., and Altstädt, V. (2015). Microcellular to nanocellular polymer foams: Progress (2004-2015) and future directions - A review. *European Polymer Journal*, 73:500–519.

Palm, G., Dupaix, R. B., and Castro, J. (2006). Large strain mechanical behavior of poly(methyl methacrylate) (PMMA) near the glass transition temperature. *Journal of Engineering Materials and Technology, Transactions of the ASME*, 128(4):559–563.

Pantoula, M. and Panayiotou, C. (2006). Sorption and swelling in glassy polymer/carbon dioxide systems. *The Journal of Supercritical Fluids*, 37(2):254–262.

Pantoula, M., von Schnitzler, J., Eggers, R., and Panayiotou, C. (2007). Sorption and swelling in glassy polymer/carbon dioxide systems. Part II-Swelling. *Journal of Supercritical Fluids*, 39(3):426–434.

Pardoen, T., Ferracin, T., Landis, C. M., and Delannay, F. (2005). Constraint effects in adhesive joint fracture. *Journal of the Mechanics and Physics of Solids*, 53:1951–1983.

Patel, R. D. (1980). Bubble growth in a viscous Newtonian liquid. *Chemical Engineering Science*, 35(11):2352–2356.

Pearce, P. J., Arnott, D. R., Camilleri, A., Kindermann, M. R., Mathys, G. I., and Wilson, A. R. (1998). Cause and effect of void formation during vacuum bag curing of epoxy film adhesives. *Journal of Adhesion Science and Technology*, 12(6):567–584.

Pearson, G. H. and Connelly, R. W. (1982). Use of extensional rheometry to establish operating parameters for stretching processes. *Journal of Applied Polymer Science*, 27(3):969–981.

Pinto, J. (2014). *Fabrication and Characterization of the Physical Properties of Nanocellular Polymers: the Transition from the Micro to the Nanoscale*. PhD thesis, University of Bordeaux.

Pinto, J., Notario, B., Verdejo, R., Dumon, M., Costeux, S., and Rodríguez-Pérez, M. Á. (2017). Molecular confinement of solid and gaseous phases of self-standing bulk nanoporous polymers inducing enhanced and unexpected physical properties. *Polymer*, 113:27–33.

Pinto, J., Solórzano, E., Rodriguez-Perez, M. A., and De Saja, J. A. (2013). Characterization of the cellular structure based on user-interactive image analysis procedures. *Journal of Cellular Plastics*, 49(6):555–575.

Plateau, J. (1873). Experimental and theoretical statics of liquids subject to molecular forces only. *Memoires of the Academy of Belgium*.

Plesset, M. (1949). The dynamics of caviation bubbles. *Journal of Applied Mechanics*, 16:277—-282.

Rajendran, A., Bonavoglia, B., Forrer, N., Storti, G., Mazzotti, M., and Morbidelli, M. (2005). Simultaneous measurement of swelling and sorption in a supercritical CO2-poly(methyl methacrylate) system. *Industrial and Engineering Chemistry Research*, 44(8):2549–2560.

Ree, T. and Eyring, H. (1955). Theory of non-Newtonian flow. I. Solid plastic system. *Journal of Applied Physics*, 26(7):793–800.

Reglero Ruiz, J. A., Dumon, M., Pinto, J., and Rodriguez-Pérez, M. A. (2011). Low-density nanocellular foams produced by high-pressure carbon dioxide. *Macromolecular Materials and Engineering*, 296(8):752–759.

Rice, J. R. (1967). Discussion: "Stresses in an infinite strip containing a semi-infinite crack" (Knauss, W. G., 1966, ASME J. Appl. Mech., 33, pp. 356–362). *Journal of Applied Mechanics*, 34(1):248–250.

Rice, J. R. (1968). A path independent integral and the approximate analysis of strain concentration by notches and cracks. *Journal of Applied Mechanics*, 35(2):379.

Roiter, Y. and Minko, S. (2005). AFM single molecule experiments at the solid-liquid interface: In situ conformation of adsorbed flexible polyelectrolyte chains. *Journal of the American Chemical Society*, 127(45):15688–15689.

Rouse, P. E. (1953). A Theory of the linear viscoelastic properties of dilute solutions of coiling polymers. *The Journal of Chemical Physics*, 21(7):1272.

Rubinstein, M. and Colby, H. R. (2003). *Polymer Physics*. Oxford University Press.

Ryvkin, M. (2000). K -Dominance zone for a semi-infinite mode I crack in a sandwich composite. *International Journal of Solids and Structures*, 37:4825–4840.

Salomonsson, K. and Andersson, T. (2008). Modeling and parameter calibration of an adhesive layer at the meso level. *Mechanics of Materials*, 40(1-2):48–65.

Sanchez, I. C. and Lacombe, R. H. (1974). Theory of liquid-liquid and liquid-vapour equilibria. *Nature*, 251:281–283.

Santini, A. and Miletic, V. (2008). Comparison of the hybrid layer formed by Silorane adhesive, one-step self-etch and etch and rinse systems using confocal micro-Raman spectroscopy and SEM. *Journal of Dentistry*, 36(9):683–691.

Schmidt, D., Raman, V. I., Egger, C., du Fresne, C., and Schadler, V. (2007). Templated cross-linking reactions for designing nanoporous materials. *Materials Science and Engineering C*, 27(5-8 SPEC. ISS.):1487–1490.

Scigrip Europe (2017). Scigrip 300 Technical Data Sheet.

Sekiguchi, Y., Katano, M., and Sato, C. (2017). Experimental study of the Mode I adhesive fracture energy in DCB specimens bonded with a polyurethane adhesive. *Journal of Adhesion*, 93(3):235–255.

Shafi, M. A., Lee, J. G., and Flumerfelt, R. W. (1996). Prediction of cellular structure in free expansion polymer foam processing. *Polymer Engineering and Science*, 36(14):1950–1959.

Sharudin, R. W. B. and Ohshima, M. (2011). CO2-induced mechanical reinforcement of polyolefin-based nanocellular foams. *Macromolecular Materials and Engineering*, 296(11):1046–1054.

Shieh, Y. T. and Liu, K. H. (2002). Solubility of CO2 in glassy PMMA and PS over a wide pressure range: The effect of carbonyl groups. *Journal of Polymer Research*, 9(2):107–113.

Smith, T. L. (1958). Dependence of the ultimate properties of a SBR rubber on strain rate and temperature. *Journal of Polymer Science*, 32(124):99–113.

Smith, T. L. (1963). Ultimate tensile properties of elastomers. I. Characterization by a time and temperature independent failure envelope. *Journal of Polymer Science Part A: General Papers*, 1(12):3597–3615.

Span, R. and Wagner, W. (1996). A new equation of state for carbon dioxide covering the fluid region from the triple-point temperature to 1100 K at pressures up to 800 MPa. *Journal of Physical and Chemical Reference Data*, 25(6):1509–1596.

Stigh, U., Alfredsson, K. S., Andersson, T., Biel, A., Carlberger, T., and Salomonsson, K. (2010). Some aspects of cohesive models and modelling with special application to strength of adhesive layers. *International Journal of Fracture*, 165(2):149–162.

Street, J. R. (1968). The rheology of phase growth in elastic liquids. *Journal of Rheology*, 12(1):103.

Street, J. R., Fricke, a. L., and Philip Reiss, L. (1971). Dynamics of phase growth in viscous, non-newtonian liquids: Initial stages of growth. *Industrial and Engineering Chemistry Fundamentals*, 10(1):54–64.

Sun, C., Thouless, M., Waas, A., Schroeder, J., and Zavattieri, P. (2008a). Ductile-brittle transitions in the fracture of plastically deforming, adhesively bonded structures. Part II: Numerical studies. *International Journal of Solids and Structures*, 45(17):4725–4738.

Sun, C., Thouless, M., Waas, A., Schroeder, J., and Zavattieri, P. (2008b). Ductile–brittle transitions in the fracture of plastically-deforming, adhesively-bonded structures. Part I: Experimental studies. *International Journal of Solids and Structures*, 45(10):3059–3073.

Suo, Z. (1990). Failure of brittle adhesive joints. *Appl. Mech. Rev*, 43(5S):276–279.

Tada, H., Paris, P., and Irwin, G. (2000). *The Stress Analysis of Cracks Handbook*. Wiley, 3rd edition.

Timoshenko, S. and Goodier, J. N. (1970). *Theory of Elasticity*. McGraw-Hill, 3rd edition.

Trantina, G. G. (1972). Fracture mechanics approach to adhesive joints. *Journal of Composite Materials*, 6:192–207.

Treloar, L. G. (1975). *The Physics of Rubber Elasticity*. Oxford University Press, 3rd edition.

Treloar, L. G., Hopkins, H. G., Rivlin, R. S., and Ball, J. M. (1976). The mechanics of rubber elasticity [and discussions]. *Proceedings of the Royal Society A: Mathematical, Physical and Engineering Sciences*, 351(1666):301–330.

Tsou, A. H., Greener, J., and Smith, G. D. (1995). Stress relaxation of polymer films in bending. *Polymer*, 36(5):949–954.

Tvergaard, V. and Hutchinson, J. W. (1992). The relation between crack growth resistance and fracture process parameters in elastic-plastic solids. *Journal of the Mechanics and Physics of Solids*, 40(9):1377–1397.

Tvergaard, V. and Hutchinson, J. W. (1994). Toughness of an interface along a thin ductile layer joining elastic solids. *Philosophical Magazine A*, 70(4):641–656.

Tvergaard, V. and Hutchinson, J. W. (1996). On the toughness of ductile adhesive joints. *Journal of the Mechanics and Physics of Solids*, 44(5):789–800.

Van Krevelen, D. W. and Te Nijenhuis, K. (2009). *Properties of Polymers*. Elsevier Science, 4th edition.

Van Loock, F. and Fleck, N. A. (2018). Deformation and failure maps for PMMA in uniaxial tension. *Polymer*, 148:259–268.

Varias, A., Suo, Z., and Shih, C. F. (1991). Ductile failure of a constrained metal foil. *Journal of the mech*, 39(7):963–986.

Verreck, G., Decorte, A., Li, H., Tomasko, D., Arien, A., Peeters, J., Rombaut, P., Van den Mooter, G., and Brewster, M. E. (2006). The effect of pressurized carbon dioxide as a plasticizer and foaming agent on the hot melt extrusion process and extrudate properties of pharmaceutical polymers. *Journal of Supercritical Fluids*, 38(3):383–391.

Vinogradov, G. (1975). Viscoelasticity and fracture phenomenon in uniaxial extension of high-molecular linear polymers. *Rheologica Acta*, 14(10):942–954.

Von Konigslow, K., Park, C. B., and Thompson, R. B. (2017). Polymeric foaming predictions from the Sanchez-Lacombe equation of state: application to polypropylene-carbon dioxide mixtures. *Physical Review Applied*, 8(4):1–14.

Wang, C. H. (1997). Analysis of cracks in constrained layers. *International Journal of Fracture*, 83:1–17.

Wang, G., Wang, C., Zhao, J., Wang, G., Park, C. B., and Zhao, G. (2017). Modelling of thermal transport through a nanocellular polymer foam: toward the generation of a new superinsulating material. *Nanoscale*, 9(18):5996–6009.

Wang, S. S., Mandell, J. F., and McGarry, F. J. (1978). An analysis of the crack tip stress field in DCB adhesive fracture specimens. *International Journal of Fracture*.

Ward, I. M. and Sweeney, J. (2012). *Mechanical Properties of Solid Polymers*. John Wiley & Sons, 3rd edition.

Williams, M. L. (1957). On the stress distribution at the base of a stationary crack. *Journal of Applied Mechanics*, 24(1):109–114.

Williams, M. L., Landel, R. F., and Ferry, J. D. (1955). The temperature dependence of relaxation mechanisms in amorphous polymers and other glass-forming liquids. *Journal of American Chemical Society*, 77(12):3701–3707.

Wissinger, R. G. and Paulaitis, M. E. (1991). Glass transitions in polymer/CO2 mixtures at elevated pressures. *Journal of Polymer Science Part B: Polymer Physics*, 29(5):631–633.

Wu, P. D. and Van Der Giessen, E. (1993). On improved network models for rubber elasticity and their applications to orientation hardening in glassy polymers. *Journal of the Mechanics and Physics of Solids*, 41(3):427–456.

Wu, P. D. and van der Giessen, E. (1995). On neck propagation in amorphous glassy polymers under plane strain tension. *International Journal of Plasticity*, 11(3):211–235.

Xia, W. and Keten, S. (2014). Size-dependent mechanical behavior of free-standing glassy polymer thin films. *Journal of Materials Research*, 30(01):36–45.

Yan, C., Mai, Y. W., Yuan, Q., Ye, L., and Sun, J. (2001). Effects of substrate materials on fracture toughness measurement in adhesive joints. *International Journal of Mechanical Sciences*, 43(9):2091–2102.

Yannas, V. and Luise, R. R. (1982). Distinction between two molecular mechanisms for deformation of glassy amorphous polymers. *J. Macrom. Sci. Phys.*, 21(3):443–474.

Yee, A. F. and Pearson, R. A. (1986). Toughening mechanisms in elastomer-modified epoxies - Part 1 Mechanical studies. *Journal of Materials Science*, 21(7):2462–2474.

Youn, J. R. and Suh, N. P. (1985). Processing of microcellular polyester composites. *Polymer Composites*, 6(3):175–180.

Young, R. and Lovell, P. A. (2011). *Introduction to Polymers*. CRC Press, 3rd edition.

Zhou, C., Vaccaro, N., Sundarram, S. S., and Li, W. (2012). Fabrication and characterization of polyetherimide nanofoams using supercritical CO2. *Journal of Cellular Plastics*, 48(3):239–255.